

AIX-MARSEILLE UNIVERSITÉ
FACULTÉ DES SCIENCES DU SPORT DE LUMINY
163. avenue de Luminy
13288 Marseille CEDEX 03
FRANCE

THÈSE DE DOCTORAT

Spécialité : Robotique bio-inspirée

présentée par

Fabien EXPERT

en vue d'obtenir le grade de docteur de l'Université d'Aix-Marseille

FLYING ROBOT INSPIRED BY INSECTS: FROM OPTIC FLOW SENSING TO
VISUALLY GUIDED STRATEGIES TO CONTROL A MICRO AERIAL VEHICLE

UN ROBOT VOLANT INSPIRÉ DES INSECTES : DE LA MESURE DU FLUX OPTIQUE AUX
STRATÉGIES DE GUIDAGE VISUEL POUR UN MICRO HÉLICOPTÈRE

Soutenue le 21 Octobre 2013 devant le jury composé de :

M. SRINIVASAN	Prof. University of Queensland	QBI	Australia	Rapporteur
P. BONNIFAIT	Prof. UTC	Heudiasyc	Compiègne	Rapporteur
P. FRAISSE	Prof. Univ. Montpellier 2	LIRMM	Montpellier	Examineur
F. CHAUMETTE	DR INRIA	IRISA	Rennes	Examineur
F. BOYER	Prof. EMN	IRCCYN	Nantes	Examineur
O. LY	MCF-HDR Univ. Bordeaux 1	LaBRI	Bordeaux	Examineur
G. MONTAGNE	Prof. Aix-Marseille Université	ISM	Marseille	Examineur
F. RUFFIER	CR-HDR CNRS	ISM	Marseille	Directeur de thèse

École Doctorale des Sciences du Mouvement Humain - ED 463
UMR 7287 Institut des Sciences du Mouvement Étienne-Jules Marey

Remerciements

Je tiens en tout premier lieu à remercier Franck Ruffier pour l'opportunité de découvrir et travailler dans le monde de la biorobotique couplant ma passion de la robotique avec la recherche dans la nature des idées novatrices à la base des découvertes de demain. Je le remercie pour sa confiance, ses multiples conseils et sa grande disponibilité qui ont permis de mener à bien ces travaux et ont grandement contribué non seulement à leur réalisation mais aussi à leur présentation.

Je tiens à exprimer ma gratitude à l'ensemble des membres du jury pour avoir accepté d'évaluer mon travail.

Je tiens tout particulièrement à remercier Marc Boyron et Julien Dipéri pour avoir tous deux grandement contribué à l'ensemble des réalisations de cette thèse par leur assistance technique couplée à une quotidienne bonne humeur et disponibilité. Leurs expertises respectives pour la réalisation des cartes électroniques et la conception mécanique des bancs d'expérimentations sont à l'origine des résultats obtenus au cours de ce projet.

Je remercie aussi Nicolas Franceschini pour des discussions à travers lesquelles ressortent toute sa passion pour la recherche scientifique, Stéphane Viollet et Thibaut Raharijaona pour leurs conseils et leur écoute et Julien Serres pour m'avoir permis d'encadrer avec lui des projets à l'école des Mines.

Je remercie également Geoffrey Portelli pour son accueil au sein de l'équipe et les nombreuses discussions sur des points aussi bien techniques qu'écologiques. Il fut le premier avec qui j'ai partagé mon bureau mais je remercie aussi les autres : Bérénice Batut, Guillaume Sabiron, Fabien Colonnier, Bruno Boisseau et Stefano Mafrica car ils pourront confirmer que cela n'a pas été facile tous les jours.

En espérant ne pas en oublier, je voudrais aussi remercier tous les chercheurs, doctorants, stagiaires et personnels que j'ai cotoyé et avec qui j'ai travaillé au cours de ces 4 ans. Parmi eux, je pense notamment aux doctorants de l'équipe Raphaël Juston, Frédéric Roubieu, Lubin Kerhuel et bien sur Augustin Mannezy même si parfois mes jambes lourdes ont regretté de l'avoir suivi. Bien sur, je remercie chaleureusement tous les stagiaires croisés au cours de cet épisode pour les moments constructifs et agréables passés ensemble notamment Nicolas Leroux, Simon Benacchio, Antoine Bongard et Benoît-Jérémy Fuschlock. Merci aussi à

Erick Ogam, Jean-Louis Vercher, Reinoud Bootsma, Christophe Bourdin, Nathalie Fenouil, Bernadette Besson, Jessica Blanc et Richard Ferrato.

Je voudrais de plus exprimer ma gratitude à l'ensemble des membres du consortium CurvACE pour leur ouverture d'esprit et l'atmosphère agréable qu'ils ont créé contribuant à la réalisation d'un véritable travail d'équipe.

Comme un doctorat n'est qu'une partie de la vie, je voudrais aussi remercier ma famille et mes amis pour leur soutien et l'ensemble des souvenirs qui resteront. Je suis sûr qu'ils ont eu à supporter quelques discussions sur les robots ou les insectes dont ils se seraient bien passés. En particulier, je remercie mon grand père qui a été à l'origine de ma passion pour les sciences.

Enfin, je remercie Angie pour son amour, son soutien et sa patience. Because you're mine, I walk the line.

Publications

Journal Papers

D. Floreano, R. Pericet-Camara, S. Viollet, F. Ruffier, A. Brückner, R. Leitel, W. Buss, M. Menouni, **F. Expert**, R. Juston, M. K. Dobrzynski, G. L Eplattenier, H. A. Mallot and N. Franceschini (2013),

Miniature curved artificial compound eyes,

Proceedings of the National Academy of Sciences (PNAS), 110:9267-9272.

F.L. Roubieu, **F. Expert**, G. Sabiron and F. Ruffier (2012)

A two-directional 1-gram visual motion sensor inspired by the fly's eye

IEEE Sensors Journal, 13(3):1025-1035

F. Expert, S. Viollet and F. Ruffier (2011)

Outdoor field performances of insect-based visual motion sensors

Journal of Field Robotics, Wiley, 28(4):529-541

Patent

F. Ruffier and **F. Expert**

Motion sensor assembly for determining the angular velocity of a moving contrast in its field of view with a high accuracy

Patent BET 12P2802

Book chapter

T. Raharijaona, L. Kerhuel, J. Serres, F. Roubieu, **F. Expert**, S. Viollet, F. Ruffier and N. Franceschini (2013)

Insect Inspired Visual Motion Sensing and Bio-Inspired Flying Robots

Handbook of biomimetics and bioinspiration.

Peer-reviewed proceedings

F. Expert, F.L. Roubieu and F. Ruffier (2012)

Interpolation based "time of travel" scheme in a Visual Motion Sensor using a small 2D retina

IEEE Sensors Conference, Taipei, Taiwan, October, 29-31, pages 2231-2234

F. Expert and F. Ruffier (2012)

Controlling docking, altitude and speed in a circular high-roofed tunnel thanks to the optic flow

IEEE/RSJ International Conference on Intelligent Robots and Systems (IROS), Vilamoura, Portugal, October 8-11, pages 1125-1132

F. Ruffier and **F. Expert** (2012)

Visual motion sensing onboard a 50-g helicopter flying freely under complex VICON-lighting conditions

IEEE/CME Conference on Complex Medical Engineering, Kobe, Japan, July 1-4, pages 634-639

R. Pericet Camara, M. Dobrzynski, G. L'Eplattenier, J.-C Zufferey., **F. Expert**, R. Juston, F. Ruffier, N. Franceschini, S. Viollet, M. Menouni , S. Godiot, A. Brückner, W. Buss, R. Leitel, F. Recktenwald, C. Yuan, H. Mallot and D. Floreano (2011)

CURVACE - CURVed Artificial Compound Eyes.

2nd European Future Technologies Conference and Exhibition 2011, 7 pp. 308-309, Budapest, Hungary.

F. Expert, S. Viollet and F. Ruffier (2011)

A mouse sensor and a 2-pixel motion sensor exposed to continuous illuminance changes

IEEE Sensors 2011 conference, Limerick, Ireland, pages 974-977

Best Student paper award (First place)

F.L. Roubieu, **F. Expert**, M. Boyron, B.-J. Fuschlock, S. Viollet and F. Ruffier (2011)

A novel 1-gram insect based device measuring visual motion along 5 optical directions

IEEE Sensors 2011 conference, Limerick, Ireland, pages 687-690

F. Ruffier, S. Benacchio, **F. Expert** and E. Ogam (2011)

A tiny directional sound sensor inspired by crickets designed for Micro-Air Vehicles

IEEE Sensors 2011 conference, Limerick, Ireland, pages 970-973

Posters

F. Expert, S. Viollet and F. Ruffier (2010)

Miniature bio-inspired Optic flow sensor

ESF Conf. Functional Neurobiology in Minibrains: From Flies to Robots and Back Again

17-22 Octobre 2010, Sant Feliu de Guixols, Espagne

Domestic conferences

F. Expert, F.L. Roubieu, S. Viollet and F. Ruffier (2011)

Miniature visual motion sensors

Annual forum GDR Vision, INT, Marseilles

F.L. Roubieu, **F. Expert**, S. Viollet and F. Ruffier (2011)

Miniature visual motion sensors

GT UAV meeting, ENSAM, Paris

Contents

1	Introduction	13
1.1	Taking inspiration from insects	13
1.1.1	The compound eye of insects	13
1.1.2	Sensory modalities of the flying insects	18
1.1.3	How insects use optic flow	20
1.2	Measuring optic flow	28
1.2.1	Definition of the optic flow	28
1.2.2	Algorithms processing the local or global optic flow	32
1.2.3	Time of travel scheme	35
1.2.4	Several technologies of optic flow sensors	39
1.2.5	Design of an artificial compound eye	44
1.3	Taking inspiration from biology to develop new robots	47
1.3.1	Bio-inspired locomotion	48
1.3.2	Biomimetic vision-based robots	50
1.3.3	Bio-inspired robots developed at our laboratory	55
1.4	Objectives of the thesis	63
2	Performances of Optic flow sensors	65
2.1	Article 1: Outdoor Field Performances of Insect-Based Visual Motion Sensors	65
2.1.1	Abstract	68
2.1.2	Introduction	69
2.1.3	Description of the local visual motion sensors	71
2.1.4	Benchmarking of the visual motion sensors	76
2.1.5	Experimental results	77
2.1.6	Conclusion	81

2.2	Comparison with a mouse sensor	85
2.3	Article 2: Two-Directional 1-g Visual Motion Sensor Inspired by the Fly’s Eye	88
2.3.1	Abstract	90
2.3.2	Introduction	90
2.3.3	Description of the device	92
2.3.4	Experiment	96
2.3.5	Results	99
2.3.6	Estimation of the direction and the magnitude of the visual motion .	99
2.3.7	Conclusion	104
2.4	Article 3: Interpolation based “time of travel” scheme in a Visual Motion Sensor using a small 2D retina	106
2.4.1	Abstract	109
2.4.2	Introduction	109
2.4.3	Optimized implementation	110
2.4.4	Experiment and results	112
2.4.5	Conclusion	114
2.5	Conclusion	115
3	The first artificial compound eye: the CurvACE sensor	117
3.1	Introduction	117
3.2	Article 4: Miniature Curved Artificial Compound Eyes	121
3.2.1	Abstract	121
3.2.2	Introduction	121
3.2.3	Fabrication process	123
3.2.4	Results	126
3.2.5	Discussion	132
3.2.6	Supplementary Information	133
3.3	Conclusion	145
4	BeeRotor: a visually guided bio-inspired robot	147
4.1	Article 5: Autonomous optic flow-based speed control, ground-hugging and landing without any need for an accelerometer	149

4.1.1	Abstract	151
4.1.2	Introduction	151
4.1.3	OF-based strategies defined in a unique reference frame attached to the aerial robot's eye	153
4.1.4	The BeeRotor robot and its environment	164
4.1.5	Results in autonomous flight	169
4.1.6	Beerotor autopilot without any need for an accelerometer and an air- speed sensor	176
4.1.7	The vertical OF: an additional cue for the Beerotor autopilot	180
4.1.8	Discussion	184
4.2	Fully cylindrical CurvACE on the BeeRotor robot	189
4.2.1	Mechanical assembly of fully cylindrical CurvACE and BeeRotor	189
4.2.2	BeeRotor autopilot	190
4.2.3	Experimental results	192
4.2.4	Robustness to the background illuminance changes	193
4.3	Conclusion	194
5	Conclusion	197
5.1	Accomplished work	197
5.2	Toward optic flow sensors of the future	198
5.2.1	Global optic flow processing vs fusion of local motion sensors	199
5.2.2	Interesting regions of interest for insects and robots	199
5.2.3	Light adaptation mechanisms	200
5.2.4	Event-based chip in the future	200
5.3	Toward curved compound eyes of the future	201
5.3.1	Dynamically changing regions of interest	201
5.3.2	Various shapes for different applications	202
5.4	Toward smarter bio-inspired robots of the future	202
5.4.1	BeeRotor's commonalities with flying insects	203
5.4.2	Limitations of the BeeRotor autopilot	207
5.4.3	Possible applications	208
5.5	Feedback to biology	209

A Additional information about CurvACE	211
B Description of the BeeRotor aircraft	219
Bibliography	253
Résumé de thèse en français	273



Chapter 1

Introduction

1.1 Taking inspiration from insects

1.1.1 The compound eye of insects

In order to navigate in an unknown environment and to perform vital tasks, flying insects rely on several sensorial modalities. Among them, the vision is the most important one. In particular, their compound eye (see Figure 1.1) is the main source of information that will ensure an autonomous flight. The compound eye of insects is really different from the mammalian eye where the light is captured by a single lens and projected on a layer of photoreceptors, the retina. The compound eye is composed of a mosaic or repeating units called ommatidia, each consisting of a hexagonal lens, a transparent crystalline cone and light-sensitive visual cells (Franceschini, 1975). The main advantage of the compound eye is its compactness. Indeed, the design of the insect eye allows visual processing mechanisms to be situated immediately beneath the ommatidia, thus saving space and weight compared to the vertebrate eye composed of one single lens and where the space between the lens and the retina is wasted. An ommatidium is separated from its neighbors by an angle called the inter-ommatidial angle $\Delta\varphi$ which varies all along the compound eye and whose resolution becomes finest in the frontal region. The smaller the inter-ommatidial angle, the further objects (flowers, preys, predators) can be detected (Land, 1997). Due to the small size of the lens, the light is diffracted by the lens giving each ommatidium a Gaussian angular sensitivity (Götz, 1964) characterized by its full width at half maximum $\Delta\rho$ (also called acceptance angle) realizing a spatial low-pass filtering of the scene which is the first step of visual processing (Horridge, 1977) (see Figure 1.2). Each ommatidium is able to see only a



Figure 1.1: Picture of the compound eyes of a Robber Fly (*Holcocephala fusca*) from Thomas Shahan <http://www.flickr.com/photos/7539598@N04/3085177911/>.

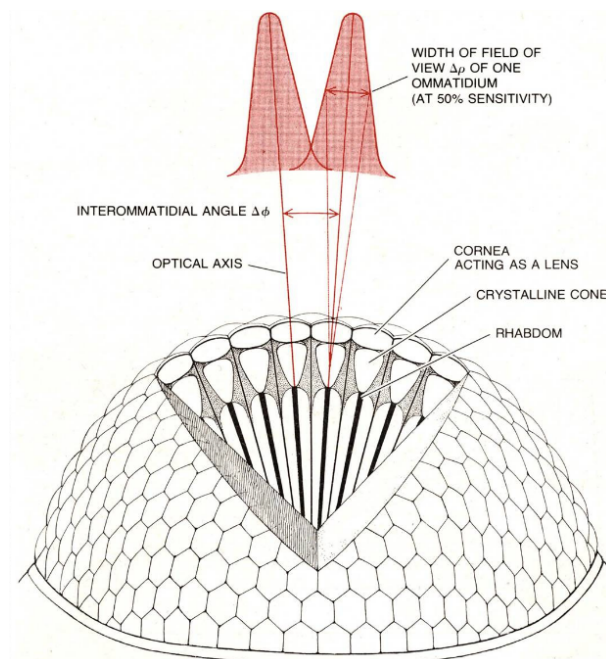


Figure 1.2: The compound eye of flying insects is made up of repeating units, the ommatidia, each of which is composed of a hexagonal lens called facet and several photoreceptors. In the fly's eye called neural superposition eye, each of the photoreceptors of an ommatidium has its own optical axis which can be parallel to the optical axis of one photoreceptor of a neighboring ommatidia. The ommatidia are characterized by their inter-ommatidial angle $\Delta\phi$ which varies along the compound eye. The resolution is better in the frontal region than in the lateral or ventral regions. Each ommatidium features a Gaussian angular sensitivity characterized by its full width at half maximum $\Delta\rho$. Adapted from (Horridge, 1977).

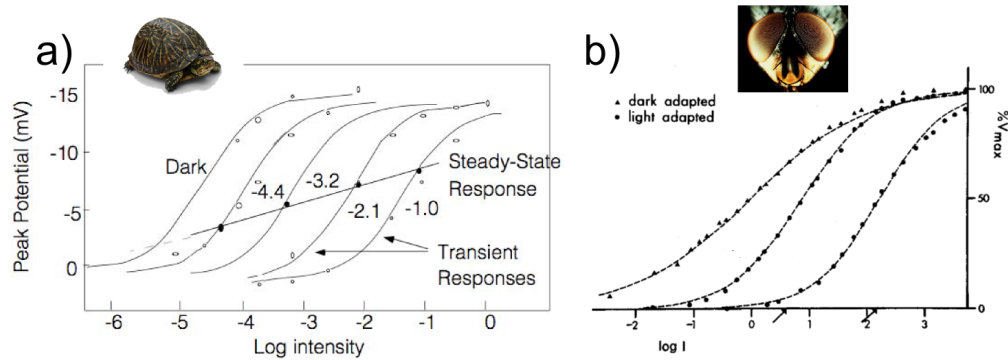


Figure 1.3: a) S-shape responses of the red and green cone photoreceptors recorded in the retina of the turtle under several decades of background illuminance. b) $V/\log I$ curves recorded from the fly *Calliphora*. Depending on the background illuminance value, the output response slope changes, but the voltage range of the light adapted curves remains the same. Adapted from (Normann & Perlman, 1979; Matic & Laughlin, 1981).

small region of the environment.

Even though authors observed strong variations of the number of ommatidia or the angular resolution between different flying insects, Land showed that, for diurnal insects, the acceptance angle $\Delta\rho$ is roughly equal to the inter-ommatidial angle $\Delta\varphi$ (Land, 1997) ensuring that there is little or no aliasing without oversampling the image.

1.1.1.1 Adaptation to the background illuminance

Like humans, insects are able to navigate as easily indoors where the illuminance generally ranges between a few lux to 1000 lux than outdoors where the illuminance can increase up to 100 000 lux. With electronic photoreceptors, it is very difficult to cover such a wide range of illuminance values without saturating or compressing the signal too much for low illuminance values. To cope with this issue, animal eyes like the turtle's eyes have the ability to automatically adapt to the background illuminance (Normann & Perlman, 1979) (see Fig.1.3a). For flying insects, a similar sensory adaptation mechanism capable of compensating for large changes in light intensity right at the photoreceptor level has also been discovered (Matic & Laughlin, 1981) (see Fig.1.3b) and extensively studied (Laughlin, 1989; Juusola & Hardie, 2001; Gu et al., 2005).

1.1.1.2 Information processing in the fly's eye

As can be seen in Figure 1.4, the ommatidia of the compound eye of the fly are connected to three ganglia or neuropils called the lamina, the medulla, and the lobula complex (lobula

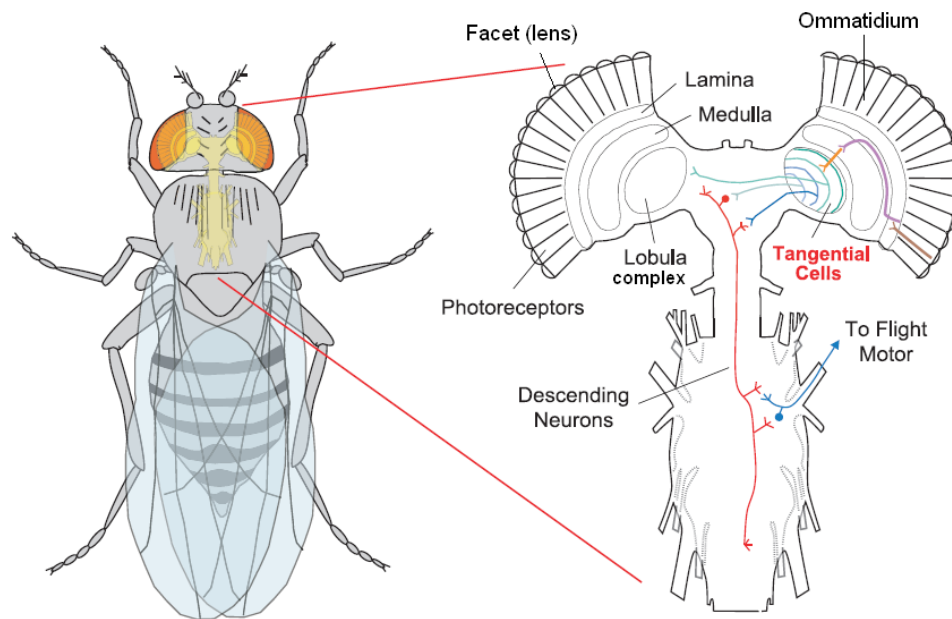


Figure 1.4: Fly visual and central nervous systems (cross section of the fly’s brain). Photoreceptors signals are transmitted to the lamina, which accentuates temporal changes and then to the medulla which computed the local angular speeds between adjacent photoreceptors. The lobula plate is made up of wide-field, motion-sensitive tangential neurons that send information to the contralateral optic lobe as well as to the thoracic ganglia, which control the wings. Adapted from (Humbert, 2005).

and lobula plate), corresponding to three centers of vision processing.

- The first optic lobe, the lamina, is placed directly under the ommatidia and receives direct input from photoreceptors. The neurons in this ganglion act as high-pass filters by amplifying temporal changes. It is also in this neuropil that the auto-adjustment to the background illuminance happens. The transient signals corresponding to contrasts in the environment are then transmitted to the medulla.
- Due to their small size, the neurons in the medulla are extremely difficult to record and little is known about it (Douglass & Strausfeld, 1996). However, behavioral experiments suggest that local motion detection between adjacent photoreceptors occurs at this level.
- The spatial convergence of the local Elementary Motion Detectors is performed in the third optic ganglion, the lobula plate. Information from several thousand of photoreceptors converge onto large neurons sensitive to specific motions.

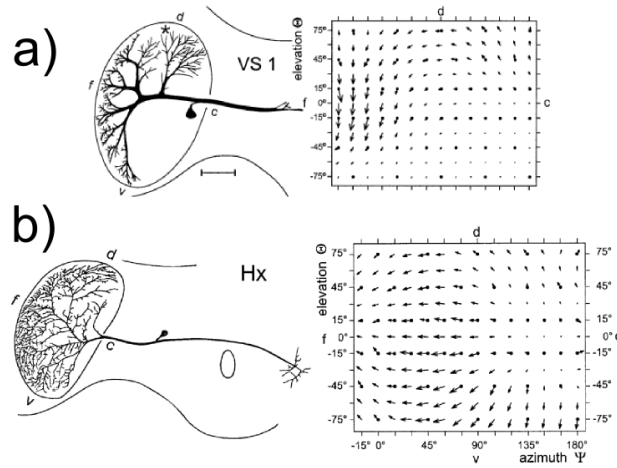


Figure 1.5: **a)** Anatomy and response field of the VS1 neuron. VS1 responds strongly to downward motion in the frontal and frontolateral area of the visual field. In the dorsolateral region, it responds to horizontal back-to-front motion and in the dorsocaudal region to the upward motion. Thus, the structure of the VS1 response field is tuned to be sensitive to a rotation along the pitch axis. **b)** Anatomy and response field of the Hx neuron. Hx is highly sensitive to horizontal back-to-front motion in the frontolateral visual field. Thus, the structure of the Hx response field is remarkably similar to a translatory optic flow field. Reprinted from (Krapp et al., 1998).

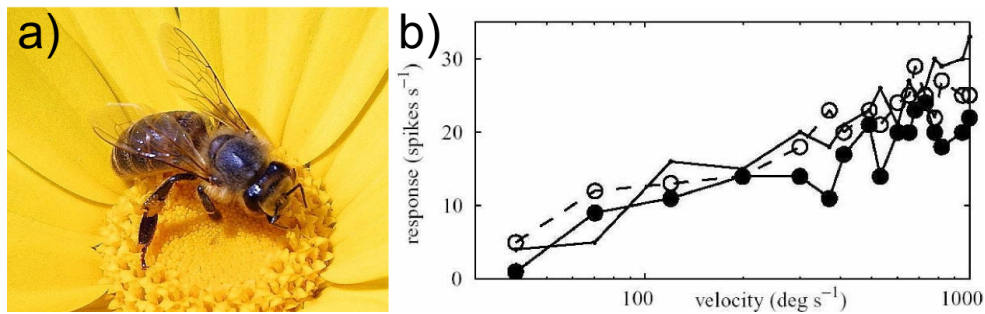


Figure 1.6: **a)** Picture of the honeybee *Apis Mellifera* from Jon Sullivan. **b)** Monotonic velocity response of a VT neuron for an optic flow ranging between $40^\circ/s$ and $1000^\circ/s$ for gratings with three different spatial periods (dots 38° , filled circles 19° , open circles 76°). The optic flow measured by VT neuron is independent of the spatial frequency of the contrasts. Reprinted from (Ibbotson, 2001).

1.1.1.3 Wide-Field Motion Sensitive Tangential Neurons

The third visual neuropil (see Fig.1.4) is a host to approximately 60 tangential interneurons called Lobula Plate Tangential Cells (LPTCs) that receive inputs from local motion detectors (Krapp & Hengstenberg, 1996) over a wide region of the field of view. Among these neurons are the groups of horizontal (HS) cells (Hausen, 1982) and vertical (VS) cells (Hengstenberg et al., 1982). These neurons are very interesting because they are sensitive to a specific direction of motion (from back to front for the H1 neuron). From extensive studies on flies (Krapp et al., 1998) of the receptive field organization and response characteristics of these neurons, it was possible to establish a map of their dendritic structures which are suitable to detect specific rotations and translations (see Fig.1.5). Similar neurons have been discovered by Ibbotson on the honeybee. They have been called Velocity-Tuned neurons or VT cells (Ibbotson, 2001) (see Figure 1.6) and optomotor neurons (Ibbotson, 1991) respectively for neurons sensitive to translatory and rotary motions.

1.1.2 Sensory modalities of the flying insects

Besides their compound eyes which is the main sensor involved in flight control, flying insects use other perceptive organs that are important to their navigation.

1.1.2.1 Halteres

For many animals, inertial information that can be detected faster than visual information is used in particular for compensatory reactions. For diptera, the hind wings have degenerated into an organ called halteres that can sense angular velocities along the 3 rotation axes (Fraenkel & Pringle, 1938). The halteres are oscillated in antiphase with the forewings and can sense Coriolis forces normal to their plane of oscillation that are generated during turns (Hengstenberg, 1984). However, behavioral experiments have shown that angular speed is better estimated using vision than inertial sensors at speeds lower than $50^\circ/s$ (Hengstenberg, 1988). Although the vast majority of insects can fly quite well without halteres, the better flying performances observed with Diptera can surely be explained partly by the presence of halteres.

1.1.2.2 Ocelli

Ocellar systems, which are present in many flying insects, can be very different depending on the species. In flies, the ocelli are three unfocused photoreceptors that form a triangle placed on the top of the head. As they are unlikely to detect any detailed spatial information on the visual scene, the ocelli are thought to be fast and ultra-sensitive horizon detectors, detecting tilted directions along two axes thanks to their triangular organization and therefore contributing to the dorsal-light response which compensates for attitude changes by fast head and body movements (Schuppe & Hengstenberg, 1993).

1.1.2.3 Antennae

Winged insects all possess a single pair of antennae performing various roles. For flies, antennae are believed to play an important role in the regulation of flight speed. Amputating the antennae of free-flying insects provides direct evidence that they are involved in flight control as we observe a decrease in the forward speed of Diptera with antennae amputation (Campan, 1964). Based on such an experiment, it is however hard to tell if the decrease in the forward speed reflects a specific effect on the regulation of airspeed, or a general degradation of flight performances. For this reason, authors have performed studies in which airspeed can be controlled accurately. In general, tethered insects decrease stroke amplitude in response to increases in the imposed airspeed, but, Burkhardt and Gewecke showed that when both antennae were amputated on Diptera, the stroke amplitude was almost insensitive to airspeed (Burkhardt & Gewecke, 1965) leading to the conclusion that the antennae play a role in airspeed control. The position of the antennae is actively controlled and adjusted during flight in the “antennal positioning reaction”. By orienting the antennae with respect to the oncoming flow, this presumably allows the mechanosensors to operate over a wider range of airspeed than would otherwise be possible (Mamiya et al., 2011). However, this also acts as a high-pass filter and therefore enhances the ability of insects to sense changes in airspeed.

1.1.2.4 Other sensory organs

Insects are also richly covered in trichoid sensilla which are sensitive to wind stimuli and involved in flight control. Finally, insects wings are instrumented with Campaniform sensilla

which can sense wing load and are involved in the precise regulation of wing kinematics for Diptera (Hengstenberg, 1988). More details about these organs and the other sensorial modalities of insects can be found in the in-depth review (Taylor & Krapp, 2007).

1.1.3 How insects use optic flow

Winged insects are able to navigate in unfamiliar environments by relying heavily on the optic flow that is generated by their own motion. Among all the behaviors, we will describe with more details how optic flow is used by insects for 6 typical behaviors which are of great interest for robotic purposes.

1.1.3.1 Course stabilization to fly straight

Being able to fly in translation is a very important characteristic for insects. Indeed, we saw that the rotational optic flow only contains information of the insect's own rotations whereas the translatory optic flow will depend on the ratio between the horizontal speed of the insect and the distance to the objects which can be used to navigate autonomously. This is the reason why at least 4 different mechanisms that will now be described, namely the optomotor response, the vestibulo-ocular reflex, the head reorientation and the saccade which have been found to help the insects to always perform translation providing the visual system with less complicated optic flow fields, hence facilitating extraction of useful information.

The optomotor response (yaw axis)

By tethering an insect in a rotating striped drum, authors have shown that the insect will try to turn in the direction of the rotation (Reichardt, 1969) (see Figure 1.7). If the drum rotates clockwise, the insect will generate a yaw torque in the clockwise direction, and vice versa. This reaction helps the insect maintain a straight course by compensating for undesired deviations, for example a lateral wind causing the insect to turn to the left will be compensated by a yaw rotation to the right. This optomotor response depends on the temporal frequency of contrasts and is therefore well explained if the motion is processed using Reichardt correlator (Hassenstein & Reichardt, 1956) (see section 1.2.2).

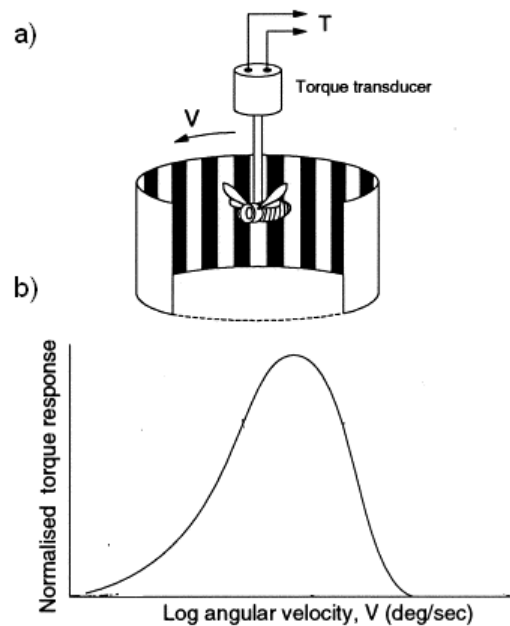


Figure 1.7: Optomotor response of insects. **a)** When a flying insect is placed in a rotating drum covered with textured pattern, it attempts to turn in the direction of rotation of the drum. **b)** The resulting yaw torque registered by a torque transducer reflects the strength of this optomotor response. The strength of the optomotor response is a bell-shaped function of the rotational speed of the drum, peaking at a specific angular velocity of rotation. This response depends on the temporal frequency of the contrasts. Adapted from (Srinivasan et al., 1999).

Vestibulo-ocular reflex (roll axis)

For flies, but also for humans, a vestibulo-ocular reflex is used to compensate for any roll rotation of the body allowing the insect to keep its gaze straight independently of its body (see Figure 1.8) and therefore extract a more straightforward optic flow (see Figure 1.10 lower part). This reflex disappeared when the halteres were disabled with glue (Hengstenberg, 1988) showing that this reflex is mediated by the inertial measurements of the halteres sensing angular velocities very quickly allowing for a rapid head compensation. This reflex is however enhanced with vision (see Figure 1.8d) since the head roll compensation is coarser in the absence of visual features in the environment.

Head reorientation (pitch axis)

When flying, the body pitch of *Drosophila* is elevated more steeply than during resting or walking on even ground. However, Hengstenberg showed that the fly's head is pitched downward during flight compensating for the body angle in order to keep its eyes in the same

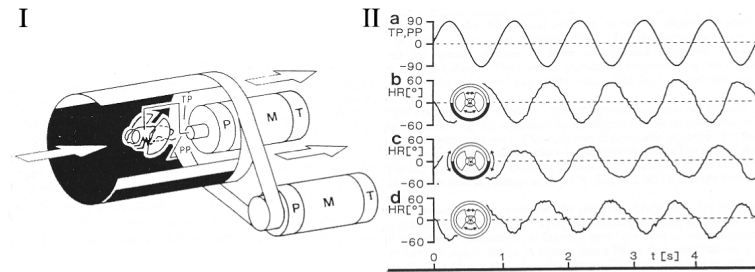


Figure 1.8: I) Tethered fly placed inside a drum covered with artificial patterns. The drum or the fly can be rotated along their roll axes thanks to two separate motors. II) **a)** A periodic rotation is imposed to the fly or the artificial environment. **b)** Head roll compensation when the fly rotates around its roll axis in a stationary environment. We can see that the head position is out of phase in comparison with the body angle indicating a perfect roll compensation. **c)** Head roll compensation when only the drum is rotating. **d)** Head roll compensation when the fly is forced to rotate around its roll axis without any visual contrast in the environment. Adapted from (Hengstenberg, 1988).

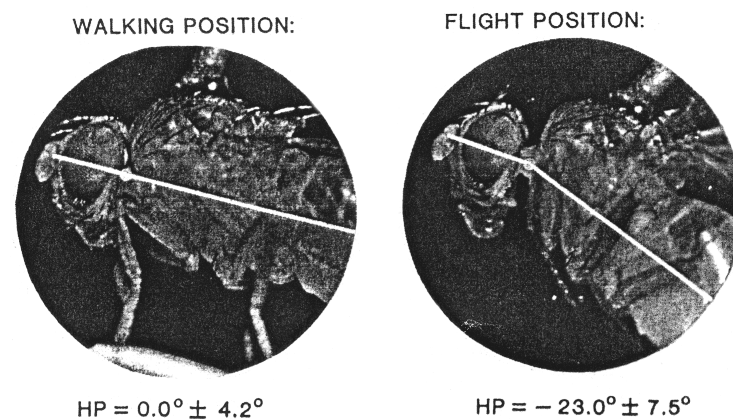


Figure 1.9: Comparison of the head pitch angle of the *Drosophila* walking and flying. Although the body pitch axis is more important during flight, the head is pitched downward in order to keep the gaze direction constant. Reprinted from (Hengstenberg, 2001).

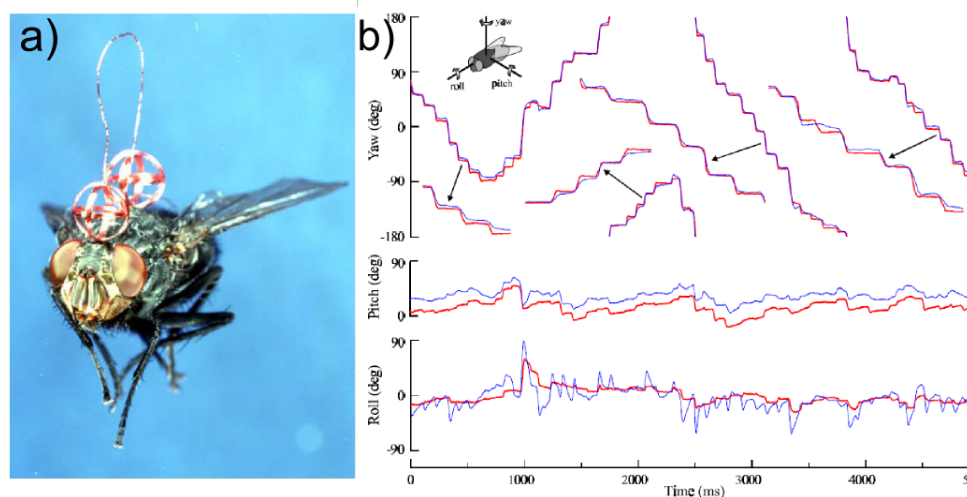


Figure 1.10: **a)** Blowfly *Calliphora vicina* with sensor coils attached to the thorax and the head placed in a Helmholtz cage. The position and orientation of the head and the thorax are determined thanks to the sensor coils measuring during flight externally generated magnetic fields. **b)** Angles during a typical blowfly flight. Blue lines represent thorax movement, and red lines represent the corresponding head movement. We can see that the blowfly regularly performs strong yaw saccades of its head and body. Steps in pitch usually occur simultaneously in the thorax and head but the head pitch does not exactly follow the body pitch. The thorax makes fast and large roll movements during flight, because they are required to make turns. The head roll, in contrast, is quite modest for most of the time because most of the thorax rotation is effectively compensated by counter rolls of the head relative to the thorax based on the halteres measurements. Reprinted from (van Hateren & Schilstra, 1999).

direction (Hengstenberg, 1992) (see Figure 1.9). In “free” flight, the only ones who succeeded in recording the thorax and head orientations of the fly are van Hateren and Schilstra (van Hateren & Schilstra, 1999). The middle part of the Figure 1.10 shows the simultaneous steps in pitch of the thorax and the head. These variations in thorax pitch mainly affect the direction of the flight force, thus producing variations in forward speed. By examining the results, they noticed that, between steps, the head pitch is slightly more stable than the thorax pitch suggesting that a feedback is used to control the head pitch and cancel undesirable rotations of the head along the pitch axis.

Saccades (yaw axis)

The three behaviors we have just described are not all triggered by the visual system but they strongly limit the rotations of the head during flight favoring the extraction of translational optic flow richer in useful information for autonomous navigation. However, it is not possible in order to fly autonomously to always go straight in the same direction. This is the reason why the insects have been found to regularly perform very fast body

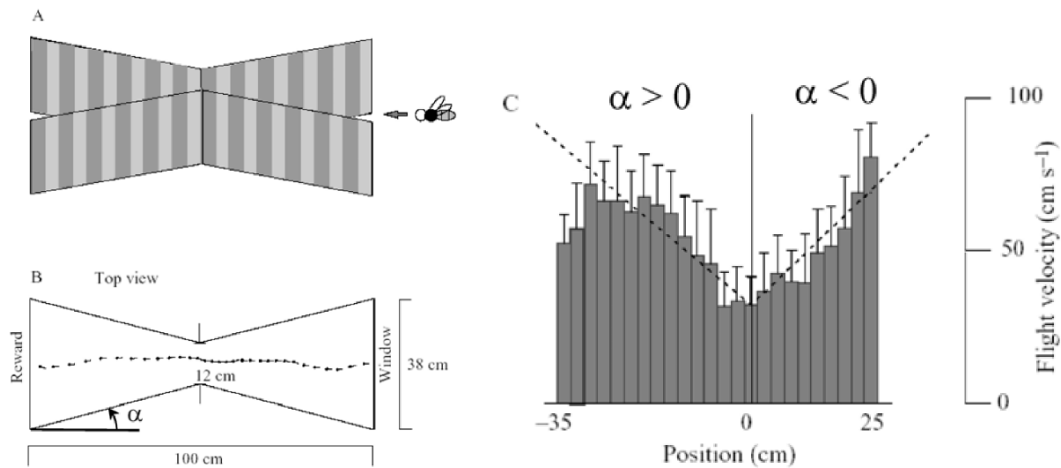


Figure 1.11: **a)** Honeybees are trained to fly in a 1-m long tapered tunnel lined with vertical black and white gratings. **b)** The width of the tunnel varies from 38cm to 12cm. **c)** Variation of flight speed during the flight. Speed decreases as the tunnel narrows, and increases as it widens. Reprinted from (Srinivasan et al., 1996).

saccades and head rotations (Collett & Land, 1975; van Hateren & Schilstra, 1999). We can see these strong saccades along the yaw axis in Figure 1.10. Generally, head saccades are shorter than the corresponding thorax saccades. However, during these head rotations, the rotational optic flow can be up to $1400^\circ/\text{s}$ and the Elementary Motion Detectors of the compound eye of insects have been found to not be sensitive to such high values of angular speed (Franceschini et al., 1989). All these behaviors previously described seem to allow the insects to mainly fly in translation and therefore extract translational optic flow during straight flight paths interspersed with fast rotations during which motion vision may not be used.

1.1.3.2 Speed control

Experiments performed on honeybees have shown that the visually perceived optic flow is used to control their forward speed (Srinivasan et al., 1996; Baird et al., 2006; Fry et al., 2009). In particular, Srinivasan et al. (1996) proved that honeybees reduce their speed when flying in a narrowing corridor and their forward speed increase when the corridor is widening (see Figure 1.11). Baird et al. (2006) showed, in a tunnel with moving lateral walls, that when the wall is moving in the direction of flight (decreasing the perceived optic flow), flight speed increases and reciprocally. These two studies led to the conclusion that the bees adjusted their flight speed so as to hold the speed of the image on the retina constant which has been confirmed to be true in both the horizontal and the vertical planes (Portelli et al., 2011).

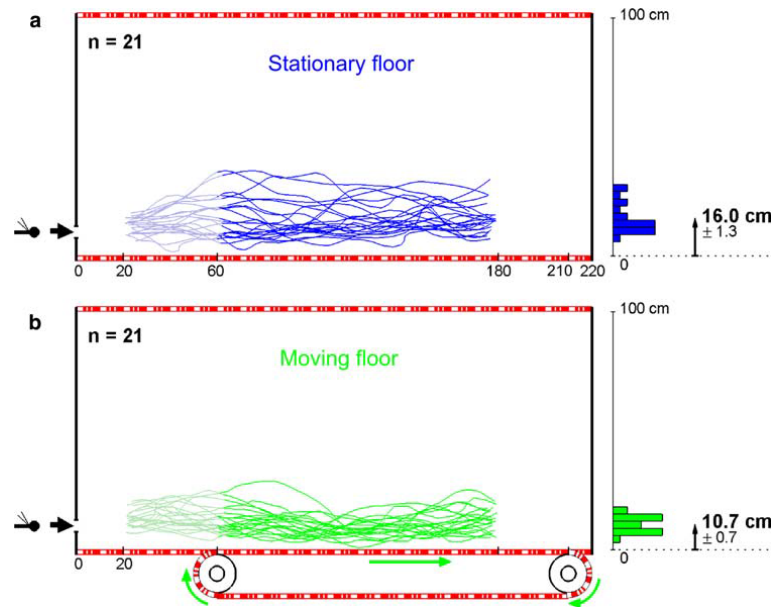


Figure 1.12: Side view of the trajectories of honeybees flying freely along a 1-m high, 2.2m-long tunnel lined with contrasts. **a)** Honeybees flew over a stationary floor at a mean altitude of 16 ± 1.3 cm. **b)** When the floor was set in motion in the same direction as the honeybees' flight, the insects descended and flew at a height of only 10.9 ± 0.7 cm above the floor. Reprinted from (Portelli et al., 2010).

1.1.3.3 Altitude control and obstacle avoidance

Recent studies have shown that the ventral optic flow plays an important role in insects altitude control (Barron & Srinivasan, 2006; Baird et al., 2006; Portelli et al., 2010). In the last study, authors used a tunnel with a moving floor and recorded the height of flying honeybees over the stationary floor and the moving floor. They observed that when flying over the moving floor, which moved in the same direction as their flight, honeybees may descend at a lower height in order to restore the measured ventral optic flow to the same value as the one perceived when they were flying over the stationary part of the floor (see Figure 1.12). The fact that they lowered their height of flight instead of increasing their forward speed is consistent with the optic flow regulator hypothesis proposed in previous studies (Ruffier & Franceschini, 2004, 2005; Franceschini et al., 2007).

Very recently, a new study has been published contradicting the optic flow regulator hypothesis. Indeed, Straw et al. (2010) showed in a 3D reality environment that the flies control their altitude using three reflexes:

- Edge tracking: they tend to fly at the same height as nearby horizontal edges,
- Wide-field stabilization: when presented with vertical motion, the flies change their

climb rate to stabilize the perceived motion (this behavior is similar to the optomotor response in the horizontal plane),

- Expansion avoidance: Flies climb away from a ventral expansion of the optic flow.

Although these results indicate that several behaviors are responsible of the altitude control of insects, they do not explain how honeybees descend when presented with ventral regressive optic flow (Portelli et al., 2010) confirming that a regulation of the ventral optic flow has to be encoded in the insects brain to control their altitude.

1.1.3.4 Odometry based on optic flow

When searching for new food sources, honeybees typically fly over large distances describing complex trajectories. Yet, when they have found a food source, they fly a direct route back to their home (von Frisch, 1967). After returning to the hive, these bees communicate the distance and direction of the food source to their nest mates . The information is encoded in the waggle dance (von Frisch, 1967), which consists of a series of alternating clockwise and anticlockwise loops, interspersed by a phase in which the bee waggles its abdomen from side to side. The length of this waggle run signals the distance flown and the orientation of the waggle axis (relatively to gravity) signals the azimuthal direction of the food source, relative to the direction of the sun (von Frisch, 1967). To do so, it is now established that bees estimate the distance flown by measuring the optic flow perceived during flight (Esch & Burns, 1995; Srinivasan et al., 1996; Eckles et al., 2012). This odometer is influenced by the richness in terms of visual information of the overflown terrain (Tautz et al., 2004) and the presence of celestial cues (Dacke & Srinivasan, 2008).

1.1.3.5 Automatic landing and Docking

By filming freely flying bees as they landed on a flat, horizontal surface, Srinivasan et al. (2000) showed that the bees “tend to hold the angular velocity of the image of the surface constant as they approach it with an instantaneous speed of descent proportional to the instantaneous forward speed” (see Figure 1.13a). These characteristics reflect a simple and effective strategy for achieving a smooth landing, by simultaneously reducing their forward speed and their distance to the ground until reaching touchdown with almost no speed. No explicit knowledge of flight speed or height above the ground is necessary. Wagner has shown

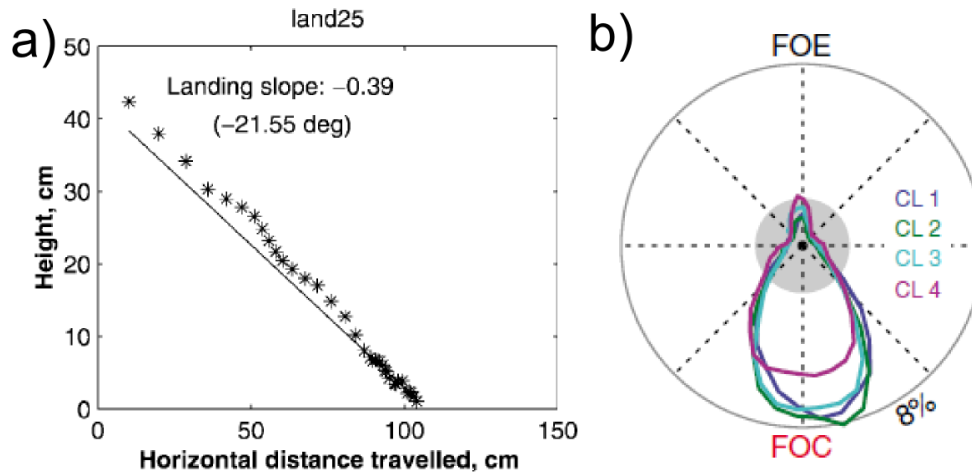


Figure 1.13: a) Variation of the bee's height as a function of the horizontal distance travelled during landing. b) Histogram of the mean orientation of a fly when presented with a focus of expansion for several Contrast Levels (CL) in a drum where patterns can be projected. Regardless of the contrast of the pattern, the flies robustly oriented toward the focus of contraction (FOC). Reprinted from (Srinivasan et al., 2000; Reiser & Dickinson, 2010).

that a landing behavior can also be elicited by an important image expansion of a target (Wagner, 1982).

1.1.3.6 Expansion avoidance

It was recently established on experiments over tethered *Drosophila* that these insects strongly avoid the focus of expansion (FOE) due to the vicinity of an object (Tammero et al., 2004; Reiser & Dickinson, 2010) (see Figure 1.13b) which is, as Reiser and Dickinson pointed out, paradoxical as in order to move forward, an animal must tolerate a frontal FOE as it navigates through a visual landscape (Reiser & Dickinson, 2010). This can be explained by the fact that this collision avoidance reflex is overridden by an attractive target (Reiser & Dickinson, 2010) like a long vertical stripe contrary to a small spot (that could correspond to a predator or another insect) which is considered repulsive (Maimon et al., 2008). Very recently, Reiser and Dickinson have shown that the flies are attracted by a focus of expansion at low speeds whereas the behavior transforms to expansion avoidance at higher speeds (Reiser & Dickinson, 2013). As already discussed, for the altitude control, it has been recently demonstrated that a similar ventral expansion avoidance system exists in the brain of insects (Straw et al., 2010).



Figure 1.14: Schematic representation of the optic flow vector field generated on the retina of an agent during a landing phase. Each vector magnitude and direction represents the angular speed of this point of the environment. The point right in front of the agent where the angular speed is zero is called the focus of expansion. Reprinted from (Gibson, 1950).

1.2 Measuring optic flow

1.2.1 Definition of the optic flow

In order to navigate in an unknown environment, animals use information coming from all their sensory modalities and in particular their vision. When moving in a 3D environment, the textured objects create a 2D vector field of angular speeds on the retina (Gibson, 1950). This motion field generates a motion of the image intensities called the optic flow (OF). It is an angular speed vector field (see Fig.1.14) which is generally complex because it results from the motion of the agent relatively to the moving or stationary objects of the environment.

1.2.1.1 Mathematical expression of the optic flow

We assume the vantage point corresponding to our retina is at the origin O and we are looking at a fiducial point in the direction $d_i(\Phi, \Theta)$ characterized by the azimuthal angle Φ and the elevation angle Θ . The object in that direction is situated at a distance $D_i(\Phi, \Theta)$ corresponding to a nearness $\sigma_i(\Phi, \Theta) = \frac{1}{D_i(\Phi, \Theta)}$. In that situation, the movement of the vantage point can always be decomposed into a translation vector \vec{T} and a rotation vector \vec{R} . The motion field or parallax $p(\Phi, \Theta)$ is given by Koenderink & van Doorn (1987):

$$p(\Phi, \Theta) = -\sigma_i(\Phi, \Theta)(\vec{T} - (\vec{T} d_i(\Phi, \Theta))d_i(\Phi, \Theta)) - \vec{R} \times d_i(\Phi, \Theta) \quad (1.1)$$

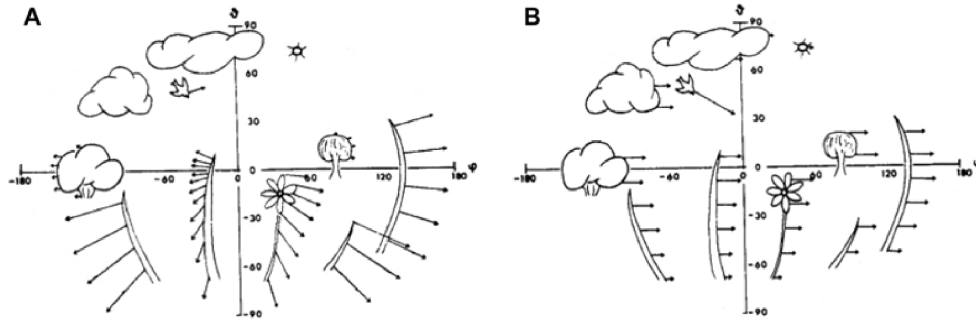


Figure 1.15: Optic flow vector field generated for a specific motion of an agent **a)** Translation of the agent through the point O. We notice that the generated optic flow is greater for closer objects. **b)** Rotation of the agent along the vertical axis. The magnitude of the optic flow is the same for every object in the environment. Compared to all the stationary objects, the moving bird generates a specific optic flow. Reprinted from (Buchner, 1984).

Although the motion parallax is a 3D vector, it is always orthogonal to the direction $d_i(\Phi, \Theta)$. This is the reason why the optic flow field is generally represented using a Mercator projection where each position is defined by the angles of azimuth Φ and elevation Θ . As we can see from the previous expression, only the translatory component of the motion parallax is linked to the nearness and can therefore be used to estimate the distance to objects if the rotation is null.

Figure 1.15 shows the optic flow vector field generated respectively during a translation and a rotation. In translation, we notice that the closer the objects, the higher the angular speed. On the other hand, in rotation, the angular speed does not depend on the distance to objects .

Definition of the degrees of freedom of a flying agent

In a 3-dimensional environment, a flying agent can move along 6 directions called degrees of freedom. It can translate along its body axes and rotate around the same axes (see Fig.1.16). Each of these motions generates a characteristic optic flow pattern on the eyes.

Expression of the optic flow for a pure rotation

During a pure rotation, for example around the roll axis (see Fig. 1.17 right), the generated optic flow depends on:

- The rotational speed of the agent around the roll axis Ω_{roll} ,

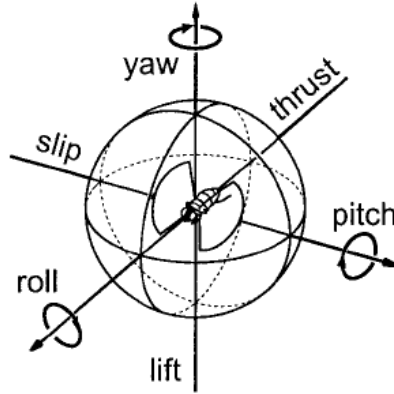


Figure 1.16: Motions of the fly can be described by their translatory (thrust, slip, lift) and rotatory components (roll, pitch, yaw) around the 3 body axes (longitudinal, transverse, vertical). Adapted from (Krapp et al., 1998).

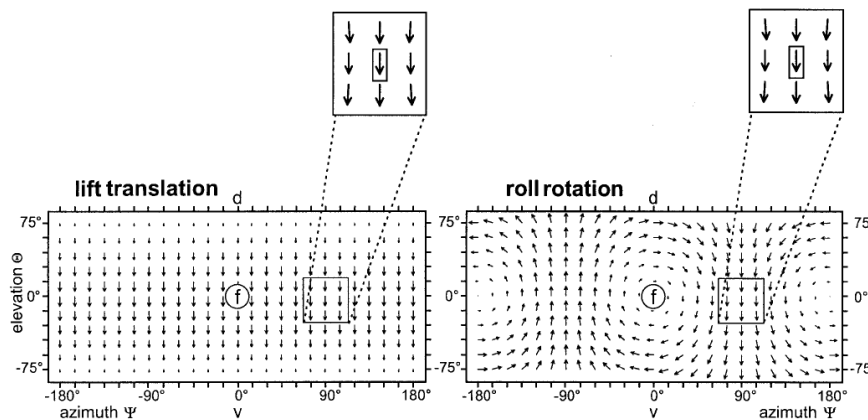


Figure 1.17: Mercator projections of the structure of the optic flow vector field generated during a lift translation along the vertical body axis and a roll rotation around the longitudinal body axis of an agent. The direction of the arrows correspond to the direction of the local angular speeds generated with a magnitude reflected by the length of the arrows. Overall, the 2 optic flow fields can easily be distinguished from one another. However, we have seen in section 1.1.1 that in the visual system of insects, motion is analyzed locally thanks to Elementary Motion Detector (EMD) neurons. The magnified views of specific regions of the Field of View show that the local optic flow pattern generated by an upward lift translation can not be discriminated from the one of a roll rotation to the left which illustrates the necessity to fuse an important number of EMD neurons. This problem is known as the aperture problem. Adapted from (Krapp et al., 1998).

- The pitch angle θ ,
- The yaw angle Ψ .

The rotational optic flow can, in that case, be written:

$$\vec{\omega}_R = \Omega_{roll} * \sqrt{(1 - \cos^2\Psi \times \cos^2\Theta)} \quad (1.2)$$

The equation 1.2 shows that the rotational optic flow is independent of the distance between the agent and the considered objects.

Expression of the optic flow for a pure translation

During a pure translation, for example along the vertical axis z (see Fig. 1.17 left), the generated optic flow depends on:

- The translation speed of the agent \vec{V} ,
- The distance D between the agent and the object in that direction,
- The angle between the motion direction and the direction of the object (here the pitch angle θ).

The translational optic flow can, in that case, be written:

$$\vec{\omega}_T = \frac{V}{D} \times \sin\theta \quad (1.3)$$

Contrary to the rotational optic flow, the angular speed due to a translational motion varies with the ratio between the forward speed of the agent and the distance to the objects of the environment. This clearly shows that the translational optic flow will reflect how dangerous an object of the environment can be. In the visual field, two specific points stand out : the focus of expansion in the direction of motion, where all the optic flow vectors diverge, and the focus of construction in the opposite direction, where all the optic flow vectors converge. At both points, the magnitude of the optic flow is zero.

Although the optic flow does not give an immediate measurement of distance or speed, it can be used on robots like on animals to fly safely thanks to reflexive behaviors (see section

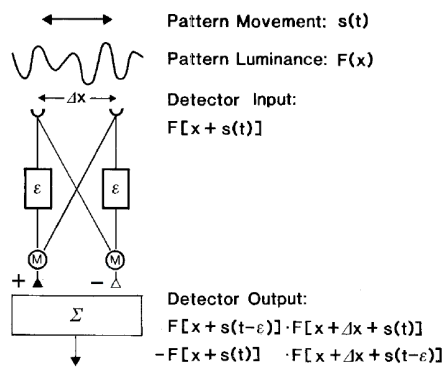


Figure 1.18: Schematic representation of a correlation-based elementary motion detector. In this version of the detector model, the input signal of one branch of each unit is delayed by a brief time interval ϵ . In each unit, the delayed signal from one channel is multiplied with the non-delayed signal of the neighboring input channel. The final detector output is given by the difference of the units' output. Reprinted from (Egelhaaf & Reichardt, 1987).

1.3.2). It has also been used in computer vision for visual servoing tasks (Crétual, 1997; Crétual & Chaumette, 2001).

1.2.2 Algorithms processing the local or global optic flow

Numerous algorithms have been proposed in the last decades to process optic flow. They can be classified into two main categories (Ullman, 1981):

- the intensity-based schemes where motion measurements are based directly on the local changes in light intensity values,
- the token-matching schemes which first identify features such as edges, lines or regions and then measure motion by matching these features over time and detecting their changing positions.

1.2.2.1 Intensity-based schemes

Again, the intensity-based schemes can be subdivided into two categories: the correlation schemes and the gradient-based techniques.

Correlation schemes

Correlation schemes compare the outputs of two photodetectors to illuminance variations at two adjacent positions. The output of the first pixel at time t is compared with that of

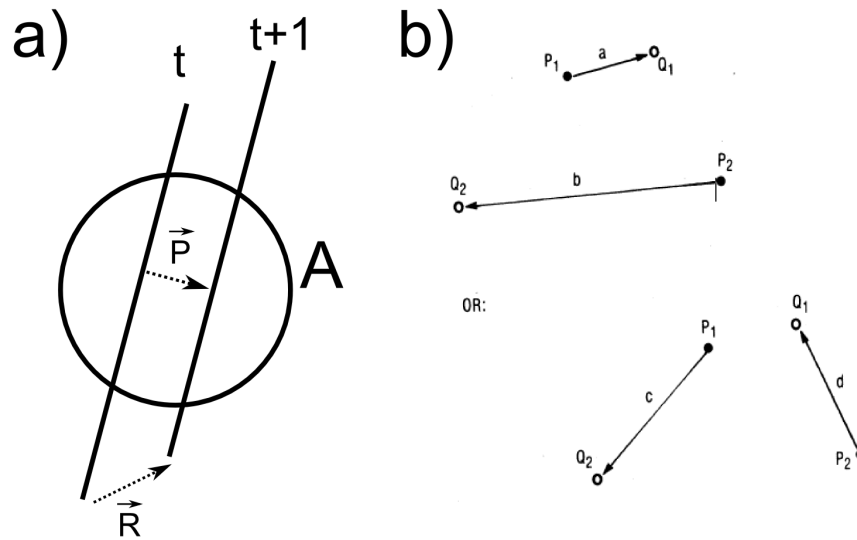


Figure 1.19: **a)** The aperture problem. The direction of motion of a one-dimensional object cannot be recovered when we look at this object through an aperture A small in comparison with the object. In this example, the real motion of the object is described by the vector \vec{R} but the perceived motion \vec{P} is only the component normal to the object. Motion along the object itself is invisible. To determine the motion completely, a second stage must combine several local measurements. **b)** The correspondence problem. P_1 and P_2 are shown on the first frame, Q_1 and Q_2 on the next. Two one-to-one matches are possible, leading to two possible patterns of perceived motion. Adapted from (Ullman, 1981).

the second pixel at time $t - \delta t$. The general representation of a correlation scheme is given in Figure 1.18. The most famous one is the Hassenstein and Reichard correlator which has been inspired by the visual system of the cockroach and where the delay has been replaced by a low-pass filter. Besides, this scheme provides a successful model for the optomotor behavior of various insects in response to motion in their visual fields (see section 1.1.3).

However, they have some obvious limitations. For example, the speed of motion must lie within a certain range, determined by the delay (or the low-pass filtering) and the separation between the receptors even if a wider range of velocities can be covered by a family of several detectors with different internal delays and interreceptor separations. Besides, motion measurement cannot be determined reliably from the output of a single detector of this type as these schemes do not resolve the aperture problem (see Figure 1.19a). In order to solve it, the output of several correlators have to be integrated spatially over a larger field of view like presented in (Bülthoff et al., 1989) but it generally requires a lot of computational power which makes it unsuitable for real-time computation. By performing the search over time instead of over space, Camus (Camus, 1995) ended up with a very efficient algorithm processing the optic flow in real time.

Gradient-based techniques

A number of gradient-based schemes for motion detection and measurement have been considered for use in computer vision systems. These methods are all based on the relation between the intensity gradient at a given point and the temporal intensity change produced at that point when the intensity pattern is moving. If $I(x, y)$ denotes the light intensity in the image, then

$$-\frac{dI}{dt} = I_x u + I_y v \quad (1.4)$$

where $\frac{dI}{dt}$ is the temporal intensity change at position (x, y) ; I_x and I_y represent the intensity gradient at that image point; and u, v , are the local velocities in the x and y directions, respectively. Since $\frac{dI}{dt}$, I_x and I_y are all measurable, we can theoretically determine a linear relation between u and v thanks to the above equation. However, uniquely determining the values of u and v requires more than a single measurement. This means that certain assumptions about the velocity field have to be made.

Depending on the constraints on the velocity vector, we end up with a more or less complex algorithm. Among the most famous ones are the Horn and Schunck algorithm (Horn & Schunck, 1981) and the Lucas-Kanade algorithm (Lucas & Kanade, 1981) which both start by assuming that the intensity of the image is conserved (i.e. $\frac{dI(x,t)}{dt} = 0$). Plenty of others schemes have been proposed using first or second temporal derivatives and a review of their performances can be found in Barron et al. (1994). One main issue with these algorithms is the difficulty to accurately estimate optic flow at low speeds and high speeds because the accuracy depends on the frame rate of the acquisition system. By adapting the frame intervals based on the speed of the objects, Chen et al. (2012) proposed a scheme based on the Lucas-Kanade algorithm and using High-Frame-Rate videos able to process optic flow in a wide range of velocities. Although not exactly a gradient-based method, Srinivasan (1994) proposed a new algorithm called the Image Interpolation Algorithm (I2A), which minimizes the error at each time step between the acquired image and the interpolated one based on a set of the previous images. The main advantage of this algorithm is its robustness in comparison to the required computational power which makes it suitable to be embedded on microcontrollers.

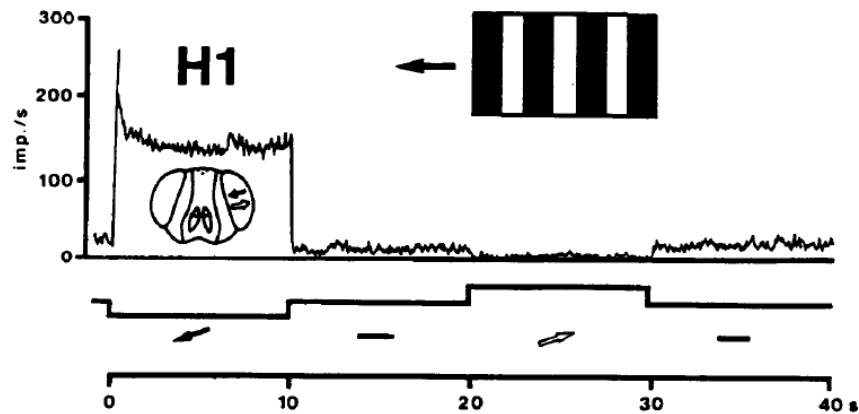


Figure 1.20: Characteristic response of the H1 neuron to horizontal motion of a striped pattern presented to the eye in the preferred (\leftarrow) and the non-preferred (\rightarrow) directions. We notice an important firing rate of the neuron in the preferred direction and its rapid decay to its resting level when the pattern is stationary. During motion in the non-preferred direction, the H1 neuron is inhibited. Reprinted from (Riehle & Franceschini, 1984).

1.2.2.2 Token matching schemes

In token-matching schemes for measuring motion, identifiable elements called tokens like edges or gray-level discontinuities are located and then matched over time (Potter, 1977; Chown & Aggarwal, 1977). The main limitation of such schemes is what we call the correspondence problem (see Figure 1.19b). Indeed, if the sampling rate is too low compared to the velocity of the image, the risk increases to match two different tokens over time leading to a false measurement of the optic flow. By taking inspiration from electrophysiological experiments performed on the fly's eye, Franceschini et al. proposed a token-matching scheme (Pichon et al., 1989) which has been later called the “time of travel” scheme.

1.2.3 Time of travel scheme

1.2.3.1 Biological inspiration

Among the 60 wide-field tangential cells sensitive to motion in the fly's lobula plate, Franceschini et al. (Riehle & Franceschini, 1984; Franceschini et al., 1989) chose the H1 neuron to analyse the visual processing of the fly's eye. They electrophysiologically recorded the activity of the H1 neuron while simulating two adjacent photoreceptors of the same om-

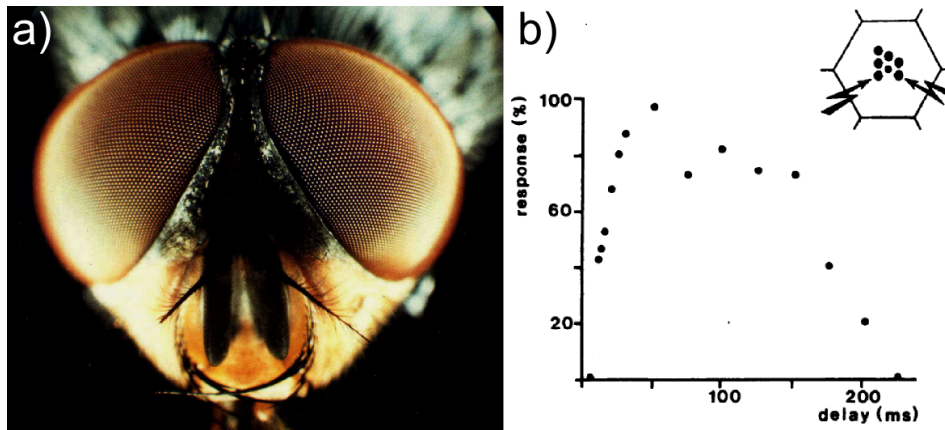


Figure 1.21: **a)** Head of the blowfly *Calliphora erythrocephala* with its panoramic compound eyes. **b)** Relative increase in firing rate of H1 in response to a 10-ms long flash presented to two adjacent photoreceptors in the preferred direction with a varying delay represented on the abscissa. The obtained response profile describes the impulse response of an Elementary Motion Detector neuron of the fly’s eye. Reprinted from (Franceschini, 2004; Franceschini et al., 1989).

matidium. As these photoreceptors have different optical axes, by simulating consecutively one after the other, we create an “apparent motion” in the field of view of the ommatidium. They noticed that by simulating successively only two photoreceptors of the same ommatidium, the H1 neuron firing rate increased when presented with a motion in the preferred direction and was inhibited when the motion was in the non-preferred direction (Riehle & Franceschini, 1984) (see Figure 1.20). By varying the interstimulus interval (see Figure 1.21), they measured the impulse response of the Elementary Motion Detector neuron in the fly’s eye (Franceschini et al., 1989). We can see that the H1 neuron is not activated when the delay between the stimuli is too short ($<10\text{ms}$) or too long ($>230\text{ms}$) which limits the range of the EMD neuron (between $16^\circ/s$ and $360^\circ/s$ for the considered ommatidium having an interreceptor angle of 3.6°). Besides, their results showed two peaks in the response of the H1 neuron when applying 100-ms long flashes without overlap. This can be explained by the existence of two separate pathways sensitive respectively to ON-ON sequences (successive dark to light transitions of the two adjacent photoreceptors) and OFF-OFF sequences (successive light to dark transitions of the two adjacent photoreceptors). Based on these findings, the authors proposed a functional diagram describing the processing of the angular speed which has since then been implemented in several technologies (see next subsection). Recent experiments have shown the existence of separate brightness increments and decrements circuits controlled by the L1 and L2 neurons (Reiff et al., 2010).

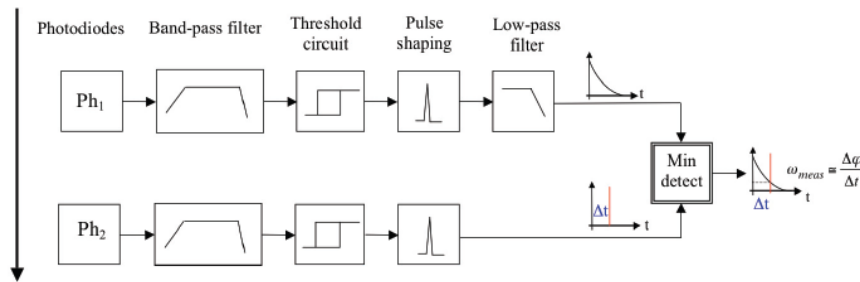


Figure 1.22: Principle of the initial fully analog optic flow sensor derived from electrophysiological analyses of the housefly's EMD neuron (Blanes, 1986, 1991). Reprinted from (Franceschini et al., 2009).

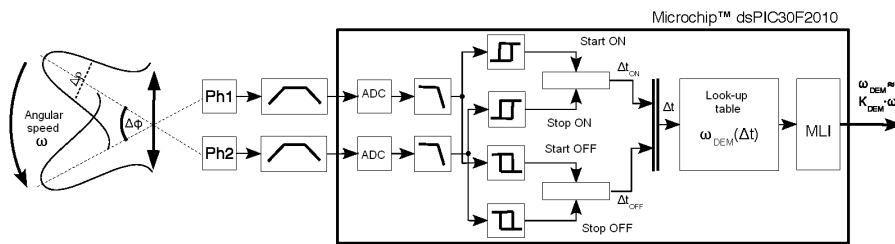


Figure 1.23: Description of the hybrid 2-pixel LMS circuit. Steps 1 and 2 were performed prior to digitization. The output from each analog filter was digitized through an analog-to-digital converter (ADC) and the other steps of the processing were realized onboard the microcontroller. Two separate pathways process the angular speed of ON and OFF contrasts. Among the two measured delays Δt_{OFF} and Δt_{ON} , only the most recent one is kept to obtain a better refresh rate of the data. Reprinted from (Serres, 2008).

1.2.3.2 Evolution of the bio-inspired 2-pixel local motion sensor

Based on the experiments performed on the fly's eye, Franceschini et al. proposed a first implementation of a bio-inspired scheme that we call 2-pixel Local Motion Sensor (LMS) realized using analog electronics (Blanes, 1986; Pichon et al., 1989) (Figure 1.22). This processing which measures the time delay between two signals originating from two adjacent photoreceptors can be decomposed in 4 main steps:

- Spatial sampling and low-pass spatial filtering (which is achieved by defocusing the miniature camera lens to obtain a Gaussian angular sensitivity for each pixel).
- Band-pass filtering to cancel the high frequency noises and to differentiate the visual signals in order to enhance the transient signals.
- Thresholding with hysteresis to detect a contrast. This threshold value is critical to the performances of the 2-pixel LMS: too low a value will trigger measurements corresponding to noisy signals, too high a value will decrease the refresh rate of the data.

- Measuring the time delay Δt between the two detected contrasts. In this first implementation, the time delay was measured by sampling when an impulse was generated by the second signal, a decreasing exponential function generated by the first signal. The optic flow $\omega = \frac{\Delta\varphi}{\Delta t}$ was then approximated by a function $e^{-\frac{\Delta t}{\tau}}$ which is monotonically increasing. By compressing the optic flow values with this non-linear function, the noise on the value of the optic flow at high speed was reduced.

This processing which mimics the behavior of the H1 neuron processes the time delay between the two signals in a preferred direction (here photodiode 1 has to see the contrast before photodiode 2). A bi-directional measurement can be done by adding a second 2-pixel LMS in the opposite direction and by taking the maximum value between the two (Blanes, 1991).

A few years later, a hybrid version mixing analog and digital processing was proposed (Amic, 2002; Ruffier et al., 2003; Pudas et al., 2007; Serres, 2008) (see Figure 1.23). The bandpass-filtering step was still done using analog filtering to differentiate the visual signals but also to avoid aliasing before digitization. The following steps of the processing were carried onboard a microcontroller (here a dsPIC30F2010) where the signals were first low-pass filtered to cancel the high frequencies, in particular the 100Hz of the artificial lighting and then two separate pathways were used to process ON and OFF contrasts. The optic flow was finally estimated using an exponential function or a look-up table. This implementation has also been implemented successfully onboard a FPGA (Aubépart & Franceschini, 2007).

A very different implementation of a 2-pixel LMS measuring the time delay between two signals has been proposed. In this implementation, the time delay is not measured only when a contrasting edge crosses successively two adjacent photoreceptors but continuously by tracking the time delay Δt between the two signals (Kerhuel, 2009; Kerhuel et al., 2009). Although not bio-inspired, this processing allows to process the angular speed in both directions with good accuracy without being dependent on a threshold value. However, this algorithm is more costly in terms of computational power and is sensitive to the initial condition because the initial value of the delay will influence the convergence of the processing.

Finally, it has been recently shown that, by adjusting the optical characteristics and the filtering steps, it was possible to adapt the range of such sensors in particular to measure low angular speeds (Sabiron et al., 2013), i.e. low optic flows.

1.2.4 Several technologies of optic flow sensors

As we have just seen, a lot of different algorithms have been proposed to process the optic flow vector field or the angular speed and to be used onboard robots. These algorithms have been implemented on optical mouse sensors, sensors based on a standard CMOS camera and sensors based on an analog Very Large Scale Integration (aVLSI) chip.

1.2.4.1 Computer mouse sensors

Lyon's optical mouse (Lyon & Haeberli, 1982) was the first digital motion detection chip. Photocurrent over a photodiode is integrated over time on a capacitor, and transduced to a digital signal by a simple inverter. The time for charging up the capacitor depends on the input light level. Through lateral inhibition a cell exposed to a brighter pattern which reaches a high state earlier will suppress the neighbors. Thus by tracking the location of the winner cells, the movement of the input image can be determined.

Since the 80's, a lot of improvements have been made to the retina and the algorithm used in computer mouse sensors to process a 2-D local optic flow. Very little is known about the onboard processing or the performances of such sensors except for the results of one study which recently characterized such sensors (Chan et al., 2010) and the results of a comparative analysis of the possibility to use optical mouse sensors to track vehicles instead of more standard technologies like GPS, accelerometers or laser rangefinders (Jackson et al., 2007).

Recently, such sensors have been used outside the context of their original purpose as optic flow sensors onboard flying robots. By simply adjusting their lens, these mouse sensors turned out to be accurate optic flow sensors which now equip several outdoor robots (more details are given in section 1.3.2).

1.2.4.2 CMOS camera

Recently, authors have designed new motion sensors suitable for robotic applications based on standard CMOS camera. For example, Díaz et al. (2008) developed a very high-frame-rate optical-flow processing system. This system is based on a high-frame-rate CMOS camera followed by a superpipelined, fully parallelized architecture for optical-flow processing implemented onboard a FPGA. The 2-D optic flow is estimated using a gradient-based method

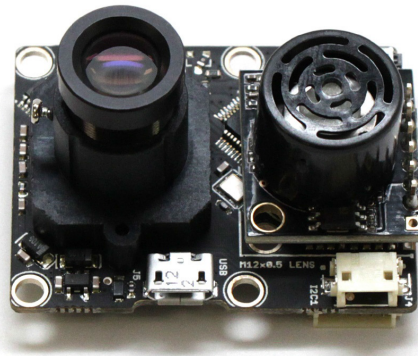


Figure 1.24: The PX4FLOW optical flow sensor estimating the optic flow using block matching with mounted lens on the left and ultra sonic distance sensor on the right. The distance sensor can be used to scale the measured optic flow which is derotated based on the embedded rate gyro. Reprinted from (Honegger et al., 2013).

which is an improved version of the Lucas-Kanada algorithm and can process up to 170 frames/s at a resolution of 800×600 pixels.

Another sensor based on a CMOS camera of 320×240 pixels and implementing a correlation scheme onboard a FPGA has been designed (Watman & Murayama, 2011). Although it was only a prototype on a larger scale, such sensors could be strongly minimized to meet the needs of Micro Aerial Vehicles (MAVs) as the computational cost is quite low. The Reichardt correlator has also been implemented on a FPGA coupled to a CMOS camera equipped with a fisheye lens to visually sense rotations around different body axes (Plett et al., 2012) similarly to the fly’s tangential cells of the lobula plate. In order to have a good measurement, the authors embedded 57.600 Elementary Motion Detectors covering a field of View of 185° and acquiring visual signals at 300 frames/s.

In May 2013, a new optic flow sensor based on a CMOS imager and using a block matching algorithm implemented onboard a ARM Cortex microcontroller was presented (Honegger et al., 2013). This small sensor which is also equipped with a rate gyro and an Ultra Sonic distance sensor can automatically compensate rotations of the camera and scale the optic flow to metric values (see Figure 1.24 b).

1.2.4.3 Analog Very Large Scale Integration (aVLSI) chip

Since the 90’s, a lot of aVLSI chips processing a 1-D angular speed or a 2-D optic flow have been designed. Only a few of them are presented here but the advised reader is encouraged to take a detailed look at Sarpeshkar et al. (1993); Indiveri et al. (1996); Sarpeshkar et al.

(1996); Etienne-Cummings et al. (1997); Sicard et al. (1998); Moini (1999); Liu & Usseglio-Viretta (2001); Higgins & Shams (2002); Laviana et al. (2005); Stocker (2006); Okuno & Yagi (2009); Brinkworth et al. (2009); Orchard et al. (2009); Xu et al. (2011) and Deutschmann (1997) for review.

Tanner and Mead’s optical flow chip

Tanner and Mead (Tanner & Mead, 1986; Mead, 1989) designed a chip which was supposed to globally solve the optical flow equation:

$$\frac{d}{dt}I(x, t) = 0 \Leftrightarrow \frac{\delta I}{\Delta x}v_x + \frac{\delta I}{\Delta y}v_y = -\frac{\delta I}{\Delta t} \quad (1.5)$$

The previous equation is computed by each pixel and the errors of all the pixels are added up to estimate the global velocity. However, the result of this chip was unsatisfactory due to device mismatch. Moore and Koch’s motion detector (Moore & Koch, 1991) was a variation of the Tanner Mead sensor where the temporal derivative was multiplied instead of divided by the spatial derivative.

Delbrück’s velocity tuned motion sensor

A very different motion detection implementation was presented by Delbrück (Delbrück, 1993). Contrary to the previous scheme depending on spatial and temporal derivatives, the motion is extracted using temporal correlation. This implementation is an extension of the Reichardt detector with a delay line acting as a tuned filter. An edge passing creates a traveling signal that spreads and decays over time. If the velocity of the edge is matched with the delay line, the output signal increases. This chip, which is inspired by biological systems, was the first implementation of a functional 2-D motion detector which computes local motion information.

Kramer et al.’s Facilitate and sample velocity sensor

Kramer et al.’s proposed a chip strongly inspired by the “time of travel” scheme presented in Blanes (1986); Pichon et al. (1989). This 1-D velocity sensor (Kramer et al., 1995) detects

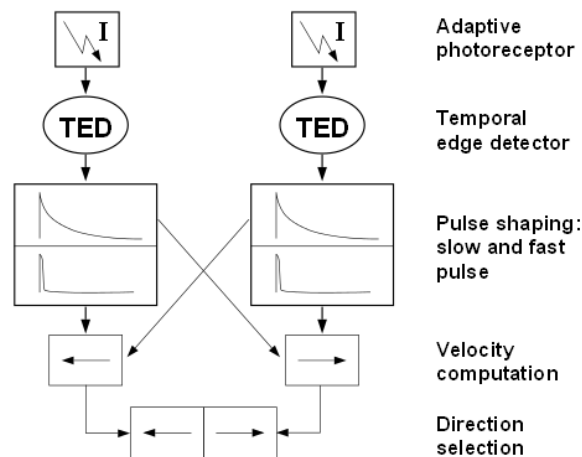


Figure 1.25: Block diagram of the elementary velocity computing unit of the Facilitate and Sample (FS) sensor. The Temporal Edge Detector (TED) generates a spike in response to a fast enough change in the light intensity. A slowly decaying facilitation signal and a fast and short pulse are generated in the pulse shaping stage. In the velocity computing stage with the fast pulse, the slow signal of the neighbor is sampled. In the direction selection stage, this sampled voltage is compared with the voltage of the opposite direction. Whichever is larger is reported as output. This processing is similar to the one previously described in (Blanes, 1991). Reprinted from (Deutschmann, 1997).

temporal edges and computes the time of travel of an edge from one pixel to the next. A block diagram of the elementary velocity detector is shown in Figure 1.25. This processing scheme is the aVLSI implementation of the “time of travel” scheme presented in section 1.2.3 and inspired by electrophysiological experiments performed on the fly’s eye. At the time of the occurrence of an edge at one pixel, a capacitor is charged and starts to decay logarithmically. When the edge reaches the next pixel, the voltage of this capacitor is sampled. The slower the velocity of the edge is, the further the capacitor has discharged and the smaller the reported voltage is. A new chip based on this architecture but with light adaptation has been designed in 2007 where it has been called for the first time “time of travel” algorithm (Moeckel & Liu, 2007).

Barrows’ competitive feature tracker motion detection chip

Barrows proposed a new design of a motion detection chip based on the Competitive Feature Tracker algorithm (Barrows & Neely, 2000). The outputs from the photoreceptors are sent to an array of four feature detectors that output four analog feature signals (see Figure 1.26). A feature detector circuit reaches its highest output value when the feature to which it is tuned appears on its input photoreceptors. Among the many possible feature

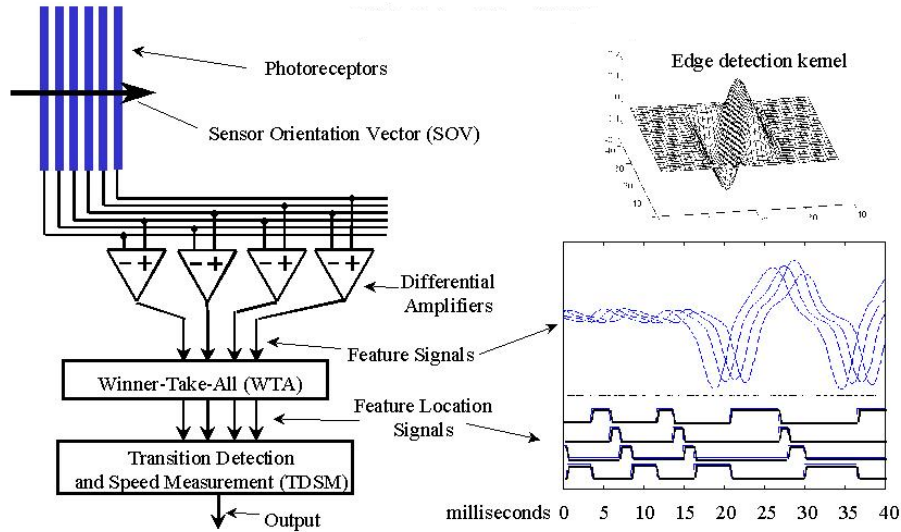


Figure 1.26: Block diagram of the Competitive Feature Tracker (CFT) Elementary Motion Detector. Reprinted from (Barrows & Neely, 2000).

detectors, a differential amplifier is the most common one. Indeed, the output of such a feature detector will be high when an edge is located between the input photoreceptor with the brighter side on the positively connected photoreceptor and the input photoreceptor with the darker side on the negatively connected photoreceptor.

Automatic light adaptation

By looking at the visual system of animals, it appeared that one common characteristic of natural retina is the ability to automatically adapt to the background illuminance. Many authors have proposed electronic circuits mimicking such an ability like for example Delbrück and Mead who designed pixels with a small static gain and a very important transient gain enhancing the contrasts in the environment (Delbrück & Mead, 1994). Sicard et al. developed a bio-inspired chip extracting edges to measured motion over a large dynamic of illuminance and velocity (Sicard et al., 1998; Labonne et al., 2006). Based on experiments performed on several species, authors discovered that the output of the pixels of natural retinas can be approximated by a mathematical function called Naka-Rushton:

$$I_{out} = \frac{I_{in}}{I_{in} + I_{avg}} \quad (1.6)$$

when I_{out} is the intensity response of one pixel receiving an intensity of light I_{in} and I_{avg} is

the average intensity of light received by all the pixels. This property has been reproduced on artificial retinas sensitive to contrasts over several decades of illuminance (Prokopowicz & Cooper, 1995; Vu & Caplier, 2009).

1.2.5 Design of an artificial compound eye

As we have seen in section 1.1.1 about the compound eye, the individual facets are optically isolated from one another, each providing part of the total scene. This is similar to having individual cameras arranged spherically. This allows fast motion detection along a wide Field of View (FOV). The trade-off, however, is that the brightness of the image is substantially diminished, as each facet can only capture a small amount of light. However, artificial implementation of compound eyes has attracted researchers, because the wide Field of View exhibits a huge potential for medical, industrial, and military applications. So far, imaging with a FOV over 90° had been achieved only with bulky and expensive fish eye lenses. The first step in the design of an artificial compound eye is to be able to manufacture an array of microlenses that can be precisely aligned with a photosensitive layer.

1.2.5.1 Fabrication of curved microlens array

The first artificial ommatidia by self-aligned microlenses and waveguides were created by Kim et al. (2005). They fabricated these biomimetic structures by using microlens-induced self-writing of polymer waveguides assuring a good alignment between the lens and the waveguide (see Figure 1.27a). This was followed by a 3D compound eye with self-aligned waveguides and individual microlens units on a spherical surface by Jeong et al. (2006). The ommatidia were arranged along a hemispherical polymer dome such that each would point to a different direction, allowing for a wide field of view. The spherical configuration of the microlenses was accomplished by a polymer replication process with the use of the deformed elastomer membrane, which had microlens patterns. The formation of self-aligned polymer cones and waveguides with respect to microlenses on the hemispherical dome was also achieved by a self-writing process in a photosensitive polymer resin (see Figure 1.27b). The first image-providing artificial spherical compound eye objective based on the apposition principle was presented by Radtke et al. (2007). It consisted of an array of microlenses and an array of pinholes arranged on spherical surfaces of small radius of curvature. The microstructures

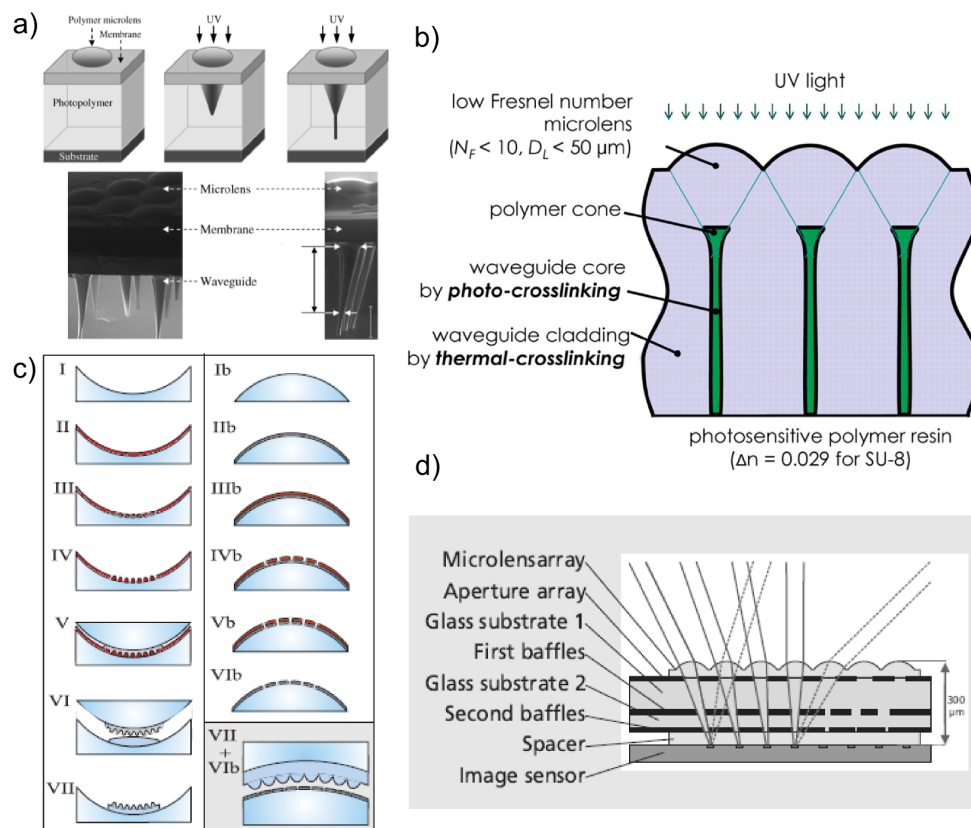


Figure 1.27: Examples of fabrication protocols of microlens arrays. **a)** Microfabrication procedure of a microlens array by exposure of a photo-polymer placed below microlenses to form a waveguide. **b)** Polymer synthesis of artificial ommatidia by UV exposure and two-step cross-linking mechanisms. **c)** Fabrication flow of a microlens array (left, I-VII) and the pinhole array (right, Ib-VIb) using laser lithographic fabrication. **d)** Schematic section of an artificial compound eye with high field of view on a flat surface based on a microlens array with additional baffle aperture arrays used to tilt the optical axes of the photoreceptors increasing the field of view suppressing the cross-talk. Reprinted from (Kim et al., 2005; Jeong et al., 2006; Radtke et al., 2007; Brückner et al., 2010).

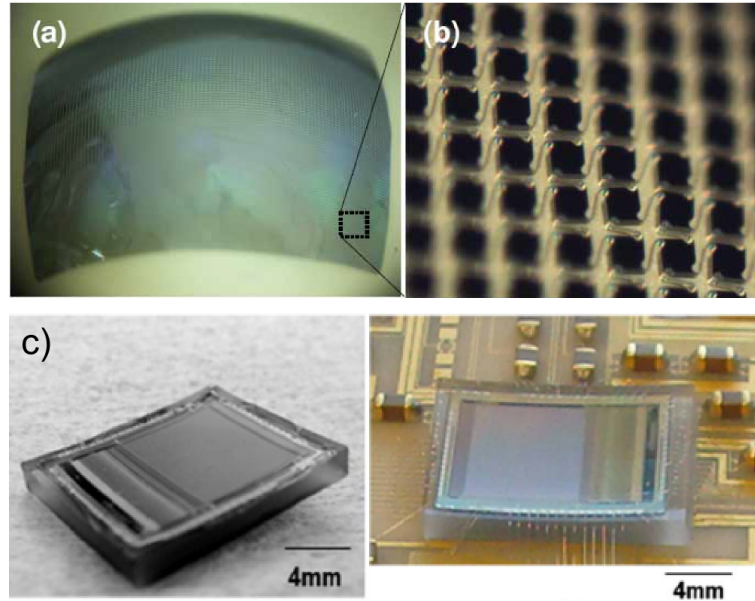


Figure 1.28: **a)** Curved die on a spherical surface with radius of curvature of 1cm. **b)** Magnified view of the curved die showing the silicon island housing the photodetectors mechanically and electronically connected thanks to springs. **c)** Pictures of the curved microbolometer on a glass holder (left) and bonded onto an electrical board (right). Reprinted from (Dinyari et al., 2008; Dumas et al., 2012).

were fabricated with low shape deviation on curved surfaces using a unique laser lithography system (see Figure 1.27c). Due to the lack of cross-talk avoiding structures, the field of view was severely constrained to prevent the appearance of ghost images. This problem was overcome by adding baffle structures in the glass structure to prevent cross-talk (Duparré et al., 2005; Brückner et al., 2010) (see Figure 1.27d). The field of view of the device could therefore be greatly increased in particular by tilting the optical axes of the photoreceptors thanks to a shift between the two baffle structures. Recently, authors manufacturing the microlens array have mainly been focused on simplifying the processes for mass fabrication (Pulsifer et al., 2010; Qu et al., 2012).

1.2.5.2 Fabrication of curved photodetector array

As we have seen, several authors have developed a curved microlens array to be used to design compound eyes, but due to manufacturing constraints, the detectors were planar. This led to complex optical systems with multiple lenses in order to connect the curved microlens array with the flat detector. Presently, some solutions exist to correct aberrations by a computational treatment but a simpler solution could be to change the geometrical shape of the detector. By curving the focal plane array as nature does, we would be able to

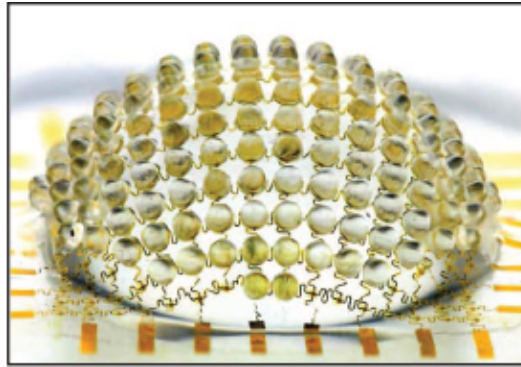


Figure 1.29: Image of a the compound eye designed by Song et al. after hemispherical deformation. This device is composed of an array of elastomeric microlenses and a corresponding collection of silicon photodiodes interconnected by wires. The components are fabricated with planar geometries and then elastically deformed into a hemispherical shape creating an apposition compound eye. Reprinted from (Song et al., 2013).

exactly fit the focal surface with the detector.

A first solution has been proposed by Dinyari et al. (2008) based on a dedicated architecture. The detector is structured in small separated islands of devices interconnected by metallic lines that can then be twisted and flexed to form a hemispherical shape (see Figure 1.28a and b). However, this solution complexifies the fabrication process and the fill factor is decreased because of the bending.

A new solution which relies on thinning the detector has been demonstrated by Dumas et al. (2012). They developed a process to curve into a hemispherical shape a monolithic 320×256 pixel detector adding only one thinning step during the fabrication process (see Figure 1.28c).

Very recently, Song et al. (2013) proposed a new solution based on an elastomeric microlens array placed on top of a stretchable array of photodiodes interconnected by filamentary serpentine wires which is then deformed into an hemispherical shape (see Figure 1.29).

1.3 Taking inspiration from biology to develop new robots

During a long time, robotic researchers have mainly tried to design wheeled or anthropomorphic robots able to walk like humans. However, wheeled robots are not adapted for natural terrains and reproducing bipedal locomotion with its refinements is a very complex task.

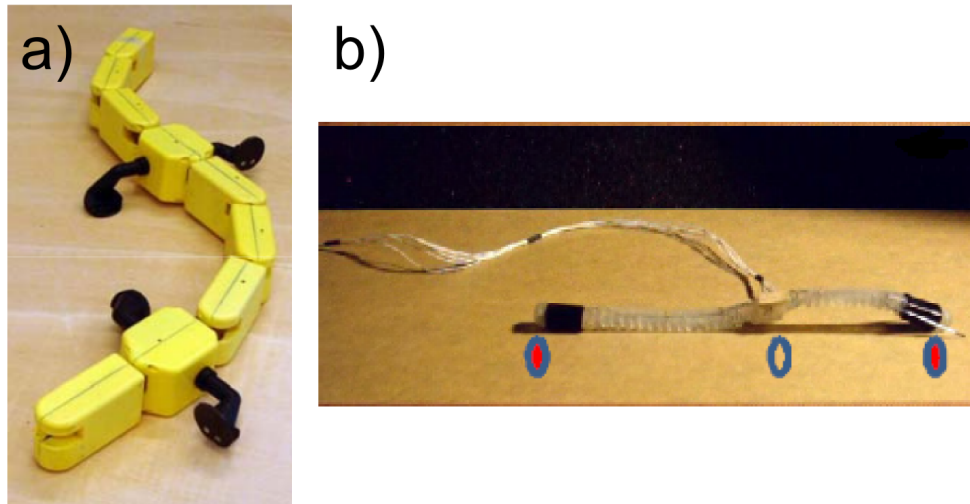


Figure 1.30: a) Picture of the Salamandra robotica II, one of the very few robot able to swim, crawl, and walk. b) GoQBot soft body during a crawling motion induced by imposing a sequence of commands on the two flexors. Reprinted from (Ijspeert et al., 2007; Lin et al., 2011).

This is the reason why researchers are now looking under rocks for biological inspiration to develop robots of the future endowed with biomimetic locomotion systems to crawl, swim or fly based on Nature's best solution found through thousand of years of evolution.

1.3.1 Bio-inspired locomotion

1.3.1.1 Swim and walk like a salamander

The transition from aquatic to terrestrial locomotion was a key development in vertebrate evolution. Ijspeert et al. (2007) designed an amphibious salamander robot that can explain their ability to switch between swimming and walking (see Figure 1.30a). Recently, a modeling approach has been proposed which can be used for any hyper-redundant or continuous robot like the ones mimicking the locomotion of snakes, worms or caterpillars (Boyer et al., 2012).

1.3.1.2 Crawl like a caterpillar

Based on the curling behavior of the caterpillars, Lin et al. (2011) were able to design a crawling robot generating its own rolling momentum by changing its body configuration thanks to two flexors (see Figure 1.30b).

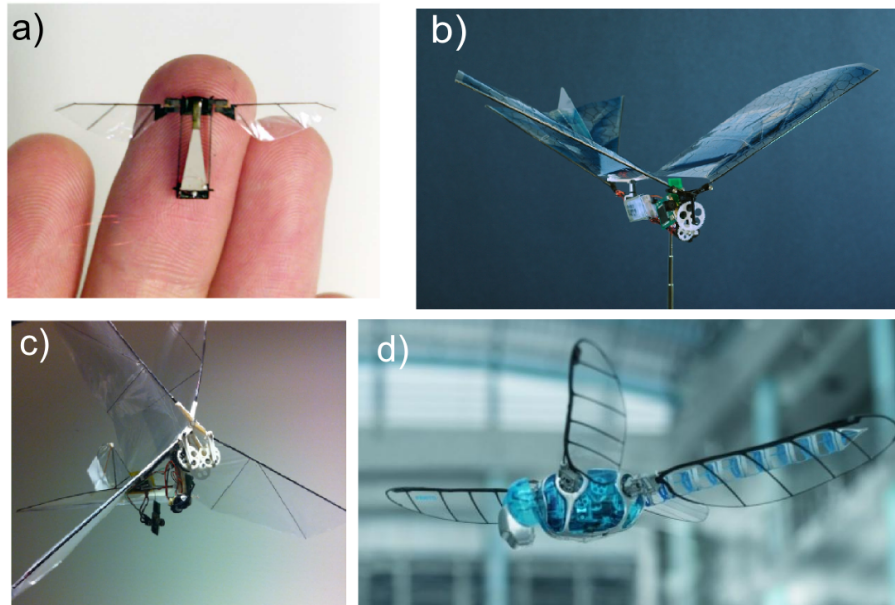


Figure 1.31: **a)** First insect-scale (60mg) flying robot able to takeoff **b)** Flapping-wing flying platform modified from Interactive Toy's VAMP RC ornithopter. **c)** Photo of the biplane-wing configuration of the DelFly II. **d)** Photo of the BionicOpter developed by Festo and mimicking the dragonfly flight. Reprinted from (Wood, 2008; Bermudez & Fearing, 2009; de Croon et al., 2012) and www.festo.com.

1.3.1.3 Fly like an insect

Mimicking the flapping wing mechanism of flying insects or birds has attracted several teams of researchers in the last years. By looking at the flapping-wing aerodynamics of insects and how they are able to generate sufficient thrust to sustain flight, Wood (2008) created the first insect-sized (60mg) Micro Air Vehicle capable of Diptera-like wing trajectories by producing sufficient thrust to accelerate vertically (see Figure 1.31a). They successfully embedded on such ultra light MAV an optic flow sensor used to estimate the altitude by integrating the optic flow (Duhamel et al., 2012). Recently, they showed more details about the performances of this tethered robot able to hover and perform basic controlled flight maneuvers (Ma et al., 2013).

Other authors developed flapping-wing robots on a larger scale like the 10g ornithopter designed by Bermudez & Fearing (2009) (see Figure 1.31b) or the DelFly which is a biplane wing designed by de Croon et al. (2012) (see Figure 1.31c). On this last bio-inspired robot, the authors used optic flow computed using the Lukas-Kanade algorithm to determine the position of the focus of expansion thanks to a least-squares approximation and took the median value of the estimated Time-To-Contact to trigger saccades in order to avoid obstacles. Very recently, the Festo company has launched a new flying robot inspired by the

dragonfly called BionicOpter (see Figure 1.31d). This lightweight robot (175g) can perform complex maneuvers thanks to its 13 degrees of freedom allowing to control the amplitude, the frequency and the twist angle of each of its 4 wings.

1.3.2 Biomimetic vision-based robots

As we saw, by taking inspiration from biology, authors developed a generation of robots endowed with new locomotion systems. A lot of researchers have also tried to use biomimetic principles and in particular the use of optic flow in insects as a main sensory input to autonomously navigate in unknown environments first on wheeled robots and then on aerial vehicles.

1.3.2.1 Wheeled robots

As we will see in the section 1.3.3, the “robot mouche” was the first wheeled robot navigating in a complex environment based on optic flow. A few years later, Srinivasan et al. (1999) developed a small wheeled robot equipped with a camera facing forward (see Figure 1.32a). This camera captured views of the side walls (one of each wall) thanks to two mirrors positioned above the lens. Video information from the camera was transmitted to a desktop computer, where the image velocities of the two walls, induced by the motion of the robot, were measured using a simplified version of the image-interpolation algorithm described in section 1.2.2. The computer then issued appropriate steering commands to the robot to ensure that it stayed close to the midline of the tunnel as had been observed in honeybees flight and had been called the centering response (Srinivasan et al., 1996). Similar approaches but using different optic flow processings have been implemented by Argyros et al. (2004) or on the mobile robot called Robee (Santos-Victor et al., 1995). In this last study, authors pointed out that such strategy will lead to a crash of the robot on a featureless wall and they endowed their robot with a wall following behavior triggered by the absence of optic flow measurement from one side. A few years later, authors reproduced a robot very similar to the “robot mouche” (see Figure 1.34) equipped with a panoramic visual sensor inspired by insect vision and implemented for real-time autonomous robot navigation (see Figure 1.32b) (Zwaan & Santos-Victor, 1999). The robot was endowed with a reflex-like behavior to update its heading direction autonomously without any knowledge of the surrounding

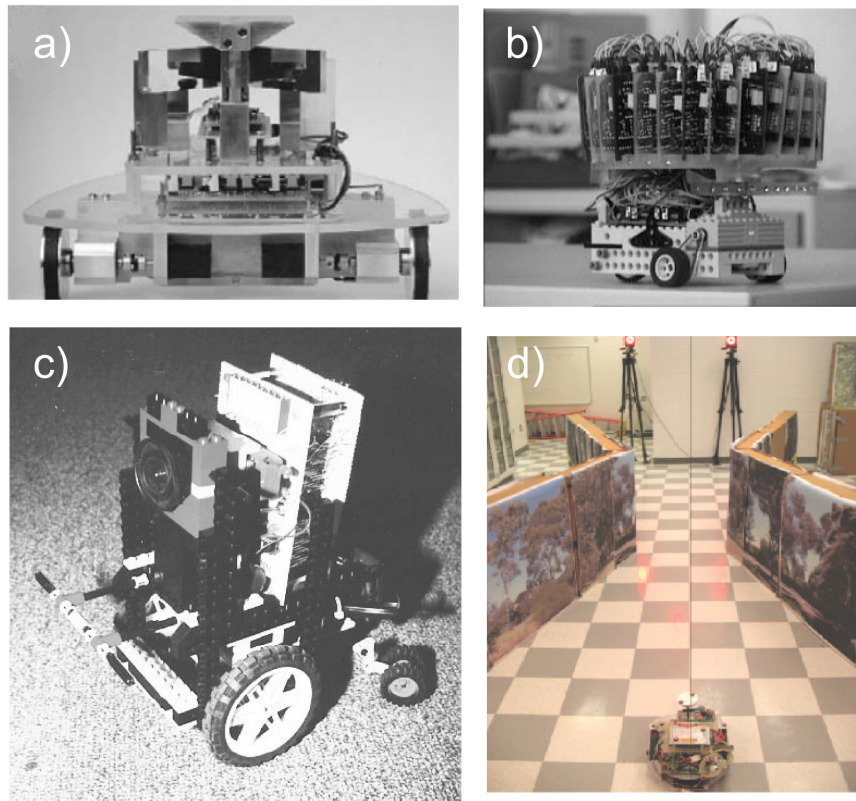


Figure 1.32: Examples of wheeled robots using optic flow to navigate. **a)** Corridor-following robot travelling in a tunnel balancing the two lateral optic flows. **b)** Reflex-like robot equipped with a 1-D panoramic sensor processing in parallel the local optic flow from every direction. **c)** Asymmetric wheeled robot equipped with an aVLSI motion sensor based on the Reichardt correlator which compensates its yaw rotations thanks to the embedded optomotor feedback loop in order to maintain straight trajectories. **d)** Ground vehicle travelling in a converging-diverging tunnel environment covered by natural contrasts using the Wide-Field Integration method to estimate vehicle states based on optic flow. Reprinted from (Srinivasan et al., 1999; Zwaan & Santos-Victor, 1999; Harrison & Koch, 1999; Humbert & Hyslop, 2010).

environment. To decrease the important computational power required to extract visual information, Harrison & Koch (1999) created a small, low-power visual sensor with integrated analog parallel processing to extract motion in real-time based on Reichardt correlators. This sensor was used on a mechanically asymmetric wheeled robot (see Figure 1.32c) compensating its course thanks to a feedback loop mimicking the optomotor response of insects. Recently, Sean Humbert proposed a new solution to estimate state vehicles based on optic flow by integrating over a wide field of view the local measurements of optic flow which are decomposed using Fourier series. They showed that the coefficients of these series depend on the states of the vehicles. This method has been called Wide-Field Integration (WFI) (Humbert et al., 2009) and is inspired by the large tangential cells of the lobula plate of the fly which integrates the visual information coming from different regions of the field of view of the fly's eye. This method has been successfully tested on a wheeled robot traveling inside a corridor to center the robot and control its forward speed (Humbert & Hyslop, 2010) (see Figure 1.32d). This method has been extended to a 6-DOF robot to navigate in unknown environments (Hyslop & Humbert, 2010) and implemented onboard a quadcopter (Conroy et al., 2009). However, in all these experiments, the optic flow measurements were coupled with other sensory modalities like a sonar and an accelerometer in Conroy et al. (2009) and a measurement of the forward speed of the robot in Humbert & Hyslop (2010). Optic flow has also been used on a wheeled robot by Dahmen et al. (2009) to record odometry thanks to optical mouse chips.

1.3.2.2 Aerial robots

During the last decade, a lot of optic flow-based aerial vehicles have been presented to solve problems which are still very challenging for aerial vehicles in unknown environments like:

- avoiding obstacles,
- hovering,
- taking-off and landing,
- following a natural terrain.

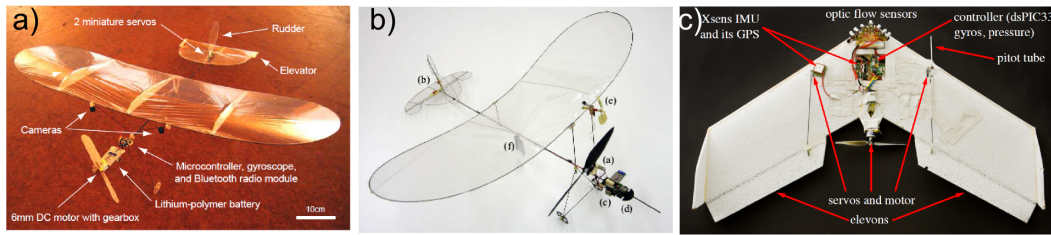


Figure 1.33: Examples of lightweight flying robots endowed with obstacle avoidance autopilot. **a)** 30g autonomous indoor airplane F2. **b)** 10g MC2 microflyer. The on-board electronics consists of (a) a 4mm geared motor with a lightweight carbon fiber propeller, (b) two magnet-in-a-coil actuators controlling the rudder and the elevator, (c) a microcontroller board with a Bluetooth module and a ventral camera with its pitch rate gyro, (d) a frontal camera with its yaw rate gyro, (e) an anemometer, and (f) a Lithium-polymer battery. **c)** 400g fixed-winged aircraft flying outdoors autonomously and avoiding obstacles thanks to optical computer mouse sensors. Reprinted from (Zufferey & Floreano, 2006; Zufferey et al., 2007; Beyeler et al., 2009).

Obstacle avoidance based on optic flow

Although not exactly based on an obstacle avoidance system, Iida (2001, 2003) demonstrated on a blimp how they could use optic flow to center it in an indoor environment and therefore avoid it from crashing into the walls. Green et al. (2004) carried out an experiment of lateral obstacle avoidance with an indoor fixed-wing aircraft equipped with a laterally-mounted 4.8g optic-flow sensor triggering saccades when the optic flow exceeded a chosen threshold. Just before, as section 1.3.3.2 will describe, the OCTAVE robot was developed (Ruffier & Franceschini, 2003). OCTAVE is a tethered rotorcraft able to autonomously avoid ground obstacles thanks to a ventral optic flow regulator.

A major breakthrough was accomplished by Zufferey & Floreano (2006) who succeeded in flying a 30g indoor airplane autonomously in a contrasted environment using really lightweight sensors and embedding a simple autopilot avoiding collisions on the basis of optic flow computed onboard using the I2A algorithm (see Figure 1.33a). One year later, similar behavior was obtained on a 10g microflyer (Zufferey et al., 2007) (see Figure 1.33b). A few years later, an avoidance system was implemented on a 400g outdoor fixed-wing vehicle measuring the local optic flow in several directions thanks to optical computer mouse sensors (Beyeler et al., 2007) (see Figure 1.33a).

Griffiths et al. (2006, 2007) also performed autonomous flights outdoors in complex environments based on optic flow to avoid obstacles in the flight path and to stay centered in a winding corridor. Recently, other avoidance systems fusing inertial information with optic flow have been proposed and tested in simulation (Zingg et al., 2010; Lippiello et al., 2011).

Visual hovering based on optic flow

Authors have started to use optic flow to visually measure the horizontal drift of aerial vehicles and therefore endow aircraft with the ability to hover like some insects can do. For example, Rondon et al. (2010) proposed a controller allowing a quadrotor to hover in simulation but in a very specific environment. Others controllers have been designed to hover and successfully tested indoors and outdoors on rotorcrafts (Herisse et al., 2008; Kendoul et al., 2009).

Automatic landing or docking based on optic flow

Automatic landing is a particularly important problem for UAV. For aircraft, automatic landing can be achieved at the price of using the information of several sensors and it generally requires substantial infrastructures on the ground and in the aircraft. One elegant solution to land automatically on an aircraft carrier has been proposed by Coutard et al. (2011) using visual servoing based on visual cues used by pilots. Following the experiments conducted by Srinivasan et al. (2000) on honeybees and how they are able to make grazing landings based on optic flow, Chahl et al. (2004) performed a landing with a robotic gantry and a fixed wing aircraft. It was also shown on the OCTAVE robot that a smooth landing could be achieved by simply pitching backward a robot equipped with a ventral optic flow regulator (Ruffier & Franceschini, 2004) (More details are given in section 1.3.3.2).

Based on optic flow and a simple motion sensor, Valette et al. simulated a planetary landing scenario validating the interest in the use of optic flow for landing scenarios of autonomous robots on other planets (Valette et al., 2010; Orchard et al., 2009).

Finally, other authors have integrated in their autonomous UAV controllers specifically designed for landing and based on optic flow measurements (Beyeler et al., 2009; Kendoul et al., 2010; Zufferey et al., 2010; Herisse et al., 2012)

Terrain following based on optic flow

Based only on optic flow, it has been proven on the OCTAVE robot that we could achieve a nap-of-the-earth flight (see section 1.3.3.2) (Ruffier & Franceschini, 2003, 2004, 2005).

By combining a measurement of ground speed from another sensor such as a global positioning system, optic flow can be used to provide a measure of an aircraft's height above terrain. This principle has been applied to the control of height in a 80kg unmanned helicopter (Garratt & Chahl, 2008). Using feedback of the height estimated from optic flow scaled thanks to the pitch control of the helicopter, it has been possible to maintain terrain clearance in flights of up to 2km long. However, recent research suggests that optical flow alone can not sufficiently explain the altitude control behavior of *Drosophila*: those insects may consider other environmental features like local edges (Straw et al., 2010). Inspired by these results, Stowers et al. (2011) proposed a biomimetic altitude control and avoidance strategy which analyzes horizontal edges in the image and is able to successfully control the flight of a quadrotor helicopter in a simulated environment.

1.3.3 Bio-inspired robots developed at our laboratory

It all started in our team thanks to Nicolas Franceschini through anatomic and electrophysiological studies (Franceschini, 1985; Franceschini et al., 1989) or ethologic studies (Serres et al., 2008; Portelli et al., 2010, 2011) on flying insects and in particular flies and honeybees. These studies have led to the simulation of several bio-inspired robots (Martin & Franceschini, 1994; Mura & Franceschini, 1994; Serres et al., 2008; Portelli et al., 2010) and the conception of autonomous vehicles (Pichon et al., 1989; Blanes, 1991; Franceschini et al., 1992; Netter & Franceschini, 2002; Ruffier & Franceschini, 2003, 2004, 2005; Franceschini et al., 2007; Ruffier & Franceschini, 2008; Roubieu et al., 2012). The idea in the Biorobotics team is to observe and model the behavior and sensorimotor control feedback loops which are hard-wired into the brains of flying insects and to validate our models thanks to a bio-inspired robotic demonstrator.

1.3.3.1 The “robot mouche” (robot fly)

After several years studying the morphological and neurological aspects of the visual system of the fly and its way of detecting optic flow (Franceschini et al., 1989) and in order to test their hypothesis on how the fly could use optic-flow, Franceschini et al. built 118 analog electronic circuits modeled upon the neural circuitry of the fly brain and interfaced it with a circular array of photoreceptors on a 12-kg wheeled robot (see Figure 1.34). This robot

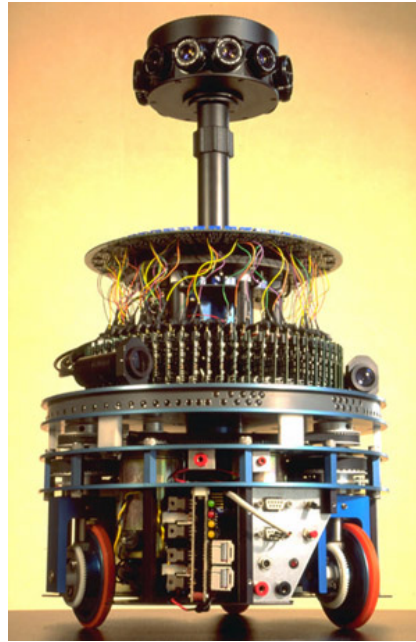


Figure 1.34: Picture of the “robot mouche”. Fully autonomous, the 12kg wheeled robot navigates at 50cm/s in a cluttered environment based on the optic flow measured thanks to a network of Elementary Motion Detectors. Reprinted from (Franceschini, 2003).

called the “robot mouche” was capable of approaching a goal while avoiding obstacles on its way (Pichon et al., 1989; Franceschini et al., 1992). The robot was traveling in translation at a known forward speed of 50cm/s scaling the optic flow measurements and allowing to determine the distance to objects. In 1999, a first simulation showed that, thanks to the optic flow, it was possible for an aircraft to follow terrain and land without any knowledge of its speed (Netter & Franceschini, 1999). This strategy was implemented on the 850g FANIA robot which was able to fly away from obstacles based on a retina of 20 photoreceptors (Netter & Franceschini, 2002).

1.3.3.2 Optic flow regulation in the vertical plane: The OCTAVE robot

Inspired by observations on mosquitoes and locusts, Kennedy hypothesized that flying insects maintain a preferred retinal velocity with respect to the ground below (Kennedy, 1939, 1951). Inspired by these results, Ruffier et al. proposed that flying insects control their altitude thanks to a ventral optic flow regulator and came up with an autopilot called OCTAVE (OCTAVE stands for Optical altitude Control system for Autonomous VEHicles) that is little demanding in terms of implementation. Based on a ventral optic flow sensor always looking downward, this autopilot acts on a robot’s lift and hence on its altitude in order

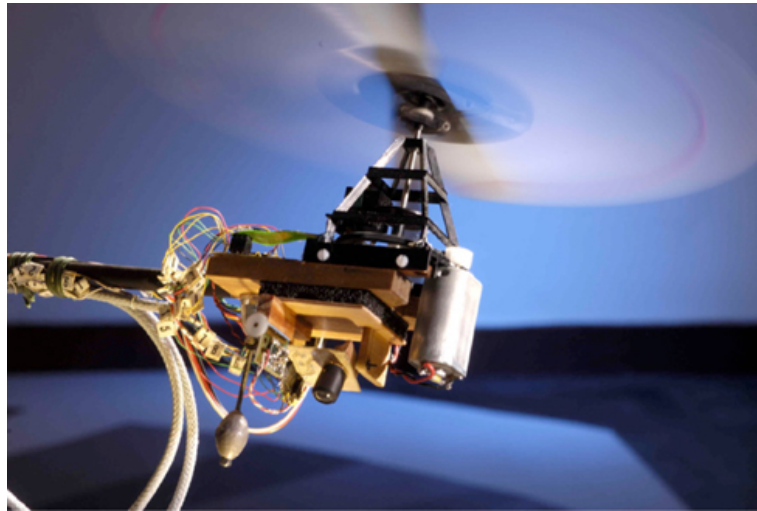


Figure 1.35: Picture of the OCTAVE robot. The OCTAVE (Optic flow based Control system for Aerial Vehicles) robot is a 100g tethered rotorcraft able to automatically take off, cruise and land, while reacting appropriately to wind disturbances (head wind and tail wind) based on a visual control system that adjusts the thrust so as to keep the downward optic flow (OF) at a constant value. Copyright H. Raguet.

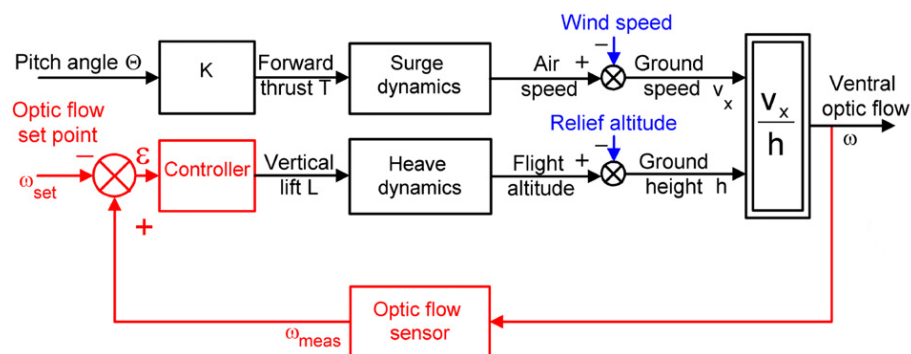


Figure 1.36: Schematic diagram of the OCTAVE autopilot. The upper pathway describes how an increase in pitch angle θ of the mean flight-force vector results in a proportional increase in forward thrust, and thus in groundspeed V_x via the surge dynamics. The red pathway shows how the ventral OF is measured ω_{meas} and compared with an OF set-point ω_{set} . The error signal ϵ delivered by the comparator drives a controller adjusting the vertical lift L , and thus the ground height h via the heave dynamics, so as to maintain a constant OF ω , whatever the groundspeed. Reprinted from (Franceschini et al., 2007).

to regulate the measured OF around a chosen setpoint value (Ruffier & Franceschini, 2003, 2004, 2005; Franceschini et al., 2007; Ruffier & Franceschini, 2008). This autopilot (see Figure 1.36) has been successfully implemented on a 100g tethered rotorcraft (see Figure 1.35) flying over a contrasted ground. This simple aircraft can explain several flying abilities observed on flying insects and perform challenging tasks such as taking-off, terrain following, reacting suitably to wind, and landing.

Take-off

David showed that the fly pitches forward in order to increase its speed (David, 1978). If this insect is equipped with a ventral OF regulator like the OCTAVE autopilot, as soon as it pitches forward, it will then simultaneously increase its forward speed V_x and its height h in order to maintain a constant OF. In the same way, the OCTAVE autopilot automatically takes-off when we pitch the aircraft forward using an external servomotor (Ruffier & Franceschini, 2005).

Terrain following

By regulating the ventral optic flow to a constant value, any change in the height h caused for example by a relief will be compensated by increasing/decreasing the robot's lift and therefore its altitude. This behavior will lead to an automatic terrain following suitable to uneven terrains. It has been observed that flying insects fly above obstacles instead of bypassing them (Williams, 1965) which would save energy. This proves that the terrain following behavior results more from a reflex behavior than a planned response. However, by looking only downward, the robot will not be able to anticipate an important obstacle which could result in a crash of the aircraft. This is the reason why the OCTAVE robot has also been equipped with an optic flow sensor looking forward coupled with a feed-forward controller (Ruffier & Franceschini, 2008).

Wind reaction

From experiments on locusts, Kennedy showed that these insects reduce their altitude

with a headwind and vice versa (Kennedy, 1951) which has since then been confirmed among migrating species (Srygley & Oliveira, 2001). Equipped with a ventral optic flow regulator, the OCTAVE autopilot leads to the same behavior by increasing/decreasing the robot's lift with a tailwind/headwind because the forward speed of the robot increases/decreases and the robot has to ascend/descend in order to keep its ventral optic flow constant (Ruffier & Franceschini, 2005).

Loss of altitude over a non-contrasted zone

A very famous study from Heran and Lindauer showed that bees traveling over a featureless water would gradually lose altitude until they drowned except on windy days when the water was rippled or when a bridge was placed on the water to provide sufficient contrast (Heran & Lindauer, 1963). In the same way, an aircraft equipped with the OCTAVE autopilot and relying on its ventral optic flow regulator will not measure anything when flying over a non-contrasted zone (Ruffier & Franceschini, 2005). This will be detected by the optic flow regulator as a null measurement leading to a decrease in the robot's lift and therefore in groundheight in order to get closer to the surface.

Automatic landing

As we already discussed, Srinivasan et al. have shown that honeybees' landings occur with a constant slope (Srinivasan et al., 2000) as their forward speed is kept proportional to their speed of descent. Although the OCTAVE autopilot based on an OF regulator only control the robot's lift, the aircraft's forward speed and descent speed automatically decrease proportionally as soon as we pitch the aircraft backward leading to a smooth landing (Ruffier & Franceschini, 2005).

1.3.3.3 Regulation of optic flow on the horizontal plane: The LORA III autopilot

Kirchner and Srinivasan observed that honeybees flying through a narrow tunnel tend to navigate at equal distance from the lateral walls (Kirchner & Srinivasan, 1989). To explain this centering response, these authors hypothesized that the animal may balance the apparent

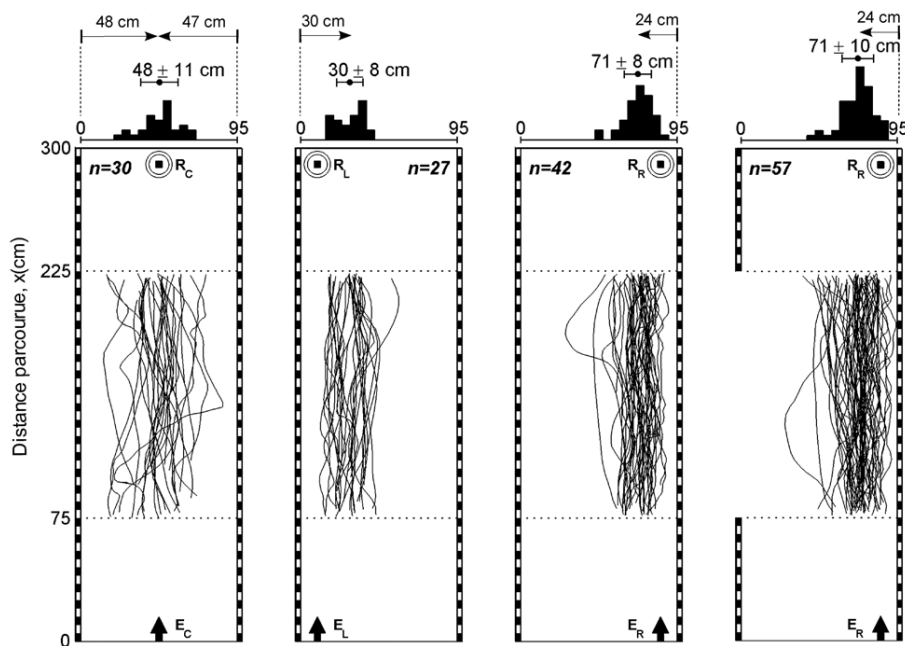


Figure 1.37: Trajectories of individual bees flying in a wide corridor. Depending on the entrance and the feeder positions, bees were not systematically centered in the corridor and exhibited a wall following behaviour. Reprinted from (Serres et al., 2008).

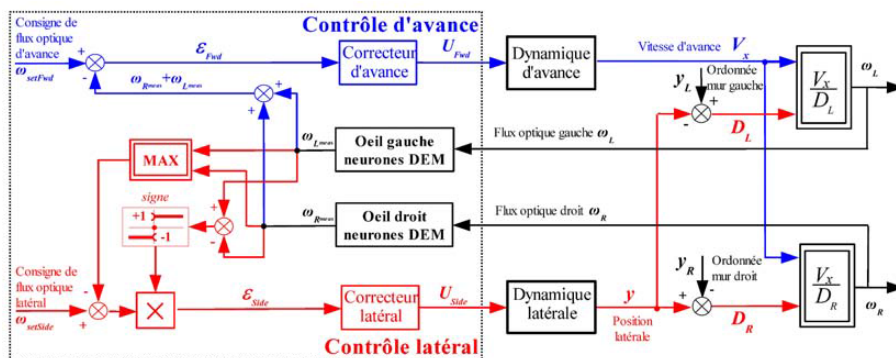


Figure 1.38: The LORA III autopilot is based on two visual feedback loops working in parallel with their own optic flow set-point and their own degree of freedom controlled: the forward control system (blue upper loop) and the side control system (red bottom loop). Reprinted from (Serres et al., 2008).

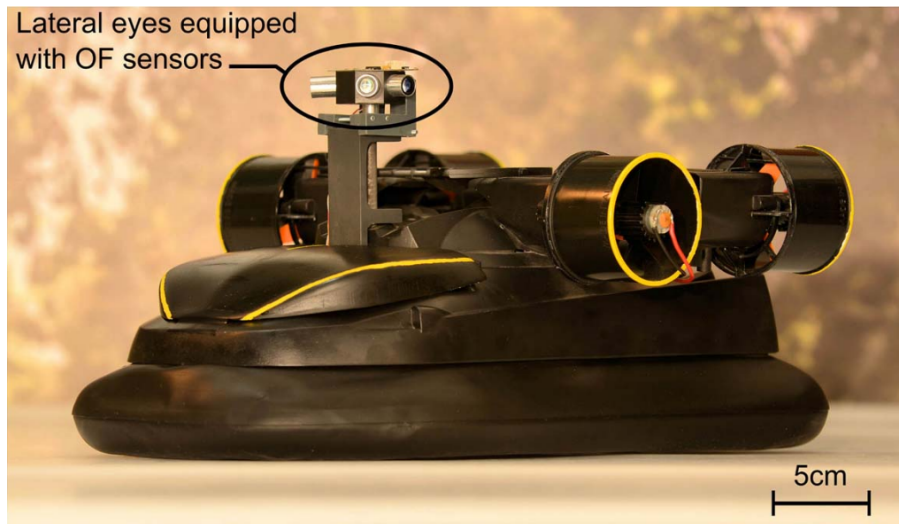


Figure 1.39: Picture of the LORA fully-autonomous sighted hovercraft equipped with miniature elementary eyes and a bio-inspired dual lateral optic flow regulator. Reprinted from (Roubieu et al., 2012).

motion of the images of the walls between their two eyes. Despite the success of the ‘optic flow balance’ hypothesis in robotics, new behavioral experiments have shown that honeybees actually do not necessarily center when crossing a corridor (Serres et al., 2008) but they may follow one of the two walls at a certain distance (see Figure 1.37). Besides, honeybees flying through a narrow, tapered corridor tend to keep their flight speed proportional to the local corridor width by regulating the image velocity (Srinivasan et al., 1996). Based on these two results from behavioral experiments on honeybees, Serres et al. (2008) proposed a bio-inspired autopilot, called LORA (Lateral Optic Flow Regulation Autopilot) III, consisting of a dual OF regulator (see Figure 1.38) in which each regulator has its own OF set-point. LORA III regulates the OF by side and forward controls, according to the following principles:

- the first lateral OF regulator adjusts the air vehicle’s lateral thrust (which determines the lateral speed V_y) so as to keep the lateral OF equal to the sideways OF set-point. Therefore, the distance to the wall becomes proportional to the vehicle’s forward speed V_x : the faster the air vehicle travels, the further away from the walls it will be. The clearance from the walls will depend directly on the sideways OF set-point.
- the second lateral OF regulator adjusts the air vehicle’s forward thrust (which determines the forward speed V_x) so as to maintain the sum of the two (right and left) OFs equal to the forward OF setpoint.

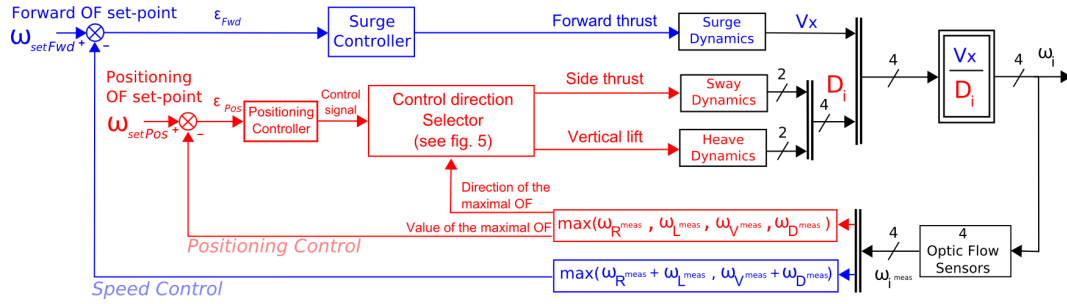


Figure 1.40: Schematic diagram of the ALIS autopilot which is based on two interdependent visual feedback loops, each with its own OF set-point: a speed control loop (in blue) and a positioning control loop (in red). The surge controller adjusts the pitch angle θ_{pitch} (that determines V_x via the bees' surge dynamics) on the basis of whichever sum of the two coplanar (horizontal or vertical) OFs measured is the larger. The positioning controller controls the roll angle θ_{roll} (or the stroke amplitude $\delta\varphi$), which determines the distances to the walls (or the distances to the ground and to the roof), depending on the sway (or heave) dynamics on the basis of whichever of the four measured OFs is the largest. Reprinted from (Portelli et al., 2008).

Thanks to these two intertwined feedback loops, the vehicle forward speed will automatically adjust to the size of the corridor. The forward speed attained by the vehicle will directly depend on the forward OF set-point and the lateral OF set-point according to the following equation:

$$V_x(t) = \frac{\omega_{setSide} \cdot (\omega_{setFwd} - \omega_{setSide})}{\omega_{setFwd}} D(t) \quad (1.7)$$

where $D(t)$ is the sum of the distances between the robot and each wall.

This autopilot has been embedded in a miniature hovercraft traveling in a corridor first in simulation (Serres et al., 2008) and then on a 800g real prototype (Roubieu et al., 2012) (see Figure 1.39).

1.3.3.4 Generalization to a free-flying agent: the ALIS autopilot

To generalize the OCTAVE and LORA autopilots in order to control the position and speed of an agent freely-flying in a 3D environment, The ALIS (AutopiLot using an Insect based vision System) autopilot has been proposed and successfully tested with a simulated flying agent (Portelli et al., 2008, 2010) (see Figure 1.40). The ALIS autopilot regulates the OF by both positioning and forward control systems, according to the following principles:

- the first OF regulator adjusts the bee' lateral or vertical position so as to keep the maximal OF equal to the positioning OF set-point. The outcome is that the clearance from the nearest wall (lateral walls, ground, or ceiling) will become proportional to the bee's forward speed.

- the second OF regulator adjusts the bee's forward speed so as to keep the maximum of the sum of the two opposite OFs equal to a forward OF set-point.

The outcome of both regulators is that the bee's forward speed will become proportional to the narrower dimension (either width or height) of the flight tunnel.

1.4 Objectives of the thesis

As we have seen in section 1.2.4, in the last two decades, several authors have worked on developing visual sensors extracting the local or global optic flow based on various technologies and algorithms. However, none of them seem to be satisfactory for the Micro Aerial Vehicles of the future due to the important computational load necessary, the very limited illuminance range or the slow refresh rate of the visual signals preventing from detecting fast motion.

- The first part of this thesis is dedicated to the development and characterization of optic flow sensors based on the time of travel scheme which has known several improvements. The performances of these sensors are compared in natural conditions depending on the used front end and with off-the-shelf optical mouse sensors.
- The results of these experiments have contributed to the design and development of the first curved artificial compound eye including fast motion detection in a very large range of illuminations: the CurvACE sensor. We have shown how such wide field of view sensor equipped with adaptive pixels can be used to extract optic flow using different algorithms.
- By taking inspiration from behavioral experiments performed on flies and bees and, in particular, the recent results on the honeybees' trajectories in tunnels, we developed a tethered miniature aerial robot equipped with sensors and control strategies mimicking flying insects that can navigate in a high-roofed tunnel. This robot may explain how honeybees control their speed and position thanks to optic flow, while demonstrating alternative solution to classical robotic approach relying on ground-truth and metric sensors. Based only on visuomotor control loops reacting suitably to the environment, this rotorcraft has shown its ability to fly autonomously without any accelerometer in complex and unstationary tunnels.

Chapter 2

Performances of Optic flow sensors

Article 1: Outdoor Field Performances of Insect-Based Visual Motion Sensors

As we have seen in the introduction, several algorithms have been proposed to extract optic flow and they have been implemented using various retinas (CMOS camera, aVLSI retina, mouse sensors, pixels array..). In our laboratory and based on experiments performed on the visual system of the fly, we have chosen to compute the local angular speed using the “time of travel” scheme described in section 1.2.3. However, we were interested in assessing the performances of our sensors and in particular their robustness to illuminance changes to embed them on flying robots that could, in the future, navigate in unknown environments. We developed a benchmark that can easily be placed indoors or outdoors to test our optic flow sensors while rotating in a stationary environment. As we saw, in that case, the generated rotational optic flow only depends on the rotational speed imposed to the board and can be compared with the output of the rate gyro. In this study, we were particularly interested in characterizing the performances of two sensors computing the angular speed thanks to the “time of travel” scheme but based on two very different retinas: one with linear amplification and one custom-made aVLSI retina composed of pixels automatically adapting to the background illuminance. The two retinas used in this study are shown in Figure 2.1. The front-end of the LSC-based local motion sensor is an off-the-shelf photodiode array (LSC is a component purchased from iC-Haus) (see Figure 2.1a) where the 2 rows of 6 pixels have been summed in pairs to obtain a sensitive area of $300\mu m * 1600\mu m$. This chip has been chosen

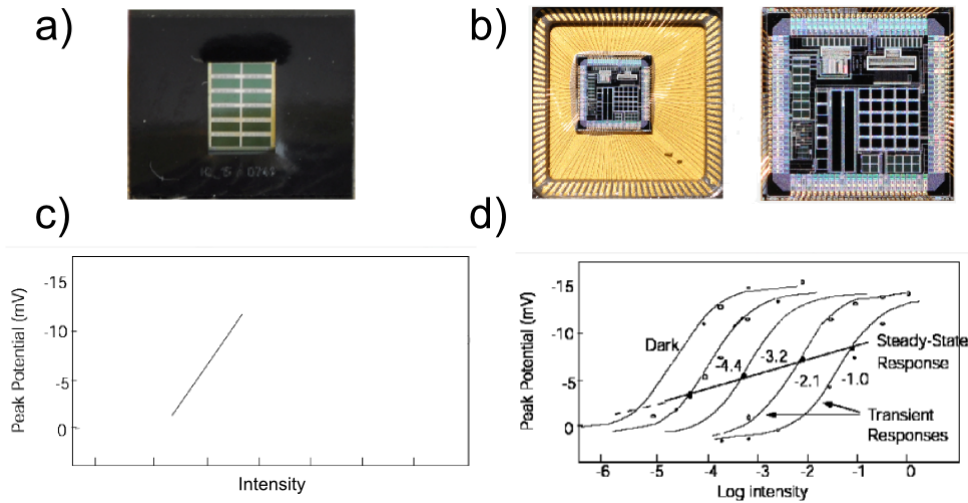


Figure 2.1: LSC and APIS front-ends. **a)** Picture of the off-the-shelf photodiode array called LSC composed of 2 rows of 6 pixels **b)** Picture of the APIS (Adaptive Pixels for Insect-based Sensors) retina, a custom-made VLSI retina comprising 25 pixels **c)** The LSC photodiode array is equipped with a linear on-chip preamplification circuit reducing the noise. **d)** Each pixel of the APIS retina is an adaptive, time-continuous, logarithmic circuit having a dynamic range of 100dB.

for the on-chip preamplification unit strongly reducing the noise on the photodiode signals. These photodectors are combined with a fixed gain current amplifier. The front-end of the APIS-based local motion sensor is a custom-made VLSI retina comprising 25 pixels (each of them having a sensitive area of $250\mu\text{m} * 250\mu\text{m}$) (see Figure 2.1b) based on the pixel circuit proposed by Delbrück et al. (Delbrück & Mead, 1994). This retina has been developed in collaboration with the Center for Particle Physics (CPPM) in Marseilles (Aubépart et al., 2007; Viollet et al., 2010) and has been designed to respond over a very wide range of illuminance values from 1 lux to 10000 lux thanks to adaptive pixels automatically adapting to the background illuminance.

Although it could be predicted that the APIS-based sensor composed of adaptive pixels would give the best performances in terms of its invariance to the illuminance, we were interested in this study to assess the performances of these sensors also in terms of accuracy, range and refresh rate. The conclusion of this study is that the LSC-based motion sensor gave the best results in terms of the accuracy and the average refresh rate in a narrow illuminance range (1.5 decades), whereas the APIS-based motion sensor turned out to be capable of measuring the angular speed in a 3-decade range of illuminance values.

Outdoor Field Performances of Insect-Based Visual Motion Sensors¹

Article published in 2011 in *Journal of Field Robotics*: volume 28(4), pages 529-541.

Authors: Fabien Expert, Stéphane Viollet and Franck Ruffier.

2.1.1 Abstract

Considerable attention has been paid during the last decade to navigation systems based on the use of visual optic flow cues. Optic flow-based visuo-motor control systems have been implemented on an increasingly large number of sighted autonomous robots designed to travel under specific lighting conditions. Many algorithms based on conventional cameras or custom-made sensors are being used nowadays to process visual motion. In this paper, we focus on the reliability of our optical sensors which can be used to measure the local 1-D angular speed of robots flying outdoors over a visual scene in terms of their accuracy, range, refresh rate and sensitivity to illuminance variations. We have designed, constructed and characterized two miniature custom-made visual motion sensors: (i) the APIS-based local motion sensor involving the use of a custom-made VLSI array (APIS stands for “Adaptive Pixels for Insect-based Sensors”), which is equipped with Delbrück-type auto-adaptive pixels, and (ii) the LSC-based (LSC is a component purchased from iC-Haus) local motion sensor involving the use of off-the-shelf linearly amplified photosensors, which is equipped with an on-chip pre-amplification circuit.

By combining these photodetectors with a low-cost optical assembly and a bio-inspired visual processing algorithm, highly effective miniature sensors were obtained for measuring the visual angular speed in field experiments. The present study focused on the static characteristics and the dynamic responses of these local motion sensors over a wide range of illuminance values, ranging from 50lux to 10000lux both indoors and outdoors. Although outdoor experiments are of great interest to equip Micro-Air Vehicles with visual motion sensors, we also performed indoors experiments as a comparison. The LSC-based visual motion sensor was found to be more accurate in a narrow 1.5-decade illuminance range, while the APIS-based visual motion sensor is more robust to illuminance changes in a larger 3-decade range. The method presented in this study provides a new benchmark test for thoroughly characterizing visual motion and optic flow sensors designed to operate outdoors under various lighting conditions, in unknown environments where future Micro-Aerial Vehicles will be able to navigate safely.

¹Expert, F., Viollet, S. and Ruffier, F.(2011). Outdoor Field Performances of Insect-Based Visual Motion Sensors. *Journal of Field Robotics*, 28(4): 529-541.

2.1.2 Introduction

Several optic flow-based navigation systems have been developed during the last decade for use onboard terrestrial and aerial robots. Some terrestrial robots are now being equipped with similar means of detecting and processing the optic flow to those providing insects such as flies and bees with the vital cues they need to control their own trajectories (Franceschini et al., 1992; Harrison & Koch, 1999; Humbert & Hyslop, 2010; Zwaan & Santos-Victor, 1999). Systems of this kind have even been recently used to make flying robots able to avoid obstacles (Beyeler et al., 2009; Green et al., 2004; Iida, 2001; Ruffier & Franceschini, 2008; Zufferey & Floreano, 2006), hover (Herisse et al., 2008; Kendoul et al., 2009), track a moving target (Kendoul et al., 2009; Kerhuel et al., 2010; Viollet & Franceschini, 1999) and take off, follow a terrain and land (Franceschini et al., 2007; Ruffier & Franceschini, 2005).

We have subdivided these visual motion sensors sensitive to optic flow cues into two categories, as follows:

- 1-D local motion sensors, which are based on a one dimensional (1-D) retina and compute a 1-D angular speed,
- 2-D photosensor arrays, which resolve the optic flow vector by measuring its 2 orthogonal components, the so-called 2-D optic flow sensors.

Many methods of measuring the visual angular speed have been used for robotic purposes, such as those involving the local 1-D Hassenstein and Reichardt correlator (Hassenstein & Reichardt, 1956), which was mounted on terrestrial robots (Harrison & Koch, 1999; Liu & Usseglio-Viretta, 2001), the Interpolation Image Algorithm (I2A) (Srinivasan, 1994) combined with a 1-D camera array, which was used onboard an indoor microflyer (Zufferey & Floreano, 2006), and the “time of travel” scheme (Blanes, 1986) combined with off-the-shelf photodiodes, which was implemented on both a terrestrial robot (Franceschini et al., 1992) and several tethered flying robots (Netter & Franceschini, 2002; Ruffier & Franceschini, 2005; Ruffier et al., 2003; Viollet & Franceschini, 2001).

In addition, some indoor terrestrial robots (Etienne-Cummings, 1999; Santos-Victor et al., 1995) have been equipped with standard cameras combined with navigation systems based on optic flow principles (see (Barron et al., 1994) for a review of the main optic flow techniques). Off-the-shelf computer mouse sensors measuring local 2-D optic flow were recently characterized (Chan et al., 2010) and mounted onboard terrestrial (Dahmen et al., 2009; Jackson et al., 2007) and aerial robotic platforms (Beyeler et al., 2009; Griffiths et al., 2006) navigating under constant lighting conditions.

Other visual motion sensors have been developed using analog and digital Very-Large-Scale Integration (VLSI) technology (see (Barrows & Neely, 2000; Brinkworth et al., 2009; Orchard et al., 2009; Sarpeshkar et al., 1993; Xu et al., 2011) in the case of 1-D motion sensors, (Higgins & Shams, 2002; Sarpeshkar et al., 1996) in the case of 2-D optic flow sensors, and see also (Mead, 1989; Moini, 1999) for a general review). Some other VLSI sensors based on the use of optic flow cues have been developed for collision detection purposes, such as that (Laviana et al., 2005) inspired by the locust.

However, to our knowledge, very few robotic studies have been published so far in which visual motion sensors have been implemented and tested outdoors, where the illuminance cannot be easily controlled (see (Barrows & Neely, 2000) for linear 1-D motion sensors and see (Beyeler et al., 2009; Garratt & Chahl, 2008; Griffiths et al., 2006; Kendoul et al., 2010) for 2-D optic flow sensors).

Although visual motion sensors are of great interest for robotic applications, very few attempts have been made so far to characterize systems of this kind. Some authors have tested their visual motion sensors with virtual objects presented on a video screen (using a 1-D local motion sensor (Moeckel & Liu, 2007) or 2-D optic flow sensors (Díaz et al., 2008; Okuno & Yagi, 2009)) and the performances of some VLSI motion sensors have been described in detail (see (Brinkworth et al., 2009; Harrison & Koch, 1999) for a 1-D motion sensor characterized indoors and in front of photographs of natural scenes, respectively, and see (Stocker, 2006) for a 2-D optic flow sensor characterized indoors).

It therefore seemed to be worth developing means of testing the reliability of the visual motion systems developed at our laboratory in terms of their resolution, accuracy, sensitivity and invariance to contrast in real environments under a large range of illuminance values. In this study, it was proposed to determine and compare the output signals of two custom-made bio-inspired 1-D local motion sensors (Viollet et al., 2010) based on a 2-pixel system with different front-ends, namely:

1. The APIS-based local motion sensor involving the use of a custom-made VLSI array (APIS stands for “Adaptive Pixels for Insect-based Sensors”) equipped with Delbrück-type auto-adaptive pixels (Delbrück & Mead, 1994), and
2. The LSC-based local motion sensor involving the use of off-the-shelf linearly amplified photosensors (the LSC component was purchased from iC-Haus) equipped with an on-chip pre-amplification stage.

Our visual motion scheme processes the time elapsing between the detection of any contrasting feature by two adjacent photoreceptors (Blanes, 1986, 1991; Franceschini et al., 1992, 2009; Ruffier et al., 2003): this scheme was originally inspired by the fly’s Elementary Motion Detector neurons (EMDs), since studies in which individual optical micro-stimulations were applied successively to two adjacent fly photoreceptors showed that “the first contrast change is able to facilitate the response to the second contrast change” (Franceschini et al., 1989): these responses were recorded electro-physiologically in the fly’s large tangential H1 neuron. This local motion processing system belongs to the token-matching category of schemes (Ullman, 1981) and was later called the “time of travel” scheme (Benson & Delbrück, 1992; Moeckel & Liu, 2007). In the mid-1990’s, a similar principle was used again to design a smart VLSI circuit called the “facilitate and sample” sensor (Kramer et al., 1995).

The characteristics of the two local motion sensors in question were determined here by recording their responses to a purely rotational optic flow generated by rotating the sensors mechanically indoors and outdoors. In the case of a stationary environment, the rotational optic flow ω , which is by definition independent of the distance from the sensors to the surrounding objects (Koenderink & van Doorn, 1987), can be directly compared to the rate gyro output signal denoted Ω_{gyro} .

In this study, we also analysed the refresh rate of our local motion sensors, as this is a key parameter in optic flow-based robotic applications. The average refresh rate $f_{refresh}$, was defined here as the number of new visual motion measurements obtained per second: a new measurement occurred whenever a contrast was detected by the first pixel and then by the second pixel with a time lag corresponding to our measurement range. The refresh rate was computed and analysed under various illuminance conditions, both indoors and outdoors.

A description of the two local motion sensors tested here is given in section 2.1.3. Section 2.1.5 gives an account of the performances of these visual motion sensors, which were tested

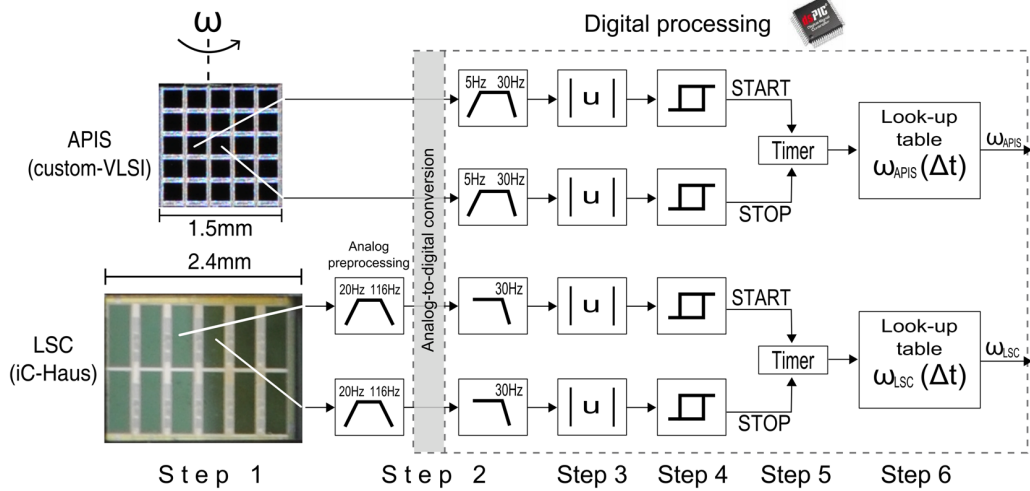


Figure 2.2: General processing architecture of the APIS-based and LSC-based local motion sensors. In each sensor, the output signals emitted by two adjacent pixels were spatially and temporally filtered and thresholded to determine the angular speed ω . The “time of travel” scheme previously developed at Franceschini’s Laboratory (Blanes, 1986, 1991; Franceschini et al., 2009) was used to measure the local visual motion. The angular speed measured by each sensor ω_{meas} is the ratio between the constant inter-receptor angle $\Delta\varphi$ and the time Δt elapsing between the first and second thresholded signals. The overall processing of the two local motion sensors was carried out in parallel on the same microcontroller (dsPIC 33FJ128GP804) at a sampling frequency of 2kHz.

In the case of the LSC-based motion sensor, the two photodiode outputs were first filtered by an analog band-pass filter with cut-off frequencies [20Hz, 116Hz] before being filtered by a digital second order low-pass filter with a cut-off frequency of 30Hz.

In the case of the APIS-based motion sensor, the two photodiode outputs were filtered by a digital band-pass filter with cut-off frequencies [5Hz, 30Hz].

both indoors and outdoors in a large range of illuminance levels. For the sake of clarity, constant thresholds and settings were applied throughout this study: the performances of both visual motion sensors were found to be remarkably satisfactory in terms of their accuracy, refresh rate and robustness to changes in the visual environment and the illuminance.

The LSC-based visual motion sensor proved to work more efficiently in terms of the refresh rate and the accuracy over a narrow dynamic range of 1.5 decades, whereas the APIS-based visual motion sensor measured the angular speed accurately over a much wider 3-decade range of illuminance values.

2.1.3 Description of the local visual motion sensors

Basically, each of the APIS-based and LSC-based visual motion sensors consists of a lens placed in front of a photosensor array: each visual motion sensor processes the output signals generated by 2 photodiodes. Each photodiode’s output signal is transmitted to a processing unit, where a digital version of the visual motion algorithm assesses the relative angular speed ω of any contrasting features encountered in the environment (i.e., a 1-D component of the optic flow). In this study, two 2-pixel motion sensors based on the same “time of travel” principle but equipped with two different front-ends were compared (see figure 2.3).

The front-end of the APIS-based local motion sensor was based on adaptive pixels, originally suggested by (Delbrück & Mead, 1994). The whole APIS (Adaptive Pixels for Insect-

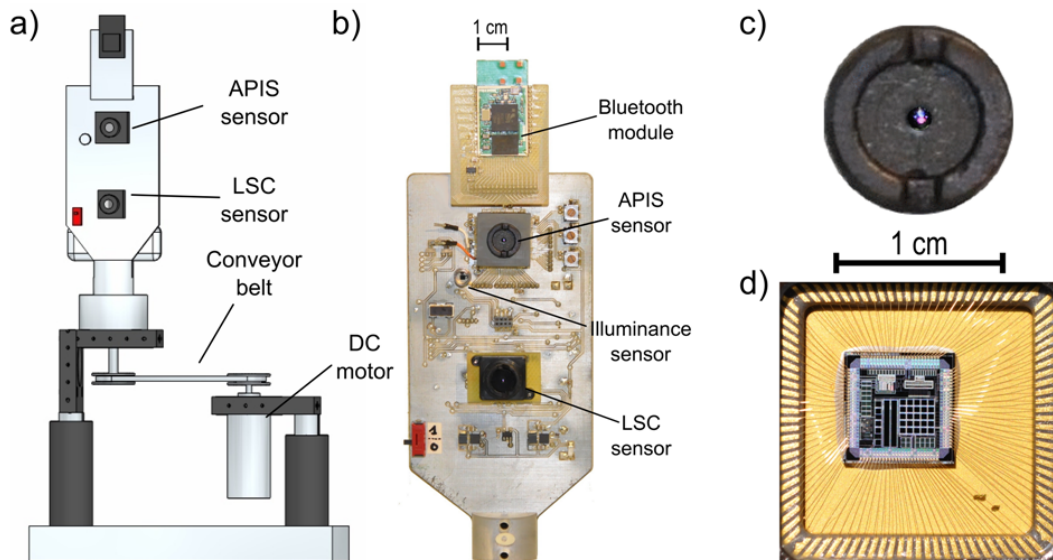


Figure 2.3: Test-board that includes both local motion sensors

a) Sketch of the full mechanical system. A mechanical rotational angular speed Ω was imposed on the board by means of a DC motor (2233012S from Minimotor) regulated via a proportional-integral controller.

b) Picture of the sensor board, which included the two custom-made visual motion sensors, an illuminance sensor based on a single elementary photodiode, and on the other side of the board (not visible here), a rate gyro (Analog Devices, ADIS 16100) measuring the reference mechanical angular speed (i.e., the rotational speed of the board) and a 16-bit microcontroller (dsPIC 33FJ128GP804) equipped with several 12-bit ADC (Analog to Digital Converter) inputs. The microcontroller processes the visual signals received by the two visual motion sensors at a sampling frequency of 2kHz. The measured visual motion ω_{meas} and the rotational speed Ω_{gyro} are recorded synchronously and sent to a computer via a Bluetooth module connected to a small battery (LiPo, 300mAh-3.3V). This wireless link leaves the sensor board free to rotate autonomously.

c) The visual motion sensors' miniature camera lens (Sparkfun SEN-00637, focal length 2mm, f-number 2.8) is defocused with respect to the focal plane to create a Gaussian angular sensitivity.

d) The APIS sensor along with the 5x5 photodiode array and an auto-adaptive circuit: only two pixels are connected to the dsPIC microcontroller.

based Sensors) retina, a custom-made VLSI retina comprising 25 pixels (figure 2.3d), was developed in collaboration with the Center for Particle Physics (CPPM) in Marseilles (Aubépart et al., 2007; Viollet et al., 2010). Each pixel features an integrated photodiode with a sensitive area of $250\mu m * 250\mu m$ connected to an adaptive, time-continuous, logarithmic circuit having a dynamic range of 100dB.

The front-end of the LSC-based local motion sensor was based on an off-the-shelf photodiode array (LSC is a component purchased from iC-Haus) consisting of 2 rows of 6 pixels. To make the sensor able to distinguish a larger number of contrasting patterns at low illuminance levels, we summed together the 2 pixels in the same column to improve the signal-to-noise ratio by increasing the sensitive area to $300\mu m * 1600\mu m$. These two “elongated photosensors” were combined with a classical fixed-gain photocurrent amplifier implemented using Surface Mount Device (SMD) components. The original local motion detector (Blanes, 1986; Franceschini et al., 2009; Ruffier et al., 2003) (also called “time of travel”) consisted of an analog circuit producing an output signal that increased as the time lag Δt between its two inputs decreased. The output signal therefore increased with the angular speed ω . Like the fly’s motion-detecting neurons from which it was originally inspired (Franceschini et al., 1989), our visual motion sensors can react to either dark-to-light (ON) or light-to-dark (OFF) contrasts. The bio-inspired signal processing method implemented in each of the two local motion sensors can be decomposed into 6 steps (Blanes, 1986; Franceschini et al., 2009; Ruffier et al., 2003) (see figure 2.2) as follows:

- Step 1: Spatial sampling and low-pass spatial filtering (which is achieved by defocusing the miniature camera lens to obtain a Gaussian angular sensitivity for each pixel),
- Step 2: Band-pass temporal filtering: high-pass temporal filtering to differentiate the visual signals and low-pass temporal filtering to reduce the noise such as the 100-Hz interference originating from artificial lighting (this step is partially analog in the case of the LSC-based visual motion sensor),
- Step 3: Taking the absolute value of the signals to detect both dark-to-light and light-to-dark contrast transitions,
- Step 4: Thresholding with fixed values regardless of the illuminance background,
- Step 5: Measuring the time Δt (time of travel) elapsing between the thresholded signals,
- Step 6: Computing the local angular speed by applying:

$$\omega_{meas} = \frac{\Delta\varphi}{\Delta t} \quad (2.1)$$

Each angular speed measured was then fed via a tiny Bluetooth module (F2M03GLA from Free2move company) into a computer for analysis.

This overall processing was carried out on a dsPIC 33FJ128GP804 microcontroller working at a sampling frequency of 2kHz in floating-point arithmetic. The simultaneous processing of the two sensors (APIS-based and LSC-based) including the serial readout interface occupies

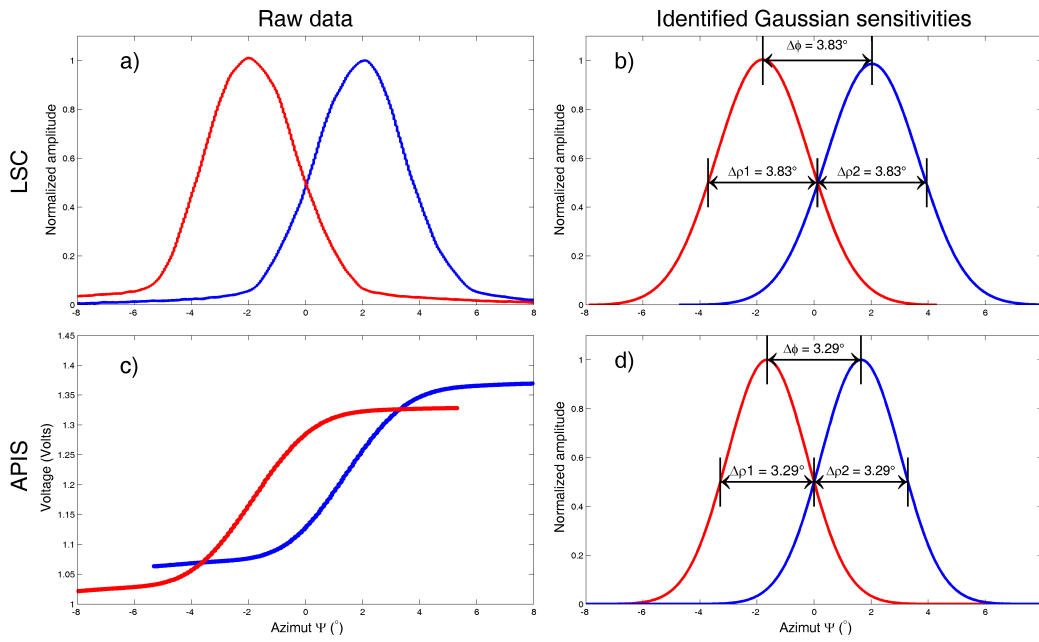


Figure 2.4: Gaussian angular sensitivities of the LSC and APIS photosensors

a) Outputs of the two linearly amplified photosensors in the LSC array during a slow rotation of the sensor placed 50cm in front of a fixed point light source.

b) Gaussian sensitivity of the two photodetectors approximated using *cftool* (Matlab). The defocusing was adjusted in order to obtain $\Delta\varphi = \Delta\rho$. As the correlation coefficient ($R_{LSC}^2 > 0.994$) is very nearly equal to 1, this confirms that we can obtain Gaussian sensitivity by defocusing.

c) Outputs from the two photosensors used out of the 25 pixels on the APIS retina, when rotated horizontally in front of a vertical black-and-white contrasting edge.

d) Gaussian sensitivity of the APIS photoreceptors computed from the approximated error function, *erf* ($R_{APIS}^2 > 0.999$).

10% of the program memory, 13% of the data memory of the microcontroller and accounts for 52% of the processing time available at a sampling frequency of 2kHz. The overall signal processing tasks do not require performing any time-consuming tasks such as division because a look-up table was used to transform the Δt into the visually perceived angular speed ω_{meas} (see equation (2.1)). All embedded algorithms were developed on Matlab with a Simulink blockset for dsPIC called Embedded Target for dsPIC.

The angular sensitivity function of a single fly photoreceptor is a Gaussian distribution (Götz, 1964), which results from the spatial convolution of the photoreceptor's diameter with the point spread function of the facet lenslet (Franceschini & Kirschfeld, 1971; Stavenga, 2003). As shown in figure 2.4, a similar Gaussian sensitivity profile to that of the fly was obtained here by defocusing the lens of a miniature camera (by reducing the distance between the lens and the retina). In each local motion sensor, the full width at half-height of the Gaussian curve (which is called the acceptance angle) $\Delta\rho$ directly determines the cut-off frequency of the low-pass spatial filtering process (step1), whereas the inter-receptor angle $\Delta\varphi$ determines the angular speed (ω) measurement range. As occurs in some diurnal insects (Land, 1997), these angles were adjusted in this study to obtain the following optical property:

$$\Delta\varphi = \Delta\rho \quad (2.2)$$

It is worth noting that these two optic sensors were both constructed using the same optic assembly originating from a low-cost miniature camera lens (Sparkfun SEN-00637, focal length 2mm, f-number 2.8).

In the case of the LSC-based photoreceptors, the angular sensitivity function of the lens/photodiode assembly was assessed by slowly rotating the photoreceptors placed 50cm in front of a fixed point light source. The angular sensitivity measured fitted a Gaussian curve (cf. figure 2.4a and b) having the width at half-height $\Delta\rho_{LSC} = 3.8^\circ$, the inter-receptor angle $\Delta\varphi_{LSC} = 3.8^\circ$ and the correlation coefficient $R_{LSC}^2 > 0.994$. In the case of the APIS-based photoreceptors, the angular sensitivity function of the lens/photodiode assembly was assessed from the Gaussian error function (cf. figures 2.4c and 2.4d) obtained by quickly rotating in the horizontal plane the visual motion sensor placed 1 meter in front of a vertical contrasting edge (Kerhuel, 2009). The correlation coefficient between the raw data and the Gaussian error function (erf) was $R_{APIS}^2 > 0.999$ in this case when $\Delta\rho_{APIS} = \Delta\varphi_{APIS} = 3.3^\circ$.

The main characteristics of the two sensors are summarized in the table 2.1. In previous local motion sensors (Pudas et al., 2007; Ruffier et al., 2003), the temporal band-pass filter consisted of a 1st order high-pass filter with a cut-off frequency of 20Hz and a 4th order Butterworth low-pass filter with a cut-off frequency of 30Hz. To reduce the processing burden on the microcontroller, the order of the Butterworth filter of both sensors was reduced two-fold thanks to the on-chip pre-amplification unit, which reduced the noise. A 2nd order digital low-pass filter was therefore implemented in the dsPIC microcontroller (cf. figure 2.2). In addition, as the on-chip auto-adaptive circuit already features an illuminance-dependent high-pass filter effect, the cut-off frequency of the high-pass filter in the present APIS-based visual motion sensor was reduced to 5Hz.

Figure 2.3b shows the two local motion sensors mounted on an identical printed-circuit board (PCB). An additional illuminance sensor (an OSRAM photodiode BPX65) was connected to an analog amplifier circuit operating in the photovoltaic mode in order to measure

Local motion Sensor	APIS-based	LSC-based
Inter-receptor angle $\Delta\varphi(^{\circ})$	3.3	3.8
Acceptance angle $\Delta\rho(^{\circ})$	3.3	3.8
Photodiode size (μm)	250 x 250	300 x 1600
Pixel pitch (μm)	300	420
Focal length of the lens (mm)	2	
F_{number} of the lens (#)	2.8	
Angular velocity Range ($^{\circ}/s$)	[50, 350]	
Resolution ($^{\circ}/s$) [Min; Max]	[0.4; 18.32]	[0.33; 15.14]
Sensitivity ($^{\circ}/s/LSB$)	1.53 e-3	
Estimated mass with optics in a stand-alone version (g)	< 2g	< 1g

Table 2.1: Specifications of the APIS-based and LSC-based visual motion sensors.

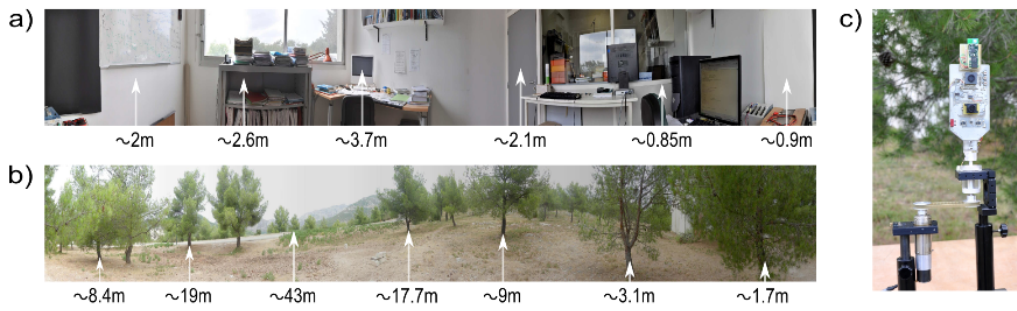


Figure 2.5: a) Picture of the indoor scene where the local motion sensors were tested. b) Picture of the outdoor scene where the local motion sensors were tested. Distances to the surrounding objects (indicated by a white arrow) are given below each picture. c) Picture of the sensor board and the mechanical system placed outdoors.

the effective illuminance of the scene scanned by the visual motion sensors. The photocurrent I_{ph} output of this illuminance sensor was determined as follows:

$$I_{ph} = (e^{V_{out}/0.125} - 1)I_{dark} \quad (2.3)$$

where the dark current I_{dark} is equal to $1nA$ and V_{out} is the amplifier's output voltage (Riggs, 1983). The sensor board was rotated by means of a DC motor (see figure 2.3a) controlled by a proportional-integral regulator.

2.1.4 Benchmarking of the visual motion sensors

The two visual motion sensors were tested both indoors and outdoors (see figures 2.5a and 2.5b) by comparing their output signals with the angular speed Ω_{gyro} measured on a rate gyro (Analog Devices, ADIS 16100), which can measure angular speeds in the 0 to $300^{\circ}/s$ range. For the outdoor measurements, the sensor board was placed on a table equipped with 4 rugged wheels.

As shown in figure 2.3a, the sensor board was connected to a DC motor via a belt, which made it possible to finely adjust the mechanical angular speed of the board, Ω ranging between $60^\circ/s$ and $300^\circ/s$. In both environments, the static and dynamic responses of the visual motion sensors were measured with several background illuminance values:

- indoors: (i) 50lux, (ii) 2000-10000lux, corresponding to (i) a dim artificial light and (ii) a large amount of sunlight from the windows;
- outdoors: (i) 100lux, (ii) 10000lux, corresponding to (i) dusk and (ii) a sunny day.

The low illuminance values used indoors and outdoors were chosen to allow the LSC-based local motion sensor to detect contrasts and the high illuminance values were the maximum possible values obtained at this period of the year (April 2010) in Marseilles when a luxmeter was oriented at the same direction than the sensors. The background illuminance values were measured in lux by a digital lux-meter (Roline, RO-1332), which gives only an estimate of the overall environmental illuminance. The static responses of the sensors were assessed by applying a series of $30^\circ/s$ fifteen-second steps at a rotational speed Ω ranging from $60^\circ/s$ to $300^\circ/s$. To test the dynamic characteristics of the sensors, a 50-second stimulus was applied, during which variably long periods of constantly increasing and decreasing velocity ranging between $60^\circ/s$ and $300^\circ/s$ were imposed.

2.1.5 Experimental results

2.1.5.1 Static angular speed characteristics

Figure 2.6 gives the static characteristics of the two sensors indoors and outdoors, as assessed by applying $30^\circ/s$ steps (lasting 15 seconds) to the rotational speed from $60^\circ/s$ to $300^\circ/s$. The background illuminance ranged indoors between 50lux and 2000lux (apart from some peaks at 10000lux) and outdoors between 100lux and 10000lux. With each visual motion sensor and at each illuminance level, the mean standard deviation of the data was computed as follows:

$$\overline{Std} = \overline{std(\omega_{meas})} \quad (2.4)$$

To estimate the accuracy of the sensor, the best linear approximation was calculated with each sensor and each illuminance background, based on the equation (2.5).

$$\omega_{meas} = a \times \Omega \quad (2.5)$$

The regression coefficient of this function was used to compute the linearity error according to the equation (2.6).

$$LinearityError(\%) = |(a - 1)| \times 100 \quad (2.6)$$

As shown in figure 2.6, the LSC-based local motion sensor showed a high level of invariance to the illuminance, while the linearity of its static characteristics remained unchanged, provided the illuminance and the rotation speed were maintained at a relatively high level. Regardless of the illuminance, both sensors responded accurately, as shown by the small linearity error rate ($<4.5\%$ in most cases). As shown in figure 2.6e, the LSC-based local motion sensor remained silent at a 50-lux illuminance level and at rotational speeds below $150^\circ/s$. The

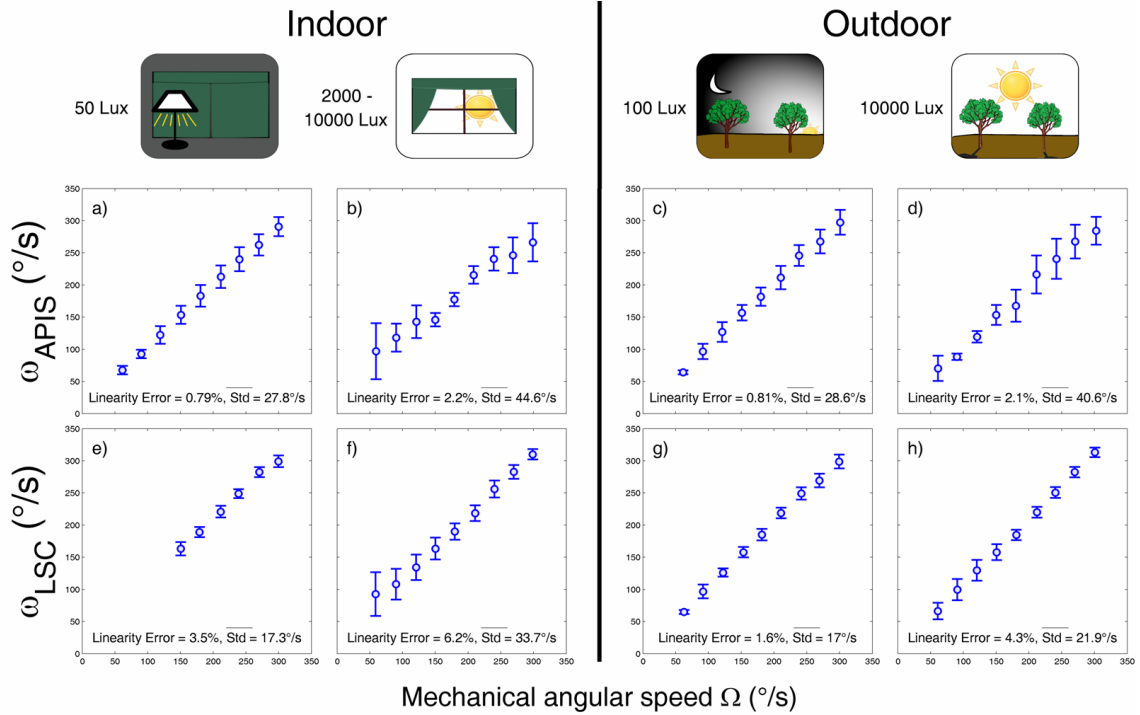


Figure 2.6: Static indoor and outdoor characteristics of the LSC- and APIS-based local motion sensors assessed by applying $30^\circ/s$ steps (lasting 15 seconds) to the rotational speed from $60^\circ/s$ to $300^\circ/s$. The background illuminance ranged indoors between 50lux and 2000lux (apart from some peaks at 10000lux) and outdoors between 100lux and 10000lux. The mean visual motion recorded at each angular speed Ω is plotted in this figure with its standard deviation. The best linear approximation obtained in each experiment was computed and the departure from linearity is given as a percentage.

a-b-c-d) Static indoor and outdoor characteristics of the APIS-based local motion sensor.

e-f-g-h) Static indoor and outdoor characteristics of the LSC-based local motion sensor.

b-d) When the illuminance increased, the dispersion of the data recorded with the APIS-based visual motion sensor increased due to several matching errors occurring because of the adaptation process of the auto-adaptive circuit at work during the data capture.

e) At low angular speeds and low illuminance values, the LSC-based local motion sensor did not detect any contrasts during the 15-second steps.

f-g-h) The LSC-based local motion sensor responded as soon as the background illuminance values and the rotational speed were high enough. In addition, the LSC-based local motion sensor showed good linearity and little dispersion.

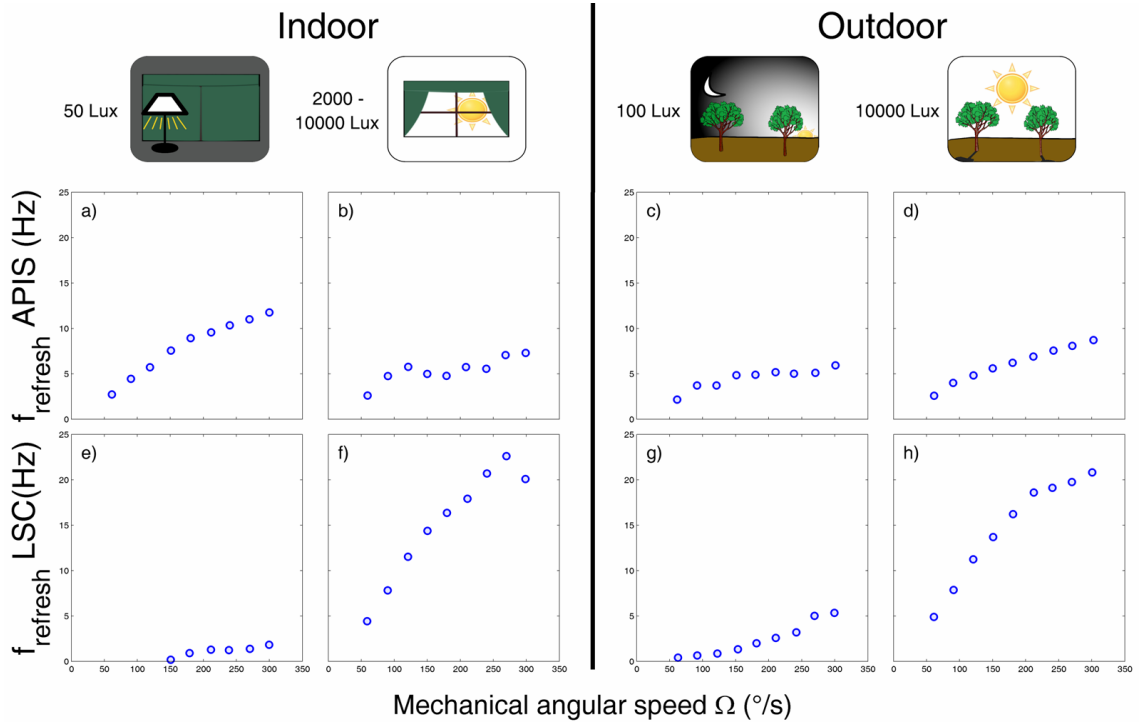


Figure 2.7: Refresh rates of the LSC- and APIS-based local motion sensors measured indoors and outdoors at a rotational speed ranging from $60^\circ/s$ to $300^\circ/s$ in $30^\circ/s$ steps (lasting 15s).

a-b-c-d) Refresh rate of the APIS-based local motion sensor indoors and outdoors with an illuminance background varying from 50lux to 10000lux. The on-chip auto-adaptive circuit rendered the APIS-based local motion sensor invariant to the illuminance in terms of the refresh rate.

e-f-g-h) Refresh rate of the LSC-based local motion sensor indoors and outdoors with an illuminance background ranging from 50lux to 10000lux. The LSC-based local motion sensor showed the occurrence of considerable refresh rate variations at several illuminance levels. The LSC-based local motion sensor was found to have much higher refresh rates at high illuminance values than the APIS-based visual sensor.

static characteristics of the APIS-based local motion sensor also showed good invariance to the lighting conditions, whereas the dispersion of the values increased slightly with the illuminance at the lowest and highest speeds tested (figures 2.6b and 2.6d).

The dispersion of the data obtained with the APIS-based local motion sensor was no doubt mainly attributable to the presence, at the pixel level, of an auto-adaptive circuit with no anti-aliasing filter. The digitization process may therefore have distorted the photodiode signals, thus causing visual motion measurement errors. The frequency response of the adaptive circuit showed a dramatic increase in the bandwidth with the illuminance, ranging from 700Hz at 1lux to 1MHz at 10^5 lux.

2.1.5.2 Refresh rate analysis

The refresh rates of the two sensors measured indoors and outdoors are shown in Figure 2.7. The refresh rate was defined as the number of new motion measurements per second: a new measurement occurs when a contrast transition is detected by one pixel and then by the second pixel with a time lag Δt in our measurement range, corresponding to an angular speed in the $[50^\circ/s, 350^\circ/s]$ range (see equation (2.1)). A contrast was detected whenever the two adjacent photodiode outputs exceeded the threshold values in the preferred direction. On the whole, the refresh rate of the LSC-based visual motion sensor was found to depend on the illuminance and to vary quasi-linearly with the rotational speed Ω_{gyro} .

Landolt and Mitros (Landolt & Mitros, 2001) have stated that an eye rotating at an angular speed ω converts spatial frequency into temporal frequency as given by the equation:

$$f_T = \omega \times f_S \quad (2.7)$$

(where f_T is the temporal frequency of the photoreceptor output signal, ω is the angular speed of the visual sensor with respect to the contrasting pattern, and f_S is the spatial frequency associated with the contrasting pattern).

According to the above equation (2.7) and assuming that the local motion sensor detected the same contrasts regardless of the angular speed, the number of new angular speed measurements per second could be expected to increase linearly with the rotational speed as the temporal frequency f_T increased. However, as shown by figures 2.7f and 2.7h, the refresh rate of the LSC-based visual motion sensor stopped increasing at high angular speeds. Spatial low-pass filtering (cf. figure 2.4) combined with a temporal second order low-pass filter (cf. figure 2.2) limited the range of the temporal frequency f_T of each photoreceptor output signal to a frequency of 30Hz and therefore limited the refresh rate of the LSC-based motion sensor to below 30Hz at high angular speeds.

Contrary to the refresh rates of the LSC-based motion sensor, which showed considerable variations (between 5Hz and 23Hz at $300^\circ/s$, see figures 2.7e, 2.7f, 2.7g and 2.7h), those of the APIS-based visual sensor were found to be independent of the illuminance and to increase slightly with the angular speed (see figures 2.7a, 2.7b, 2.7c and 2.7d). In each environmental condition, the illuminance background dispersion was computed from the illuminance sensor data recorded at each angular speed during the static experiments (figure 2.6 and 2.7). Based on the mean values obtained in each experiment, the dispersion was found to be quite low at low illuminance levels (58nA at 50lux and $1.3\mu A$ at 100lux) and greater at high illuminance levels (8.4mA at 2000-10000lux indoors and 1.1mA at 10000lux outdoors). Because of these marked variations in the background illuminance, the Delbrück's pixels in the APIS chip were constantly adapting to a new background illuminance with a relatively slow time constant

varying with the illuminance (from $\sim 10\mu\text{s}$ at 100lux to $\sim 1\text{ms}$ at 10000lux). Therefore, during the tests, the photoreceptor output signals frequently exceeded the switch-on point of the hysteresis function (step 4 in figure 2.2) without dropping fast enough below the switch-off point before the next contrast was encountered. A linear increase in the angular speed therefore did not lead to a linear increase in the APIS-based motion sensor's refresh rate. The switch-on and switch-off points of the hysteresis threshold function in the APIS-based motion sensor were selected because they gave the best trade-off between its refresh rate and the angular speed measurement accuracy.

2.1.5.3 Dynamic visual motion characteristics

The dynamic indoor and outdoor responses of the two visual motion sensors are shown in figure 2.8, where the angular speed ω_{LSC} , ω_{APIS} measured (blue dots) is superimposed on the reference angular speed Ω_{gyro} (red). In the dynamic experiments, the data dispersion was taken to be the standard deviation of the difference between the angular speeds measured by the rate gyro and the local motion sensor output signal, according to the following equation (2.8):

$$Std_{error} = std(\Omega_{gyro} - \omega_{meas}) \quad (2.8)$$

Despite the great difference in the illuminance, which ranged between 50lux and 10000lux (figures 2.8i, 2.8j, 2.8k and 2.8l), the responses of both the APIS and LSC-based visual motion sensors faithfully obeyed the triangular law imposed on the rotational speed of the board. During the indoor experiment at 2000lux, as the light coming mainly from a single window was non-uniformly distributed, strong variations in the illuminance (between 2000 and 10000lux) were observed during a 360° rotation, as shown in figure 2.8j.

As shown in figures 2.8b and 2.8d, the error and the standard deviation of the APIS-based local motion sensor increased slightly with the illuminance.

At low illuminance levels, the average refresh rate of the LSC-based motion sensor was below 3Hz (2.8e and 2.8g). As the illuminance increased, the average refresh rate $\overline{f_{refresh}}$ of the LSC-based local motion sensor increased without strongly increasing the corresponding standard deviation (figures 2.8f and 2.8h). As mentioned above in connection with the static measurements, the APIS-based motion sensor's refresh rate increased slightly with the illuminance, whereas the refresh rate of the LSC-based motion sensor increased from 1.26Hz to 15.3Hz between 100lux and 10000lux.

Local motion sensors with average refresh rates greater than 6Hz and standard deviations below $50^\circ/\text{s}$ can be said to constitute remarkable tools for performing robotic tasks such as obstacle avoidance or terrain following. It can therefore be seen from figures 2.6-2.7-2.8 that the LSC- and APIS-based local motion sensors are both highly suitable for performing tasks of this kind even outdoors at illuminance levels ranging between 300-10000lux (1.5 decades) and 10-10000lux (3 decades), respectively.

2.1.6 Conclusion

Two 1-D visual motion sensors were tested and characterized here in field experiments under various lighting conditions. The benchmark test presented above can be used to fully characterize various visual motion sensors indoors and outdoors under several decades of

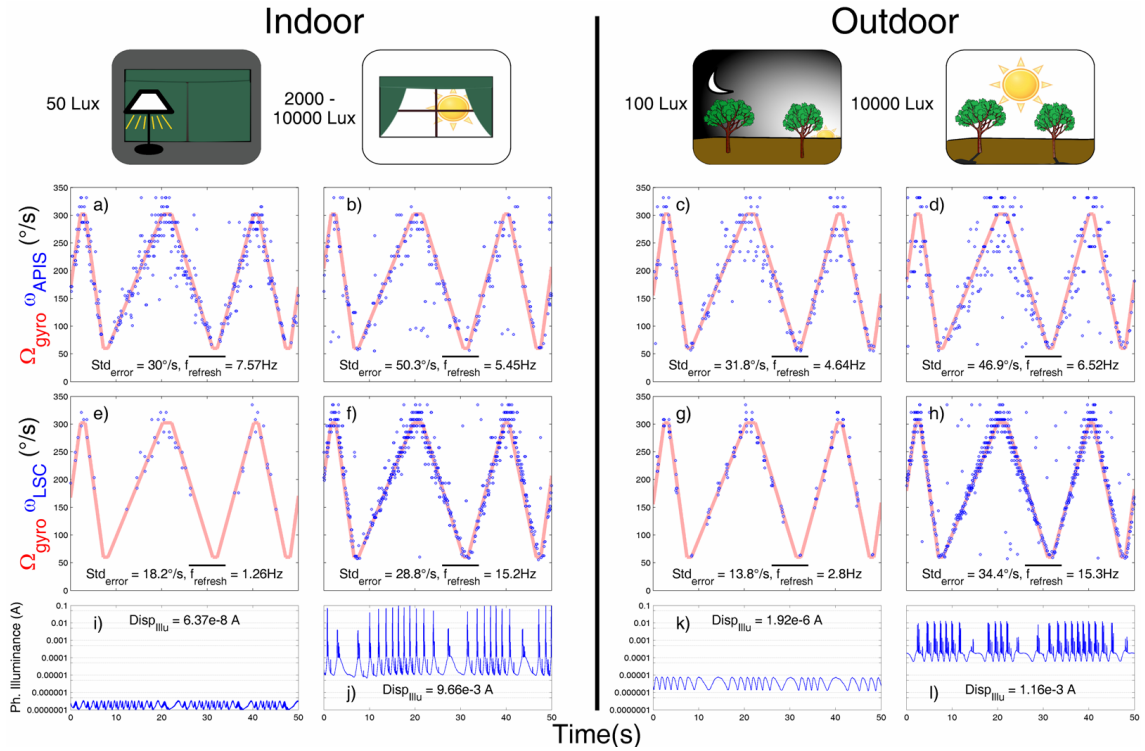


Figure 2.8: Dynamic indoor and outdoor responses of the two visual motion sensors (blue dots, figure 2.5a and 2.5b). The visual motion sensors mechanically rotated, giving a triangular pattern of angular speed variation (red) involving a series of velocity ramps ranging between $60^\circ/\text{s}$ and $300^\circ/\text{s}$ with different slopes under four different lighting conditions. Despite the strong illuminance variations, both visual motion sensors followed the rotational angular speed quite faithfully. With both sensors, the error between the measured local motion ω_{meas} and the angular velocity measured by the rate gyro Ω_{gyro} was used to compute the standard deviation of the error. The average refresh rate of the sensor was defined here as the number of new measurements occurring during the whole experiment divided by the duration of the experiment.

a-b-c-d) Dynamic indoor and outdoor responses of the APIS-based local motion sensor. Despite the considerable variations in the illuminance, the average refresh rate of the APIS-based sensor was always of a similar order of magnitude thanks to the auto-adaptive circuit. As shown in (b) and (d), the standard deviation of the error increased with the illuminance.

e-f-g-h) Dynamic indoor and outdoor responses of the LSC-based local motion sensor. As was to be expected from the static characteristics, the average refresh rate of the LSC-based sensor can be seen in these figures to have increased with the illuminance.

i-j-k-l) Dynamic response of the illuminance sensor and dispersion of the photodiode's output current. The large variations in the values detected by the illuminance sensor shown in (j) and (l) increased the dispersion of the APIS-based local motion sensor's response as shown in (b) and (d).

illuminance. The performances of the visual motion sensors tested with this method can be said to correspond fairly well to those which could be obtained with a flying robot because the sensors were tested here in field experiments under various lighting conditions.

As expected in view of its auto-adaptive pixels, the APIS-based local motion sensor based on a custom-made VLSI retina equipped with adaptive pixels gave the best performances in terms of its invariance to the illuminance. Although the LSC-based local motion sensor equipped with linearly amplified photosensors failed to respond to contrasts encountered at low angular speeds ($<150^\circ/\text{s}$) under low illuminance conditions ($<300\text{lux}$), all its measurements were highly accurate. Thanks to the auto-adaptive circuit designed to detect visual motion in several decades of illuminance, the characteristics of the APIS-based motion sensor are fairly consistent in this range, although some improvements could be made in terms of the average refresh rate and the accuracy. In the new APIS chip, it is proposed to integrate in the future an additional first order low-pass filter at the pixel level to decrease the dispersion of the APIS-based motion sensor.

The average refresh rate of the visual motion sensors, which is a key parameter in visual control systems based on motion sensors, was studied in particular here. It was established that the LSC-based motion sensor gives higher refresh rates at high angular speeds and strong illuminance levels than the APIS-based motion sensor. However, the average refresh rate of the latter sensor endowed with auto-adaptative pixels is suitably high even at low illuminance levels.

The LSC-based motion sensor gave the best results in terms of the accuracy and the average refresh rate in a narrow illuminance range (1.5 decades), whereas the APIS-based motion sensor turned out to be capable of measuring the angular speed in a 3-decade range of illuminance values.

To summarize, it was established here that these miniature visual motion sensors consisting of low cost optics and classical electronic components combined with appropriate visual signal processing methods give accurate and reliable results under natural conditions even in an outdoor environment. Besides, the “time of travel” scheme along with fixed thresholds and settings proved to be efficient in an illuminance range of several decades. In this study, we focused consistently on the same parameters in order to be able to make valid comparisons, but the performances of the sensors could be improved by dynamically adjusting the thresholds, (see figure 2.2, step 4) depending on the illuminance.

A stand-alone version of these sensors will predictably weigh less than 2g in the case of LSC-based and APIS-based local motion sensors.

These sensors could be used in natural environments on aerial or terrestrial robots for obstacle avoidance, take-off and landing, speed control purposes. Depending on what type of robotic behaviour is required, the Gaussian angular sensitivity has to be adjusted to fit a specific altitude and speed range. The inter-receptor and acceptance angles determine the most suitable distance at which objects should be detected, and thus the angular speed range that can be measured on the basis of the motion sensor’s range. In our case, a similar visual motion sensor ($\Delta\varphi = \Delta\rho = 4^\circ$) to those tested here has been successfully used on the aerial robot OCTAVE (Ruffier & Franceschini, 2005), which was able to fly at altitudes of up to 1.5m and speeds of up to 3m/s.

Depending on the field of application for which visual motion sensors are intended, great care has to be taken in choosing appropriate electronic circuits at the pixel level. It was established in this study that auto-adaptive pixels do not always yield the most accurate measurements in terms of the angular speed. In conclusion, this study brings us one step

further towards implementing tiny, light, robust visual motion sensors that could be applied in many fields such as automotive, robotic and avionic design, planetary landers and free-flying micro-aerial vehicles weighing less than 10 grams.

2.2 Comparison with a mouse sensor ²

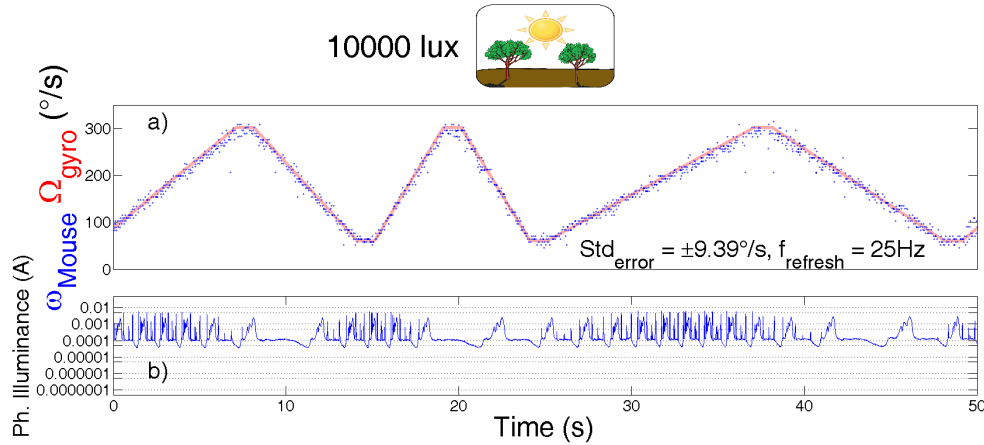


Figure 2.9: a) Outdoor dynamic response of the mouse sensor, ω_{Mouse} , under 10000 lux lighting conditions. At high illuminance levels, the data obtained with the mouse sensor showed little dispersion, and the maximum refresh rate possible at this R/O frequency (25Hz). b) Dynamic response of the illuminance sensor.

As we have seen in section 1.2.4, authors have recently started to use off-the-shelf optical mouse sensors as optic flow sensors onboard flying robots navigating outdoors. Indeed, such sensors seem to give satisfactory results to control an aircraft while being lightweight and passive which make them suitable with the constraints of Micro Aerial Vehicles. However, these sensors have always been used for outdoor applications and we were curious to assess their performances in various illuminance conditions.

This is the reason why we chose to compare the characteristics of our LSC-based local motion sensor with the mouse sensor the most commonly used in robotics: the ADNS-9500 from Avago. Thanks to the benchmark previously developed, we determined the performances of these two sensors thanks to their responses to a purely rotational optic flow both indoors and outdoors which were compared with the output of a rate gyro.

The mouse sensor's dynamic response was measured in the outdoor environment (see Figure 2.9) on a sunny day under 10000 lux lighting conditions. As was to be expected, the dispersion of the data obtained with the mouse sensor was found to be very low ($< \pm 10^\circ/s$) and the refresh rate was equal to the readout frequency. This confirms that this optical sensor is suitable for use on outdoor flying robots.

However, as can be seen in Figure 2.10 showing the indoor dynamic responses of both visual motion sensors, the mouse sensor failed to accurately measure the angular speed in

²Expert, F., Viollet, S. and Ruffier, F.(2012). A mouse sensor and a 2-pixel motion sensor exposed to continuous illuminance changes. *IEEE Sensors Conference 2011*, 974-977.

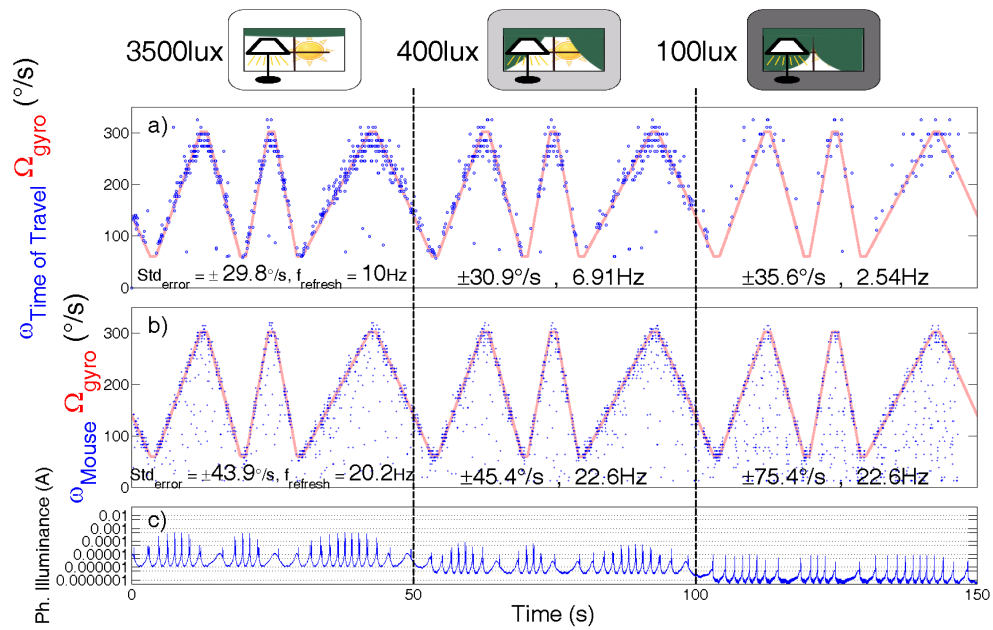


Figure 2.10: **a)** Dynamic response of the bio-inspired 2-pixel local motion sensor, $\omega_{TimeOfTravel}$ (blue dots). The sensor can be seen here to have rotated, giving a triangular pattern of variation (red) involving a series of velocity ramps ranging between $60^\circ/s$ and $300^\circ/s$ with different slopes under three different lighting conditions. Despite the strong illuminance variations, the bio-inspired 2-pixel LMS followed the rotational angular speed faithfully. The difference between the measured local motion and the angular velocity measured by the rate gyro Ω_{gyro} was used to compute the standard deviation of the error under each environmental condition. **b)** Dynamic response of the mouse sensor, ω_{Mouse} (blue dots) superimposed on the reference angular speed Ω_{gyro} measured by the rate gyro. Only measurements differing from zero were plotted. **c)** Dynamic response of an illuminance sensor based on the use of a single photodiode to measure the effective illuminance of the scene scanned by the visual motion sensors. Strong variations were observed because the light was mainly provided by a single window.

the indoor environment. Indeed, despite the continuous changes in the illuminance which can be seen to have occurred in Figure 2.10(c), the response of the bio-inspired 2-pixel LMS faithfully obeyed the triangular law imposed on the rotational speed of the board and the dispersion was low. On the other hand, with the mouse sensor, the dispersion increased a lot at low illuminance levels as the angular speed was frequently under-estimated (see Figure 2.10b) because the sensor did not detect a sufficiently large number of valid features.

This study shows that our bio-inspired sensor processing the 1D angular speed from only two adjacent pixels competes satisfactorily in terms of accuracy with a 900-pixel mouse sensor. However, the mouse sensor computes the angular speed simultaneously in two directions.

Article 2: Two-Directional 1-g Visual Motion Sensor Inspired by the Fly's Eye

In the previous studies, we have shown that our bio-inspired sensors give robust measurements of the angular speed based on only two adjacent photoreceptors. Although these sensors are suitable for robotics applications, it seems clear that the accuracy of the measurements could be increased by fusing the output of several 2-pixel LMSs processing the angular speed in a specific Region Of Interest (ROI). Besides, the presented implementation of the “time of travel” scheme is limited in the sense that the direction of motion has to be known.

This is the reason why we have developed a new stand-alone optic flow sensor (see Figure 2.11) fitted to the very strong constraints of the Micro Aerial Vehicles of the future which are:

- a very small weight of less than 1g with optics,
- a small size $23.3 \times 12.3mm$,
- a limited power consumption ($< 0.23W$).

This Visual Motion Sensor (VMS) is based on a 6 pixels retina having a Field Of View (FOV) of 28.8° and computing on a dsPIC microcontroller 5 LMSs at a 2kHz frame rate in both directions. The outputs of these 5 LMSs are then fused thanks to the median operator giving a more frequently refreshed and more accurate measurement of the visual angular speed making this sensor a very good candidate for robotic applications as it constitutes a good trade-off between the need for reliable motion sensors and the limited power and avionic payload available on MAVs. Thanks to the two-directional measurements of the angular speed, we show in this study that we are also able to extract with no error the direction of motion simply by taking the maximum value of the angular speed between the measurements of the two opposite directions.

Two-Directional 1-g Visual Motion Sensor Inspired by the Fly's Eye³

Article published in 2011 in *IEEE Sensors Journal*, 13(3): 1025-1035.

Authors: Frédéric L. Roubieu, Fabien Expert, Guillaume Sabiron and Franck Ruffier.

2.3.1 Abstract

Optic flow based autopilots for Micro-Aerial Vehicles (MAVs) need lightweight, low-power sensors to be able to fly safely through unknown environments. The new tiny 6-pixel visual motion sensor presented here meets these demanding requirements in term of its mass, size and power consumption. This 1-gram, low-power, fly-inspired sensor accurately gauges the visual motion using only this 6-pixel array with two different panoramas and illuminance conditions. The new visual motion sensor's output results from a smart combination of the information collected by several 2-pixel Local Motion Sensors (LMSs), based on the "time of travel" scheme originally inspired by the common housefly's Elementary Motion Detector (EMD) neurons. The proposed sensory fusion method enables the new visual sensor to measure the visual angular speed and determine the main direction of the visual motion without any prior knowledge. By computing the median value of the output from several LMSs, we also ended up with a more robust, more accurate and more frequently refreshed measurement of the 1-D angular speed.

2.3.2 Introduction

Micro Aerial Vehicles (MAVs) constitute a class of Unmanned Aerial Vehicles (UAVs) which can be used for the remote observation of hazardous environments without any risk to human life. MAVs need to be equipped with onboard sensors and flight control devices in order to perform tasks such as those performed by optic flow (OF) based aerial robots: obstacle avoidance (Iida, 2001; Green et al., 2004; Zufferey & Floreano, 2006; Ruffier & Franceschini, 2008; Beyeler et al., 2009; Humbert et al., 2009; de Croon et al., 2012), terrain following and automatic landing (Ruffier & Franceschini, 2003; Green et al., 2004; Ruffier & Franceschini, 2005; Franceschini et al., 2007; Zufferey et al., 2010; Herisse et al., 2012), tracking a moving target (Kendoul et al., 2009; Kerhuel et al., 2010) and controlling their forward speed (Roubieu et al., 2012). MAVs endowed with these abilities would acquire greater autonomy, and at the same time, the ground operators' arduous task of piloting an almost constantly invisible aircraft would be greatly simplified.

Nature has taught us that flying insects, which came into existence several hundred million

³Roubieu, F.L., Expert, F., Sabiron, G. and Ruffier, F.(2012). Two-Directional 1-g Visual Motion Sensor Inspired by the Fly's Eye. *IEEE Sensors Journal*, 13(3): 1025-1035.

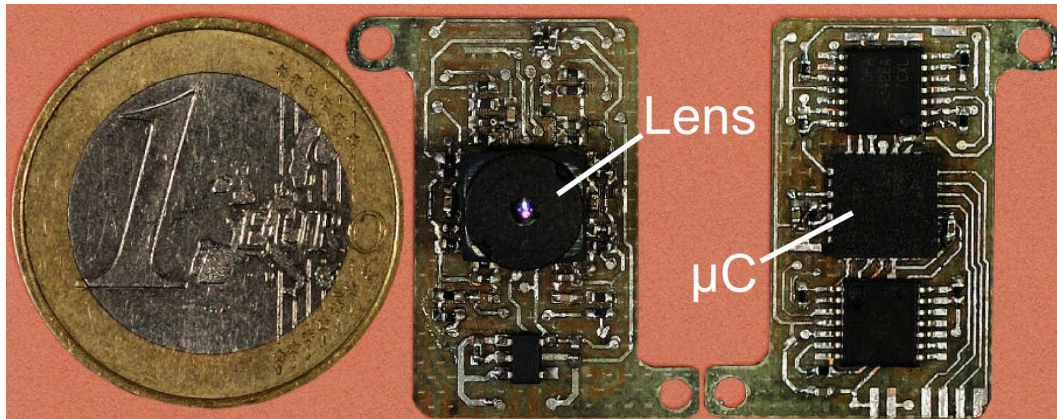


Figure 2.11: Top view of the 1-gram microcontroller-based visual motion sensor (size: $23.3 \times 12.3 \text{ mm}$) with its lens (focal length: 2 mm) mounted on the one-dimensional 6-photosensor array, and bottom view of the PCB (thickness: 0.4 mm) with its tiny low-power 16-bit μC (dsPIC from Microchip Company).

years ago, have developed particularly elegant solutions to the problem of navigating swiftly in unfamiliar and complex environments. Winged insects are able to enter and explore unknown environments without any sonar or laser range-finder: their visually guided performances depend mainly on OF sensing processes (Collett, 1980; Wagner, 1982; Srinivasan et al., 1996; Tammero & Dickinson, 2002; Baird et al., 2006; Franceschini et al., 2007; Serres et al., 2008; Baird et al., 2010; Straw et al., 2010; Portelli et al., 2011; Srinivasan, 2011). The OF perceived by a moving agent (an animal, human or robot) is a vector field that gives the angular speed ω (magnitude in $^\circ/s$) at which any contrasting object in the environment is moving past the eyes (Gibson, 1950). The fly's eye has been shown to be sensitive to two-directional motion (Hausen, 1984) and also to be driven by a minimum of two photoreceptors inside the same ommatidium (Franceschini, 1985; Franceschini et al., 1989). The fly's eye is therefore one of the most suitable animal models available for studies on motion detecting neurons. Based on studies of the fly's visual system previously conducted at our Laboratory, in which electrophysiological recordings were performed on single neurons while microstimuli were being applied to single photoreceptor cells in a single ommatidium of the compound eye (Franceschini, 1985), a 2-pixel Local Motion Sensor (LMS) was developed (Blanes, 1986), based on the principle known today as the "time of travel" scheme (Pichon et al., 1989).

Using such bioinspired sensors, various simulated vision-based autopilots (Pichon et al., 1989; Martin & Franceschini, 1994; Serres et al., 2008; Portelli et al., 2010) based on OF sensing techniques were subsequently developed at our Laboratory, and a series of terrestrial (Pichon et al., 1989; Franceschini et al., 1992) and aerial robots (Netter & Franceschini, 2002; Ruffier & Franceschini, 2005; Kerhuel et al., 2010; Expert & Ruffier, 2012) were constructed. The "robotfly" ("Robot Mouche" in French) built by Franceschini's team in 1991 was a completely autonomous wheeled robot equipped with a compound eye consisting of 114 electronic LMSs implemented in analog technology using Surface Mounted Devices (SMDs) (Franceschini et al., 1992). The "robotfly" was able to steer its way through an unknown field full of obstacles at a relatively high speed (up to 50 cm/s) (Franceschini et al., 1992). The "robotfly" also implemented two-directional analog LMSs using a maximum operator to determine the direction of motion (Blanes, 1991; Franceschini et al., 1992). However, the size and mass of these analog sensors were not compatible with the drastic constraints imposed on free flying MAVs in terms of their mass (they have to weigh less than 100 g), size (they must measure

less than 15 cm) and power consumption.

Several teams therefore started to design new visual motion sensors by mixing analog and digital processing, which are lighter and easier to implement onboard MAVs than a camera-based system (Plett et al., 2012) or fully analog sensors. One possible approach consisted of developing visual motion sensors using analog and digital Very-Large-Scale Integration (VLSI) technologies, such as those based on the Reichardt correlator (Harrison & Koch, 1999; Liu & Usseglio-Viretta, 2001; Brinkworth et al., 2009; Xu et al., 2011), the Pulse-based velocity sensor (Kramer et al., 1997) or Barrows' design (Barrows & Neely, 2000). Only a few VLSI-based sensors have been implemented onboard MAVs so far (flight with limited degrees of freedom: (Duhamel et al., 2012), free-flight: (Barrows & Neely, 2000; Green et al., 2004)).

Off-the-shelf mouse sensors were also recently characterized (Chan et al., 2010) and mounted onboard terrestrial (Jackson et al., 2007; Dahmen et al., 2009) and aerial robotic platforms (Griffiths et al., 2006; Beyeler et al., 2009). The performances of these systems have not been properly assessed so far in terms of their resolution, accuracy, invariance to illuminance and contrast, apart from two studies (Beyeler et al., 2009; Expert et al., 2011a).

At our Laboratory, several versions of 2-pixel motion sensors based on the "time of travel" scheme originally based on the fly's eye (Franceschini et al., 1989) were developed using either a Field Programmable Gate Array (FPGA) (Aubépart et al., 2007) or a microcontroller (μC) (Ruffier et al., 2003; Pudas et al., 2007; Viollet et al., 2010; Expert et al., 2011b; Roubieu et al., 2011; Ruffier & Expert, 2012; Expert & Ruffier, 2012).

In the current study, we present a new tiny μC -based visual motion sensor weighing only 1 gram (Fig. 2.11), which receives visual inputs from a 6-pixel array integrated circuit. By combining several 2-pixel motion sensors, the performances of the visual motion sensor were highly improved. The first sensory fusion method of this sensor produces a combined output based on the median value of 5 LMS measurements in a single pre-determined direction of motion which drastically improved the accuracy and the refresh rate ($f_{refresh}$) of the angular speed measurements (Roubieu et al., 2011). An improved sensory fusion method determines an accurate estimation of the direction and the magnitude of the angular speed in the detected direction of motion. This whole processing was embedded into a μC which has sufficient computational resources for carrying out the requisite signal processing tasks efficiently, while its mass is compatible with the very low avionic payload allowed on MAVs. The first sensory fusion method implemented in our tiny μC -based visual motion sensor is presented in the section 2.3.3 that gives a short description of the bio-inspired visual system and the principles underlying the 2-pixel "time of travel" scheme. Experiments performed on the visual motion sensor, which was tested indoors, are described in Section 2.3.4. The results of these experiments are presented in Section 2.3.5. Section 2.3.6 describes the results obtained thanks to an improved sensory fusion method able to perfectly determine the direction of motion without any prior knowledge and to give an accurate and robust assessment of the magnitude of the motion in term of angular speed.

2.3.3 Description of the device

2.3.3.1 Photoreceptor configuration

The front end of the visual motion sensor designed and developed in this study was based on an off-the-shelf photosensor array (iC-LSC from iCHaus Company, <http://www.ichaus.de>)

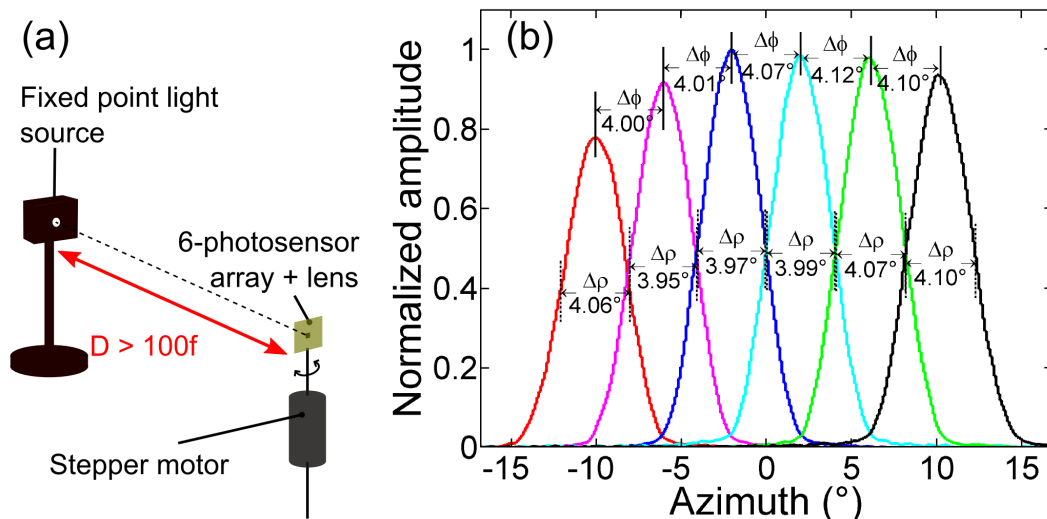


Figure 2.12: (a) Scheme of the test bench used to determine the Gaussian ASFs of the 6-photosensor array obtained by slowly rotating the visual motion sensor mounted on the motor shaft of a stepper motor and placed at a distance $D = 50 \text{ cm}$ in front of a fixed point light source. (b) Raw Gaussian ASFs of the photosensor array.

consisting of 2 rows of 6 photodiodes. A fixed-gain current amplifier is integrated into each photodiode. In order to detect a large number of contrasting objects at low illuminance levels, the photosensors in each column were paired to increase the signal to noise ratio by increasing the sensitive surface two-fold from $300 \mu\text{m} \times 800 \mu\text{m}$ to $300 \mu\text{m} \times 1600 \mu\text{m}$. This one-dimensional 6-pixel array was then mounted on a cheap, lightweight lens (Sparkfun SEN-00637) borrowed from a mobile telephone camera (Fig. 2.11).

As in flies, each photosensor features a Gaussian Angular Sensitivity Function (ASF), (Götz, 1964) [Fig. 2.12(b)], which results in insects from the spatial convolution of the photoreceptor's diameter with the point spread function of the facet lenslet (Franceschini & Kirschfeld, 1971; Stavenga, 2003) and in our sensor, from the defocusing of the lenslet.

The ASF of the “lens-photoreceptor” system was assessed by slowly rotating the visual motion sensor placed 50 cm in front of a point light source [Fig. 2.12(a)]. By defocusing the lens (i.e., by reducing the distance between the lens and the array), we obtained a similar Gaussian sensitivity profile to that of the housefly. The full width at half height of the Gaussian curve (the acceptance angle) $\Delta\rho$ determines the cut-off frequency of the low-pass spatial filtering process (Fig. 2.13), whereas the inter-receptor angle $\Delta\varphi$ (i.e., the angle between two adjacent optical axes) determines the angular speed (ω_i^m) measurement range.

The defocusing process was adjusted to obtain an appropriate bell-shaped ASF projected onto the photosensor array, as occurs in some diurnal insects (Land, 1997), where:

$$\Delta\varphi = \Delta\rho \quad (2.9)$$

The visual photoreceptor axes are separated by an inter-receptor angle $\Delta\varphi = 4^{\circ}$ and each pixel features an acceptance angle $\Delta\rho = 4^{\circ}$ [Fig. 2.12(b)]. The horizontal Field Of View (FOV) of the visual motion sensor is 28.8° .

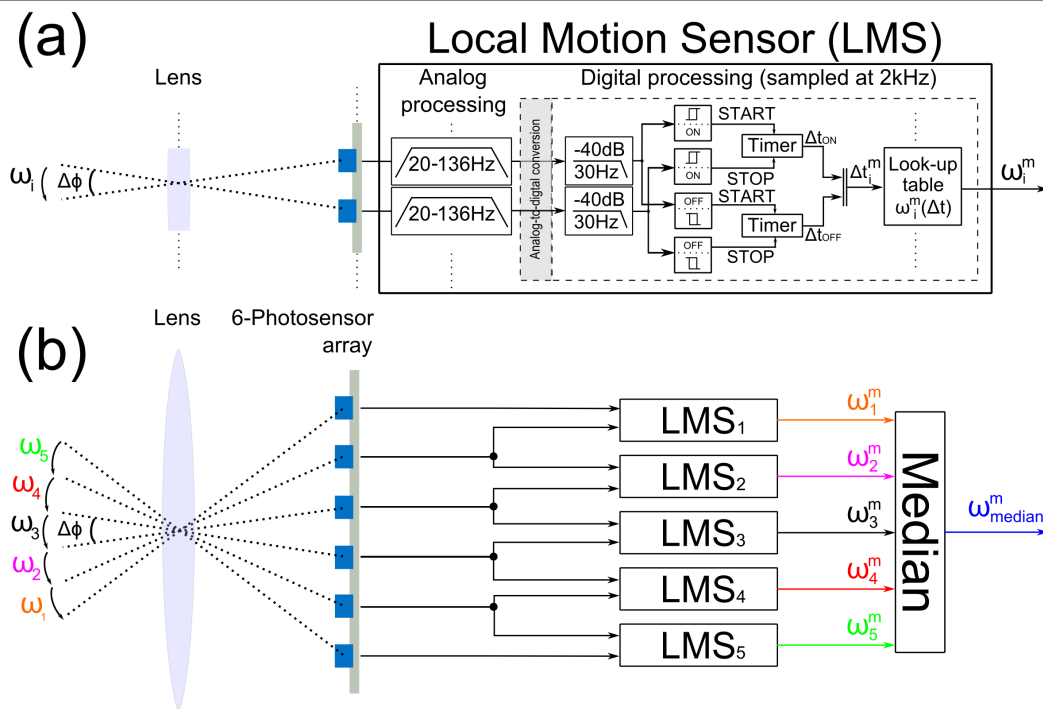


Figure 2.13: General processing architecture of the visual motion sensor, including its 5 LMSs. (a) Processing architecture of one LMS. The visual signals delivered by neighboring photoreceptors are filtered both spatially and temporally by an analog bandpass filter with cut-off frequencies [20 Hz, 136 Hz] and a second order fixed-point digital low-pass filter with a cut-off frequency of 30 Hz. The filtered photoreceptor signals are then thresholded to determine the angular speed ω_i^m , using the “time of travel” scheme previously developed at our Laboratory (Blanes, 1986; Pichon et al., 1989; Pichon, 1991; Franceschini et al., 2009). The “time of travel” Δt_i , which is proportional to the inverse of ω_i^m , elapsing between two filtered photoreceptor signals is measured by a timer: Δt_{ON} and Δt_{OFF} are measured by means of ON and OFF contrast distinguishing processes (Franceschini et al., 1989). These delays Δt_i are used to generate the 1-D angular speed ω_i^m in the visual field of the 1-D LMS. (b) The 5 LMS output signals are combined to generate a more robust and frequently refreshed 1-D median measured angular speed ω_{median}^m . The overall processing was carried out on a tiny low-power 16-bit μC at a sampling rate of 2 kHz.

2.3.3.2 Local Motion Sensor (LMS)

Each LMS assesses the angular speed ω_i [i.e., a 1-D component of the OF, Fig. 2.13(a)] of any dark-to-light (ON) or light-to-dark (OFF) contrast in the same way as the fly’s motion-detecting neurons. This “perceived” angular speed ω_i is transformed by the optical system into a delay Δt_i between 2 neighboring photosensor signals defined as follows:

$$\Delta t_i = \frac{\Delta \varphi}{\omega_i} \quad (2.10)$$

The functional “time of travel” scheme used here consists of 6 processing steps (Blanes, 1986; Ruffier et al., 2003; Franceschini et al., 2009) measuring the delay Δt_i , thus giving the angular speed ω_i^m (Fig. 2.13):

- Step 1: Low-pass spatial filtering is achieved by defocusing the lens, thus giving each pixel a Gaussian ASF.
- Step 2: Analog bandpass filtering: high-pass filtering ($f_c = 20$ Hz) enhances the contrast information and eliminates the DC component of the photoreceptor signals.

This step is followed by a first-order low-pass filtering step, where $f_c = 136 \text{ Hz}$.

- Step 3: Digitizing and filtering: second-order fixed-point digital low-pass filtering ($f_c = 30 \text{ Hz}$) reduces any high frequency noise introduced by the artificial indoor lighting (100 Hz).
- Step 4: Hysteresis thresholding is performed to distinguish between “ON” and “OFF” contrast transitions (i.e. dark-to-light and light-to-dark transitions, respectively) in each channel.
- Step 5: A time delay circuit is triggered by one channel and stopped by the neighboring channel. This circuit measures the time Δt_i elapsing between similar (“ON” or “OFF”) transitions occurring in two adjacent photoreceptors.
- Step 6: Computing the 1-D angular speed of a contrast in the visual field of the LMS, using a look-up table which converts the delay Δt_i into the measured angular speed ω_i^m .

2.3.3.3 Implementation and optimization

Our visual motion sensor generates 5 simultaneous local measurements ω_i^m of the 1-D angular speed of a moving natural panorama in a measurement range of more than one decade, ranging from $25 \text{ }^\circ/\text{s}$ to $350 \text{ }^\circ/\text{s}$. The sensor output is the median value ω_{median}^m of the 5 LMSs. The whole processing of the 5 LMSs and the computation of the median value were carried out on a dsPIC33FJ128GP802 μC working at a sampling frequency of 2 kHz and running at 40 MIPS. This low-power 16-bit μC was a very good candidate in term of size footprint (28 pins QFN-S package, see Table 2.2 for dimension), power consumption and performances allowing it to carry out the whole processing using a 16-bit MAC unit (“Multiplier + ACcumulation”), 1 SPI and $6 \times 12\text{-bit}$ ADCs (Analog to Digital Converters) while meeting with the constraints of MAVs [see Fig. 2.13(a)].

The μC embedded onboard the visual motion sensor (Fig. 2.11) is connected to an external Bluetooth module via a test-board. This radio link allows the operator to record all the data synchronously and to convey it to a computer for analysis. The program of the 16-bit μC was developed on Matlab/Simulink© environment and compiled using a specific toolbox (available on <http://www.kerhuel.eu>) developed for dsPIC μCs .

In order to be able to perform all the processing with the limited computational power of a tiny μC , several optimizations in the sensory fusion method were required to reduce the computational load. The order of the digital low-pass filter embedded in the μC was reduced two-fold from the 4th (Ruffier et al., 2003) to 2nd order. This reduction was possible thanks to the on-chip pre-amplification unit of the LSC retina, which reduces the noise. One simple 16-bit free counter was used to measure the 10 delays Δt (Δt_{ON} and Δt_{OFF} of the 5 LMSs) required to estimate visual motion in the FOV of the 5 LMSs.

2.3.3.4 Characteristics of the visual motion sensor

The mass balance of our tiny device, including all the electronics, does not exceed 1 gram, which amounts to only 0.2 g per LMS (Table 2.2). It is also a low-power visual motion sensor with a consumption of only 74 mA . The specifications of the visual motion sensor are summarized in Table 2.3.

<i>Parts</i>	<i>Mass (g)</i>
PCB thickness 0.4 mm, 3 cm ²	0.402
Lenslet Sparkfun SEN-00637	0.17
Lenslet-mount	0.11
LSC iC-Haus retina	0.13
μC dsPIC 6 × 6	0.1
Electronic components	0.162
Estimated total mass	1.074
Real mass = 0.98 g	
Mass per 1-D LMS < 0.2 g	

Table 2.2: Mass balance of the visual motion sensor

Retina	LSC iC-Haus
Inter-receptor angle $\Delta\varphi$ (°)	4
Acceptance angle $\Delta\rho$ (°)	4
Photodiode size (<i>m</i>)	300 × 1600
Pixel pitch (<i>m</i>)	420
Focal length of the lens (<i>mm</i>)	2
F_{number} of the lens	2.8
Angular velocity range (°/s)	[25; 350]
Resolution (°/s) [Min; Max]	[7 × 10 ⁻² ; 14.5]
Sensitivity (°/s/LSB)	7.63 × 10 ⁻⁴
Measured mass with optics (g)	0.98 g

Table 2.3: Specifications of the visual motion sensor

We recently showed that using the same fusion algorithm, the measurement range of a similar sensor can be tuned to lower angular speeds by adjusting the optical parameters as shown in (Sabiron et al., 2013).

2.3.4 Experiment

The visual motion sensor was tested indoors in natural light at a constant illuminance of approximately 1500*lux*, corresponding to the sunny daylight coming from a window.

The visual motion sensor was placed at an orthogonal distance D_h from a printed belt of wallpaper showing a natural colored panorama. The printed band was stretched between 2 drums actuated thanks to a motor and a V-belt (see enclosed frame Fig. 2.14). The visual motion sensor was oriented at an arbitrary angle α between the direction of the wall motion (\vec{V}_{wall}) and the main sensor axis (Fig. 2.14). The panorama was therefore made to move horizontally with respect to the visual motion sensor at an ground-truth optic flow ω_{wall} , as given by (2.11):

$$\omega_{wall} = \frac{V_{wall}}{D_h} \times \sin^2 \alpha \quad (2.11)$$

By imposing an arbitrary orientation angle α to the visual motion sensor, we wanted to

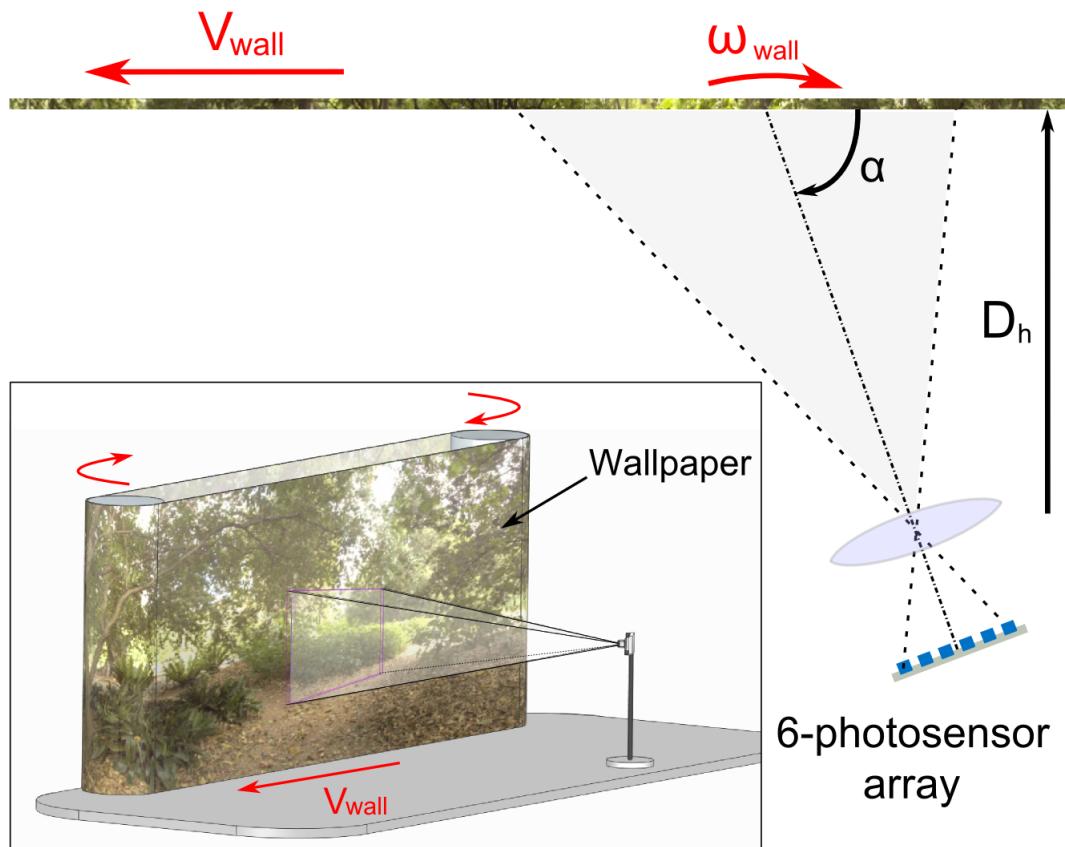


Figure 2.14: Test bed used to assess the performances of the first sensory fusion method of the visual motion device based on a 6-pixel 1-D array. The visual motion sensor was placed at an orthogonal distance D_h from a piece of wallpaper (forming a printed belt), at an arbitrary angle α between the direction of the wall motion (\vec{V}_{wall}) and the main sensor axis. The printed belt depicting a natural colored panorama (inset) was stretched between two drums actuated thanks to a motor and a V-belt. The printed belt was made to move horizontally in a pre-determined preferred direction in front of the visual motion sensor at an angular speed ω_{wall} .

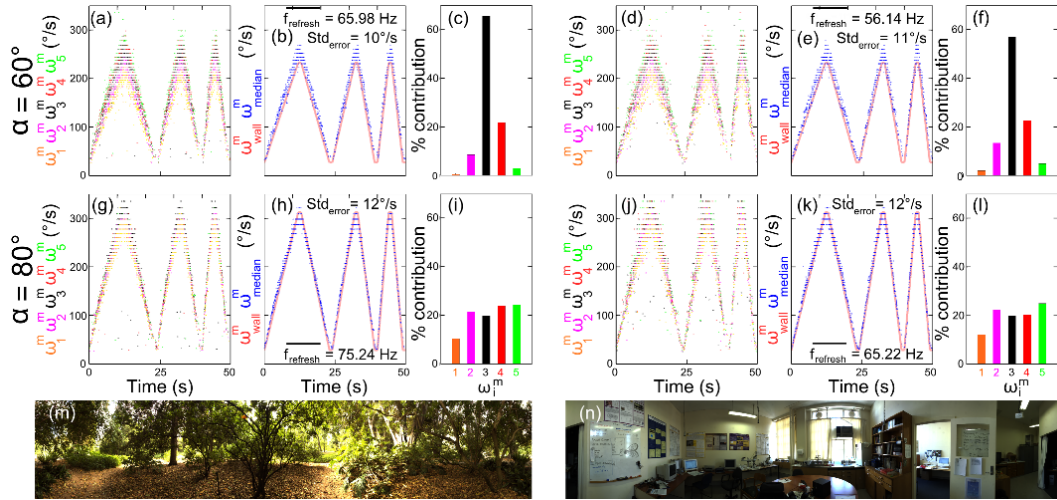


Figure 2.15: Dynamic indoor responses of the visual motion sensor. The visual motion sensor was placed at an orthogonal distance $D_h = 24 \text{ cm}$ from a moving printed belt lined with a colored natural panorama depicting either bushes and trees or a laboratory. The visual motion sensor was placed at 2 different orientation angles $\alpha = 60^\circ$ and $\alpha = 80^\circ$ between the direction of the wall motion (\vec{V}_{wall}) and the main sensor axis to check that each LMS measures visual motion in its own visual field [see (2.12)]. The printed belt was moved using a triangular law giving a triangular pattern of angular speed variations involving a series of velocity ramps with different slopes ranging from $27^\circ/s$ to $230^\circ/s$ ($\alpha = 60^\circ$) and from $28^\circ/s$ to $312^\circ/s$ ($\alpha = 80^\circ$) [see (2.11)]. (a), (d), (g) and (j) Dynamic indoor responses of each LMS in the visual motion sensor placed at an orientation angle $\alpha = 60^\circ$ [(a) and (d)] and $\alpha = 80^\circ$ [(g) and (j)]. Note that each LMS output differed from the others because of the different orientations of the LMS visual axes in the sensor's FOV as expected according to (2.12). (b), (e), (h), and (k) Dynamic indoor responses in terms of median values in comparison with those predicted by the main contributor, along with the standard deviation error (Std_{error}) and refresh rate ($f_{refresh}$) characteristics. (c), (f), (i), and (l) Vertical bar graph showing which LMS in the visual motion sensor was the main contributor to the median value computed. (m) and (n) The natural colored panorama depicted on the printed belt (Fig. 2.14) used to assess the visual motion sensor's performances.

check if the measurements obtained with each i^{th} LMS were in line with (2.12):

$$\omega_i^m = \frac{V_{wall}}{D_h} \times \sin^2(\alpha + (i - 3) \times \Delta\varphi) \quad (2.12)$$

The dynamic indoor responses were assessed by the visual motion sensor at $\alpha = 60^\circ$ and $\alpha = 80^\circ$ with 2 different printed belts:

- The first belt was decorated with a natural colored panorama [Fig. 2.15(m)],
- The second one was lined with a colored indoor panorama featuring a laboratory [Fig. 2.15(n)].

The wallpaper was moved using a triangular speed law involving a series of velocity ramps with various slopes ranging from $27^\circ/s$ to $230^\circ/s$ with $\alpha = 60^\circ$ and from $28^\circ/s$ to $312^\circ/s$ with $\alpha = 80^\circ$.

2.3.5 Results

The dynamic indoor responses of the visual motion sensor and the median output of the 5 LMSs were studied in terms of the refresh rate ($f_{refresh}$) and the standard deviation error (Std_{error}) computed as follows:

$$Std_{error} = std(\omega_i^m - \omega_{wall}) \quad (2.13)$$

The Std_{error} therefore corresponds to the dispersion of the data between the measured angular speed ω_i^m and the ground-truth value ω_{wall} . The main contributor is that of the 5 angular speed measurements ω_i^m which is most frequently used to calculate the median angular speed ω_{median}^m . The refresh rate ($f_{refresh}$) was defined as the number of new motion measurements per second. A new motion measurement occurs when a contrast transition is detected by one pixel and then by the second pixel with any delay Δt in the angular speed measurement range [i.e. in the $25^\circ/s$ to $350^\circ/s$ range, see (2.10)].

As was to be expected in view of (2.12), the 5 LMS output measurements are different [Fig. 2.15(a), (d), (g) and (j)] because of the different orientations of the visual axes of the LMSs in the sensor's FOV. Figs. 2.15(c), (f), (i) and (l) show that the main contributors to the median value at the orientation angles $\alpha = 60^\circ$ and $\alpha = 80^\circ$ were the 3rd LMS and the 5th LMS, respectively. For both panoramas, the median value accurately followed the angular speed of the wall ω_{wall} , giving a Std_{error} smaller than $12^\circ/s$ in comparison with the value obtained with the main contributor, which was between $19^\circ/s$ and $24^\circ/s$. In addition, the refresh rate of the median value was found to increase more than 4-fold (67 Hz) in comparison with that observed in the case of the LMS main contributor (15.7 Hz) [Figs. 2.15(b), (e), (h) and (k)].

2.3.6 Estimation of the direction and the magnitude of the visual motion

2.3.6.1 Device description

The improved sensory fusion method of the new visual motion sensor presented in this section is based on the front end described in section 2.3.3.1, having the optical characteristics described in Table 2.3 in terms of the inter-receptor angle $\Delta\varphi$ and the acceptance angle $\Delta\rho$. This visual motion sensor is able to estimate the direction and the magnitude of the visual motion ω_{median}^{max} on the basis of 10 angular speed measurements: 5 LMSs are used to compute the median angular speed $\omega_{median+/-}^m$ in each direction of motion (“+” or “-”)

(Fig. 2.16). In order to determine the direction of the visual motion without any prior knowledge, empirical findings (Blanes, 1991) have shown that, within a given angular speed range, the angular speed of the contrasts detected in the correct motion direction is usually greater than that measured in the opposite direction. Based on this finding, by simply choosing the maximum value of the median angular speeds in the two directions $\omega_{median+}^m$ and $\omega_{median-}^m$, it is possible to determine the direction of the visual motion accurately in the $[-350^\circ/s; -80^\circ/s] \cup [80^\circ/s; 350^\circ/s]$ range. The $]-80^\circ/s; 80^\circ/s[$ range corresponds to an uncertainty range, where the direction and the magnitude of the angular speed cannot be assessed accurately. As soon as the sensor detects visual motion in the $]-80^\circ/s; 80^\circ/s[$ range, the output signal ω_{median}^{max} magnitude and direction are voluntarily set to “no value” without any error.

2.3.6.2 Optimization of the motion direction estimates

To optimize the motion direction estimation, we decided to filter each median angular speed measurement ($\omega_{median+}^m$ and $\omega_{median-}^m$) using a rate-limiter that removes any value that is too different from the previous angular speed measurement knowing the OF rate is bounded. A sliding window filters out any motion direction error by selecting the direction occurring more than 8 times among the last 16 detected motion directions. Thanks to this filtering process, the motion direction was perfectly determined (Fig. 2.16).

The improved sensory fusion method was optimized in order to increase the number of LMSs embedded into the same μC two-fold. The same filtered visual signals were recombined in order to compute an accurate visual angular speed and the direction of the visual motion while keeping the digital processing frequency at 2 kHz . The median computation step was optimized by computing the median value only whenever a new visual motion measurement occurred, i.e., whenever a new i^{th} LMS angular speed $\omega_{i+/-}^m$ was measured: this algorithm optimization prevents the μC from being overloaded by computing the median value at all the time steps at which none of the LMS outputs are refreshed.

All these improvements have made the tiny μC capable of carrying out all the processing operations required to determine the median 1-D angular speed of a natural panorama ω_{median}^{max} and to estimate the direction of motion with a mean computational load of only 53% (minimum: 43%; maximum: 82% -very short peaks-) at a sample frequency of 2 kHz .

2.3.6.3 Experiment

The static and dynamic responses of the improved sensory fusion method of the visual motion sensor presented here were obtained under 2 lighting conditions. The background irradiance values were measured in $W.cm^{-2}$ using a digital radiometer (ILT1700) which gives the irradiance in the direction of the radiometer's sensor. The visual motion sensor was placed at an orthogonal distance $D_h = 24\text{ cm}$ from a printed belt, oriented at an angle $\alpha = 90^\circ$. The printed belt was stretched between 2 drums actuated by a motor and a V-belt which could be made to rotate either clockwise or anticlockwise (see inset in Fig. 2.17). The panorama was therefore made to move horizontally in two directions with respect to the visual motion sensor at an angular speed ω_{wall} according to (2.11). The static responses of the visual motion sensor were assessed by applying a series of $30^\circ/s$ fifteen-second steps to the moving wall at a rotational speed ω_{wall} in the $[-315^\circ/s; -105^\circ/s] \cup [105^\circ/s; 315^\circ/s]$ range in the two opposite directions. These experiments were conducted with an irradiance of $5 \times 10^{-3}\text{ W.cm}^{-2}$.

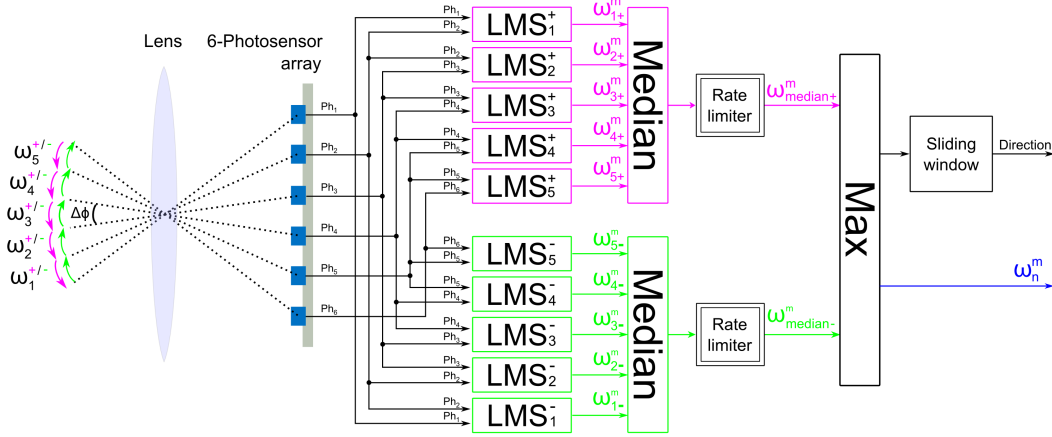


Figure 2.16: General processing architecture of the improved sensory fusion method based on 10 LMSs. The visual signals delivered by the photoreceptors are filtered and thresholded by the LMSs to determine the angular speeds $\omega_{i+/-}^m$ using the “time of travel” scheme in the two directions of motion (Blanes, 1986; Pichon et al., 1989; Blanes, 1991; Franceschini et al., 2009). The visual motion is measured in the opposite direction by reversing the inputs to each LMS. A rate limiter function filters out any median angular speed measurement that changes too fast. The motion direction and magnitude ω_{median}^{max} are estimated based on a simple algorithm, using the maximum median value of the angular speed $\omega_{median+}^m$ and $\omega_{median-}^m$ computed from the 5 LMSs in the 2 directions of motion. A sliding window removes any motion direction error by selecting the direction occurring more than 8 times among the last 16 detected motion directions. This improved sensory fusion method allows to measure the motion magnitude efficiently in the $[-350^\circ/s; -80^\circ/s] \cup [80^\circ/s; 350^\circ/s]$ range and to determine the direction of motion without any prior knowledge.

The dynamic characteristics of the visual motion sensor were assessed at two different illuminance values: at $2.5 \times 10^{-2} W.cm^{-2}$, which corresponds to strong sunlight coming from a windows and $5 \times 10^{-3} W.cm^{-2}$, which corresponds to strong indoor lighting. We applied a 60-second stimulus to the moving wall, involving a series of velocity ramps with different slopes in the $[-300^\circ/s; 300^\circ/s]$ range. The belt was covered with a natural colored panorama showing bushes and trees [Fig. 2.18(g)] or with a colored indoor panorama featuring a laboratory [Fig. 2.18(h)].

2.3.6.4 Results

To assess the static characteristics of the visual motion sensor, we studied the mean standard deviation of the data, which was computed as follows:

$$\overline{Std} = \overline{std(\omega_{median}^{max})} \quad (2.14)$$

The best linear approximation was computed to determine the accuracy of our visual motion sensor. This criterion was calculated on the basis of (2.15):

$$\omega_{median}^{max} = a \times \omega_{wall} \quad (2.15)$$

where ω_{median}^{max} is the output signal of the visual motion sensor and ω_{wall} is the angular speed of the moving wall as seen by the visual motion sensor. The regression coefficient a of (2.15) was used to compute the linearity error given by (2.16):

$$Linearity\ Error(\%) = |(a - 1)| \times 100 \quad (2.16)$$

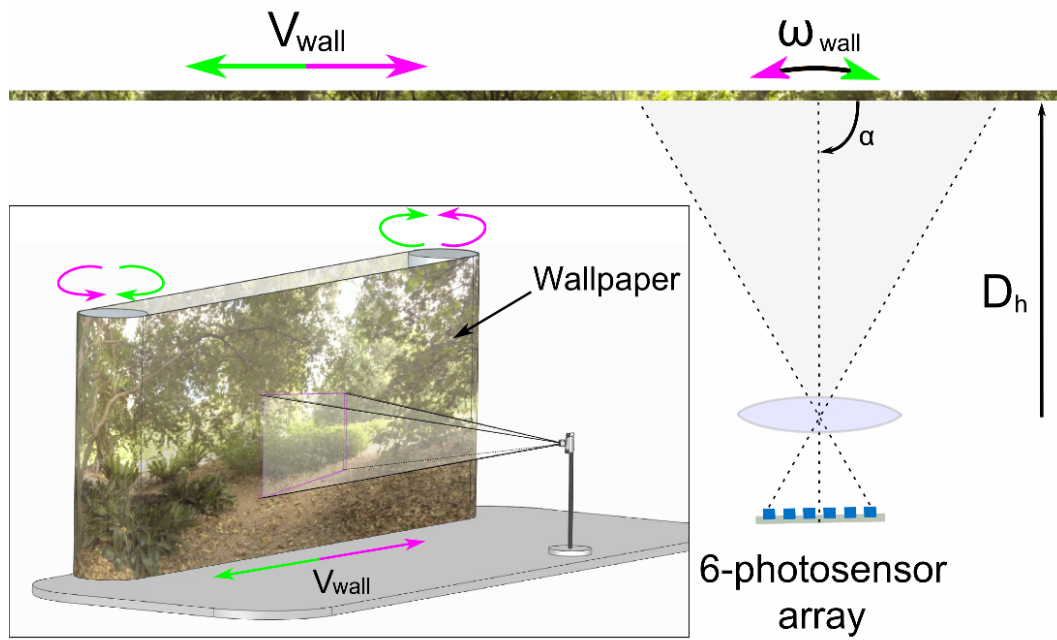


Figure 2.17: Test bed used to assess the performances of the visual motion device including the 10 LMSs and the motion direction detection unit. The visual motion sensor was placed at an orthogonal distance $D_h = 24 \text{ cm}$ from a printed belt. In this case, the angle α between the direction of the wall motion (\vec{V}_{wall}) and the main sensor axis was $\alpha = 90^\circ$. The belt printed with a natural colored panorama depicting either bushes and trees or a laboratory, was stretched between two drums actuated by a motor and a V-belt: the belt could be made in this case to rotate either clockwise or anticlockwise. The panorama was therefore made to move horizontally in either direction.

The dynamic responses of the median output ω_{median}^{max} of the tiny visual motion sensor were assessed in comparison with the perceived angular speed ω_{wall} in terms of the refresh rate and the Std_{error} defined in (2.13).

Static characteristics

Figs. 2.18(a) and (b) show the static characteristics of the visual motion sensor tested indoors in front of a moving wall at an irradiance value of $5 \times 10^{-3} \text{ W.cm}^{-2}$. As shown in Figs. 2.18(a) and (b), the visual motion sensor responded accurately with a really low *LinearityError* rate [see (2.16)] of less than 1% and an excellent dispersion of less than $7^\circ/s$. In the measurement range of $[-350^\circ/s; -80^\circ/s] \cup [80^\circ/s; 350^\circ/s]$, the visual motion sensor estimated the direction of motion perfectly without making a single direction error.

Dynamic characteristics

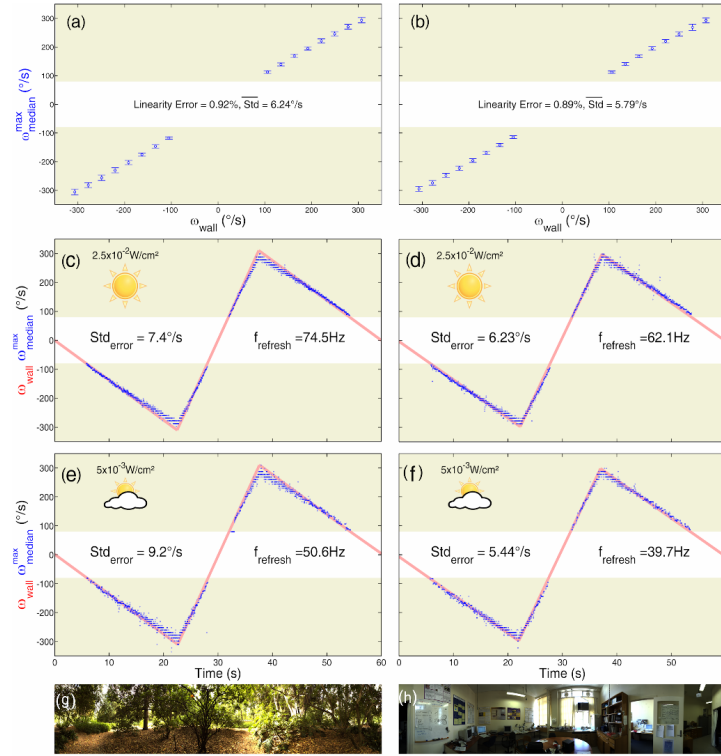


Figure 2.18: Dynamic and static indoor responses of the visual motion sensor placed at an orthogonal distance $D_h = 24 \text{ cm}$ from the moving wall at an angle $\alpha = 90^\circ$. The static indoor characteristics of the visual motion sensor were assessed by applying $30^\circ/s$ steps (lasting 15s) to the printed belt in the $[-315^\circ/s; -105^\circ/s] \cup [105^\circ/s; 315^\circ/s]$ range. The mean visual motion recorded at each angular speed ω_{wall} is plotted in the figure with its standard deviation. The best linear approximation obtained in each experiment was computed, and the departure from linearity is given as a percentage. The dynamic responses of the visual motion sensor were assessed at two different irradiance values of $5 \times 10^{-3} \text{ W.cm}^{-2}$ and $2.5 \times 10^{-2} \text{ W.cm}^{-2}$ with the two printed panoramas. The printed belt was moved using a triangular law giving a triangular pattern of angular speed variation involving a series of velocity ramps ranging from $-300^\circ/s$ to $300^\circ/s$. A fusion algorithm based on the maximum median value of the two opposite directions was used to determine the magnitude ω_{median}^{max} and the direction of the angular speed. (a) and (b) Static indoor characteristics of the visual motion sensor. With both panoramas, the visual motion sensor yielded accurate median angular speed measurements with only a small *LinearityError* of less than 1% and an excellent *Std* of less than $7^\circ/s$. (c)-(f) Dynamic indoor responses of the median angular speed ω_{median}^{max} of the visual motion sensor, along with the standard deviation error (*Std_{error}*) and refresh-rate (*f_{refresh}*) data. With the printed belt depicting bushes and trees [Fig. 2.18(c) and (e)], the results showed a small dispersion of less than $10^\circ/s$ and the refresh rate increased from 50.6 Hz to 74.5 Hz with the irradiance. With the printed belt depicting a laboratory, the results show that the dispersion was less than $7^\circ/s$, and the refresh rate again increased with the irradiance from 39.7 Hz to 62.1 Hz . (g) and (h) The natural colored panorama depicted on the printed belt (Fig. 2.17) used to assess the visual motion sensor's performances.

Figs. 2.18(c) and (d) show the dynamic responses of the visual motion sensor at an irradiance of $2.5 \times 10^{-2} \text{ W.cm}^{-2}$. The median value closely obeyed the triangular law imposed on the angular speed of the wall ω_{wall} , giving a low Std_{error} of only $7.4 \text{ }^\circ/s$ and $6.23 \text{ }^\circ/s$ with the outdoor and indoor panoramas, respectively. At a lower irradiance of $5 \times 10^{-3} \text{ W.cm}^{-2}$, the median value ω_{median}^{max} again closely obeyed the triangular law imposed on the angular speed of the moving wall ω_{wall} , with a Std_{error} of $9.2 \text{ }^\circ/s$ in the case of the bushes and trees panorama and $5.44 \text{ }^\circ/s$ in that of the laboratory panorama. Despite the difference in the irradiance, the Std_{error} was always of a similar order of magnitude. In any case, the visual motion sensor gave a highly refreshed output. As was to be expected from (Expert et al., 2011b), the $f_{refresh}$ increased with the irradiance, amounting to 50.6 Hz at an irradiance of $5 \times 10^{-3} \text{ W.cm}^{-2}$ and 74.5 Hz at a higher value of $2.5 \times 10^{-2} \text{ W.cm}^{-2}$ when the outdoor panorama was displayed on the printed belt [Fig. 2.18(c) and (e)]. Similar results were obtained with the indoor panorama: $f_{refresh}$ of 39.7 Hz at $5 \times 10^{-3} \text{ W.cm}^{-2}$ and 62.1 Hz at $2.5 \times 10^{-2} \text{ W.cm}^{-2}$ [Fig. 2.18(d) and (f)]. The motion direction was estimated perfectly by the sensor without making a single error.

In view of these performances, this novel tiny visual motion sensor can be said to provide a remarkably promising tool for performing robotic tasks such as obstacle avoidance and terrain following in forward flight, while meeting the requirements in very low avionic payload, since the total mass balance of the two-directional visual motion sensor does not exceed 1 g .

2.3.7 Conclusion

In this study, two different sensory fusion methods of a 1-gram insect-inspired visual motion sensor were evaluated indoors under two different lighting conditions. The dynamic and static responses of this novel fly-inspired visual motion sensor were used to assess the performances of these very lightweight, low-power sensors, which can be mounted onboard tomorrow's MAVs for obstacle avoidance and speed control purposes.

The first sensory fusion method of our 1-gram μC -based visual motion sensor, consisting of a 5-LMS array, gave 5 simultaneous angular speed measurements and a single combined output in the $[25 \text{ }^\circ/s; 350 \text{ }^\circ/s]$ range, in a single preferred direction of visual motion. The results obtained in the study (Fig. 2.15) show how the accuracy and the robustness of the angular speed measurement have been improved thanks to our simple method of data combination based on the median operator. This method improves the Std_{error} more than 1.7-fold from $19 \text{ }^\circ/s$ in the case of the main contributor to the median value to $11 \text{ }^\circ/s$ in the case of the median angular speed ω_{median}^m . The refresh rate of the visual motion sensor was found to have increased at least 4-fold (67 Hz) in comparison with that of the main contributor (15.7 Hz).

The excellent performances obtained with the first sensory fusion method of this 1-gram fly-inspired visual motion sensor led us to design an improved sensory fusion method incorporated into our visual sensor based on the same electronics. These improvements allowed to determine the direction and magnitude ω_{median}^{max} of visual motion without any prior knowledge by recombining the filtered visual signals and processing the "time of travel" in the two opposite directions. This improved sensory fusion method of the 1-gram μC -based visual motion sensor designed and built at our Laboratory is based on a 10 LMS-array which can measure the direction and the magnitude of motion in the $[-350 \text{ }^\circ/s; -80 \text{ }^\circ/s] \cup [80 \text{ }^\circ/s; 350 \text{ }^\circ/s]$ range, thanks to the maximum operator value computed between the median angular speed in the two directions of motion ($\omega_{median+}^m$ and $\omega_{median-}^m$). The dynamic and static character-

istics of this novel sensor (Fig. 2.18) were used to assess its performances. It consistently measured the 1-D angular speed accurately with an excellent *LinearityError* $< 1\%$. The impressive results obtained indoors were robust since the *Std_{error}* was of the same order of magnitude (less than $10^\circ/s$) under two different irradiance conditions, whether the printed belt simulating an unknown environment depicted a natural landscape or a laboratory. Due to the size of the setup we used, the performances have been assessed only indoors. Nevertheless, we have shown recently in (Expert et al., 2011b) that a very similar visual motion sensor based on the same retina could robustly and accurately measure the OF indoors and outdoors in a 1.5-decade illuminance range with strong transient variations.

This stand-alone sensor weighs less than 1 g. The outstanding performances of this tiny μC -based visual motion sensor show that it constitutes a good trade-off between the need for reliable motion sensors and the limited power and avionic payload available on MAVs. This 1g two-directional visual motion sensor yields at its output an accurate and highly refreshed angular speed measurement in the range of $[-350^\circ/s; -80^\circ/s] \cup [80^\circ/s; 350^\circ/s]$ perfectly adapted to any MAV flying forward and performing robotic tasks such as obstacle avoidance, terrain following, take-off, landing and speed-control purposes in forward flights even possibly for lunar landers (Valette et al., 2010).

In future works an other optimization of the “time of travel”, called the interpolation-based “time of travel” scheme (Expert et al., 2012) can be used to implement a larger number of 2-pixel LMS into a single dsPIC μC and therefore process the OF from a much larger 2D retina.

Article 3: Interpolation based “time of travel” scheme in a Visual Motion Sensor using a small 2D retina

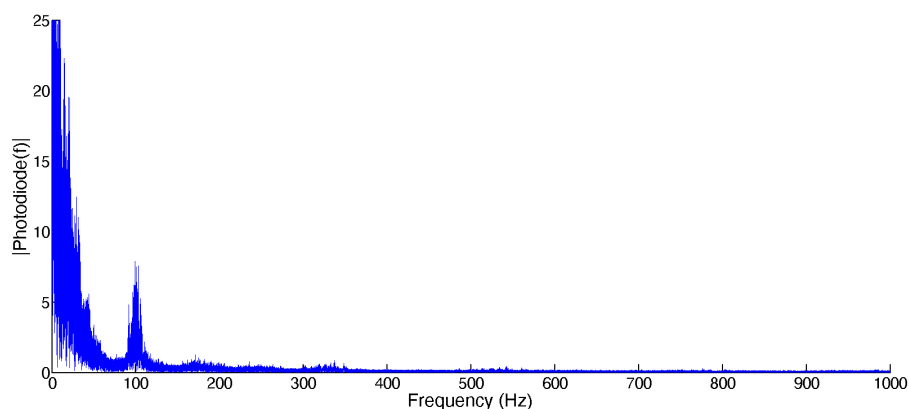


Figure 2.19: Fast Fourier transform of a photodiode signal of the LSC retina acquired at 2kHz. Except one peak at 100Hz corresponding to the artificial lights, most of the information belongs to the [0,100Hz] range.

Despite various optimizations of the “time of travel” scheme to embed more 2-pixel Local Motion Sensors inside a single microcontroller, the main limitation of the processing remains the important computational power necessary to process the angular speed preventing us from extracting the angular speed in several directions and over a wide Field of View. By looking at the visual signals and in particular their frequency content (see Figure 2.19), we noticed that their Fast Fourier transform is close to zero for frequencies higher than 100Hz. This means that, theoretically, based on the Nyquist-Shannon sampling theorem, we could sample the visual signals at 200Hz without losing any information. However, as we measure the angular speed from the time delay between the two signals, we would lose a lot in terms of accuracy by sampling the visual signals at a lower frequency. These findings have led us to propose a new implementation of the “time of travel” scheme called “interpolated time of travel” scheme where the visual signals are sampled at a lower frequency to reduce the computational burden of the microcontroller but the time lag between the two signals is still measured accurately thanks to a linear interpolation of the visual signals. From visual signals sampled at several frequencies, we determined in simulation that 200Hz is a good

trade-off between accuracy and computational power because the dispersion of the data was low and it reduced by more than four times the computational load of a 2-pixel LMS. The performances of the sensors indoors on a natural colored scene under natural light conditions are presented in this article showing that we greatly reduced the necessary processing power without badly affecting its performances.

Interpolation based “time of travel” scheme in a Visual Motion Sensor using a small 2D retina ⁴

Article published in 2012 in *IEEE Sensors Conference 2012*, 2231-2234.

Authors: Fabien Expert, Frédéric L. Roubieu and Franck Ruffier.

2.4.1 Abstract

Insects flying abilities based on optic flow (OF) are nice bio-inspired models for Micro Aerial Vehicles (MAVs) endowed with a limited computational power. Most OF sensing robots developed so far have used numerically complex algorithms requiring large computational power often carried out offline. The present study shows the performances of our bio-inspired Visual Motion Sensor (VMS) based on a 3x4 matrix of auto-adaptive aVLSI photoreceptors pertaining to a custom-made bio-inspired chip called APIS (Adaptive Pixels for Insect-based Sensors). To achieve such processing with the limited computational power of a tiny micro-controller (μC), the μC -based implementation of the “time of travel” scheme requiring at least a 1kHz sampling rate was modified by linearly interpolating the photoreceptor signals to run the algorithm at a lower sampling rate. The accuracy of the measurements was assessed for various sampling rates in simulation and the best trade-off between computational load and accuracy determined at 200Hz was implemented onboard a tiny μC . By interpolating the photoreceptors signals and by fusing the output of several Local Motion Sensors (LMSs), we ended up with an accurate and frequently refreshed VMS measuring a visual angular speed and requiring more than 4 times less computational resources.

2.4.2 Introduction

Despite their small size, airborne insects such as flies and bees can navigate autonomously in unknown environments on the basis of Optic Flow (OF) cues. Several bio-inspired terrestrial and aerial robots have been developed during the past decade based on similar principles (Franceschini et al., 1992; Ruffier & Franceschini, 2005; Beyeler et al., 2009). However, the computation of the OF onboard Micro Aerial Vehicles (MAVs) is still a challenging task, as most OF algorithms require a heavy computational load (Lucas & Kanade, 1981; Horn & Schunck, 1981) conflicting with their limited payload. Several methods of measuring the visual angular speed requiring few computational resources have been developed, such as those involving the local 1-D Hassenstein-Reichardt correlator (Hassenstein & Reichardt, 1956), which was mounted on a terrestrial robot (Harrison & Koch, 1999); the Interpolation Image Algorithm (I2A) (Srinivasan, 1994) which was used onboard an indoor microflyer (Zufferey

⁴Expert, F. , Roubieu, F.L. and Ruffier, F.(2012). Interpolation based “time of travel” scheme in a Visual Motion Sensor using a small 2D retina. *IEEE Sensors Conference 2012*, 2231-2234.

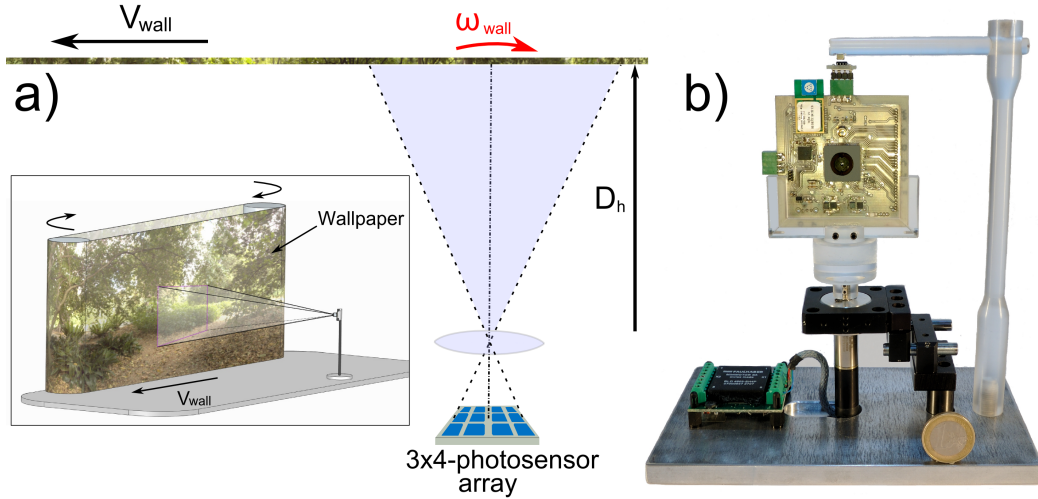


Figure 2.20: **a)** Test-bed for testing the visual motion device including the 3x4-photosensor array placed at an orthogonal distance D_h from a wall lined with a natural pattern moving at a speed V_{wall} . **b)** Picture of the test-board used for the experiments with the 25 auto-adaptive pixel array covered by its lens (Sparkfun SEN-00637, focal length 2mm, f-number 2.8) in the center. Each pixel features an integrated photodiode with a sensitive area of $250 \times 250 \mu m$ connected to an adaptive, time-continuous, logarithmic circuit having a dynamic range of 100 dB.

& Floreano, 2006) and the “time of travel” scheme (Blanes, 1986; Ruffier et al., 2003) originally inspired by the fly’s Elementary Motion Detector (EMD) neurons (Franceschini et al., 1989).

Recently, we focused on developing lightweight OF sensors embedded into tiny μC (Ruffier et al., 2003; Pudas et al., 2007; Viollet et al., 2010; Expert et al., 2011b) based on this scheme. In a previous study, we showed how 5 Local Motion Sensors (LMSs) measuring the angular speed (i.e., a 1-D component of the OF) can be embedded into a small μC to robustly and accurately determine the angular speed using the median operator (Roubieu et al., 2011). Nevertheless, we were limited in the ability to implement more LMSs inside the same μC by the high sampling rate (at least 1kHz) that was necessary to determine accurately the time-lag Δt between two adjacent visual signals. In this study, we show that a linear interpolation of the visual signals acquired at lower sampling rates can also result in an accurate angular speed measurement at a lower cost in terms of computational load and therefore allow to increase the number of LMS implemented into a single μC . The performances of this optimized implementation have been tested on a 3x4 matrix of Delbrück-type auto-adaptive aVLSI pixels (Delbrück & Mead, 1994) pertaining to a custom-made bio-inspired chip called APIS (Adaptive Pixels for Insect-based Sensors) (Aubépart et al., 2007; Viollet et al., 2010) in front of a moving wall lined with a natural panorama (see Fig. 2.20).

Section 2.4.3 gives a short description of the bio-inspired visual system and optimized implementation of the “time of travel” scheme. Section 2.4.4 describes the experiments and the results obtained with the Visual Motion Sensor (VMS), which was tested indoors under natural light conditions.

2.4.3 Optimized implementation

Each LMS assesses the angular speed ω_i of any contrasting object detected by 2 neighboring photosensor signals thanks to the *new interpolation based “time of travel” scheme* which can

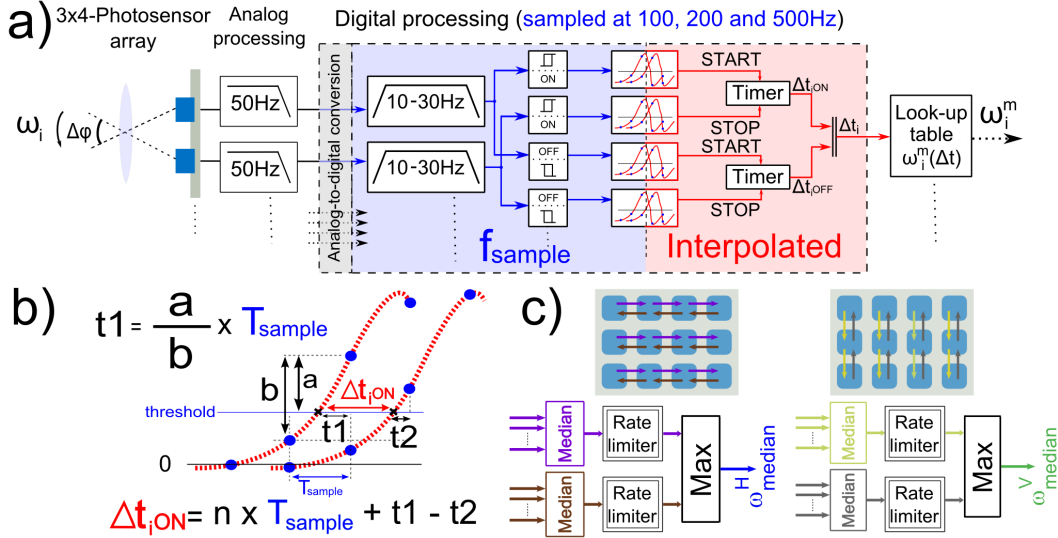


Figure 2.21: **a)** General processing architecture of the Local Motion Sensor (LMS): the output signals of two adjacent pixels were spatially and temporally filtered and thresholded to determine each 2-pixel angular speed ω_i^m . The data acquired at f_{sample} were linearly interpolated to measure the time-lag Δt between the two signals. **b)** Linear interpolation method to increase the resolution of the time difference measured between the signals of two adjacent pixels. Every time both visual signal exceed the positive threshold, the times (t_1 and t_2) are computed to estimate the interpolated $\Delta t_{i,ON}$, in this case. **c)** Fusion algorithm based on the maximal median value of both directions (Blanes, 1991; Franceschini et al., 1992) used to determine the magnitude and the direction of the 1-D angular speeds ω_{median}^H and ω_{median}^V . A rate limiter function filters out any median angular speed measurements that change too fast.

now be described in 7 processing steps including the new Interpolation Step n°5 (see Fig. 2.21a):

- Step 1: Low-pass spatial filtering is achieved by defocusing the lens, thus giving each pixel in the array a Gaussian angular sensitivity function defined by an inter-receptor angle $\Delta\varphi = 3.8^\circ$ and an acceptance angle $\Delta\rho = 3.8^\circ$.
- Step 2: Analog low-pass anti-aliasing filtering $f_c = 50Hz$.
- Step 3: Digitizing and filtering: second order fixed-point digital low-pass filtering ($f_c = 30Hz$) reduces any high frequency noise introduced by the artificial indoor lighting (100Hz) and first order fixed-point high-pass filtering ($f_c = 10Hz$).
- Step 4: Hysteresis thresholding is performed to distinguish between ‘ON’ and ‘OFF’ contrast transitions (i.e. dark-to-light and light-to-dark transitions, respectively) in each channel.
- Step 5: Linear interpolation of the photoreceptor signals acquired at a frequency f_{sample} to improve the temporal resolution of the angular speed computation. As shown in Fig. 2.21b, each time a signal exceeds a threshold, the time delays t_1 or t_2 are estimated with a 2kHz resolution assuming a linear variation of the signal between two samples.
- Step 6: A time delay circuit is triggered by one channel and stopped by the neighboring channel. This function measures the delay $\Delta t_i = n \times T_{sample} + t_1 - t_2$ elapsing between similar (‘ON’ or ‘OFF’) transitions occurring in two adjacent photoreceptors.

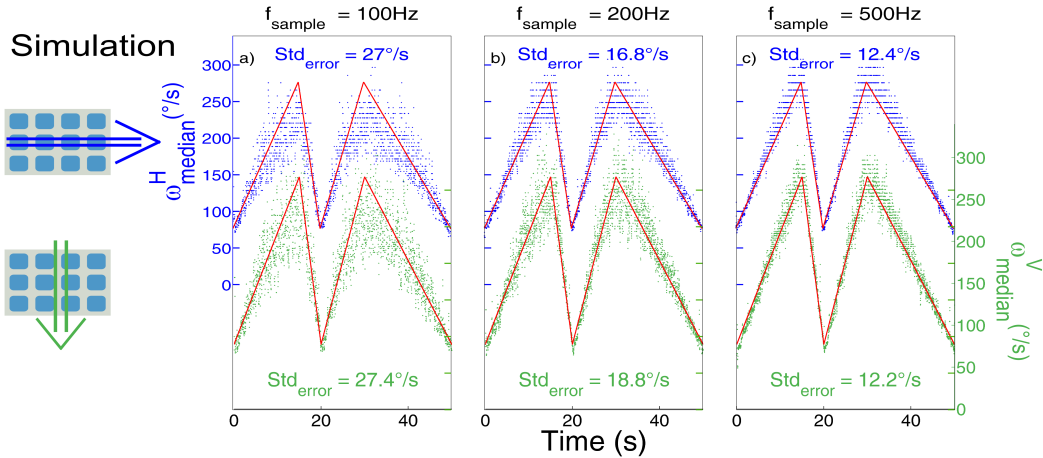


Figure 2.22: a-b-c) Simulated dynamic responses of the median angular speed of the visual motion sensor for three sampling rates for a horizontal translation (blue dots) and a vertical translation (green dots) in front of the textured wall moving according to a triangular law (red) (angular speed ranging from $75^\circ/s$ to $275^\circ/s$ with different slopes). In any case, the angular speed was measured thanks to a linear interpolation and faithfully obeyed the triangular law imposed to the moving wall. As expected, the accuracy of the measured angular speed ($\omega_{median}^H, \omega_{median}^V$) increases with the sampling rate. The dispersion was low enough ($Std_{error} < 19^\circ/s$) at 200Hz which is a good trade-off between accuracy and computational resources.

- Step 7: Computing the 1-D angular speed within the visual field of the LMS by using a look-up table that transforms the delay into the measured angular speed ω_i^m by applying $\omega_i^m = \frac{\Delta\varphi}{\Delta t_i}$.

2.4.4 Experiment and results

The visual motion sensor was tested indoors with natural light at an illuminance of around $0.7 \times 10^{-3} W/cm^2$ corresponding to the daylight provided by a window. The VMS was placed at an orthogonal distance $D_h = 27.5cm$ from a printed strip of wallpaper depicting a natural colored scene (see Fig. 2.20a) and could be rotated by an angle of 90° . The printed strip was stretched between 2 actuated drums imposing a translational speed V_{wall} to the panorama. The scene was therefore seen to move horizontally or vertically by the VMS at an angular speed ω_{wall} describing a triangular speed law involving a series of velocity ramps with different slopes ranging between $75^\circ/s$ and $275^\circ/s$.

Among the 25 pixels of the APIS retina, a 4x3-pixel array is connected to the microcontroller and 34 LMSs are computed (represented by the arrows in Fig. 2.21c) in 4 different directions (from top to bottom, from bottom to top, from left to right and from right to left). In each direction, the median value of the angular speed is computed and the maximum value between the median value of opposite directions determines respectively ω_{median}^H and ω_{median}^V .

The data dispersion was taken to be the standard deviation of the difference between the theoretical angular speed determined from the horizontal speed of the moving wall ω_{wall} and the LMS output signal ω^m , according to the following equation: $Std_{error} = std(\omega_{wall} - \omega^m)$. For each direction, the refresh rate $f_{refresh}$ was defined as the number of new motion measurements per second among the LMS of the specific direction: a new measurement occurs when a contrast transition is detected by one pixel and then by the second pixel with a time lag Δt in our measurement range, corresponding to an angular speed in the

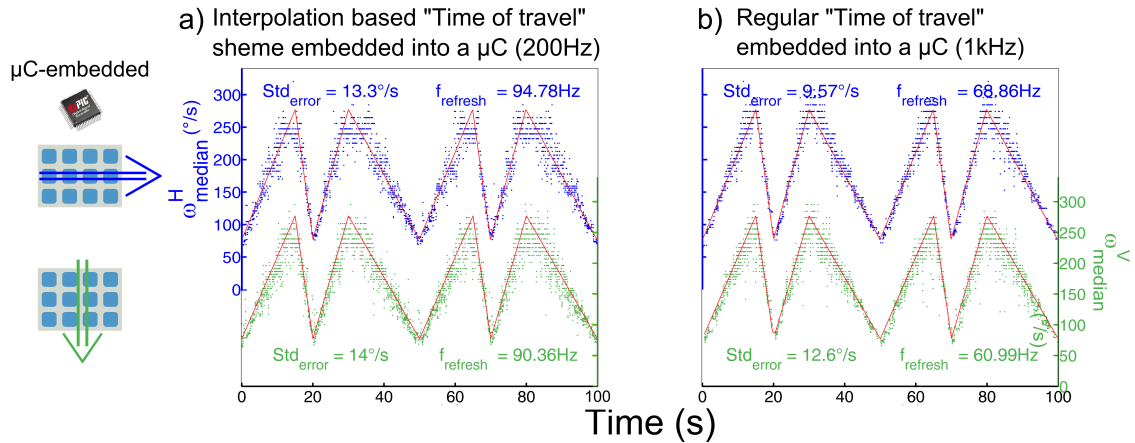


Figure 2.23: **a)** μC -embedded dynamic response of the median angular speed of the visual motion sensor at $f_{sample} = 200\text{Hz}$ measured thanks to a linear interpolation for a horizontal translation (blue dots) and a vertical translation (green dots) of the moving wall. The visual motion sensor yields at its output an accurate ($Std_{error} < 15^\circ/s$) and highly refreshed (nearly up to 100Hz) angular speed measurement (ω_{median}^H , ω_{median}^V). **b)** μC -embedded dynamic response of the median angular speed of the visual motion sensor at $f_{sample} = 1\text{kHz}$ measured thanks to the regular “time of travel” scheme. The refresh rate, which depends on the number of fused LMS, was greater for the horizontal motion than for the vertical motion as the median values were computed from 9 and 8 LMSs respectively.

$[30^\circ/s, 350^\circ/s]$ range.

In order to determine the best trade-off between accuracy and computational load, a first set of experiments has been conducted in simulation using photoreceptor signals acquired at 3 different sampling rate frequencies (100, 200 and 500Hz) for a horizontal and a vertical motion. Then, the whole processing has been embedded into a dsPIC33FJ128GP804 microcontroller with a 200Hz sampling frequency.

2.4.4.1 Simulation of the interpolation based “Time of travel”

The interpolated algorithm presented in Fig. 2.21 was tested offline with three sampling rates (f_{sample}) on visual signals coming from the APIS retina. As we can see in the Fig. 2.22, the simulated responses of the horizontal and vertical angular speed measurements (ω_{median}^H , blue dots; ω_{median}^V , green dots) faithfully obeyed the triangular law imposed to the moving wall: the dispersion decreased with the sampling rate (from $Std_{error} = 27^\circ/s$ at 100Hz to $Std_{error} = 12^\circ/s$ at 500Hz). The simulated new scheme featured good performances at 200Hz which is the best trade-off between accuracy (dispersion lower than $19^\circ/s$) and limited computational load.

2.4.4.2 Interpolation based “Time of travel” embedded into a μC

A full duplex link between the UART peripheral of the μC and the computer serial port allowed us to log data from the VMS on a host computer. As shown in figure 2.23, the experimental measured median angular speed was highly refreshed and faithfully obeyed the triangular law imposed to the moving wall ($Std_{error} < 15^\circ/s$). This processing accounts for only 10.5% in average of the processing time available at a sampling frequency of 200Hz (peak value:16%). In comparison, the same processing embedded into the μC at 1kHz requires 44.2% in average (peak value:71%) of the processing available. Although the

processing is more than 4 times less costly at 200Hz than 1kHz, we can see that the accuracy (Std_{error}) of the data is experimentally only slightly better at 1kHz which proves that linearly interpolating the photoreceptors signals sampled at 200Hz is a really interesting trade-off between computational load and accuracy.

2.4.5 Conclusion

In this study, the dynamic characteristics of a new optimized implementation of the “time of travel” scheme was tested indoors on a natural colored scene under natural light conditions. The results obtained here show that by linearly interpolating the photoreceptor signals sampled at 200Hz, we can greatly increase by at least 4 times the number of Local Motion Sensors that can be embedded in a small and lightweight microcontroller. This allowed us to compute all the possible LMSs from a 4x3 bio-inspired auto-adaptive pixel array in the 4 main directions. The overall Visual Motion Sensor (VMS) yields a median horizontal and vertical values (ω_{median}^H and ω_{median}^V respectively) which were found to be accurate and frequently refreshed. This VMS constitutes a good trade-off between the need for reliable and lightweight visual motion sensors matching the drastically limited payload of the Micro Aerial Vehicles.

As only 10.5% of the processing time available was used to process the angular speed of a small matrix of 12 pixels (4x3 pixel), this optimized implementation could be used to implement more LMSs into such tiny μ C and therefore process the optic flow from 2D retinas having about 50 pixels. In a near future, this new visual motion sensor could be implemented on Micro Aerial Vehicles to process the local optic flow in several regions of the Field of View allowing them to fly autonomously in natural environments and perform complex tasks such as collision avoidance, automatic take-off and landing (Franceschini et al., 2007; Expert et al., 2012)...

2.5 Conclusion

In this chapter, 3 articles have been presented showing the performances of the “time of travel” scheme with several retinas and also in comparison with optic mouse sensors which have known a growing interest in the past years for robotic applications. In particular, one custom-made aVLSI retina composed of pixels automatically adapting to the background illuminance has been detailed and thoroughly characterized. Then, several optimizations of the processing have been proposed to not only improve its accuracy but also reduce its complexity in terms of computational power. The idea is, of course, to be able to embed an important number of 2-pixel Local Motion Sensors processing the angular speed from several regions of the environment in order to extract from them thanks to a smart fusion the vital cues which are necessary for Micro Aerial Vehicles to fly autonomously. Recently, a new implementation of the “time of travel” scheme specifically adapted to process low angular speeds has been presented and tested onboard a rotorcraft (Sabiron et al., 2013). This work has been conducted has a preliminary phase toward the design of the first artificial curved compound eye called CurvACE (Floreano et al., 2013) composed of pixels automatically adapting to the background illuminance and processing the optic flow over a very wide FOV thanks to processing units placed in its concavity.

Chapter 3

The first artificial compound eye: the CurvACE sensor

3.1 Introduction

The mammalian eye (figure 3.1, left) has provided inspiration for the design of conventional cameras, which consist of a planar image sensor in the focal plane of single-aperture optics. Their purpose is to provide a faithful rendering of the visual world that can be processed by image analysis algorithms for a large variety of purposes, especially for object recognition. However, such vision systems require complex and fast computation in order to extract motion-related information from a sequence of high-resolution images. We have seen in the chapter 2 how we can compute optic flow on several retinas similar to the vertebrate eye featuring some characteristics of the visual processing of insects like a Gaussian angular sensitivity, a coarse resolution and an automatic adaptation to the background illuminance which are key points to extract motion in an unknown environment. However, the LSC-

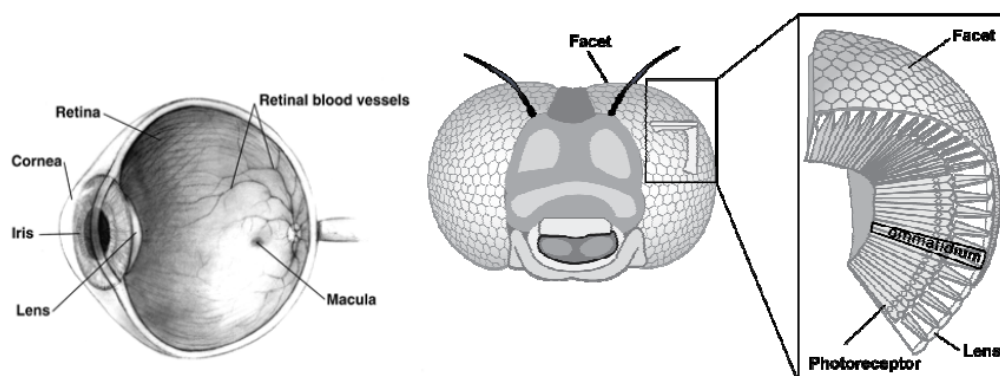


Figure 3.1: Mammalian eye (left) and insect compound eye (centre) with detailed view of a patch of ommatidia (right). Reprinted from National Eye Institute website and (Pericet-Camara et al., 2011).

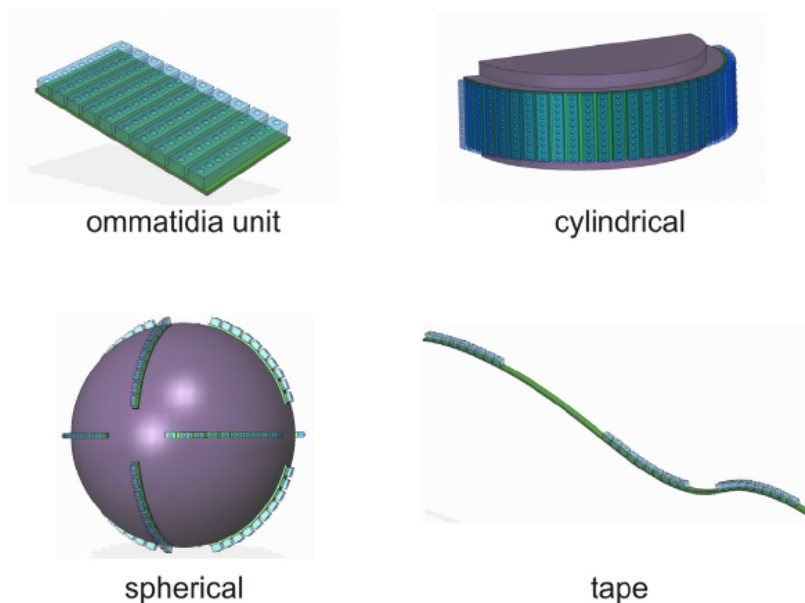


Figure 3.2: Artistic views of the different versions of CurvACE as described in the original proposal funded by the European Union (www.curvace.org) (Pericet-Camara et al., 2011).

based and the APIS-based motion sensors have a small number of pixels and a limited field of view allowing to compute the angular speed in a specific direction like the mouse sensors which are based on bigger retinas.

The insect compound eye (figure 3.1, centre and right), instead, consists of a curved array of micro-lenses, each conveying photons to a separate set of one or more photoreceptors. Although the compound eye’s design offers a comparatively lower resolution than the vertebrate eye, it is very efficient for local and global motion analysis over a large field of view (FOV), making it an excellent sensor for accurate and fast navigation in 3D dynamic environments. For flying robots like for insects, it is interesting to be able to extract motion from every direction in order to avoid collisions and fly autonomously in any environment. This is the reason why we designed the first fully functional artificial compound eyes, composed of a micro-lens arrays integrated with adaptive photoreceptors made of analog Very-Large-Scale-Integration circuits on flexible electronic substrates. This integrated vision sensor is called Curved Artificial Compound Eye (CurvACE) (Pericet-Camara et al., 2011).

Compared to conventional cameras, the CurvACE sensor offers much larger field of view, nearly infinite depth-of-field (no focusing needed), higher sensitivity, no image blurring and off-axis aberrations because the distance between the optical surface and the photoreceptors is constant over the entire field of view and because each optical channel works under perpendicular light incidence for its individual viewing direction. In comparison with classical

cameras where focal length, spatial resolution and field of view are intimately coupled, a curved compound eye allows the use of different focal lengths for the same field of view. Furthermore, the curved shape of the artificial compound eyes offers space within the convexity for embedding processing units and inertial sensors, such as accelerometers and rate gyroscopes, which can be used for motion-related computation. Instead, in conventional cameras, these components must be packaged separately because the space between the convex lens and the planar image sensor must be transparent.

The curved artificial compound eye has been fabricated by developing flat patches of artificial ommatidia (see figure 3.2 top left) that are flexed after fabrication in order to maintain perfect alignment of the optics and photoreceptors that compose each single ommatidium. This process allows to adapt the optical and imaging properties and therefore fabricate various types of curved compound eyes (see figure 3.2) that will suit the needs of different applications.

The next article presents the work accomplished by the whole CurvACE consortium which has led to the development of the first fully functional artificial compound eye. Although involved in every step of the development, the Biorobotics team was in particular in charge of specific tasks of the development process like the design of the readout protocol and the optical and optic flow characterization. In particular, I have worked intensively on the experimental setups used for the optical and the optic flow characterization to develop the interfaces, program the protocols and perform the experiments to assess the performances of the CurvACE sensor to measure optic flow (see sections 3.2.4 and 3.2.6.2). More details about these tasks are given in appendix A.

Miniature Curved Artificial Compound Eyes ¹

Article published in 2013 in *Proceedings of the National Academy of Sciences of the United States of America (PNAS)*, 110: 9267-9272.

Authors: Dario Floreano, Ramon Pericet-Camara, Stéphane Viollet, Franck Ruffier, Andreas Brückner, Robert Leitel, Wolfgang Buss, Mohsine Menouni, Fabien Expert, Raphaël Juston, Michal K. Dobrzynski, Géraud L'Éplatténier, Fabian Recktenwald, Hanspeter A. Mallot and Nicolas Franceschini.

3.2.1 Abstract

In most animal species, vision is mediated by compound eyes, which offer lower resolution than vertebrate single-lens eyes, but significantly larger fields of view with negligible distortion and spherical aberration, as well as high temporal resolution in a tiny package. Compound eyes are ideally suited for fast panoramic motion perception. Engineering a miniature artificial compound eye is challenging because it requires accurate alignment of photoreceptive and optical components on a curved surface. Here, we describe a unique design method for biomimetic compound eyes featuring a panoramic, undistorted field of view in a very thin package. The design consists of three planar layers of separately produced arrays, namely, a microlens array, a neuromorphic photodetector array, and a flexible printed circuit board that are stacked, cut, and curved to produce a mechanically flexible imager. Following this method, we have prototyped and characterized an artificial compound eye bearing a hemispherical field of view with embedded and programmable low-power signal processing, high temporal resolution, and local adaptation to illumination. The prototyped artificial compound eye possesses several characteristics similar to the eye of the fruit fly *Drosophila* and other arthropod species. This design method opens up additional vistas for a broad range of applications in which wide field motion detection is at a premium, such as collision-free navigation of terrestrial and aerospace vehicles, and for the experimental testing of insect vision theories.

3.2.2 Introduction

Insect compound eyes consist of a mosaic of tiny optical units, or ommatidia (Land & Nilsson, 2002). Compared with vertebrate single-lens eyes, compound eyes offer a versatile morphology with panoramic field of view (FOV), negligible distortion and aberration, and high temporal resolution, while trading high spatial resolution for diminutive size (Kirschfeld,

¹Floreano, D., Pericet-Camara, R., Viollet, S., Ruffier, F., Brückner, A., Leitel, R., Buss, W., Menouni, M., Expert, F., Juston, R., Dobrzynski, M.K., L'Éplatténier, G., Recktenwald, F. Mallot, H.A. and Franceschini, N.(2013). Miniature Curved Artificial Compound Eyes. *PNAS*, 110: 9267-9272

Table 3.1: Specifications of CurvACE prototype compared with the characteristics of the *Drosophila melanogaster* compound eye. deg., degree.

	CurvACE	<i>Drosophila</i> eye (Ref(s).)
Number of ommatidia	630	600 – 700
Facet diameter, μm	172	16 (Franceschini & Kirschfeld, 1971)
Eye diameter, mm	12.8	0.36 (Franceschini & Kirschfeld, 1971)
Facet diameter/eye diameter, %	1.3	4.4
Interommatidial angle, $\Delta\varphi$; deg.	~ 4.2	$\sim 4.7 - 5.5$ (Franceschini & Kirschfeld, 1971)
Acceptance angle, $\Delta\rho$; deg.	4.2	~ 4.5 (Götz, 1965)
FOV, deg.	180×60	160×180 (Heisenberg & Wolf, 1984)
Signal acquisition bandwidth, Hz	300	< 100 (Laughlin & Weckström, 1993)
Adaptability to illuminance	Yes	Yes (Gu et al., 2005)
Crosstalk prevention	Yes	Yes (Götz, 1965)

1976). These features are particularly beneficial for visually controlled navigation, including tasks like collision avoidance, take-off, landing, and other optomotor responses that do not require a high density of photoreceptors. Insect compound eyes possess local sensory adaptation mechanisms capable of compensating for large changes in light intensity right at the photoreceptor level (Laughlin, 1989; Gu et al., 2005), and they wrap around highly distributed neuronal circuitry, allowing for fast and low-power integrated signal processing (Krapp & Hengstenberg, 1996), whereas minimizing the overall size of the insect head. An artificial compound eye exhibiting all these properties would represent an ideal miniature sensor for numerous situations in which fast motion detection across wide FOVs is required (Franceschini et al., 1992; Blanchard et al., 2000; Franceschini et al., 2007; Floreano et al., 2009).

Attempts have recently been made to develop miniature compound eyes. Both planar (Duparré et al., 2005) and curved (Jeong et al., 2006; Radtke et al., 2007; Pulsifer et al., 2010; Qu et al., 2012) microlens arrays have been fabricated. In some cases, these were interfaced with conventional flat CMOS arrays, but this resulted in off-axis aberrations, crosstalk between neighboring ommatidia, or limited FOV. At first sight, recent developments in flexible sensors (Khang et al., 2006; Dinyari et al., 2008; Xu et al., 2008; Lee et al., 2011) could represent a promising avenue for curved vision sensors (Jung et al., 2011; Dumas et al., 2012). However, adapting those flexible technologies to the design of curved compound eyes is challenging due to the recurring problem of precisely aligning a curved photodetector array with a curved microlens array. None of these previous methods or other available omnidirectional camera systems (Ferrat et al., 2008) display important features of biological compound eyes, such as embedded data processing, versatile morphologies, high temporal resolution, and local light adaptation in a miniature package.

Here, we describe a unique approach to the design of a curved artificial compound eye, named CurvACE. We validate this approach by characterizing the sensitivity, angular resolution, and motion extraction capabilities of a prototype bearing a semicylindrical morphology (Fig. 3.3A) and a hemispherical FOV of $180^\circ \times 60^\circ$ (Fig. 3.3B). This prototype is a self-contained, integrated, curved artificial compound eye system with morphology and properties resembling those of primitive (Fortey & Chatterton, 2003) (Fig. 3.3C) and modern (Land

& Nilsson, 2002) (Fig. 3.3D) arthropods . In particular, the CurvACE prototype features several similarities with the eye of the fruit fly *Drosophila*, namely, spatial resolution, acceptance angle, number of ommatidia, local light adaptation, crosstalk prevention, and signal acquisition bandwidth, as well as a smaller but comparable FOV (Table 3.1). Such curved visual sensors may be useful for terrestrial and aerial vehicles, medical instruments, prosthetic devices, home automation, surveillance, motion capture systems, and smart clothing. Artificial compound eyes may also foster the development of alternative visual algorithms, and when fitted on physical robots, they could help explore fundamental principles in animal sensory-motor control (Franceschini et al., 1992, 2007; Floreano et al., 2009; Webb, 2002).

3.2.3 Fabrication process

3.2.3.1 Design method

As with biological compound eyes, CurvACE artificial ommatidia consist of three materially and functionally different layers (Fig. 3.4A): (i) an optical layer composed of an array of highly transparent polymer microlenses molded on a glass carrier (Fig. 3.9) which focus light precisely onto (ii) the sensitive areas of a silicon-based photodetector layer. This layer contains an array of analog very-large-scale integration (VLSI) photodetectors as well as additional circuitry to condition the signal for processing (Fig. 3.10). Finally, (iii) a flexible electro-mechanical interconnection layer, formed by a polyimide printed circuit board (PCB), physically supports the ensemble and transfers the output signals from the individual ommatidia (Fig. 3.4B) to the processing units. With thicknesses of $550\ \mu\text{m}$, $300\ \mu\text{m}$, and $100\ \mu\text{m}$, respectively, the total height of the three assembled layers is less than 1 mm in the prototype presented here.

The apposition and neural superposition compound eyes of many arthropod species contain pigmented sidewalls that contribute to reducing optical crosstalk between ommatidia (Land & Nilsson, 2002). Our solution to suppress optical crosstalk makes use of two low-reflective opaque metal layers with matching pinhole patterns: one subjacent to the microlens array and the other one close to the focal plane, ahead of the photodetector layer (Duparré et al., 2005) (Fig. 3.4A,B and Fig. 3.9C).

The proposed design method is based on a planar fabrication technology for each of the three layers of the artificial ommatidia array followed by high-precision cutting (dicing) of the rigid ommatidia layers to add bendability. Specifically, each of the three layers is fabricated at first with wafer-level (optical and photodetector layer) or batch-level (interconnection layer) processes using standard microengineering technologies (Fig. 3.9 and 3.10). Next, the optical and photodetector layers are aligned at micrometer accuracy and glued chip-wise (Fig. 3.4B). Subsequently, the ensemble is fixed and wire-bonded to the electro-mechanical interconnection layer. Finally, the rigid optical and photodetector layer stack is precisely separated with a chip dicing saw in columns of ommatidia down to the flexible interconnection layer, which remains intact (Fig. 3.4C and Fig. S4A). This procedure ensures accurate and reproducible alignment of the optical and photosensitive elements across the array, while providing electronic accessibility to the output signals of the individual artificial ommatidia. It results in a very thin and light package, less than 1 mm and 0.36 g in the prototype presented here, and ensures mechanically safe bending of the interconnection layer down to a small radius of curvature (Fig. 3.4D). Free space on the back side of the artificial ommatidia permits attachment to curved rigid or flexible substrates and incorporation of

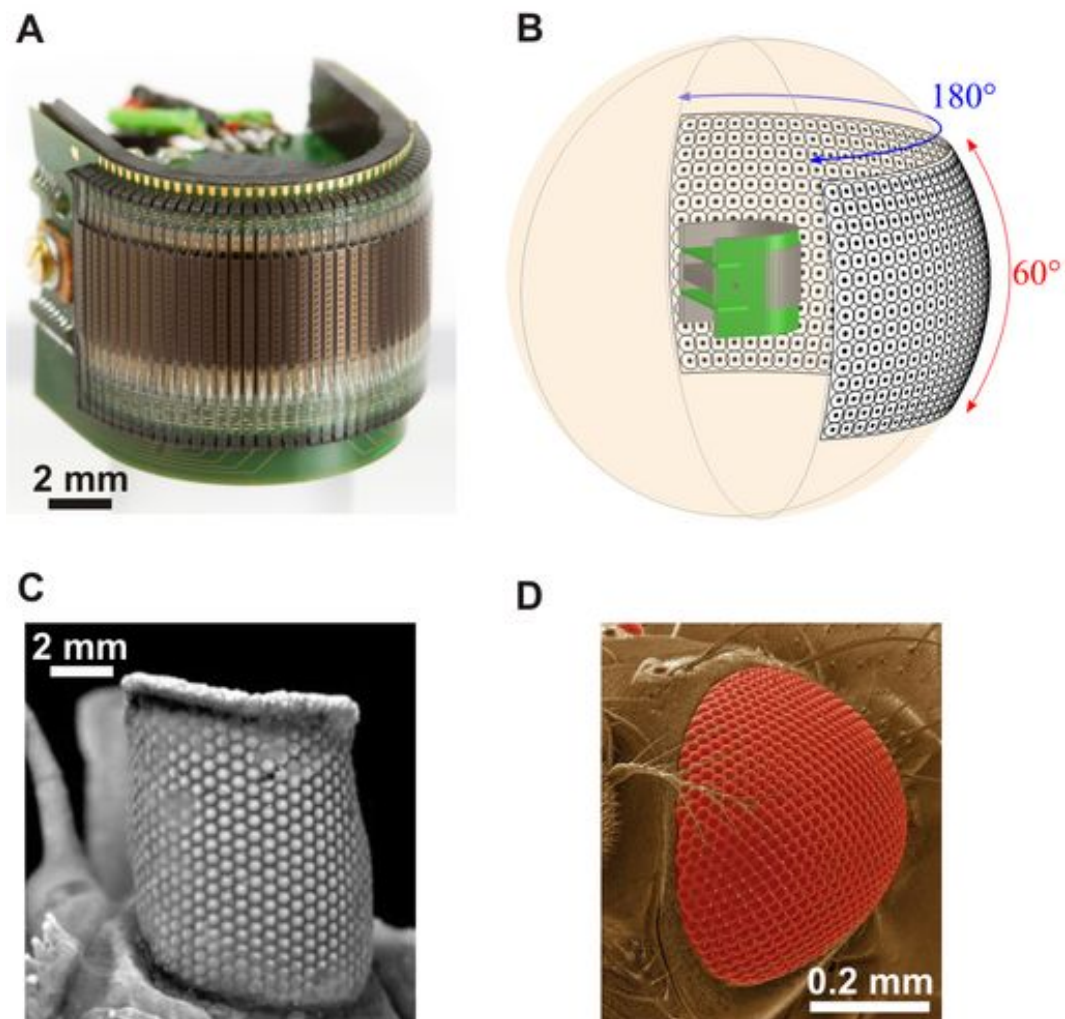


Figure 3.3: Artificial and natural curved compound eyes. (A) Image of the CurvACE prototype. The entire device occupies a volume of 2.2cm^3 , weighs 1.75 g and consumes 0.9 W at maximum power. (B) Illustration of the panoramic FOV of the fabricated prototype. The dots and circles represent the angular orientation and acceptance angle $\Delta\rho$ of every ommatidium, respectively. Compound eye of the extinct trilobite *Erbenochile erbeni* (Fortey & Chatterton, 2003) (C) and of the fruit fly *Drosophila melanogaster* (D). [(C) Reprinted from ref. (Fortey & Chatterton, 2003) with permission from AAAS; (D) Reprinted from ref. (Lee et al., 2010) with permission from AAAS.]

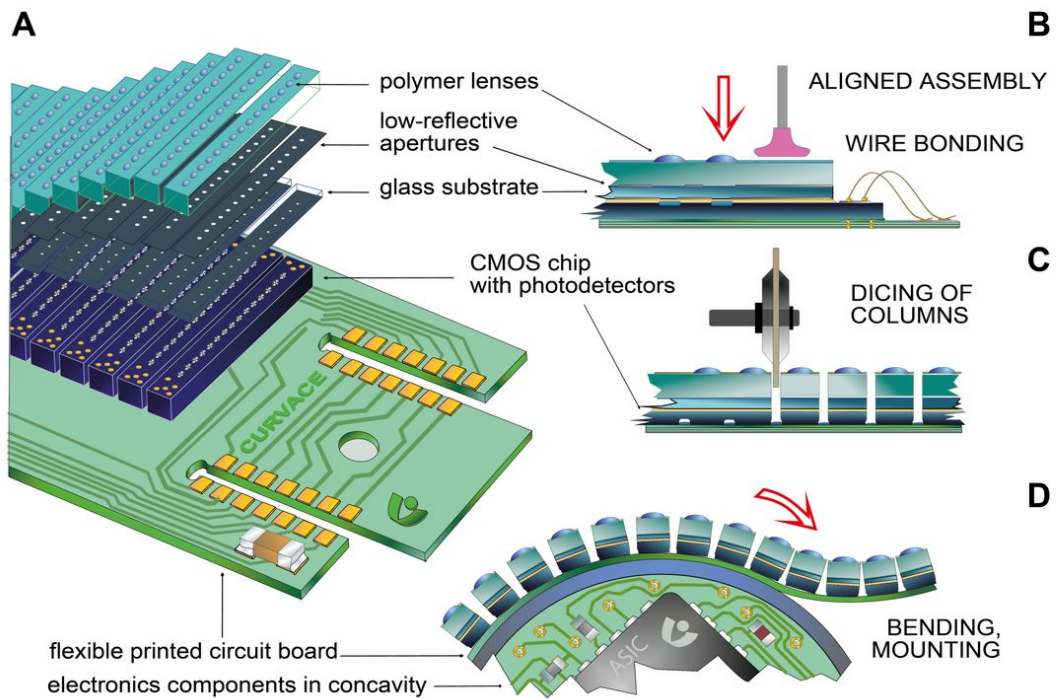


Figure 3.4: CurvACE design and assembly. (A) Scheme of the three layers that compose the CurvACE artificial ommatidia: optical (microlenses and apertures), photodetector (CMOS chip), and interconnection (PCB). (B) Accurate alignment and assembly process of the artificial ommatidia layers in planar configuration. (C) Dicing of the assembled array in columns down to the flexible interconnection layer, which remains intact. (D) Curving of the ommatidial array along the bendable direction and attachment to a rigid semicylindrical substrate with a radius of curvature of 6.4 mm to build the CurvACE prototype. Two rigid circuit boards containing two microcontrollers, one three-axis accelerometer, and one three-axis rate gyroscope are inserted into the rigid substrate concavity and soldered to the sides of the ommatidia through dedicated pads (Figs. 3.12D and 3.11).

additional electronics for signal processing in the resulting concavity (Fig. 3.4D).

3.2.3.2 Fabrication of a CurvACE prototype

We fabricated a CurvACE prototype by bending a rectangular array of 42 columns of 15 artificial ommatidia (microlens diameter = $172 \mu\text{m}$) down to a curvature radius of 6.4 mm along its longer direction to yield a 180° FOV in the horizontal plane (Fig 3.3A and B and Fig. 3.12B and C). This curvature should nominally yield an interommatidial angle $\Delta\varphi_h$ of 4.3° in the equatorial row along the bent direction. Although there is no mechanical bending along the vertical direction, it is possible to make the visual axes of the 15 ommatidia in each column fan out in the vertical plane by making the vertical pitch between the photodetectors stepwise smaller than the vertical pitch between the microlenses (Duparré et al., 2005) (Fig. 3.9C). In the prototype, the photodetector pitch was calculated so as to obtain a similar value for the interommatidial angle $\Delta\varphi_v$ along the vertical unbent direction, which results in a total vertical FOV of 60° (Fig. 3.3B). To avoid spatial aliasing or blind spots in the visual field, the acceptance angle $\Delta\rho$ of each ommatidium must closely approach the interommatidial angle $\Delta\varphi$ (Land & Nilsson, 2002; Götz, 1965) (Fig.3.5C). Therefore, the ommatidial lenslets, diaphragms, and photodetectors were designed using an optical ray tracing technique (Zemax, Radiant Zemax, LLC of Redmond, WA) to produce an acceptance angle $\Delta\rho$ of 4.3° .

The resulting concavity on the backside of the prototype after the mechanical bending along the horizontal direction is used to host two microcontrollers, two inertial sensors, and other electronic components that are fitted and soldered on two rigid PCBs (Fig. 3.4D and 3.12C and 3.6). In the experiments described below, the embedded microcontrollers are programmed to operate the visual data read-out and communicate with an external computer for analysis; in a stand-alone application, these microcontrollers can be used to process visual data onboard the prototype without any external computer.

3.2.4 Results

3.2.4.1 Characterization of Visual Sampling

To characterize the visual sampling of the environment by the fabricated CurvACE prototype, we measured the angular sensitivity function (ASF) of each of the 630 artificial ommatidia (Fig. 3.14). Fig. 3.5A and D shows representative examples of ASFs measured along a single row and a single column, respectively. Most ASFs display the expected Gaussian distribution with respect to the light incidence angle, which validates both the microoptical design and the precise alignment with each individual photodetector. We derived the experimental acceptance angles and interommatidial angles from the measured ASFs. The acceptance angle $\Delta\rho$ of an ommatidium is defined as the full width at half maximum (FWHM) of its Gaussian-like ASF. The horizontal and vertical interommatidial angles $\Delta\varphi_h$ and $\Delta\varphi_v$ were assessed from the angular position of the peak of the ASFs of two adjacent ommatidia (Fig. 3.5C). The measured acceptance angles yielded an average of $\Delta\rho = 4.2^\circ \pm 0.3^\circ$ (SD) for both horizontal (Fig. 3.5A) and vertical (Fig. 3.5D) directions. The vertical interommatidial angles resulted in an average of $\Delta\varphi_v = 4.26^\circ \pm 0.16^\circ$ (SD) (Fig. 3.5D) and the horizontal ones ranged from $\Delta\varphi_h = 4.2^\circ \pm 0.8^\circ$ (SD) in the middle row (Fig. 3.5A) to $3.7^\circ \pm 0.7^\circ$ (SD) in the top and bottom rows (Fig. 3.5B). The close match between the experimentally measured acceptance angles and interommatidial angles validates both the

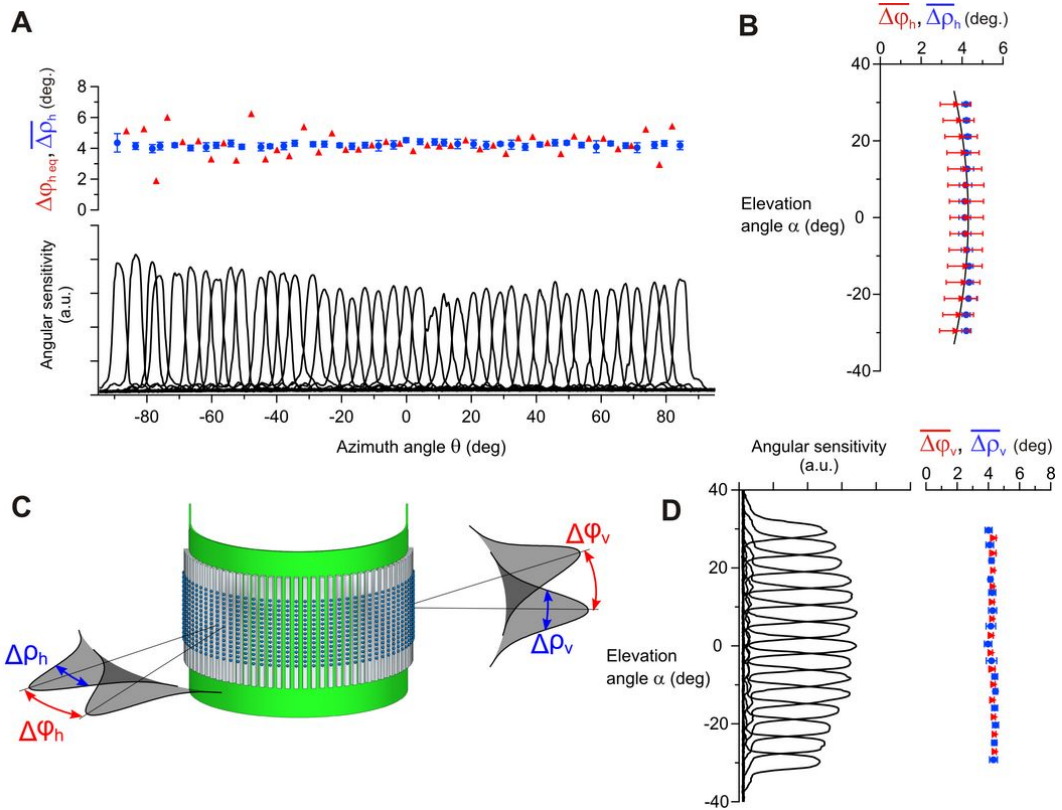


Figure 3.5: Characterization of CurvACE angular sensitivity. (A) Measured ASF along the middle (equatorial) row (black curves), with the corresponding interommatidial angles $\Delta\varphi_{heq}$ (red triangles), and mean acceptance angles $\Delta\rho_h$ (blue circles) of the CurvACE ommatidia averaged along every column. Error bars display SDs. (B) Mean horizontal interommatidial and acceptance angles averaged along every row of artificial ommatidia as a function of the elevation angle α . The black curve shows the theoretical $\Delta\varphi_h$ values obtained using Eq. 3.10 with a constant $\Delta\varphi_{hmax}$ of 4.2° . (C) Schematic representation of the acceptance angle $\Delta\rho$ of an ommatidium and the interommatidial angle $\Delta\varphi$ calculated from the peak ASFs of two neighboring ommatidia. (D) Measured ASFs along a single column of artificial ommatidia (black curves), mean vertical interommatidial (red triangles), and acceptance angles (blue circles) averaged along every row of artificial ommatidia. a.u., arbitrary units; deg., degree.

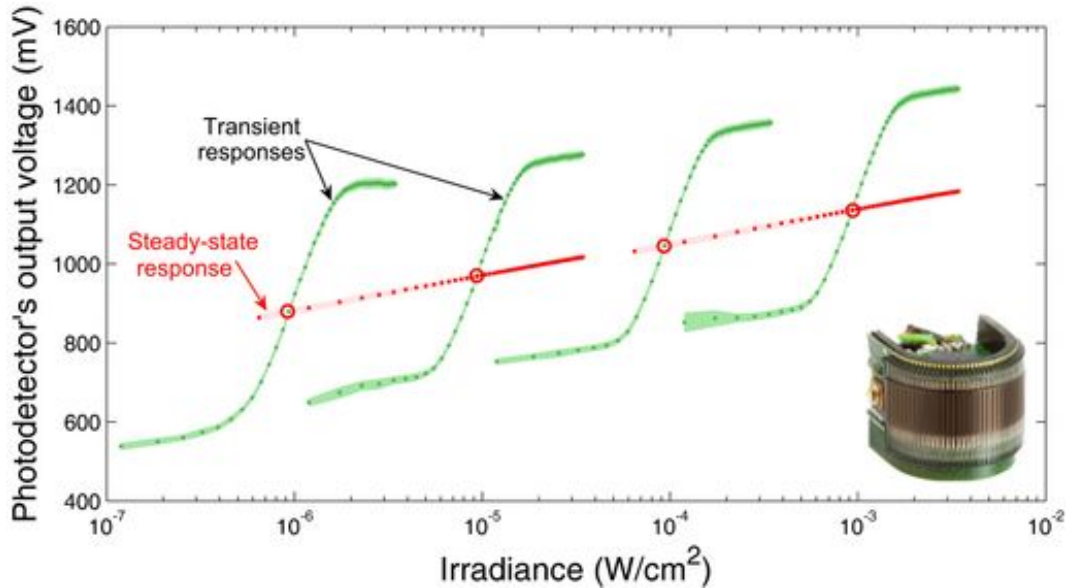


Figure 3.6: CurvACE autoadaptation to ambient light at the single ommatidium level. Steady-state (red dots) and transient (green dots) responses of the adaptive analog VLSI photodetectors [design based on a circuit proposed by Delbrück and Mead (Delbrück & Mead, 1994)]. Each of the four dynamic operating curves (in green) shows the $V(\log I)$ response, averaged over 11 ommatidia (photodetectors with optics) of one column, to step increments and decrements of irradiance (Fig. 3.15) about four steady levels (red circles).

ray-tracing design and fabrication process while indicating that the CurvACE prototype, like the fruit fly compound eye (Götz, 1965), performs an adequate sampling of its entire FOV (Fig. 3.3B). The observed spread in the values of the horizontal interommatidial angles $\Delta\varphi_h$ (Fig. 3.5A and B) is probably due to the manual process used to mechanically fix the flexible PCB supporting the artificial ommatidia array onto the rigid curved substrate.

3.2.4.2 Characterization of Ommatidium Light Adaptation

In the natural world, visual sensors must cope with a wide dynamic range of irradiance, which can span on the order of 8 decades over the course of a day. Light variations within a scene are particularly challenging because they can make part of the visual field nonresponsive due to photoreceptor saturation. Animal retinæ partly solve this crucial problem by means of a local light adaptation mechanism integrated within each photoreceptor (Laughlin, 1989; Gu et al., 2005; Normann & Perlman, 1979; Matic & Laughlin, 1981). Similarly, we have equipped each prototype ommatidium with a neuromorphic adaptation circuit (Fig. 3.10D) that operates independent of its 629 neighbors. The neuromorphic circuit originally proposed by Delbrück and Mead (Delbrück & Mead, 1994) was modified here by cascading a first-order, low-pass filter (Fig. 3.10D). This modification prevents temporal aliasing and keeps the photodetector bandwidth of 300 Hz practically constant across the entire studied range of ambient lighting conditions. The circuit design was further optimized (*SI Text, Photodetector Layer*) to minimize the transient gain dispersion of each autoadaptive circuit. Fig. 3.6 shows the mean steady state and transient responses of 11 artificial ommatidia (photodetectors with optics) in one column to light step increments and decrements presented at four different steady light levels (Fig. 3.15). At each of these four levels (red circles in Fig. 3.6), the output response of the individual ommatidia to light steps yields an S-shaped operating

curve in a semilog plot. Adaptation to a novel steady irradiance level essentially produces a horizontal shift of the curve without markedly changing its slope, which represents a dynamic sensitivity of about 1,300 mV per decade in the linear part. The steady operating curve (shown in red in Fig. 3.6) is also a logarithmic function of the adapting light, but with a slope (steady sensitivity) about 12-fold smaller. Thanks to the optimized design of the adaptive photodetector layout, the averaged dispersion of the sensitivity over the four operating curves is as small as 11 mV, that is, only about 2% of the total 600-mV dynamic range.

The four operating curves demonstrate not only the high sensitivity of the prototype ommatidia but their relative invariance in sensitivity to the ambient light. These $V(\log I)$ curves shifting with the operating points are reminiscent of those obtained in analogous experiments carried out on single vertebrate (Normann & Perlman, 1979) and invertebrate (Matic & Laughlin, 1981) photoreceptors. This local adaptation is essential for efficient sampling of natural environments because it prevents saturation of the photoreceptors by bright spots in the visual scene while allowing them to adapt quickly to untoward illumination changes, such as transitions from a shaded area to a sunny place.

3.2.4.3 Characterization of Motion Extraction

In addition to an extensive FOV (Fig. 3.5) and local adaptation to illuminance (Fig. 3.6), the CurvACE prototype ommatidia yield a signal acquisition bandwidth of 300 Hz, which is threefold higher than that measured in the ommatidia of fast-flying insects (Laughlin & Weckström, 1993). A high bandwidth contributes to the reduction of motion aliasing during fast locomotion. Furthermore, the implemented read-out protocol (Fig. 3.13) allows a maximum frame rate of 1.5 kfps, which permits frame averaging to improve the signal-to-noise ratio. We experimentally tested CurvACE motion detection capabilities by computing optic flow vectors from visual signals resulting from different types of motion in the presence of random black and white patterns on a wall (Fig. 3.16). In this first experiment, we used a modified version of the Lucas-Kanade method (Lucas & Kanade, 1981; Fleet & Langley, 1995) (*SI Text, Optic Flow Characterization* and Eqs. 3.1-3.9), which is a particularly efficient image-based processing algorithm used to calculate optic flow vectors in two dimensions. The optic flow vectors measured during roll rotation (Fig. 3.7A) and linear translation toward a textured wall 0.3 s before collision (Fig. 3.7B) show coherent patterns of visual rotation and expansion, respectively. The center of rotation and focus of expansion can be clearly identified (red dots in Fig. 3.7), allowing for estimation of the axis of rotation and of the direction of translation, respectively. The sensor egomotion can be estimated from these flow fields, for instance, by implementing matched filters (Franz & Krapp, 2000) analogous to the directionally selective, motion-sensitive neurons found in some insect visual systems (Krapp & Hengstenberg, 1996). Furthermore, the embedded inertial sensors can be used for cancelling the rotational component of the measured optic flow, assessing only the translational component. Because this component is related to distance from objects, the optic flow data provided by a CurvACE prototype could assist mobile platforms to perform collision-free navigation (Floreano et al., 2009).

We also characterized motion detection quantitatively at different ambient light levels with a bioinspired local visual processing algorithm based on the “time-of-travel” scheme (Pichon et al., 1989) (Fig. 3.17). Figure 3.8 shows the angular speed ω_{median} obtained by measuring the rotational optic flow as a function of the yaw rotational speed of CurvACE

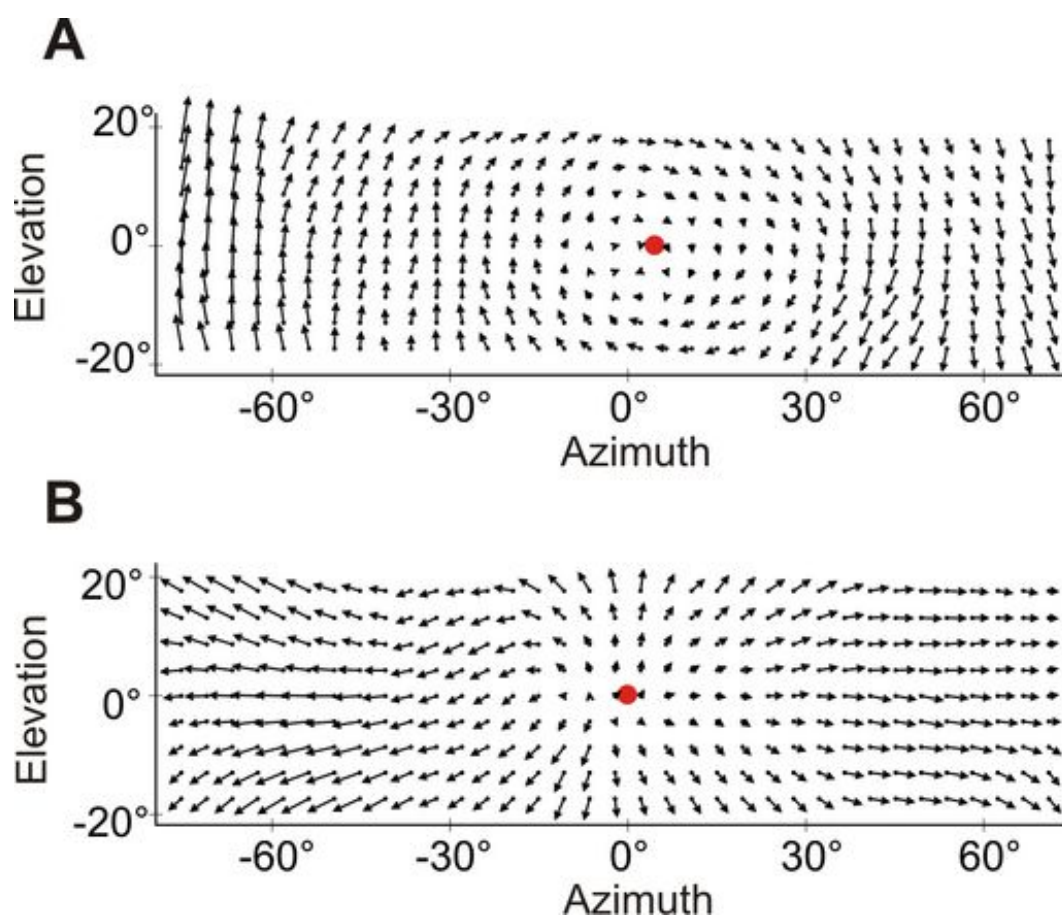


Figure 3.7: Optic flow fields from the CurvACE prototype. Cylindrical equidistant projections of the optic flow field calculated with a modified version of the Lucas-Kanade method (Lucas & Kanade, 1981; Fleet & Langley, 1995) from the visual signals obtained by the CurvACE prototype subjected to roll motion (Fig. 3.16B) at 32° per second and at a distance of about 1 m to a wall displaying random black and white patterns (A) or to linear translation (Fig. 3.16C) at 3 cm/s toward the patterned wall at a distance of 1 cm (B). The red spot displays the center of rotation (A) or the focus of expansion (B).

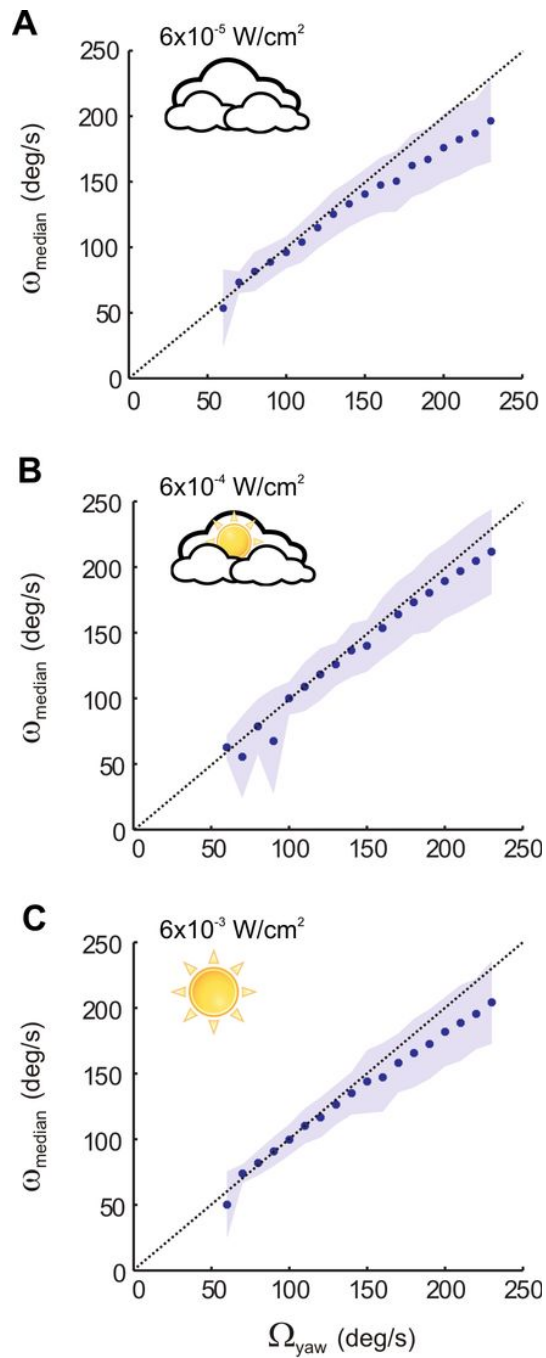


Figure 3.8: Characterization of CurvACE motion detection capabilities. (A-C) Angular speed characteristics of CurvACE calculated with a method based on the time-of-travel scheme (Pichon et al., 1989) (see Fig. 3.17) assessed by applying steps of yaw rotational speed Ω_{yaw} to the sensor at 10° per second, lasting 10 s each, with the prototype placed at the center of a 105-cm diameter arena lined with prints of a natural image. The dashed line displays the theoretical trend.

surrounded by a natural pattern. The experimental data show a good match between the rotational speed perceived by CurvACE and the true rotational speed. The error in the regression coefficient (linearity error) ranges from 5 to 10% (Fig. 3.8) at the three illumination levels, indicating that the CurvACE sensor takes full advantage of its autoadaptive analog VLSI photodetectors to make motion detection largely invariant to different illumination conditions. With the time-of-travel scheme, any pair of neighboring ommatidia driving a “Local Motion Sensor” (LMS) is able to measure angular velocities ranging from 50° to 358° per second for the interommatidial angle of 4.2° with sufficient accuracy. Measurement limitation at lower speeds is due to the signal attenuation brought about by the spatiotemporal processing present in each artificial ommatidium (see Fig. 3.17A).

3.2.5 Discussion

The prototype presented here represents one of many possible manifestations of the CurvACE design principle. It yields a compact, lightweight, energy-efficient, miniature vision sensor that suits a broad range of applications requiring fast motion detection across a panoramic FOV. The applied optical and electronic parameters enable this prototype to measure optic flow patterns caused by sensor egomotion within a contrasted environment. A prototype with these characteristics could be used for autonomous terrestrial navigation, in analogy with some crab species (Zeil & Al-Mutairi, 1996) that use quasicylindrical compound eyes to navigate in flat environments. Furthermore, the hemispherical FOV of the prototype obtained by horizontal bending and by the longer microlens vertical pitch distance resembles the FOV of flying insects (Land & Nilsson, 2002). Thus, such a prototype could also be used in Micro Air Vehicles (MAV) to support a large number of navigation tasks, such as egomotion estimation (Plett et al., 2012), collision avoidance (Franceschini et al., 1992; Blanchard et al., 2000) and flight control (Franceschini et al., 2007; Floreano et al., 2009; Kerhuel et al., 2010), at low and high speeds, even in complex indoor and outdoor environments.

The CurvACE design principle also allows for flexible customization of artificial ommatidia in terms of their number, size, focal length, and interommatidial and acceptance angles, according to the requirements of the intended use. The artificial ommatidia could be further tailored by taking inspiration from the extraordinary eye regionalization found in insects and crustaceans, where specific parts of the compound eye serve specific functions. For example, higher acuity (Horridge, 1978) may be obtained by increasing ommatidial resolution in defined areas, which could be achieved by decreasing both the acceptance angle and the interommatidial angle through redesigned microlenses and a reduced photodetector size with a consequent loss of signal-to-noise ratio. Design variations in the ommatidial optics or photodetector characteristics could yield regions of higher light capture (van Hateren et al., 1989), or different spectral (Franceschini et al., 1981) or polarization sensitivity (Labhart, 1980).

The size of the CurvACE prototype described here is comparable to that of some trilobite eyes (Fig 3.3C) (Fortey & Chatterton, 2003) and some crab eyes (Zeil & Al-Mutairi, 1996), but reaching the diminutive size of insect eyes is challenging because it implies various trade-offs. Increasing the surface density of artificial ommatidia requires decreasing photosensor size, chip circuitry, and microlens diameter at the cost of lower sensitivity and signal-to-noise ratio. Considering state-of-the-art technologies, we have estimated that the CurvACE prototype could be further reduced by a factor of 2. Further increments of surface density via hexagonal arrangement of ommatidia, similar to that found in many insect eyes, may

be possible but would require different cutting methods. In the future, the development of vertical integration of 3D electronic circuits could further reduce the footprint size at the cost of chip thickness.

The CurvACE design opens up new avenues for vision sensors with alternative morphologies and FOVs of up to 360° in small, compact packages. In particular, the realization of a fully cylindrical CurvACE with a 360° FOV in the horizontal plane is relatively straightforward, either by attaching two semi-cylindrical prototypes (Fig. 3.11D) or by fabricating a wider array with a larger number of ommatidia. A CurvACE prototype with a truly omnidirectional FOV, reminiscent of the eye morphology of most flying insects, would be especially interesting for egomotion estimation and better navigational support in three dimensions in a minimal package, providing an advantageous alternative to current cumbersome arrangements based on catadioptric or fish-eye lenses (Floreano et al., 2009). A spherical CurvACE could be realized by fabricating and individually bending several ommatidial arrays with one ommatidium per column along the meridians of a sphere to measure optic flow omnidirectionally.

The CurvACE design is expected to foster further research and applications on fully flexible vision sensors (Daneshpanah & Javidi, 2011; Dobrzynski et al., 2012) that can adapt to rigid or unsteady surfaces of arbitrary shapes. Such devices could function as thin wearable sensors on smart clothing, as sensors for intelligent homes, or integrated in the artificial skin of soft robots. Toward these applications, future work could devise methods for cost-effective mass production of artificial ommatidia, which would also allow more complex dicing to achieve alternative bending patterns. Such production methods may include the realization of all processes of ommatidia alignment and assembly at the wafer level with the help of robotic platforms for automatized pick-and-place, bonding, and dicing.

3.2.6 Supplementary Information

3.2.6.1 Prototype parts and assembly

Optics layer

The generation of the compound eye multiaperture optics involves the formation of a chirped microlens array (lenslet diameter of $172\ \mu\text{m}$) and two chirped aperture arrays (Durré et al., 2005) (Fig. 3.9C). This implies toroidal-shaped lenslets and pitch differences between the layers and the photodetectors on the sensor wafer as well (microlens pitch of $290\ \mu\text{m} >$ photoreceptor pitch of $260\ \mu\text{m}$). The microlenses are formed by reflow of photoresist and subsequent UV molding of a highly transparent polymer (Ormocer, Ormocomp, Micro Resist Technology) (Fig. 3.9A and B). Low-reflective chromium films are used to create two aperture layers, which are deposited by sputtering and patterned by UV photolithography and subsequent metal etching. The optics f-number is 2.4. The resist patterning and UV molding have been carried out using a mask aligner device (Süss Microtec AG)

Photodetector layer

This layer consists of an optoelectronic chip fabricated in silicon at wafer level using CMOS technology ($0.35\text{-}\mu\text{m}$ technology with OPTO option; X-FAB Semiconductor Foundries). Every chip has a size of $20 \times 6.765\text{mm}^2$ and consists of 42 columns, each bear-

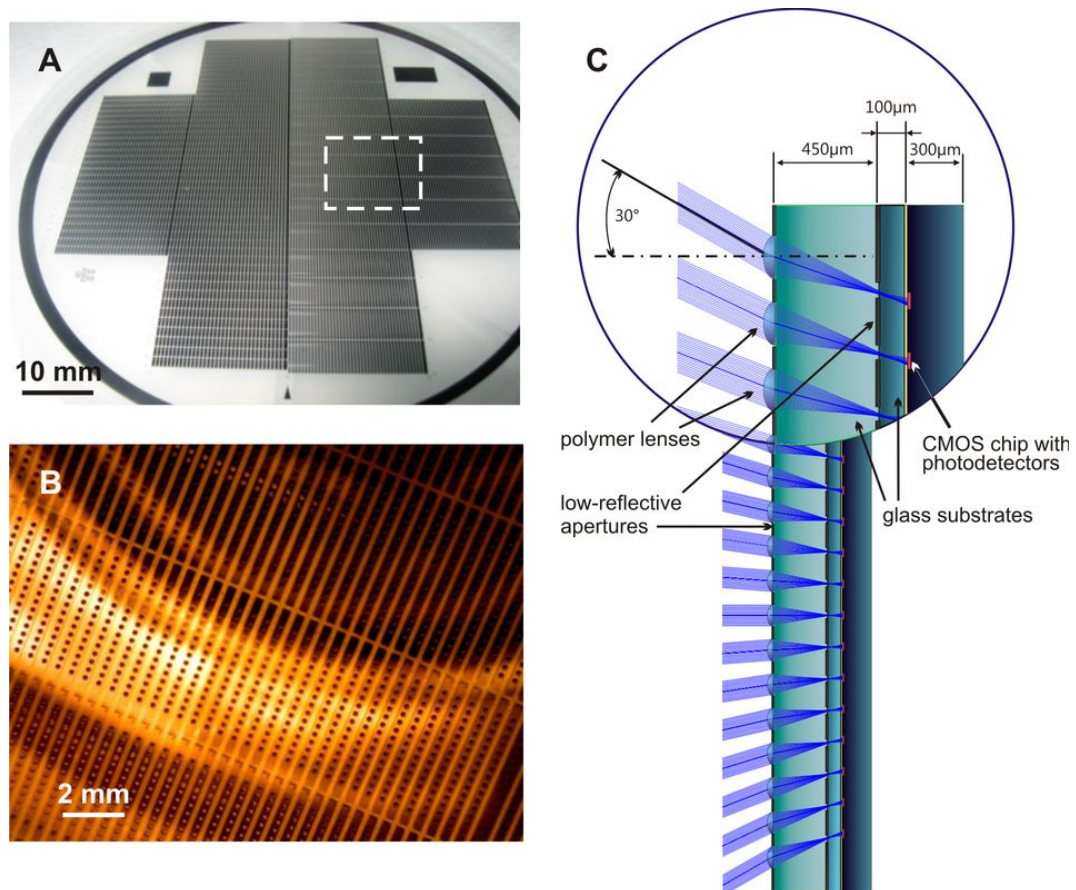


Figure 3.9: Fabrication and design of the compound eye optics. (A) Image of the full-processed optical wafer (AF32; Schott) carrying arrays of aperture patterns and microlenses. Those destined for the presented CurvACE prototypes are placed at the right half of the wafer. (B) Detail of the array wafer area shown in A with a white dashed square. (C) Cross section through an ommatidial column and ray tracing (Zemax; Radiant Zemax, LLC) in the optics layer. The blue rays show the path of the light focused by each microlens on its photoreceptor (red) via two apertures.

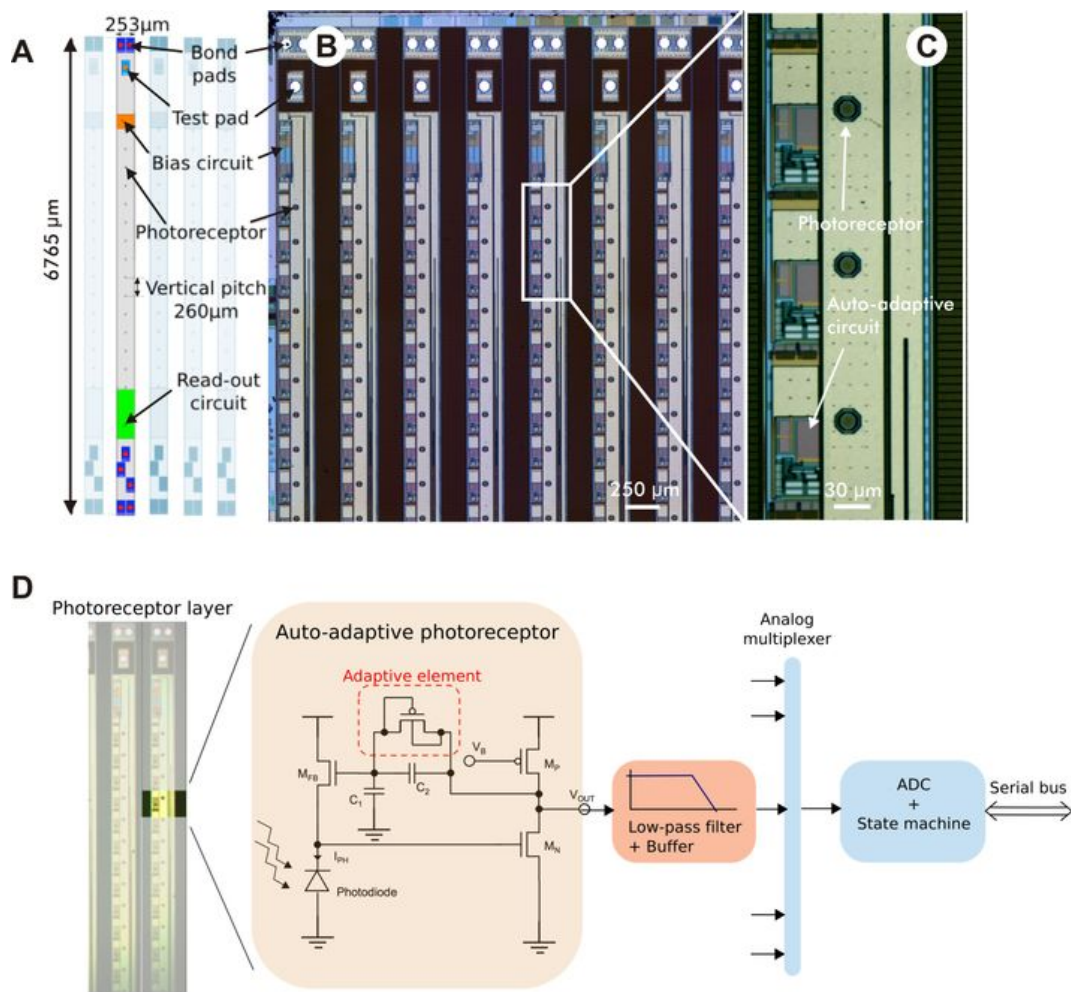


Figure 3.10: Layout of the photoreceptor layer. (A) Schematic layout of a column of the photoreceptor layer. (B) High-definition image of the top part of the columns of the photoreceptor layer. (C) Detail of three octagonal-shaped photodetectors each connected to an adaptive analog VLSI circuit. (D) Basic layout of the photoreceptor processing and read-out architecture implemented within each column of the CurvACE ommatidia. The original circuit proposed by Delbrück and Mead (Delbrück & Mead, 1994) was enhanced here by cascading a first-order low-pass filter to prevent temporal aliasing.

ing 15 VLSI autoadaptive photodetectors, a bias circuit, a 10-bit analog-to-digital converter (ADC) and a logic circuit that implements a serial interface for the read-out protocol (Fig. 3.10).

Every autoadaptive photoreceptor consists of a logarithmic circuit associated with a high-gain negative feedback loop as proposed by Delbrück and Mead (Delbrück & Mead, 1994) (Fig. 3.10D). A MOSFET transistor (M_{FB} in Fig. 3.10D) operates in the subthreshold region where the current-to-voltage characteristic follows a logarithmic law. Thus, the photoreceptor operates over several decades of ambient light level, generating the low-gain direct current operating curve shown as a red dotted line in Fig. 3.6. In addition, transient signals are amplified with a variable gain depending on the equivalent resistance of the adaptive element: The lower the output signal level (V_{out}), the higher is the gain. The autoadaptive feature is used to compensate for ambient light changes, that is, to keep the photodetectors responding to contrasting features even in intense ambient lighting. The overall bandwidth of the photoreceptor depends on the current (I_{ph} in Fig. 3.10D) flowing into the photodiode and on the time constants of the amplifier stage. For high ambient lighting levels, the bandwidth can be as large as 500 kHz. To prevent aliasing during the digitization process, we deliberately enhanced the circuit by limiting the bandwidth of each photodetector to about 300Hz by cascading it with an antialiasing filter, consisting of a first-order low-pass filter based on a transconductance amplifier. To limit the dispersion due to the CMOS technology, we finely adjusted the ratio between the two capacitors (C_1 and C_2 in Fig. 3.10D) to minimize the transient gain dispersion of the photodetectors.

Every photoreceptor column bears a multiplexer and a 10-bit ADC with a conversion time of 15 μs . The analog signal of the 15 photodetectors is sequentially converted by the multiplexed ADC and sent to the microcontroller unit through a synchronous serial interface.

Printed Circuit Boards (PCBs)

Interconnection layer

Printed circuit boards (PCBs) are used to connect the different electronic components of the curved artificial compound eye (CurvACE) electrically while ensuring their mechanical support. In the case of the ommatidia interconnection layer, a polyimide (Kapton) one-layer PCB with a thickness of 100 μm is used. The low thickness and the absence of vias allow curving the ommatidia down to the required 6.4-mm radius of curvature (ROC). The middle part of the PCB is left empty of tracks because that is the position where the photoreceptor layer is placed. Tracks for analog and digital power and ground, as well as for clock, sync, and digital data read-out, are routed to operate all columns (read-out protocol is shown in Fig. 3.13).

Rigid internal PCBs

The CurvACE prototype bears two rigid PCBs that, in addition to the interconnection layer of the artificial ommatidia, provide mechanical and electrical support to the internal electronic components. They are made of FR-4 (fiberglass with epoxy resin), have a nominal thickness of 0.5mm, and are placed in the concavity of the sensor and perpendicular to the flex PCB. They are electrically connected to the artificial ommatidia by connecting pads

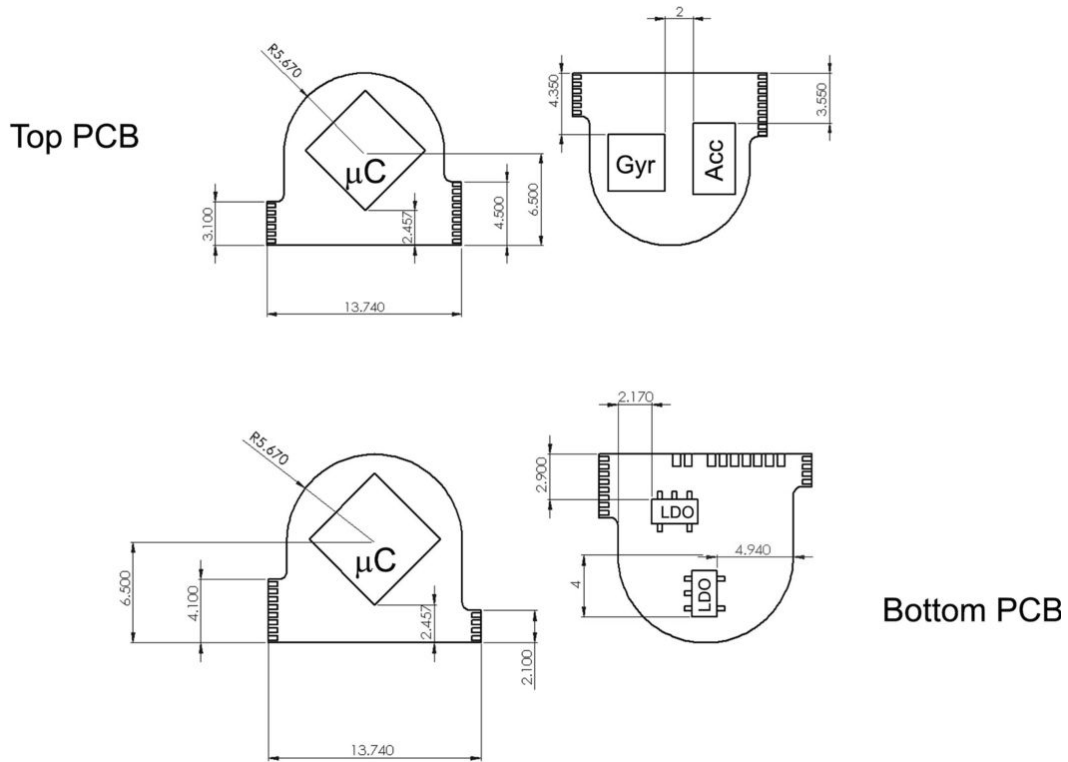


Figure 3.11: Scheme of the two rigid PCBs showing their electronic components assembled. Acc, accelerometer; μC , for microcontroller; Gyr, rate gyroscope; LDO, low-drop-out voltage regulator. The top side (Left) and bottom side (Right) of the PCB are displayed. The dimensions are in millimeters.

placed along their edges (Fig. 3.11). Both rigid PCBs are also interconnected electrically via those connecting pads through tracks designed along the outer side of the interconnection layer.

The used electronic components of the CurvACE prototype are soldered onto these rigid PCBs. More precisely, the microcontrollers of model dsPIC33FJ128GP802 (Microchip Technology) are soldered on top of each PCB. Two inertial sensors, a three-axis accelerometer MMA7455L (Freescale Semiconductor), and a three-axis rate gyroscope ITG-3200 (InvenSense) are placed at the bottom side of the top PCB. Two low-drop-out voltage regulators EXAR-SP6201EM5-L-3-3 (EXAR) and the external connector lie at the bottom side of the bottom PCB (Fig. 3.12).

Ommatidia Assembly Process

Bonding

The alignment and glue bonding assembly of the three artificial ommatidia layers is done via a Fineplacer device (Finetech GmbH & Co. KG, Berlin, Germany) that yields a precision down to $1 \mu m$. The glue bonding between the optics and photoreceptor layers is realized with a high-transparent UV-curing adhesive EPOTEK OG 146 (Epoxy Technology Inc., Billerica, MA). To improve the bonding strength, a silane-based adhesion promoter has been applied to both surfaces before gluing. The glue bonding between the photoreceptor and

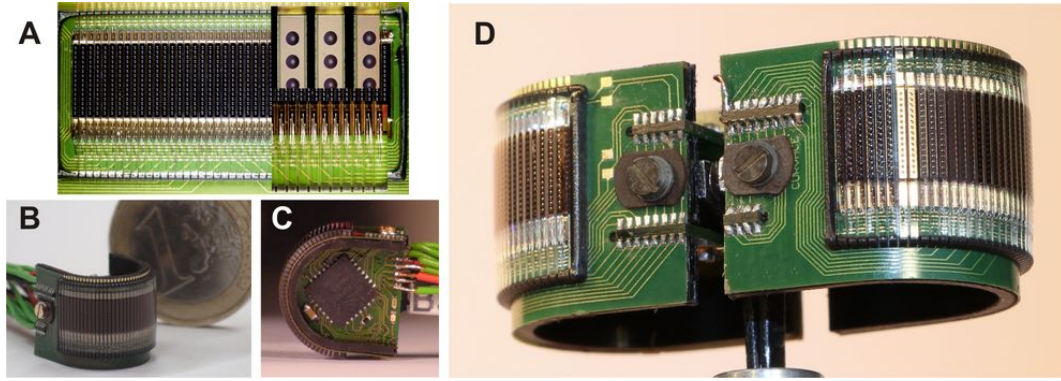


Figure 3.12: CurvACE ommatidia and prototype assembly. (A) Image of the planar ommatidial array just after assembly and column dicing. (Right Inset) Details of the microlens array surface, as well as the wire bonding between the photoreceptor and the interconnection layers, are shown. Perspective image of the CurvACE prototype (B), top view (C), and configured to provide a 360° field of view (FOV).

the interconnection layer is realized applying a thermally curing adhesive EPOTEK353ND. The photoreceptor layer is electrically connected with the interconnection layer by wedge bonding with aluminum wires of 30 μm . The wires are protected with a transparent glob-top material (Fig. 3.12A).

Intercolumn dicing

The dicing of the bonded optics and photoreceptor layer in 42 columns is realized by an automatic dicing setup (DISCO Corp.). A special 100- μm thick synthetic-resin compound dicing blade for rigorous and brittle materials was applied for trenching and dicing the columns.

Prototype assembly

A rigid and hard internal scaffold fabricated in polyoxomethylene by five-axis milling with CNC technology is used as mechanical support of the CurvACE PCBs. For the prototype assembly, the artificial ommatidia supported by the flex PCB are bent and placed onto the curved outer side of the scaffold, which bears the required ROC of 6.4 mm, and are subsequently fixed. The rigid PCBs, bearing the microcontrollers and inertial sensors soldered (Fig. 3.11), are introduced in the cylinder concavity along two mechanical guides in the scaffold. Subsequently, the rigid PCB side pads are soldered to the ommatidia flex PCB end pads.

Read-Out interface

The CurvACE prototype uses a serial direct connection protocol as a read-out interface to communicate with the controller units (Fig. 3.13). It consists of a unique clock signal sent to each ommatidial column, two sync signals used to start the ADC conversion of the associated columns, and a digital signal per column used for the serial transfer of each ommatidium output signal. The clock and sync signals are emitted by the embedded microcontrollers, which also collect the output data for processing. With a clock frequency of 1 MHz and an ADC conversion time of 16 μs for each ommatidium, the maximum frame rate that can

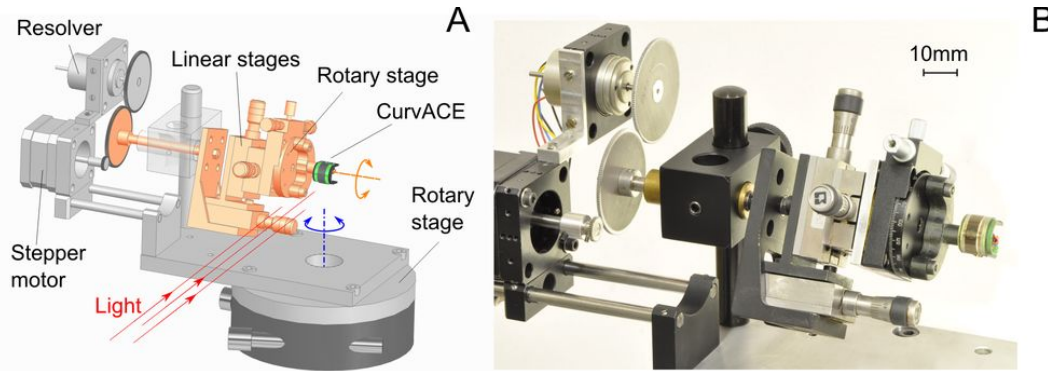


Figure 3.14: Setup for the measurement of the angular sensitivity function (ASF) of CurvACE ommatidia. (A) Computer-aided design (CAD) of the characterization bench configured for characterizing the horizontal ASF of a row of ommatidia placed in front of a point light source. The stepper motor rotates the sensor slowly about the horizontal axis (double circular orange arrow), whereas the resolver measures the actual angular position with a resolution of 0.08° . To select the row to be characterized, a second rotary stage (double circular blue arrow) allows the CurvACE to be oriented accurately with respect to the point light source. (B) Photograph of the CurvACE mounted at the tip of the characterization setup.

by a diaphragm with a diameter of 1 mm, is placed at a distance of 2.8 m from the photodetectors to illuminate them from a predetermined direction. Stepper motor control, angular measurements, and signal acquisition from the CurvACE are achieved through a LabVIEW NI Embedded Software Evaluation Toolkit (National Instruments). The obtained signal, which represents the ommatidia ASF shown in Fig. 3.5A and D, has been smoothed by means of a low-pass filter.

Light sensitivity characterization

We developed a programmable light box able to create an illuminance varying between 1 and 10,000 lux at a distance of 3 cm, where the CurvACE prototype was placed. The light intensity could be digitally adjusted through an RS232 bus. This highly controlled light environment allows the response of an ommatidium (photodetector with optics) to be measured both as a function of the steady illuminance and as a function of incremental and decremental light steps presented about the steady illuminance (Fig. 3.15). Very low illuminance values were obtained by means of an additional neutral density glass filter (thickness of 2 mm, optical density $OD = 2$, HG3; Schott) placed between the LED (TLWR7600; Vishay) and the CurvACE prototype. An additional digital input signal sent by the FPGA software was used to synchronize the changes in light intensity with the CurvACE readout. The irradiance of the light source was measured by means of a radiometer (ILT1700, International Light Technologies Inc., Peabody, MA), whose probe was placed at a distance of 28 mm from the light source.

Optic flow characterization

Optic flow was extracted from the CurvACE sensor by subjecting it to different kinds of motion while acquiring the photoreceptor signals on a personal computer. For this, the sensor was mounted at the tip of a mechanical arm, allowing for its free positioning and orientation (Fig. 3.16A). Two different setups are used. To impose a rotational motion, the

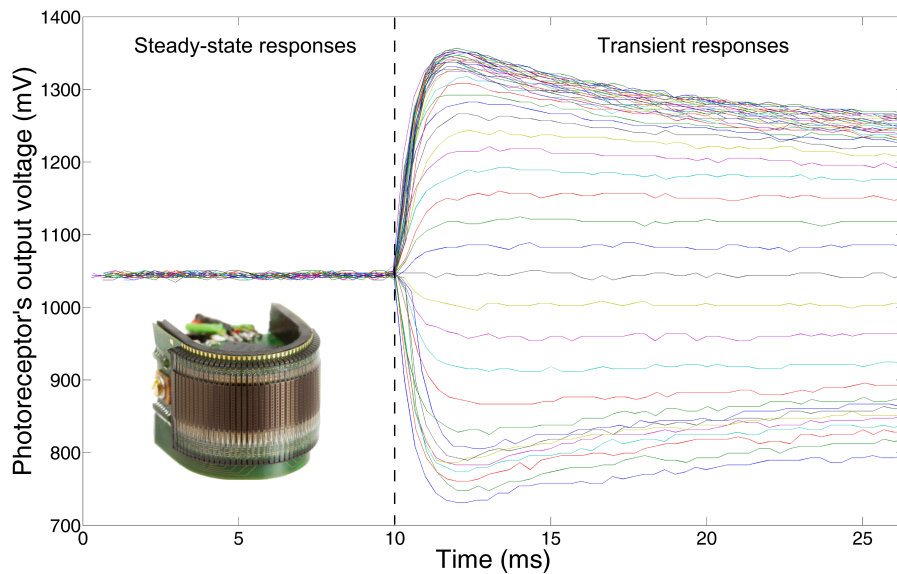


Figure 3.15: Step responses of a single artificial ommatidium (photodetector with optics) in response to incremental and decremental light steps (51 steps) applied at $t=10\text{ms}$ (vertical dotted line). The ommatidium output signal was digitized at a sampling frequency of 3kHz. The steady-state value (red circles in Fig. 3.6) was acquired 20 s after the steps were applied. Each of the four dynamic operating curves (green points in Fig. 3.6) plots the peak amplitude of the step responses of the ommatidium output signal as a function of $\log I$.

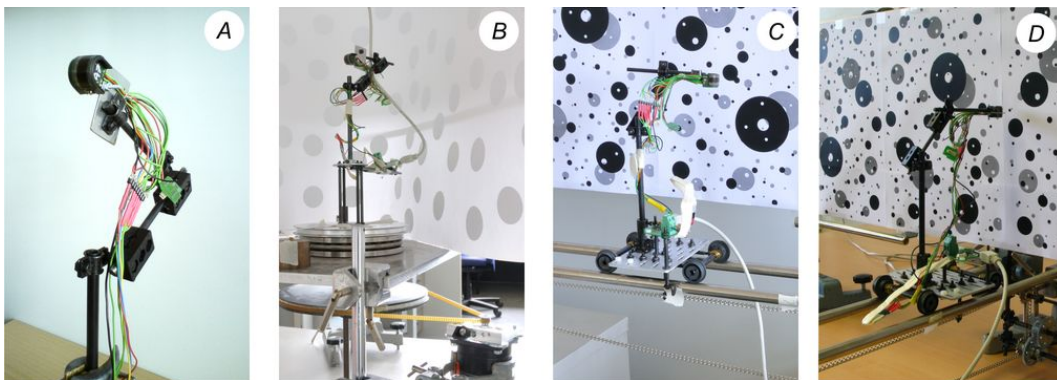


Figure 3.16: Setup for the rotation and translation experiments. (A) Mechanical arm holding the CurvACE sensor. (B) Motor-driven rotary table used for testing the ability of the CurvACE to extract rotational optic flow. Motor-driven carriage to test the ability of the CurvACE to extract panoramic translational optic flow along a corridor (C) and toward a wall (D).

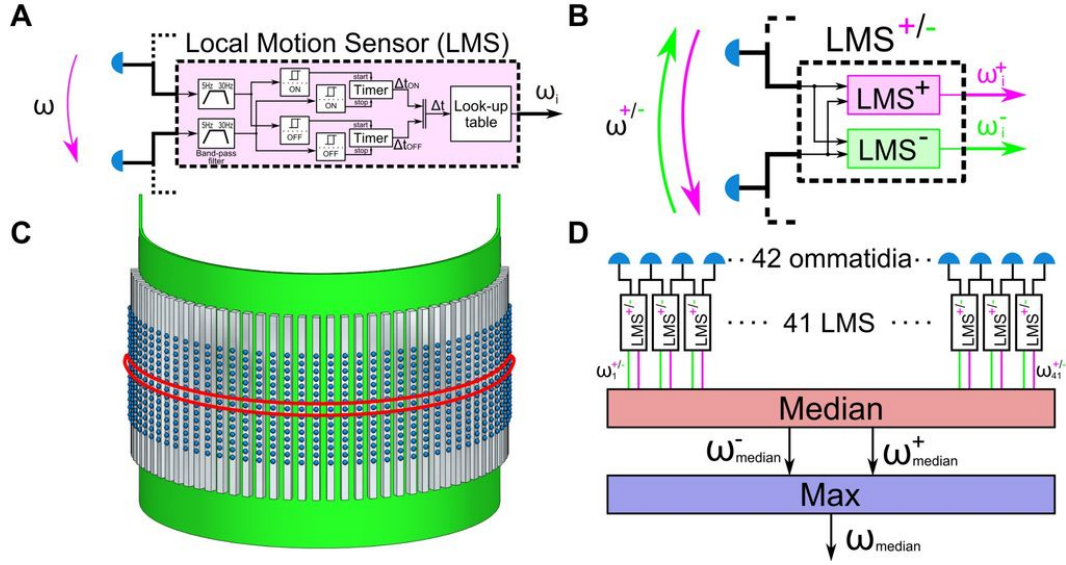


Figure 3.17: Visual motion measurement along one dimension. (A) General processing architecture of an LMS driven by two adjacent ommatidia and taking into account both ON and OFF contrast transitions. (B) Scheme of angular speeds observed by the LMS in opposite directions. (C) Scheme highlighting the central row of ommatidia in the CurvACE prototype, where the visual signals for yaw motion computation were extracted (Fig. 3.8). (D) Scheme of the statistical calculation of the observed angular speed. Max, maximum.

prototype sensor is mounted on a rotary table surrounded by a patterned cardboard. The rotary disk is driven by a stepper motor at a fixed rotational speed between 4.5° and 40° per second (Fig. 3.16B). For imposing a translational motion, the sensor is mounted on a carriage driven by a stepper motor via a tension chain. Fig. 3.16C shows the carriage on rails passing by a textured wall. For the flow pattern shown in Fig 3.7B, the sensor was frontally approaching a wall showing the same texture.

For the experiments in translation, and roll rotation (Fig. 3.7), we used a noniterative, gradient-based multiframe optic flow extraction method derived from the one developed by Lucas and Kanade (Lucas & Kanade, 1981) and inspired by the work of Fleet and Langley (Fleet & Langley, 1995). Before computation, a bias in the response of the CurvACE ommatidia is removed to improve gradient calculation. The algorithm is derived from the optic flow constraint

$$I_x u + I_y v + I_t = 0 \quad (3.1)$$

which can be derived from the image brightness constancy assumption using first-order Taylor expansion. Here, (u, v) is the flow vector and I the image function, with subscripts denoting partial derivatives. A spatiotemporal weighted least-squares solution at time t over the image patch P is given by

$$\min \sum_{i=0}^{\infty} \sum_{x,y \in P} \omega(i) (I_x(x, y, t-i)u + I_y(x, y, t-i)v + I_t(x, y, t-i))^2 = 0 \quad (3.2)$$

with $\omega(i) = (1 - \alpha)\alpha^i$ defining the exponential weighting function in the time domain. This can be solved by

$$(u, v) = G^{-1}A \quad (3.3)$$

$$G(t) = \sum_{i=0}^{\infty} \omega(i)G'(t-i) \quad (3.4)$$

$$A(t) = \sum_{i=0}^{\infty} \omega(i)A'(t-i) \quad (3.5)$$

$$G'(t) = \sum_P \nabla I \nabla I^T \quad (3.6)$$

$$A'(t) = \sum_P I_t \nabla I \quad (3.7)$$

which leads to the iterative solution

$$G(t) = (1 - \alpha)G(t-1) + \alpha G'(t) \quad (3.8)$$

$$A(t) = (1 - \alpha)A(t-1) + \alpha G'(t) \quad (3.9)$$

Using a temporal filter scheme allows to use a smaller integration window. The temporal filter value α was set to 0.04. The size of the integration window for the results shown is a 5x5 ommatidia patch. For the gradient computation, we use the kernel [-1,0,1]. Thus we require a single additional ommatidium at each border of the 5x5 integration window for optic flow computation, getting a total of 45 ommatidia. The size of the integration window and the gradient kernel limits the area for flow computation, because we wanted to avoid special cases at the border. With the given parameters, we have a border of three ommatidia where no optic flow can be computed.

For the experiments aimed at assessing CurvACE ability to extract optic flow in various light environments (Fig. 3.8), we used an optic flow extraction method based on a time-of-travel scheme (Pichon et al., 1989). Photoreceptor signals are acquired from the equatorial row of ommatidia (Fig. 3.17C). Any two neighboring ommatidia drive a local motion sensor (LMS). The two spatially low-pass-filtered photodetector signals are temporally band-pass-filtered, and a hysteresis threshold is then set on each channel to determine the time Δt elapsed between their excitations. The local angular speed ω_i is then obtained simply via a look-up table, which calculates the ratio between the interommatidial angle $\Delta\varphi_i$ and the time lag Δt_i (Fig. 3.17A). Following the results obtained on fly motion-sensing neurons (Franceschini et al., 1989; Eichner et al., 2011), the LMS is actually split into two parallel and independent channels dealing each with either the “ON” or the “OFF” component of the moving contrast (Fig. 3.17B). Furthermore, each pair of adjacent ommatidia actually drives two LMSs of opposite directions (+/-) that process ω_i^+ and ω_i^- , respectively. Because the angular speed of contrasting features moving in the preferred direction is always higher than that measured in the nonpreferred direction, the magnitude of the optic flow vector ω_{median} is measured from the maximum between the median value ω_{median}^+ and ω_{median}^- of all possible LMS outputs in the equatorial row.

Variation of the interommatidial angle $\Delta\varphi_h$ with the elevation angle

$$\Delta\varphi_h = \arccos(1 + \cos^2(\alpha)(\cos(\Delta\varphi_{hmax}) - 1)) \quad (3.10)$$

Due to the hemispherical field of view of the CurvACE sensor (Fig. 3.3B), the horizontal interommatidial angle $\Delta\varphi_h$ gradually decays with the elevation angle α (Fig. 3.5B) according to Equation 3.10, with $\Delta\varphi_{hmax}$ being the interommatidial angle at the equator ($\Delta\varphi_{hmax} = 4.2^\circ$ in our prototype) and α ranging from -30° to 30° in our prototype.

3.3 Conclusion

We have seen in this chapter that we succeeded to design a fully functional artificial compound eye, composed of a micro-lens array integrated with adaptive photoreceptors made of analog Very-Large-Scale-Integration circuits on flexible electronic substrates. The cylindrical prototype of this sensor features a very large Field of view ($180^\circ \times 60^\circ$) and is able to extract motion over several decades of background illuminance with a limited computational power.

All these characteristics make the CurvACE sensor highly suitable to be used onboard autonomous Micro-Aerial Vehicles where the weight, the computational power and the energy are strongly limited. However, it is currently too costly for mass production due to the numerous dicing stages of the fabrication process.

Chapter 4

BeeRotor: a visually guided bio-inspired robot

Inspired by several behavioral experiments performed on flying insects during the past decades, we developed a new tethered aerial robot of only 80 grams called BeeRotor that can explain how flying insects can so gracefully navigate in an unknown environment with their limited sensor suite and computational processing. In particular, the main idea during the design of this tandem rotorcraft was that flying insects mainly rely on vision and it has never been demonstrated that they were equipped with sensors allowing them to determine their attitude in the inertial frame like a gravity sensor. Although insects can use outdoors celestial cues and the polarization of light to estimate their orientation, their sensory modalities do not give them any information about their attitude, their altitude or their forward speed indoors.

Similarly, the BeeRotor robot has been equipped with a limited sensor suite:

- a quasi-panoramic eye processing the optic flow over a large field of view like the compound eye of insects,
- a rate gyro, which, similarly to the halteres of Diptera, is sensitive to the Coriolis forces,
- a custom-made anemometer sensitive to the airspeed like the antennas and hairs of insects.

Endowed with these sensory modalities and new bio-inspired visually guided strategies, the tandem rotorcraft is the first one able to navigate in a complex and non-stationary environment without the need of an accelerometer. A detailed description of the BeeRotor aircraft is given in appendix B.

The first results of the BeeRotor robot are presented in Expert & Ruffier (2012) where the pitch angle of the robot is controlled by the main microcontroller using a servomotor placed on the pantographic arm. In this configuration, the pitch angle and therefore the forward speed of the aircraft can be controlled accurately.

From these first experiments, we were able to show the reliability of an autopilot composed of two feedback loops based only on the ventral and dorsal optic flows and driving the thrust of the propellers and therefore the altitude and the robot pitch and therefore its forward speed. To simplify the whole experiment, the eye of the robot was fixed following the robot pitch angle and the environment was obstacle free and stationary.

This study showed how by regulating the optic flow generated by the closest wall and the sum of the ventral and dorsal optic flows, the BeeRotor robot automatically followed the closest surface at a safe height and forward speed. Depending on the closest detected surface at the beginning, in this obstacle free environment, the aircraft always kept following the same wall at an altitude and speed only depending on the two chosen optic flow setpoints for the two feedback loops. The rotorcraft also proved to be able to automatically land or dock with a forward speed and a distance with the followed wall decreasing simultaneously until smoothly landing or docking with almost no speed at touchdown.

Article 5: Autonomous optic flow-based speed control, ground-hugging and landing without any need for an accelerometer

Satisfied from the first results of the BeeRotor robot, we removed the servomotor controlling the pitch angle of the aircraft which was then controlled by the differential speed of the propellers. The tethered robot pilots therefore 4 degrees of freedom: heave, surge, pitch and the decoupling between its body and its quasi-panoramic lightweight (13.5-g) visual system.

To control its forward speed and its clearance from the walls thanks to optic flow, the BeeRotor robot tends to constantly keep its gaze parallel to the nearest surface thanks to a Least Squares approximation measuring the angle between the eye and the surface from the optic flow measurements.

In this article, we show that, without any need for an accelerometer or information about the robot's pitch, altitude or groundspeed, the aircraft autonomously avoids obstacles even in a moving environment and adjusts its forward speed depending on the size of the tunnel based only on optic flow, airspeed and pitch rate measurements. Without its airspeed sensor, the aircraft proved also to robustly control its altitude and forward speed but its performances were slightly degraded. As far as we know, this robot is the first rotorcraft able to control its speed and altitude based only on measurements defined in a frame of reference attached to the eye of the robot.

Finally, the robot proved to be able to automatically dock on the ceiling or land on the ground by simply regulating its dorsal or ventral optic flow while pitching backward which gradually reduces its forward speed. Two different strategies relying on optic flow have been proposed and tested showing that the aircraft can autonomously land or dock smoothly with almost no speed at touchdown.

Autonomous optic-flow based speed control, ground-hugging and landing without any need for an accelerometer¹

Authors: Fabien Expert and Franck Ruffier.

4.1.1 Abstract

Inspired by recent findings on insects, we developed a bio-inspired tandem rotorcraft called BeeRotor mimicking optic flow-based behaviors and flying in the vertical plane in a high-roofed tunnel depicting natural scenes. This tethered miniature robot (80g) is endowed with 4 degrees of freedom: heave, surge, pitch and the decoupling between its body and its 13.5-g quasi-panoramic visual system made of only 24 pixels coupled to visual motion sensors. To pilot its eye pitch, the BeeRotor robot tends to constantly visually realigns its eye in parallel to a novel reference: the orientation of the followed surface. Two optic flow regulators control its altitude via its lift produced by the tandem rotors and its forward speed via the pitch produced by the speed difference between the tandem rotors. The BeeRotor robot is able to perform complex tasks such as ground and ceiling hugging and speed control in the presence of a rugged or unstationary environment: such performance is achieved without accelerometer and without any estimation in the inertial frame of its pitch, its altitude or its groundspeed. Its robustness is shown even in the absence of the airspeed sensor or when strong perturbations were applied on the aircraft.

4.1.2 Introduction

Micro Aerial Vehicles (MAVs) of the future will have to navigate autonomously in cluttered and highly changing environments and therefore be able to cope with any unpredictable event. Such risky tasks may require novel sensors and control methods that differ from conventional approaches where all the states of the vehicles are estimated. Ethological findings have shown that complex navigation tasks such as terrain following (Kennedy, 1951; Kuenen & Baker, 1982) and speed control (Preiss & Kramer, 1984; Srinivasan et al., 1996) are performed by flying insects on the basis of optic flow (OF) cues, although insects' compound eyes have a very poor spatial resolution.

In particular, recent studies in insects have shown that the ventral (Baird et al., 2006; Barron & Srinivasan, 2006; Portelli et al., 2010) and dorsal (Portelli et al., 2011) optic flow (OF) plays an important role in altitude control. In (Portelli et al., 2010), authors used a tunnel with a moving floor and recorded the height of flying honeybees over the stationary floor and the moving floor. They observed that when flying over the moving floor, which moved in the same direction as their flight, honeybees descend to a lower height in order to

¹Expert, F., and Ruffier, F.(in prep). Autonomous optic-flow based speed control, ground-hugging and landing without any need for an accelerometer.

restore the ventral optic flow to the same value to that they had perceived when flying over the stationary part of the floor. The fact that they lowered their height of flight instead of increasing their forward speed is consistent with the optic flow regulator hypothesis proposed in (Ruffier, 2004; Ruffier & Franceschini, 2005; Franceschini et al., 2007).

Other studies have shown that the visually perceived optic flow is used by honeybees to control their forward speed (Srinivasan et al., 1996; Baird et al., 2006; Fry et al., 2009). In particular, Srinivasan et al. proved that honeybees reduced their speed when flying in a narrowing corridor and their forward speed increased when the corridor was widening (Srinivasan et al., 1996). Baird et al. showed, in a tunnel with moving lateral walls, that when the walls were moving in the direction of flight (decreasing the perceived optic flow), flight speed increased and reciprocally (Baird et al., 2006). These two studies led to the conclusion that “the bees adjusted their flight speed so as to hold the speed of the image on the retina constant” which has been confirmed to be true in both the horizontal and the vertical planes (Portelli et al., 2011). In insects, antennae are thought to play an important role in the control of flight speed. Amputating the antennae of free-flying insects provides direct evidence that they are involved in flight control as we observe a decrease in the forward speed of diptera with antennae amputation (Campan, 1964; Burkhardt & Gewecke, 1965). However, it is not quite clear if the antennae are sensing the airspeed or the changes in airspeed (Taylor & Krapp, 2007).

It was recently established in experiments on tethered *Drosophila* that these insects strongly avoid the focus of expansion (FOE) due to the vicinity of an object (Tammero et al., 2004) which is, as Reiser and Dickinson pointed out, paradoxical as “in order to move forward an animal must tolerate a frontal FOE as it navigates through a visual landscape” (Reiser & Dickinson, 2010). This can be explained by the fact that this collision avoidance reflex is overridden by an attractive target (Reiser & Dickinson, 2010). For the altitude control, it has been recently demonstrated that a similar ventral expansion avoidance system exists in the brain of insects (Straw et al., 2010).

Based on behavioral studies on honeybees (Srinivasan et al., 1996, 2000), authors started to use optic flow (i) to perform docking with wheeled robots (Santos-Victor & Sandini, 1997; McCarthy & Barnes, 2012), (ii) to land automatically on rotorcrafts (Chahl et al., 2004; Ruffier & Franceschini, 2005; Zufferey et al., 2010; Kendoul et al., 2010; Herisse et al., 2010, 2012; Expert & Ruffier, 2012) and on fixed-wing Unmanned Aerial Vehicles (UAVs) (Green et al., 2004; Zufferey et al., 2010), (iii) to avoid obstacles (Iida, 2001; Green et al., 2004; Ruffier & Franceschini, 2005; Griffiths et al., 2006; Zufferey & Floreano, 2006; Ruffier & Franceschini, 2008; Beyeler et al., 2009), (iv) to hover (Herisse et al., 2008; Kendoul et al., 2009), (v) to track a moving target (Viollet & Franceschini, 2001; Kerhuel et al., 2010), or (vi) to follow a terrain (Garratt & Chahl, 2008).

A few years ago, a biomimetic autopilot called OCTAVE (which stands for Optical altitude Control sysTem for Autonomous VEhicles) based on a ventral OF sensor was developed and integrated into a feedback loop driving a robot’s lift to compensate for any deviations of the OF sensor’s output from a given setpoint (Ruffier & Franceschini, 2003; Ruffier, 2004; Ruffier & Franceschini, 2005; Franceschini et al., 2007): this simple autopilot enabled a miniature helicopter to perform challenging tasks such as takeoff, terrain following, reacting suitably to wind and landing. Based on behavioral findings on bees (Serres et al., 2008), authors recently developed a vision-based autopilot called ALIS (which stands for Autopilot using an Insect based vision System) (Portelli et al., 2010) based on this concept of optic flow regulators (Ruffier & Franceschini, 2003, 2005) and that of intertwined feedback

loops (Serres et al., 2008; Roubieu et al., 2012) controlling respectively the position and the forward speed of an “artificial bee”.

Here we present the latest results of a tethered lightweight (80-gram) tandem rotorcraft called BeeRotor, which is equipped with a quasi-panoramic visual system capable of assessing the ventral and dorsal optic flows in an indoor environment showing natural contrasts. In a previous study (Expert & Ruffier, 2012), we showed how this aircraft can perform complex tasks such as ground and ceiling following, while automatically adjusting its forward speed based on two feedback loops driving the robot’s pitch angle and the lift. However, the pitch angle of the robot was controlled using an external servomotor attached with a vertical reference. In this study and for the first time, a tandem rotorcraft’s altitude and forward speed are controlled using only visual information, an airspeed sensor and a rate gyro. As the rotorcraft is not using the information of an accelerometer, no attitude estimation and no absolute reference are used onboard: the aircraft almost exclusively relies on optic flow to always maintain a safe distance from the ground and the ceiling and adapting its speed to the height of the high-roofed tunnel, as honeybees have been found to do (Portelli et al., 2010, 2011). To do so, the BeeRotor robot is equipped with a quasi-panoramic eye decoupled from its body similarly to the head of insects which is controlled actively by no less than 23 pairs of muscles (Strausfeld et al., 1987). This decoupling, which has proven in a recent study that it could help an aerial robot to hover (Manecy et al., 2012), is used here to always orient the eye parallel to the closest surface. Here, we show how the BeeRotor robot can automatically land by controlling the forward speed of the aircraft in order to maintain a specific value of the Vertical OF which depends on its “vertical” velocity.

In Section 4.1.3, the visuomotor control loops used to control the horizontal speed and the altitude of the BeeRotor robot are described and the optic flow-based strategies to pilot the aircraft whose unique reference frame is attached to its eye are explained. Section 4.1.4 describes the aeromechanical and electrical design of the BeeRotor robot equipped with a quasi-panoramic eye and the 12-m long experimental environment in which the flying robot was tested. The performances of the BeeRotor robot during autonomous flights are presented in Section 4.1.5. Section 4.1.6 focuses on the performances of the BeeRotor robot without airspeed sensor and in particular its ability to follow terrain and land. Finally, Section 4.1.7 describes the Vertical OF and presents how it can be used to contribute to the altitude control or to perform an automatic landing.

4.1.3 OF-based strategies defined in a unique reference frame attached to the aerial robot’s eye

In many species of flying insects, the ocelli are thought to act as horizon detectors and to be responsible of the dorsal-light response which compensates for attitude changes by fast head and body movements like it has been demonstrated on Diptera (Schuppe & Hengstenberg, 1993). Besides, the dorsal rim area of the compound eye of the dragonfly is known to be sensitive to sky light polarization and be used as a natural compass. Although these two behaviors enabling flying insects to determine their attitude or absolute orientation are probably helpful to control their flight outdoors, insects are still able to fly in indoor environments where no horizon can be detected and the polarization of light can not be used to determine its orientation relatively to the sun. Except these two reflexes, no behavior in flying insects seem to indicate that they estimate their attitude, altitude or ground speed to control their flight. In particular, no sensor like accelerometers have been found in insects

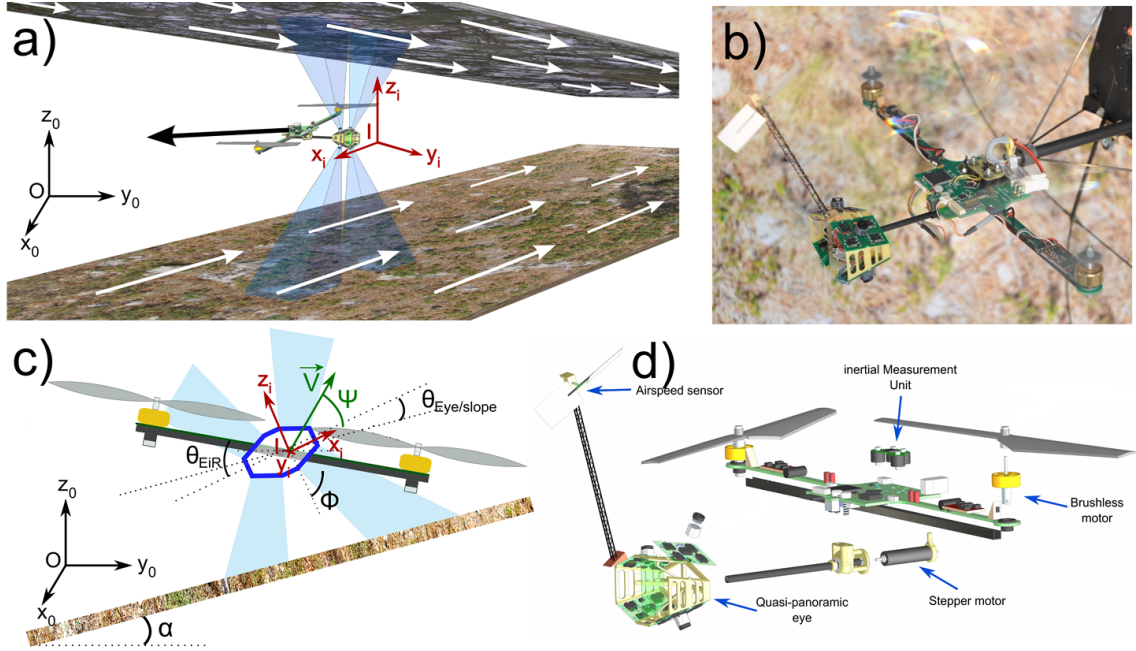


Figure 4.1: **a)** CAD drawing of the aircraft flying in a high-roofed tunnel depicting natural scenes. Due to motion of the aircraft, ventral and dorsal optic flows are generated that can be measured by the eye of the robot. In this study, the robot has no knowledge of any measurements in the inertial frame of reference $(0, x_0, y_0, z_0)$ as all the processing is based on measurements performed in the frame of reference attached to the eye of the robot (I, x_I, y_I, z_I) . **b and d)** Photograph and CAD of the 80g BeeRotor robot. The main electronic board called the body is composed of two elongated arms connected to two propellers controlled by Brushless outrunner motors. Most of the processing is carried out by the main electronic board which collects the information coming from the rate gyro of the Inertial Measurement Unit, the custom-made airspeed sensor, the magnetic sensor measuring the angle of the eye relative to the body and the quasi-panoramic eye. The rotorcraft has four degrees of freedom: the mean propellers' speed controls the elevation of the aircraft, the differential propellers' speed acts on the pitch angle and therefore determines the forward speed of the robot and a lightweight stepper motor coupled with a $\frac{1}{120}$ reductor is used to orient the eye relatively to the body. This quasi-panoramic eye, which is set apart from the main board to prevent the visual field from being occluded by the propellers, is composed of 4 visual motion sensors sampling the visual environment with a 4×24 -deg Field-Of-View. As we can see, the tandem rotorcraft is tethered to a pantographic arm but it is autonomous in terms of its computational and signal processing power requirements. **c)** Definition of the angles of the robot. The angle of the eye relatively to the body θ_{EiR} is measured thanks to a magnetic sensor and the angle $\theta_{Eye/Slope}$ representing the angle between the eye's equator and the slope of the closest surface is estimated thanks to the optic flow (see section 4.1.3.3 for the details about the method). The aircraft is assumed to be flying at a velocity \vec{V} in the direction Ψ (Ψ is the angle between the direction of the speed vector and the eye's equator). As we will see in section 4.1.4.6, the eye of the aircraft like the compound eye of insects is composed of several local motion sensors. Each of them has an elevation angle Φ with the perpendicular with the eye's equator.

allowing them to sense their own body orientations. Inspired by these observations, our aim was to build a robot whose reference frame is only attached to its eye (I, x_I, y_I, z_I) to test visually guided strategies based on optic flow measurements. Equipped with similar sensory modalities as flying insects, the idea of the rotorcraft we have developed is to fly autonomously in an unknown environment without estimating its attitude, altitude or ground speed. In particular, the autopilot implemented onto the robot does not refer at any time to the absolute vertical (earth center) direction and does not use any accelerometer.

To navigate autonomously in unknown environments without any estimation in the inertial frame $(0, x_0, y_0, z_0)$, the BeeRotor robot (see Figures 4.1a, b and d) relies on optic flow measurements computed in 4 Regions of interest (ROIs) (Down Forward: Φ ; Down Backward: $-\Phi$; Up Forward: $180^\circ - \Phi$ and Up Backward: $180^\circ + \Phi$).

As the BeeRotor robot is equipped only with sensors mimicking sensory modalities of flying insects, the robot has nor measurement nor estimation of the pitch angle of the robot θ_{Pitch} , the angle of the eye θ_{Eye} and the angle of the closest wall α in the absolute frame of reference (see Figure 4.1c).

We assume that we have a local motion sensor looking at an object situated at a distance D in the direction $d(\Phi)$ characterized by the elevation angle Φ (as can be seen in Figure 4.1c, Φ is the angle between the direction of the local motion sensor $d(\Phi)$ and the perpendicular with the eye's equator). The movement of the local motion sensor can always be decomposed into a translation vector \vec{T} and a rotation vector \vec{R} . The motion field or optic flow in that direction $\overrightarrow{\omega(\Phi)}$ is given by (Koenderink & van Doorn, 1987):

$$\overrightarrow{\omega(\Phi)} = -\frac{(\vec{T} - (\vec{T} \cdot d(\Phi))d(\Phi))}{D} - \vec{R} \times d(\Phi) \quad (4.1)$$

If we assume that the BeeRotor robot is only moving in translation ($\vec{R} = 0$), we obtain from (4.1) :

$$\overrightarrow{\omega(\Phi)} = -\frac{(\vec{T} - (\vec{T} \cdot d(\Phi))d(\Phi))}{D} \quad (4.2)$$

By expressing the translation vector \vec{T} in the orthogonal basis formed by $d(\Phi)$ (the viewing direction) and $\frac{\overrightarrow{\omega(\Phi)}}{\|\overrightarrow{\omega(\Phi)}\|}$ (the normalized optic flow vector), (Whiteside & Samuel, 1970) have shown that equation (4.2) can be expressed:

$$\omega(\Phi) = \frac{\|\vec{V}\|}{D} \sin(90 + \Psi - \Phi) \quad (4.3)$$

Ψ is the angle between the eye's equator and the direction of the speed vector \vec{V} (see Figure 4.1c). If we assume that the local motion sensor is looking at the ground and that the eye is kept parallel with the local ground orientation, the optic flow in the direction $d(\Phi)$ can therefore be expressed:

$$\omega(\Phi) = \frac{\|\vec{V}\|}{h} \cos(\Phi) \cdot \cos(\Psi - \Phi) \quad (4.4)$$

where $h = D \cdot \cos(\Phi)$ is the altitude of the aircraft.

4.1.3.1 Bio-inspired altitude control based on optic flow

As we can notice from equation (4.4), the optic flow measured by a local motion sensor looking at the ground depends on the distance between the aircraft and the ground and on the speed of the aircraft. It is therefore possible to use the optic flow measurements to regulate the distance of the aircraft with a surface and therefore automatically follow terrain if the speed of the aircraft is held constant. In particular, by fusing the outputs of the two ventral optic flow sensors in order to only depend on the horizontal or vertical component of the speed vector, we can derive from equation (4.4) :

$$\omega(\Phi) + \omega(-\Phi) = \frac{2 \|\vec{V}\| \cdot \cos^2(\Phi) \cdot \cos(\Psi)}{h} \quad (4.5)$$

$$\omega(\Phi) - \omega(-\Phi) = \frac{\|\vec{V}\| \cdot \sin(2\Phi) \cdot \sin(\Psi)}{h} \quad (4.6)$$

where $\omega(\Phi)$ is the forward optic flow (ω_{DF}) and , $\omega(-\Phi)$ is the backward optic flow (ω_{DB})

If we decompose the velocity vector \vec{V} onto its two components $V_x = V \cdot \cos(\Psi)$ and $V_z = V \cdot \sin(\Psi)$, we can see that the sum of the optic flow depends on the horizontal velocity V_x whereas the difference of the optic flow varies with the vertical velocity V_z :

$$\omega(\Phi) + \omega(-\Phi) = 2 \cdot \cos^2(\Phi) \cdot \frac{V_x}{h} \quad (4.7)$$

$$\omega(\Phi) - \omega(-\Phi) = \sin(2\Phi) \frac{V_z}{h} \quad (4.8)$$

As long as we are able to orient the eye relatively to the closest surface, we can then see that the sum of the optic flows can be used to regulate the ratio between the horizontal speed V_x and the distance to the surface h and the difference of the optic flows can be used to regulate the ratio between the vertical speed V_z and the distance to the surface h . We obtain exactly the same results if the aircraft is following the ceiling and we compute the sum and difference of the two dorsal optic flows.

To control the altitude of the aircraft, it is therefore possible to regulate the sum of the optic flows generated by the closest surface and maintain a safe distance with this surface depending on the forward speed. This optic flow regulator successfully implemented on the OCTAVE robot (Ruffier, 2004; Ruffier & Franceschini, 2005; Franceschini et al., 2007) can here be extended for the ventral and the dorsal optic flows.

4.1.3.2 Forward speed control system

The guidance strategy to control the forward speed of the rotorcraft is inspired by experimental findings on honeybees when traveling in tapered corridor where honeybees have been found to adjust their forward speed according to “the two opposite optic flows in the horizontal and vertical planes” (Srinivasan et al., 1996; Portelli et al., 2011)

In our case, if we assume for simplification that the gaze of the aircraft is kept parallel to the ground and the ceiling, we can show that:

$$\begin{aligned}
 \omega_{SumOF} &= \omega(\Phi) + \omega(-\Phi) + \omega(180^\circ + \Phi) + \omega(180^\circ - \Phi) \\
 &= \frac{2V_x \cdot \cos^2(\Phi)}{D_{Down}} + \frac{2V_x \cdot \cos^2(\Phi)}{D_{Up}} \\
 &= 2V_x \cdot \cos^2(\Phi) \cdot \left(\frac{1}{D_{Down}} + \frac{1}{D_{Up}} \right)
 \end{aligned} \tag{4.9}$$

where D_{Up} is the distance with the ceiling, D_{Down} is the distance with the ground. Of course, it is not possible for the eye to be parallel to both surfaces in a corridor with relief, but, if the eye is always parallel to the closest surface, the optic flow generated by the other surface is smaller and the error due to this simplification will not affect strongly the result.

It has been proven in (Serres et al., 2008) in the horizontal plane that by regulating the optic flow generated by the closest wall while regulating the sum of the two lateral optic flows led the LORA III autopilot to automatically adjust its forward speed proportionally to the size of the corridor. The sum of the ventral and dorsal optic flows can then be used to adjust the speed of the aircraft according to the height of the tunnel in the presence of another feedback loop controlling the altitude to automatically fly at a safe altitude and forward speed. The two previously discussed strategies allow to control the altitude and forward speed of an aircraft thanks only on optic flow measurements performed on the reference frame attached to the robot’s eye without any estimation in the inertial frame. However, these strategies require that the eye is always kept parallel to the nearest surface.

4.1.3.3 Eye reorientation based on optic flow

Biological inspiration In insects, it has been observed that the flight can be decomposed in translational motions where the head angular position is almost constant interspersed with rapid saccadic flicks in which the head takes up a new angle with respect with the visual surrounding (Land, 1973; van Hateren & Schilstra, 1999). This limits the rotational optic flow to be concentrated during the saccades, allowing the remaining time to be used for analyzing the structure of the visual environment on the assumption of translatory optic flow only. This head stabilization is achieved thanks to the optomotor response (Reichardt, 1969) compensating any undesirable yaw rotation measured thanks to the fixation of visual features on the environment and thanks to the vestibulo-ocular reflex compensating for any roll rotation of the body (Hengstenberg, 1992) measured by the halteres. On the pitch axis, little is known about the head movements during flights. Hengstenberg showed that the fly’s head is pitched downward during flight compensating for the body angle in order to keep its eyes in the same direction (Hengstenberg, 1992) as when the fly is walking. Van Hateren and Schilstra showed the existence of simultaneous steps movements of the body and the head of blowflies along the pitch axis (van Hateren & Schilstra, 1999) but they noticed that “the pitch is slightly more stable for the head than for the thorax”. However, no hypothesis has been expressed to explain this discrepancy between the pitch angle of the body and the pitch angle of the head.

Theoretical interest of reorienting the eye We consider a Micro Aerial Vehicle flying at a constant speed V_x above a tilted terrain with a discontinuity (see Figure 4.2a and b). This aircraft is equipped with an eye that can be fixed or mechanically decoupled composed of optic flow sensors looking down forward and down backward (each of them oriented at an angle Φ with the perpendicular of the eye’s equator). Depending on the angle of the eye’s equator (0 for a fixed eye and α for a decoupled eye perfectly reoriented parallel to

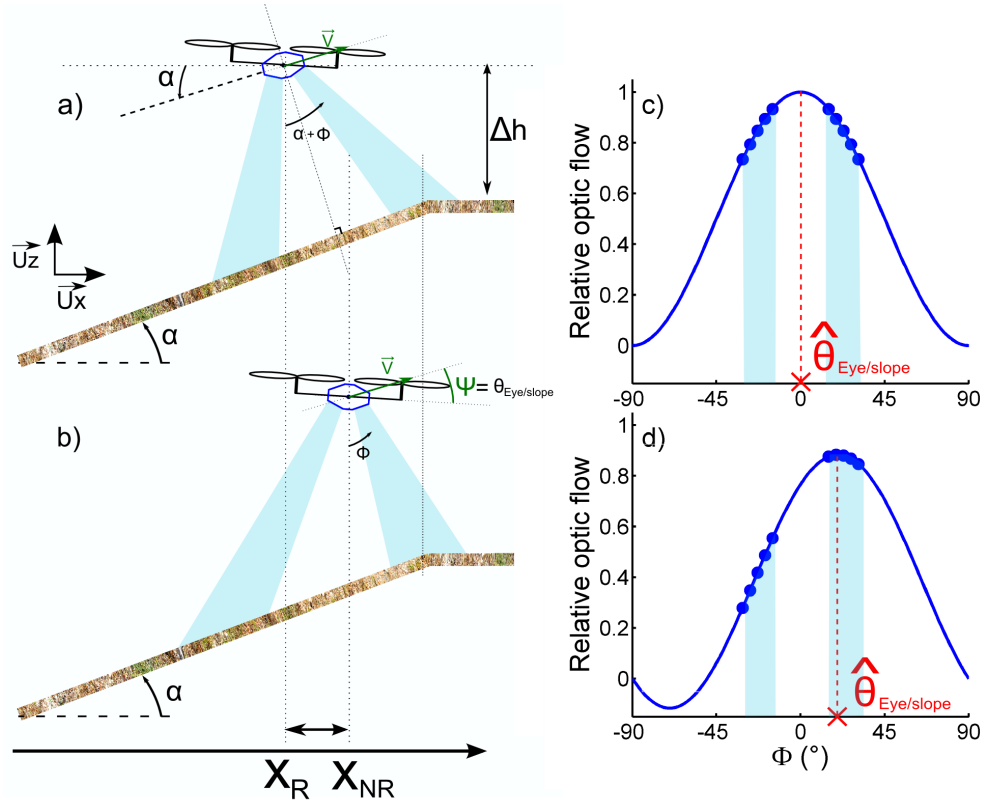


Figure 4.2: **a-b)** Distance difference in the detection of a ground discontinuity between a fixed eye and a decoupled eye reoriented in parallel with the ground. The Micro Aerial Vehicle is flying in horizontal translation above a terrain tilted with an angle α at a constant speed V_x . The aircraft altitude is separated from the altitude of the ground at the discontinuity point by a distance Δh . For clarity, only the Down-Forward optic flow sensors have been represented. These sensors forms an angle Φ with the perpendicular of the eye's equator. **a)** When the eye is perfectly reoriented in parallel with the ground, the discontinuity starts to be detected by the optic flow sensor at the position x_R . **b)** When the eye is not equipped with a reorientation reflex, the discontinuity is detected at the position x_{NR} . The reorientation of the eye can therefore help to detect obstacles faster easing their avoidance. **c)** Obtained optic flow pattern when the eye is oriented in parallel with the surface. In this case, the maximum of the bell-shape curve which corresponds to the estimated reorientation angle $\hat{\theta}_{Eye/slope}$ appears for a 0° angular position. **d)** Obtained optic flow pattern when the aircraft equipped with a fixed eye is flying horizontally above a tilted ground. The bell-shape curve representing the evolution of the relative optic flow values with the angular position of the local motion sensors is not centered around 0° . In both cases, the velocity vector is assumed to be parallel to the slope of the ground.

the surface), the discontinuity in the measured optic flow will be detected respectively for a position:

$$x_{NR} = \Delta h \times \tan(\Phi) \text{ and } x_R = \Delta h \times \tan(\alpha + \Phi) \quad (4.10)$$

As the aircraft is flying at a constant speed V_x , this distance gap will represent a delay:

$$\Delta t = \frac{x_R - x_{NR}}{V_x} = \frac{\Delta h}{V_x} \times (\tan(\alpha + \Phi) - \tan(\Phi)) \quad (4.11)$$

In a realistic case where the aircraft is flying over a tilted terrain ($\alpha = 15^\circ$) at an horizontal speed $V_x = 1m/s$, at an altitude $\Delta h = 1m$ over the relief discontinuity with a local motion sensor looking at a direction $\Phi = 23^\circ$, the eye reorientation will allow the aircraft to detect the discontinuity 0.35s before a fixed eye. In particular, it is worth noting that the reorientation of the eye increases the prediction time horizon of the system by a ratio:

$$\frac{\tau_R}{\tau_{NR}} = \frac{\Delta h}{V_x} \times \frac{\tan(\alpha + \Phi)}{\tan(\Phi)} \quad (4.12)$$

In our example, this ratio is equal to 1.84 showing that the discontinuity will be detected almost twice faster when the eye is decoupled and oriented in parallel with the ground. Through this example, we understand that reorienting the eye can help to detect obstacles faster. Of course, when following a relief with a negative slope, the eye will be oriented backwards delaying the detection of discontinuities. However, we have observed experimentally that although the detection of obstacles is delayed when following a descending ramp, the reorientation of the eye parallel to the surface improves the flying performances of the aircraft because the optic flow is underestimated with a fixed eye leading to a strong rebound or even a crash of the aircraft at the end of the descending ramp due to its inertia.

Implementation of the eye’s reorientation strategy As we want to use mainly optic flow on our robot, we tested how we can orient its eye relatively to the surface using only some local motion sensors. One simple idea was to detect the direction where the optic flow was maximal because the distance D is minimal in that case. In simulation, the robot was able to reorient its eye automatically but it was really sensitive to optic flow measurement errors. In particular, as we lose in precision with our OF sensor at high speeds, the reorientation was getting noisier when the optic flow was increasing.

Another strategy particularly robust with a set of data containing outliers would be to use the “RANdom SAmple Consensus” (RANSAC) algorithm (Fischler & Bolles, 1981) but it is too costly in our case due to the important number of iterations necessary to obtain a good fit of the data.

In order to be less sensitive to optic flow measurement errors, we determine the angle between the surface and the eye using a Least Squares approximation. Indeed, Figures 4.2c and d represent respectively the optic flow patterns measured by ventral optic flow sensors in the case where the eye’s equator and the closest surface are parallels and when there is an angle $-\alpha$ between the eye orientation and the surface.

From equation (4.3), we know in that case that the optic flow varies with the orientation of each local motion sensor Φ relatively to the eye frame of reference according to the following equation:

$$\omega(\Phi) = \frac{\|\vec{V}\|}{D} \cdot \sin(90 - \Phi - \Psi) \quad (4.13)$$

where Ψ is the angle between the eye's equator and the direction of the speed vector (see Figure 4.1c)). Geometrically, we can show that the distance D depends on the slope of the surface α , the height of the aircraft h , the angle $\theta_{Eye/slope}$ between the eye's equator and the slope of the closest surface and the orientation of the local motion sensor Φ .

$$D = h \frac{\cos(\alpha)}{\cos(\Phi + \theta_{Eye/slope})} \quad (4.14)$$

From equations (4.13) and (4.14), we can deduce that:

$$\omega(\Phi) = \frac{\|\vec{V}\|}{h \cdot \cos(\alpha)} \cdot \cos(\Phi + \Psi) \cdot \cos(\Phi + \theta_{Eye/slope}) \quad (4.15)$$

As we are seeking the direction of the maximum optic flow to determine the angle between the eye's equator and the slope of the closes surface $\theta_{Eye/slope}$, we differentiate the equation (4.15):

$$\frac{d\omega(\Phi)}{d\Phi} = \frac{\|\vec{V}\|}{h \cdot \cos(\alpha)} \cdot [-\sin(\Phi + \Psi) \cdot \cos(\Phi + \theta_{Eye/slope}) - \cos(\Phi + \Psi) \cdot \sin(\Phi + \theta_{Eye/slope})] \quad (4.16)$$

The maximum of the cosine function is then given for:

$$\frac{d\omega(\Phi)}{d\Phi} = 0 \implies \hat{\theta}_{Eye/slope} = -\max(\omega(\Phi)) = \frac{\Psi + \theta_{Eye/slope}}{2} \quad (4.17)$$

As we can see from equation (4.17), when the aircraft is moving, the maximum of the optic will not appear when the eye is parallel with the followed surface but at an angle depending on the angle between the eye's equator and the slope of the closest surface $\theta_{Eye/slope}$ and the direction of the velocity vector of the aircraft Ψ in the frame of reference attached to the eye.

HYPOTHESIS: the velocity vector is always parallel to the closest surface.

$$\Psi = \theta_{Eye/slope} \quad (4.18)$$

Indeed, as explained in section 4.1.3.1, we want to use the optic flow generated by the closest surface to always keep a safe distance from this wall which will lead to a wall following behavior and therefore the velocity vector will automatically line up with the nearest wall.

In that case, equation 4.17 becomes:

$$\hat{\theta}_{Eye/slope} = \theta_{Eye/slope} \quad (4.19)$$

The estimated Reorientation angle $\hat{\theta}_{Eye/slope}$ can therefore be used to reorient the eye parallel to the followed surface as $\theta_{EiR} = \theta_{EiR} - \hat{\theta}_{Eye/slope}$ leads to $\theta_{Eye/slope} = 0$.

In the neighborhood of the position of the maximum of the optic flow according to equation (4.15), the optic flow will vary according to:

$$\omega(\Phi) \simeq f(\Phi') = \frac{\|\vec{V}\|}{h.\cos(\alpha)}. \cos^2(\Phi') \quad (4.20)$$

The idea is therefore to use the measurements from all the local motion sensors, each of them separated from a known angle, to identify the angle between the eye's equator and the surface orientation. We seek the coefficients $\frac{\|\vec{V}\|}{h.\cos(\alpha)}$ and $\hat{\theta}_{Eye/slope}$ in the function $f(\Phi') = \frac{\|\vec{V}\|}{h.\cos(\alpha)}. \cos^2(\Phi' - \hat{\theta}_{Eye/slope})$ giving the best approximation in the sense of the Least Squares from the measurements of the optic flows $\omega(\Phi)$. This can be easily implemented in the microcontroller at almost no cost as we can estimate the cosine square function by a polynomial second order function using a Taylor expansion around 0:

$$\begin{aligned} \omega(\Phi) &\simeq \frac{\|\vec{V}\|}{h.\cos(\alpha)}. (1 - (\Phi - \hat{\theta}_{Eye/slope})^2) \\ &\simeq \frac{\|\vec{V}\|}{h.\cos(\alpha)} [-\Phi^2 + 2.\hat{\theta}_{Eye/slope}\Phi + (1 - \hat{\theta}_{Eye/slope}^2)] \end{aligned} \quad (4.21)$$

$$\iff \omega(\Phi) \simeq a.\Phi^2 + b.\Phi + c \quad (4.22)$$

We define $X = [\Phi^2, \Phi, 1]$ and from our set of measurements Γ , we determine the coefficients $[a, b, c]$ using the least-squares method:

$$[a, b, c] = inv(X * X') * X * \Gamma' \quad (4.23)$$

In that expression, only Γ depends on the optic flow measurements whereas everything else is constant and only depends on the orientation of each OF measurement inside the eye reference frame which is fixed. Finding the $[a, b, c]$ coefficients only requires one matrix multiplication and then we can determine from equations (4.21) and (4.22) that the estimated angle between the eye's equator and the slope of the followed surface can be computed as follows:

$$\hat{\theta}_{Eye/slope} = \frac{-b}{2.a} \quad (4.24)$$

In simulation, we observed that with noise on the optic flow measurements, we could end up with false measurements of the reorientation angle leading, in closed loop, to oscillations of the eye. To eliminate these false measurements, we compute what we called the confidence index:

$$Confidence = \frac{\sum_i |X' \times b - \omega_{\Phi_i}^{meas}|}{median(\omega_{\Phi_i}^{meas})} \quad (4.25)$$

Lower is the confidence index, higher is the similarity between the optic flow measurements and the approximated cosine square function. The reorientation angle is only validated when this confidence index is below a fixed threshold value.

4.1.3.4 Description of the visuomotor control loops

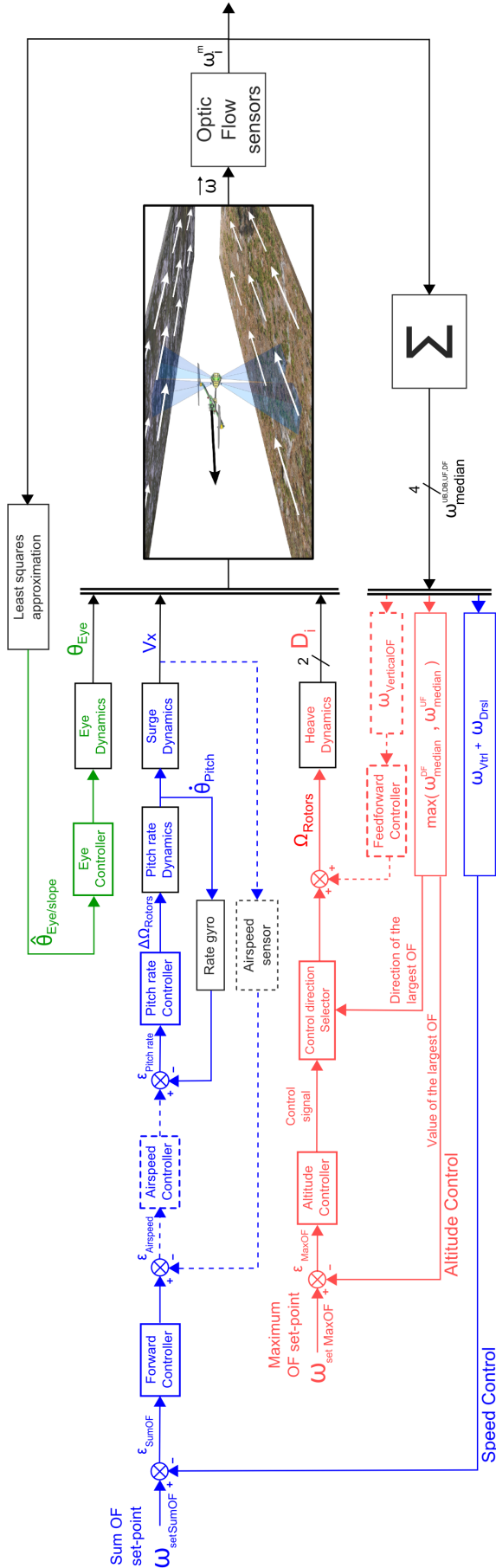


Figure 4.3: The BeeRotor autopilot relies almost exclusively on its optic flow sensors to control its eye orientation, its forward speed and its altitude thanks to three feedback loops. The first feedback loop (green) controls the orientation of the eye relative to the body and always keeps the eye parallel to the closest surface thanks to a Least Squares approximation performed on the optic flow measurements. The second feedback loop (red) controls the altitude of the aircraft in order to always keep constant the optic flow generated by the closest surface. By taking the maximal value between the forward ventral and dorsal optic flows which is then compare to the Maximum OF setpoint $\omega_{setMaxOF}$ to act on the vertical lift of the robot. Optionally, the vertical lift of the aircraft can also be controlled by a feedforward controller using the measurement of the Vertical optic flow $\omega_{VerticalOF}$ (see section 4.1.7) to reduce the oscillations of the aircraft by anticipating the changes in the ventral or dorsal optic flow during strong variations of altitude like when overflying the obstacle. The last feedback loop (blue) controls the forward speed of the robot based on the sum of the ventral and the dorsal optic flows thanks to one or two nested feedback loops. The difference between the sum of the optic flows and a setpoint value $\omega_{setSumOF}$ is used to optionally control the rotorcraft's airspeed measured thanks to a custom-made airspeed sensor and to regulate the pitch rate of the aircraft θ thanks to the rate gyro measurements. This feedback loop coupled with a ventral or dorsal regulator automatically adapts the forward speed of the aircraft to the size of the tunnel where the rotorcraft is flying by reducing its speed when the tunnel is narrowing and accelerating when the tunnel is getting wider. These last two intertwined feedback loops guarantee that the BeeRotor robot will always keep a safe distance from both walls while adapting its forward speed to the size of the tunnel without any measurements of distance or groundspeed. The dotted lines indicate optional feedback loops whose performances and usefulness will be assessed.

As we saw in the previous sections, based on the optic flow measurements given by the quasi-panoramic eye defined in the reference frame attached to the aerial robot's eye and from bio-inspired strategies found in insects, it is possible to:

- Keep the gaze of the robot parallel to the closest surface,
- Control the altitude of the aircraft based on the optic flow generated by the closest wall,
- Control its forward speed thanks to the sum of the ventral and dorsal optic flows.

The BeeRotor autopilot is therefore composed of three feedback loops controlling the mean speed of the propellers Ω_{Rotors} , the differential speed of the propellers $\Delta\Omega_{Rotors}$ and the angle of the eye $\hat{\theta}_{Eye/slope}$. The median value measured by each visual motion sensor ($\omega_{medianUF}$; $\omega_{medianUB}$; $\omega_{medianDF}$; $\omega_{medianDB}$) was used to compute the ventral and dorsal optic flows, called ω_{Vtrl} and ω_{Drsl} :

$$\omega_{Vtrl}^{meas} = \frac{1}{2 \cdot \cos^2(\gamma)} \cdot (\omega_{\Phi=\gamma}^{median} + \omega_{\Phi=-\gamma}^{meas}) \quad (4.26)$$

$$\omega_{Drsl}^{meas} = \frac{1}{2 \cdot \cos^2(\gamma)} \cdot (\omega_{\Phi=180^\circ+\gamma}^{median} + \omega_{\Phi=180^\circ-\gamma}^{meas}) \quad (4.27)$$

where $\gamma = 23^\circ$ is the tilt angle of each visual motion sensor.

The green feedback loop reorients the eye parallel to the surface based on the least squares approximation presented in section 4.1.3.3 to compute the reorientation angle $\hat{\theta}_{Eye/slope}$ which determines the angle of the eye θ_{Eye} through the eye dynamics.

The speed control loop in blue uses the following OF sum:

$$\omega_{SumOF}^{meas} = \omega_{Vtrl}^{meas} + \omega_{Drsl}^{meas} \quad (4.28)$$

The ω_{SumOF}^{meas} is compared with the Sum OF setpoint $\omega_{setSumOF}$ in order to adjust the robot's airspeed.

Two nested feedback loops regulate the pitch rate of the aircraft $\dot{\theta}$ thanks to a Proportional Integral Derivative (PID) controller based on the rate gyro measurements and the airspeed thanks to a PD controller based on the measurements of the airspeed sensor. The speed control loop acts on the differential speed of the propellers of the aircraft $\Delta\Omega_{Rotors}$, which eventually determines the groundspeed V_x through the surge dynamics. When the sum $\omega_{Vtrl}^{meas} + \omega_{Drsl}^{meas}$ is greater than the Forward Speed OF setpoint $\omega_{setSumOF}$, the forward controller will decrease the airspeed setpoint that will then be compared with the airspeed measurement leading to a decrease in the setpoint of the pitch rate feedback loop and the differential speed of the propellers $\Delta\Omega_{Rotors}$.

In order to anticipate for incoming obstacles, the altitude control loop in red uses the maximum forward optic flow generated by the two walls:

$$\omega_{MaxOF}^{meas} = \max \left(\frac{1}{\cos^2(\gamma)} \cdot \omega_{medianDF}, \frac{1}{\cos^2(\gamma)} \cdot \omega_{medianUF} \right) \quad (4.29)$$

and this value is compared with the Maximum OF setpoint $\omega_{setMaxOF}$ and used to control the rotors' mean speed Ω_{Rotors} , which will eventually determine the altitude z . When the OF of the nearest wall is greater than the Maximum OF setpoint $\omega_{setMaxOF}$, depending on

which wall is detected, the altitude controller will either increase or decrease the rotor speed command in order to drive the rotorcraft away from this wall. It is worth noting that this autopilot, mainly based on OF measurements, allow an aircraft to fly autonomously without requiring to estimate the attitude (yaw, pitch and roll), the altitude or the groundspeed of the aircraft.

4.1.4 The BeeRotor robot and its environment

Airframe The BeeRotor robot is a 80-gram tandem rotorcraft with a 47- cm wingspan, which is composed of a main electronic board weighing only 13 grams (called the “body”) reinforced by a 25-cm long carbon-fiber rod (Figures 4.1a and b). It is propelled by two miniature 8.2-gram Brushless outrunner motors controlled by Turnigy Plush Brushless speed controllers driving two 20-cm long propellers borrowed from a X-UFO quadrotor. The rotorcraft has four degrees of freedom: the elevation of the aircraft depends on the mean speed of the propellers Ω_{Rotors} , the differential propellers’ speed $\Delta\Omega_{Rotors}$ acts on the pitch angle and therefore determines the forward speed of the robot and a stepper motor is used to orient the eye respectively to the body. Although it is autonomous in terms of its computational requirements, the BeeRotor robot is connected to an external power supply via a 10-lead slip ring assembly at the extremity of the arm and also via a 40-lead slip ring assembly placed at the top of the central pole. The robot’s eye, composed of 4 custom-made visual motion sensors, can be rotated with respect to the body by a stepper motor coupled with a reductor, giving a resolution of $0.02^\circ/steps$. The eye is placed 7 cm away from the body to prevent the propellers from entering the visual field of the eye.

Electronics The body of the rotorcraft is composed of a custom-designed electronic board, on which all the main sensors and actuators are set around a dsPIC microcontroller. This microcontroller embeds the autopilot processing the data provided by the visual motion sensors and controls the actuators of the robot. This microcontroller communicates with the 4 visual motion sensors through a SPI bus and receives the output from the 20 1-D Local Motion Units, which are first computed at a rate of 1kHz by the 4 visual motion sensors, also called Elementary Motion Detectors (EMDs) (see Figure 4.5). The main electronic board is also equipped with:

- a tiny Bluetooth module (ALA from Free2move company) mediating information between the robot and a host computer,
- a custom-made positioning sensor, based on a A1391 Hall effect sensor placed a few millimeters away from 2 tiny magnets with reverse polarities measuring the orientation of the eye relatively to the body in a $[-20^\circ, 20^\circ]$ range,
- a 6-axis Inertial Measurement Unit (IMU) MPU 6000 from Invensense communicating with the main microcontroller through a SPI bus. During autonomous flight, only the information coming from the rate gyro sensing the angular velocity along the pitch axis is used by the robot to navigate. To be less sensitive to the vibrations of the aircraft in flight, the IMU has been placed on top of four rubber bushings (vibration isolators),
- a deported custom-made airspeed sensor based on a digital Hall effect sensor A1203 placed in front of a magnet attached to the axis of a propeller freely rotating (the total weight of this tiny airspeed sensor is smaller than 0.5g),

- two Hall effect sensors placed a few millimeters away from the motor shafts containing 16 magnets measuring the speed of the propellers which is regulated by a Proportional Integral controller.

4.1.4.1 Dynamics identification

The transfer functions identified and the controllers implemented on the BeeRotor robot are detailed in appendices I and II.

4.1.4.2 Propeller dynamics

In order to identify the transfer function between the propellers' control signal and the rotational speed of the propellers measured thanks to a Hall effect sensor, we applied a series of steps on the propellers' command. A first order system with the following transfer function has been identified:

$$G_{propeller}(s) = \frac{\Omega_{rotor}(s)}{u_{rotor}(s)} = \frac{K_{rotor}}{\tau_{rotor}s + 1} = \frac{4.116}{0.1398s + 1} \quad (4.30)$$

The speed of the propellers is regulated thanks to a Proportional Integral (PI) controller $C_{propeller}(s)$ in order to cancel the static error of the system. This PI controller has been adjusted in order to have a response time at 5% smaller than 0.1s and an overshoot smaller than 10%.

4.1.4.3 Forward speed dynamics

During the identification process of the dynamics of the aircraft, we noticed that, like in insects (David, 1978), the forward speed of the aircraft depends only on its body pitch and there is no coupling between the mean flight force and the horizontal speed of the aircraft. It was therefore possible to identify the transfer function between the differential speed of the propellers and the forward speed of the aircraft. To ease the feedback control, we first identified the dynamics between the pitch angle θ and the forward speed of the aircraft G_{Speed} by applying a series of steps on the pitch angle of the robot controlled thanks to a servomotor for several operating points around an initial pitch angle of 5.85° which corresponds to a forward speed of 1.3m/s.

$$G_{Speed}(s) = \frac{\delta v_x(s)}{\delta \theta(s)} = \frac{K}{\tau s + 1} = \frac{0.10498}{5.4312s + 1} \quad (4.31)$$

Then, the dynamics $G_{PitchRate}$ between the differential propellers' speed $\Delta\Omega_{Rotors}$ and the pitch rate $\dot{\theta}$ was identified after removing the servomotor used previously. In order to avoid strong rotations of the robot along its pitch axis when applying steps on the differential speed of the propellers, the identification was performed in closed loop with a Proportional Derivative controller implemented to roughly stabilize the pitch angle around a setpoint. Although not used on the robot during autonomous flight, the pitch angle of the aircraft θ was estimated here using a complementary filter (Pflimlin, 2007; Mahony et al., 2008) fusing the inertial information of the accelerometer and the rate gyro. By applying a series of steps on the pitch angle of the rotorcraft, we identified the dynamics between the differential speed and the pitch rate to be a second order system with a zero:

$$G_{PitchRate}(s) = \frac{\dot{\theta}(s)}{\Delta\Omega_{Rotors}(s)} = \frac{-0.042s - 0.02683}{0.001742s^2 + 0.05445s + 1} \quad (4.32)$$

The whole transfer function linking the differential speed of the propellers and the forward speed of the aircraft can therefore be written:

$$G_{FwdSpeed}(s) = G_{Speed}(s) \cdot \frac{1}{s} \cdot G_{PitchRate}(s) \quad (4.33)$$

The pitch rate of the aircraft $\dot{\theta}$ is stabilized thanks to a Proportional Integral Derivative (PID) controller $C_{pitchRate}(s)$ based on the rate gyro measurements and the airspeed is regulated thanks to a PD controller $C_{Airspeed}(s)$ based on the measurements of the airspeed sensor limiting the time response and the overshoot of the system. Stabilized thanks to these two nested loops, the transfer function between the airspeed setpoint and the forward speed of the aircraft $G_{speedCL}(s)$ has been identified by dynamically changing the airspeed setpoint of the robot. The open loop transfer function linking the Sum OF setpoint to the forward speed of the aircraft $G_{SumOF}(s)$ has been linearized to synthesize the $C_{Forward}(s)$ which is a double phase lead controller designed to increase the gain and the phase margin of the feedback loop,.

4.1.4.4 Altitude dynamics

Identically to the identification of the forward speed dynamics, we identified the dynamics between the mean speed of the propellers Ω_{Rotors} and the altitude of the aircraft $G_{Alt}^{\theta_{pitch}}(s)$ by applying a series of steps on the speed of the propellers for several values of the pitch angle between 3.75° and 15.3° .

Contrary to the forward speed dynamics, the altitude response does not depend only on one parameter. Indeed, the dynamical response of the aircraft depends not only on the propellers' speed Ω_{Rotors} but also on the pitch angle θ of the aircraft. We identified for each pitch angle value the transfer function between the propellers' speed and the altitude of the aircraft which always behaved like an underdamped second order system with a damping ratio ranging from $\zeta_{alt} = 0.17$ for a pitch angle of 3.75° to $\zeta_{alt} = 0.47$ for a pitch angle of 15.3° whereas the gain varied between $K_{alt} = 0.12$ and $K_{alt} = 0.42$ on the same range. In order to control the system, as we do not use the information of the accelerometer and we therefore do not know the pitch angle of the aircraft, we synthesized a controller guaranteeing the stability of the system for any value of the pitch angle.

The open loop transfer functions linking the Maximum OF setpoint to the altitude of the aircraft $G_{MaxOF}(s)$ have been linearized to synthesize the $C_{Altitude}(s)$ which is a Proportional Integral controller followed up by a double phase lead controller eliminating the static error and strongly increasing the gain of the feedback loop while avoiding to the robot to oscillate by increasing the phase margin.

4.1.4.5 Environment

The BeeRotor robot was traveling along a 12-m long circular high-roofed tunnel, the floor and ceiling of which were covered with giant horizontal printed discs (inner diameter 2.4m, outer diameter 4.5m) depicting natural scenes (Figure 4.4). In order to assess the performances of the BeeRotor autopilot and in particular its ability to avoid collisions, we added a 450-cm long

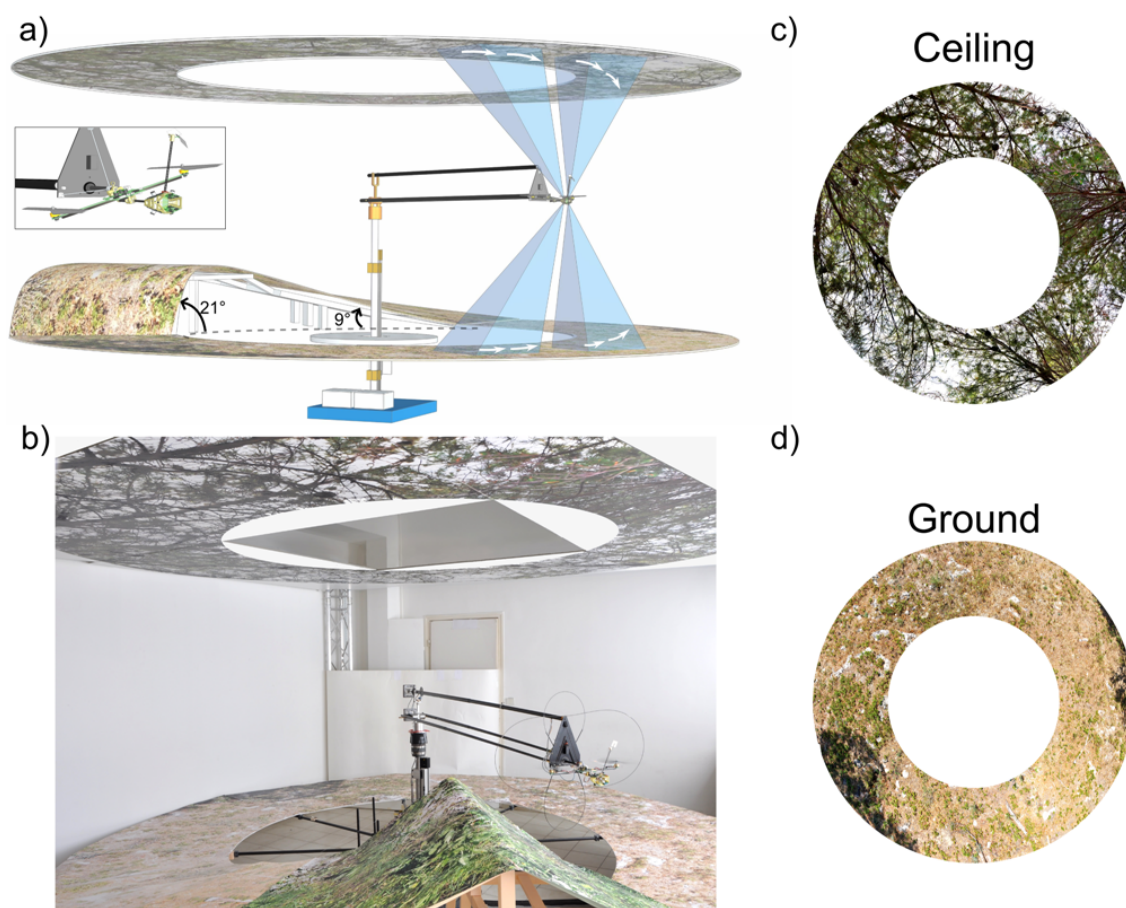


Figure 4.4: **a)** CAD drawing of the aircraft in its environment. The robot was made to travel along a 12-m long high-roofed tunnel, the floor and ceiling of which were covered with photographs depicting natural scenes. The rotorcraft was tethered to the end of a light, counterbalanced whirling pantographic arm, which was driven in elevation and azimuth by the aircraft’s lift and propulsive forces. A 4.5-m long relief was added to assess the performances of the BeeRotor aircraft while flying autonomously. This 38-cm high relief is composed of a 2.5-m long 9° ascending ramp, a 1-m long flat and a 1-m long 21° descending ramp. This surface can be actuated independently thanks to a 30W Brushless DC geared motor and a servomotor to respectively make it rotate in both directions and rise or fall. The Fields Of View of the 4 visual motion sensors indicated here show that the aircraft was looking Up-Forward, Up-Backward, Down-Forward and Down-Backward with a FOV of 24°. The main direction of each visual motion sensor was tilted around the eye’s pitch axis at an angle of $\gamma = 23^\circ$. **b)** Photograph of the experimental setup (where the 1m-long flat part of the relief has been replaced by a 30cm-high obstacle with an ascending and descending ramp of 31°) where the BeeRotor robot is navigating. **c-d)** Richly contrasted patterns used respectively for the ceiling and the ground of the experiments. Both images are composed of an assembly of real pictures corresponding to a typical soil and undergrowth of the South of France.

and 38-cm high obstacle to the ground. This obstacle is composed of a 9° ascending ramp, a 1-m long flat part and a 21° descending ramp (see Figure 4.4a). In some experiments, an even steeper relief has been used by replacing the 1m-long flat part with a 30cm-high obstacle with an ascending and descending ramp of 31° (see Figure 4.4b). Besides, to simulate an unstationary environment, the altitude of the ground of the tunnel can be actively controlled over a 64cm range using a servomotor (DBL2 from Kollmorgen) coupled with a Servostar 300 modifying the height of the tunnel from 200cm to 140cm. The ground can also rotate in both directions thanks to a 30W Brushless DC geared motor (80 149 606 from Crouzet) disturbing the perceived optic flow. The fields of view of the four visual motion sensors looking Up-Forward (UF), Up-Backward (UB), Down-Forward (DF) and Down-Backward (DB) are indicated in Figure 4.4a showing that the visual motion sensors are always looking at the contrasted patterns regardless of the altitude of the aircraft. The rotorcraft was tethered to the end of a light, counterbalanced whirling pantographic arm driven in elevation and azimuth by the rotorcraft’s main force, which provided the lift and forward propulsive force. The pantographic arm was equipped on the elevation axis with a servo-potentiometer giving the robot’s altitude, and on the travel axis, with an optical encoder giving the robot’s azimuth angle, and hence the horizontal distance traveled and the robot’s forward speed. These data are collected on the host computer using a RT1104 dSpace board and a C# dedicated program monitoring the information of the aircraft. This program also generates the control signals for the servomotor and the DC motor commanding respectively the ground altitude and rotation. The azimuthal position of the ground is measured thanks to a magnetoresistive sensor (HMC1052 from Honeywell) sensitive to the Earth magnetic field and placed on the inner disc of the ground. This measurement is sent to the dSpace board through a HF transmitter/receiver pair from Radiometrix. Although it introduced some inertial forces, the pantographic arm enabled us to reliably and reproducibly test the performances of the BeeRotor robot under safe flying conditions, while making the parameter monitoring simpler.

4.1.4.6 BeeRotor’s miniature quasi-panoramic eye and its optic flow processing

The BeeRotor’s eye is composed of four 2-gram stand-alone visual motion sensors (see Figures 4.4a and 4.5a) looking Up- Forward (UF), Up-Backward (UB), Down-Forward (DF) and Down-Backward (DB). Each visual motion sensor is tilted from the vertical axis at an angle of 23° and has a longitudinal Field-Of-View (FOV) of 24° (see Figures 4.4a). Each of the 4 visual motion sensors used on the BeeRotor robot is based on a 6-pixel off-the-shelf photosensor array (iC-LSC from iCHaus Company, <http://www.ichaus.de>) mounted on a lightweight lens (Sparkfun SEN-00637, focal length 2mm, f-number 2.8) borrowed from a mobile telephone camera lens. The optic flow $\omega_{\Phi_i}^{meas}$ is measured using the “time of travel” scheme (see Figure 4.5b) which assesses the angular speed $\omega(\Phi_i)$ of any contrasting object detected by two neighboring photosensor signals by measuring the time lag Δt , as follow:

$$\omega_{\Phi_i}^{meas} = \frac{\Delta\varphi}{\Delta t} \quad (4.34)$$

where $\Delta\varphi$ is the inter-receptor angle (the angle between two adjacent optical axes). Like the Angular Sensitivity Function (ASF) of a single fly photoreceptor, each photosensor features a Gaussian angular sensitivity function (Götz, 1964), which can be adjusted by defocusing the lens from the sensor so that an appropriate bell-shaped ASF is projected onto the photosensor array, as occurs in some diurnal insects (Land, 1997) with:

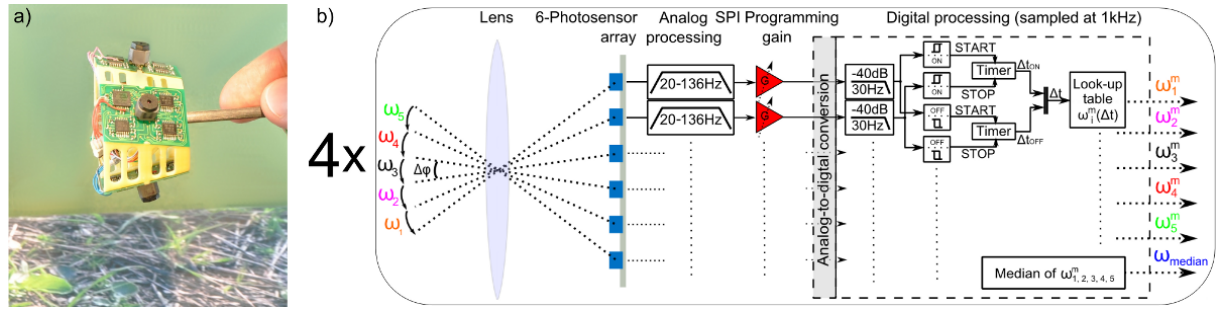


Figure 4.5: Quasi panoramic eye of the BeeRotor robot. **a)** BeeRotor’s eye with its four electronic boards composed of 5 adjacent programmable-gain visual motion sensors called “time of travel” EMDs. **b)** Processing architecture of one visual motion sensor. The visual signals emitted by each photoreceptor are filtered through an analog bandpass filter and a second order fixed-point digital low-pass filter. Before being digitized, the visual signals are amplified using the programmable gains controlled by a SPI bus in order to finely tune the dynamic range of the signals with respect to the ambient illuminance. Two neighboring signals are then thresholded. In parallel, the “time of travel” Δt elapsing between the two signals is measured by a timer: Δt_{ON} and Δt_{OFF} are measured, based on ON and OFF contrast distinguishing processes. These Δt are used to measure the 1-D angular speed $\omega_{\Phi_i}^{meas}$ within the visual field of each 1-D local motion sensor. Lastly, the 5 local motion sensors are combined to generate a robust and frequently refreshed 1-D median angular speed.

$$\Delta\varphi = \Delta\rho \quad (4.35)$$

where $\Delta\rho$ is the acceptance angle which corresponds to the width at half maximum of the Gaussian function. This defocusing acts as a spatial low-pass filtering process on the visual signals, which are then temporally filtered and amplified by means of the programmable gains which make it possible to finely tune the dynamic range of the visual signals with respect to the ambient illuminance (Ruffier & Expert, 2012). The other processing steps have been described in detail in (Roubieu et al., 2012). After digitization, the signals are low-pass filtered to eliminate high frequency signals mainly coming from the artificial lighting and then thresholded. Two separate processing pathways distinguish between ON (dark to light) and OFF (light to dark) contrasts, as previously found to occur in flying insects (Franceschini et al., 1989; Reiff et al., 2010; Eichner et al., 2011) and measure the time delay between two ON or OFF thresholded signals. Our visual motion sensor generates 5 simultaneous local measurements of the 1-D angular speed generated by a natural scene within a measurement range of more than one decade [$30^\circ/s$; $350^\circ/s$]. It also computes the median value ω_{median} of the 5 Elementary Motion Detectors (EMDs). The whole processing of the 5 local motion units and the calculation of the median value are carried out on a dsPIC33FJ128GP802 microcontroller working at a sampling frequency of 1kHz. The microcontroller embedded onboard each visual motion sensor is connected to the main electronic board via a SPI bus.

4.1.5 Results in autonomous flight

4.1.5.1 Eye reorientation

Measurement of the theoretical Reorientation angle in open loop Figure 4.6 shows the estimation of the angle of reorientation $\hat{\theta}_{Eye/slope}$ in blue superimposed with the theoretical reorientation angle $\theta_{Eye/slope}$ in red when the BeeRotor robot is flying at a constant speed and a constant altitude and we impose steps on the angle of the eye relatively to the

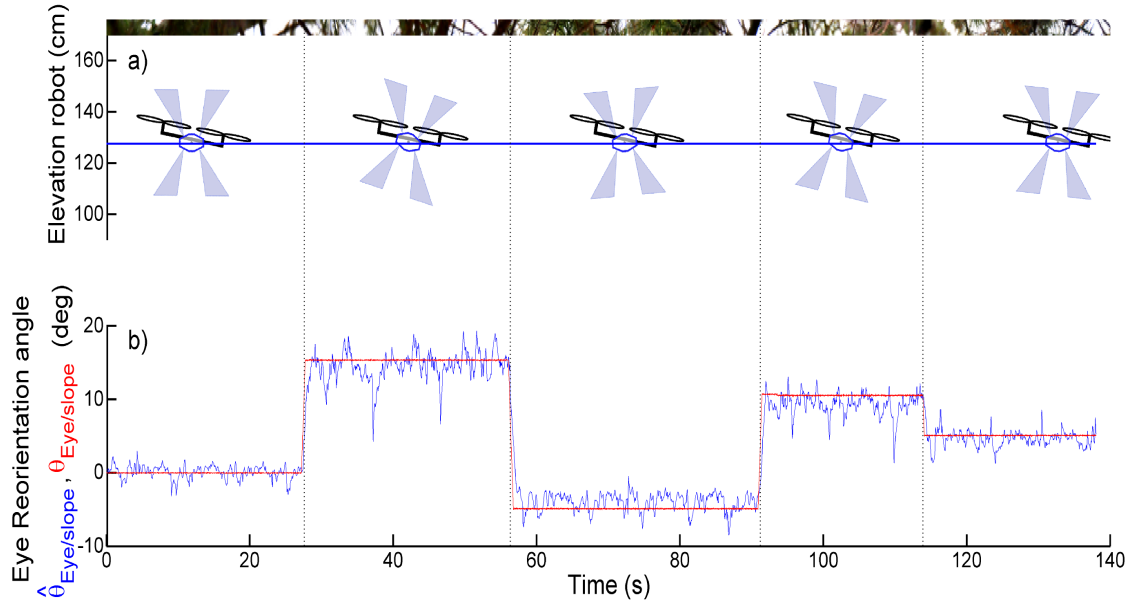


Figure 4.6: **a)** Trajectory of the BeeRotor aircraft while following a flat surface at a constant speed and constant altitude. As we can see, the gaze of the robot was regularly rotated thanks to the stepper motor modifying the estimation of the angle between the eye main direction and the closest wall $\hat{\theta}_{Eye/slope}$. **b)** Theoretical (red) and estimated (blue) reorientation angle. The reorientation angle was faithfully estimated thanks to the Least Squares approximation using the 10 measurements of the Elementary Motion Detectors.

body θ_{EiR} thanks to the stepper motor. The reorientation angle was estimated based on 10 EMDs as presented in section 4.1.3.3. Imposing a rotation of α to the eye is equivalent to the situation where the robot is following a surface tilted with the same angle α . As we can see, the reorientation angle is estimated with a good accuracy and responds almost immediately to a step of the pitch eye. The reorientation angle was slightly underestimated when the theoretical value got further away from zero due to the difference between the cosine square function and its approximation by a polynomial second order function.

Crash avoidance thanks to the reorientation of the eye This reorientation angle is then filtered and used in closed loop to always reorient the eye parallel to the surface. During flight, this reorientation angle depends on the angle between the eye's equator and the slope of the closest surface $\theta_{Eye/slope}$ and the direction of the velocity vector of the aircraft Ψ in the frame of reference attached to the eye. To assess the usefulness of the eye reorientation, we performed an experiment where we added an additional relief to the ground of the environment. The 1m-long flat part of the relief was replaced by a 30cm-high obstacle. The figure 4.7 shows the trajectory of the aircraft equipped with a fixed eye and a decoupled eye automatically kept parallel to the ground thanks to the strategy presented in section 4.1.3.3. In both cases, the forward speed and the altitude of the aircraft were automatically adjusted based on the measured optic flow thanks to the control loops described in 4.1.3.4. The fixed eye was kept at an angle of 0° relatively to the body. As we can see, thanks to the eye reorientation, the additional steep relief was avoided without crashing because the measured optic flow reflected with more accuracy the proximity of the ground. By studying at the eye orientation when flying over the obstacles, we observed that the eye pitched respectively forward in front of the ascending ramp and backward in front of

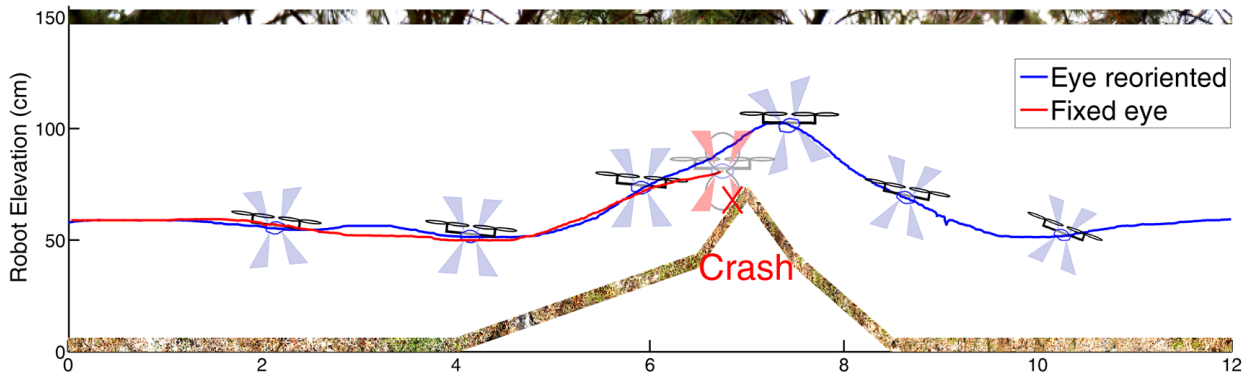


Figure 4.7: Trajectory of the BeeRotor robot while automatically following the ground thanks to a ventral optic flow regulator with a fixed eye (red) and a decoupled eye (blue) oriented in parallel with the ground thanks to a Least Squares Approximation based on the optic flow measurements. Thanks to the reorientation, the aircraft was able to detect earlier the increase of optic flow due to the added steep relief and avoid the obstacle without crashing. On the blue curve, the aircraft is represented every 1.5 second with the field of view of the 4 local motion sensors. As we can see, when flying over the ascending ramp of the ground, the eye orientation automatically pitched forward to line up with the surface and backward during the descending ramp. After a transient, the eye orientation reached back its steady state value when flying over the flat surface compensating for the pitch angle of the aircraft.

the descending ramp to align with the overflowed surface. In the flat part of the environment, the eye was oriented at an angle compensating the pitch angle of the aircraft. However, we can see that the eye reorientation process time constant is important as the eye required several meters to reach back its steady state. This is mainly due to the slow time constant chosen for the low-pass filter applied on the signal driving the stepper motor rotating the eye. We observed that, when we reduced this time constant, the eye reorientation was faster which created an important rotational optic flow superimposed with the translational optic flow and disturbing the extraction of the estimated reorientation angle $\hat{\theta}_{Eye/slope}$ often leading to oscillations of the eye.

4.1.5.2 Altitude and speed control

Figure 4.8a shows the BeeRotor robot while automatically following the terrain for several initial conditions and values of the Maximum OF setpoint $\omega_{setMaxOF}$ during ten consecutive turns in the environment described in section 4.1.4.5 with an obstacle on the ground and with an optic flow setpoint of the speed control loop $\omega_{setSumOF} = 250^\circ/s$. Regardless of the value of the Maximum OF setpoint, the aircraft avoided the relief thanks to the altitude control loop which detected an increasing optic flow when the aircraft was close to the relief and acted positively on the mean speed of the propellers to fly away from it. The magenta and green curves in Figure 4.8a correspond to a ground following behavior for two different values of the Maximum OF setpoint $\omega_{setMaxOF}$ which was equal respectively to $125^\circ/s$ and $180^\circ/s$. As expected, the aircraft flew at a higher altitude when the setpoint was smaller. Circular markers indicate the position of the robot every second showing that the forward speed of the aircraft was globally the same in the three conditions as the optic flow setpoint of the speed control loop $\omega_{setSumOF}$ was constant. However, by looking at the forward speed more precisely, we can notice that during each turn, the forward speed decreased when the aircraft was flying over the slanted relief where the size of the tunnel decreased. This decrease of the

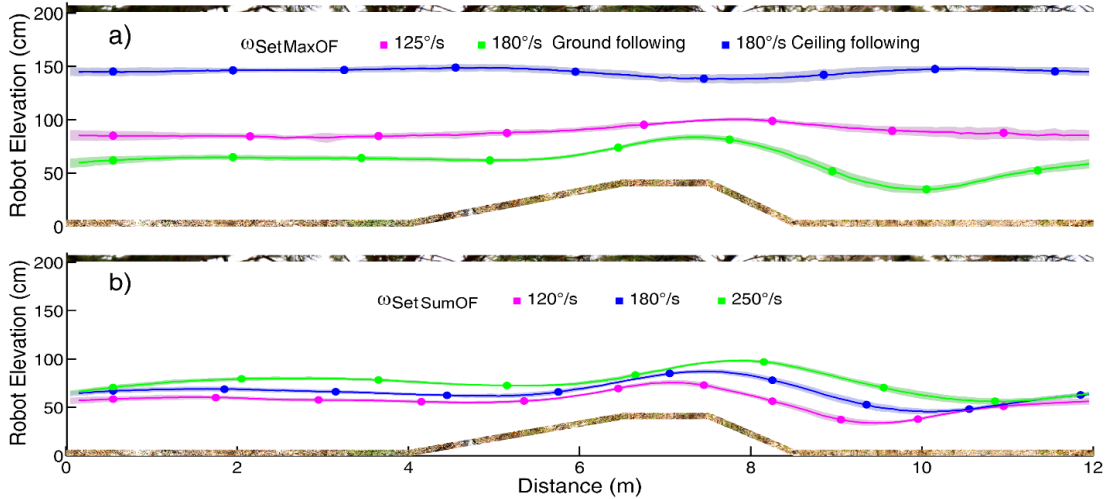


Figure 4.8: **a)** Automatic terrain following under optic flow regulation. Each curve shows the mean altitude of the aircraft with the corresponding standard dispersions during 10 consecutive turns of the aircraft on its environment with an optic flow setpoint of the speed control loop $\omega_{setSumOF} = 250^\circ/s$. Three different conditions have been represented: following the closest surface with $\omega_{setMaxOF} = 125^\circ/s$ (magenta), following respectively the ground (green) and the ceiling (blue) with $\omega_{setMaxOF} = 180^\circ/s$. As expected, the aircraft perfectly avoided the slanted relief thanks to the altitude control loop. When we increased the Maximum optic flow setpoint, the aircraft immediately came closer to the closest surface in order to reach the setpoint value. During the flight with $\omega_{setMaxOF} = 125^\circ/s$, the vehicle mainly followed the ground except when flying above the relief where at some point the ceiling was detected nearer than the ground. The reproducibility of the trajectories attest to the reliability of the BeeRotor robot in terrain following tasks. The position of the aircraft is indicated every 1s by a circular marker showing that the forward speed of the aircraft was roughly the same in the three experiments as the SumOF setpoint was the same. **b)** Altitude of the aircraft for three different values of the Sum Optic flow setpoint $\omega_{setSumOF}$ between $120^\circ/s$ and $250^\circ/s$ with an optic flow setpoint of the altitude control loop $\omega_{setMaxOF} = 150^\circ/s$. Although the MaxOF setpoint was always the same, the altitude of the aircraft increased with $\omega_{setSumOF}$ because the forward speed of the robot increased and the rotorcraft adjusted its altitude in order to maintain the ratio $\frac{V_x}{h}$ constant. As expected, the forward speed of the rotorcraft increased when we increased the setpoint value of the forward speed feedback loop. Due to the constriction of the total height of the tunnel with the relief, the forward speed of the aircraft decreased while overflying the obstacle and then increased again afterward.

forward speed was stronger when the aircraft was flying closer to the relief because the sum of the perceived ventral and dorsal optic flows increased more as the optic flow depends on the opposite of the distance with the observed surface. The blue curve represents the altitude of the aircraft when following the ceiling with the Maximum OF setpoint $\omega_{setMaxOF} = 180^\circ/s$ which is the same value than the green curve. Indeed, as soon as $\omega_{setMaxOF} \geq \frac{1}{2}\omega_{setSumOF}$, for one value of the Maximum OF setpoint, the aircraft can follow autonomously the ground or the ceiling depending on which surface is detected as the closest one. In the case the aircraft was following the ceiling, it flew at a globally constant altitude which slightly decreased when flying over the obstacle due to the tunnel constriction leading to a small decrease of the forward speed of the aircraft. Thanks to the integral coefficient of the controller, the distance between the aircraft and the ceiling was the same one than the distance between the aircraft and the ground when it was following the ground with the same value of the Maximum OF setpoint.

Figure 4.8b shows the influence of the Sum OF setpoint $\omega_{setSumOF}$ on the flight of the BeeRotor robot. The altitude of the aircraft following the ground is represented for three values of the Sum OF setpoint $\omega_{setSumOF}$ between $120^\circ/s$ and $250^\circ/s$ during 10 consecutive turns with an optic flow setpoint of the altitude control loop $\omega_{setMaxOF} = 150^\circ/s$. The altitude of the aircraft slightly increased with the Sum OF setpoint whereas the Maximum OF setpoint was constant. Indeed, due to the increase in the forward speed V_x of the aircraft when the Sum OF setpoint increased, the altitude control loop adjusted the rotorcraft's altitude by increasing the robot's thrust in order to keep the measured optic flow which depends on the ratio $\frac{V_x}{h}$ constant. The position of the aircraft is represented every second using circular markers showing that the forward speed of the aircraft increased when the Sum OF setpoint increased. Each time, due to the constriction of the tunnel with the relief, the perceived sum of the optic flows increased when flying over the obstacle causing the forward controller to decrease the setpoint of the nested feedback loop controlling the airspeed which eventually led to a decrease in the forward speed of the aircraft. Depending on the proximity of the relief, the increase of the sum of the ventral and dorsal optic flows was not detected at the same time leading to a time and magnitude differences in the deceleration of the aircraft. In this example, the magenta curves show the aircraft altitude and forward speed with $\omega_{setSumOF} = 120^\circ/s$ and $\omega_{setMaxOF} = 150^\circ/s$ which is paradoxical as the sum of the ventral and dorsal optic flows can not be smaller than the ventral optic flow. This can be explained by the fact that the forward controller which is a double phase lead controller has not been designed to guarantee a static gain of 1 of the feedback loop controlling the forward speed. All these results show the mean value of the altitude and the forward speed of the aircraft during 10 consecutive turns superimposed with their dispersion showing the robustness of the BeeRotor autopilot and the reproducibility of its trajectories.

4.1.5.3 Flight performances in non-stationary environment

As presented in section 4.1.4.5, the floor of the experimental tunnel can be rotated or moved up and down thanks to two actuators in order to assess the performances of the BeeRotor robot in a strongly unstationary environment. Figure 4.9 shows the altitude of the rotorcraft respectively for a stationary floor, a floor moving at 50cm/s in the same direction than the robot and a floor moving at 50cm/s in the opposite direction. Each curve represents the altitude of the aircraft during a 60m -long flight with $\omega_{setMaxOF} = 150^\circ/s$ and $\omega_{setSumOF} = 250^\circ/s$. As we can see, the aircraft flew at a lower altitude when the floor was rotating in the

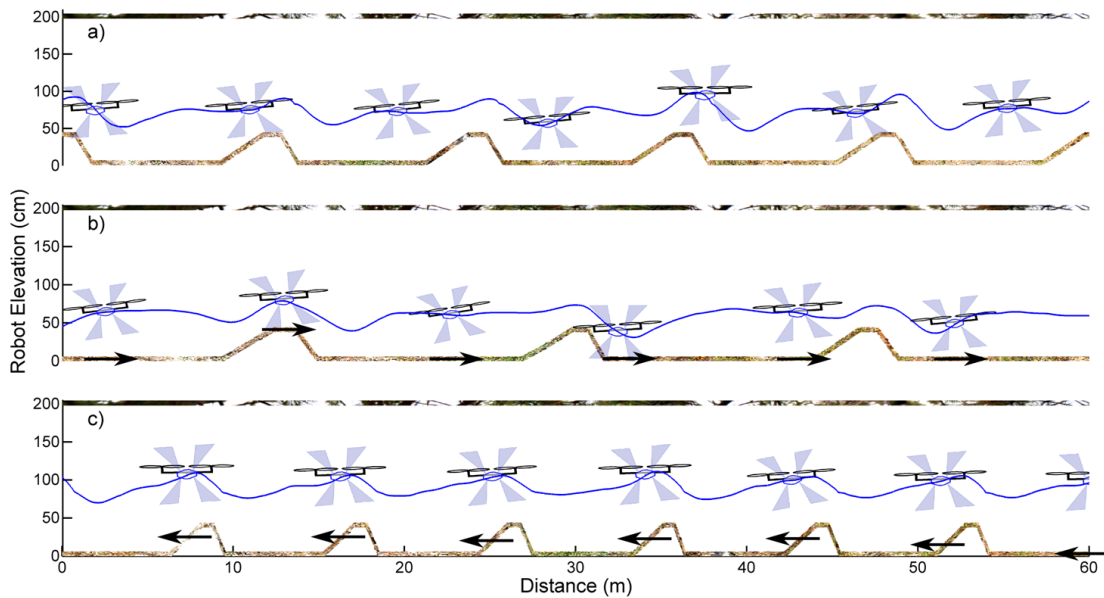


Figure 4.9: Automatic ground following under optic flow regulation with a moving floor. Each curve shows the altitude of the aircraft with $\omega_{setMaxOF} = 150^\circ/s$ and $\omega_{setSumOF} = 250^\circ/s$ respectively above a fixed, forward and backward moving floor. The aircraft oriented according to its pitch angle is represented every 6s with the fields of view of the 4 local motion sensors. **a)** Altitude of the aircraft with a stationary ground. **b)** Altitude of the aircraft with a ground moving at 50cm/s in the same direction than the aircraft. Again, the rotorcraft perfectly avoided the relief but at a smaller altitude. Indeed, in order to maintain its ventral optic flow equals to the Maximum OF setpoint value, the aircraft had to fly closer to the ground as the perceived optic flow was smaller due to the motion of the ground. **c)** Altitude of the aircraft with a ground moving at 50cm/s in the opposite direction of the aircraft. This time, the perceived optic flow was bigger due to the motion of the floor and the aircraft automatically flew at a higher altitude.

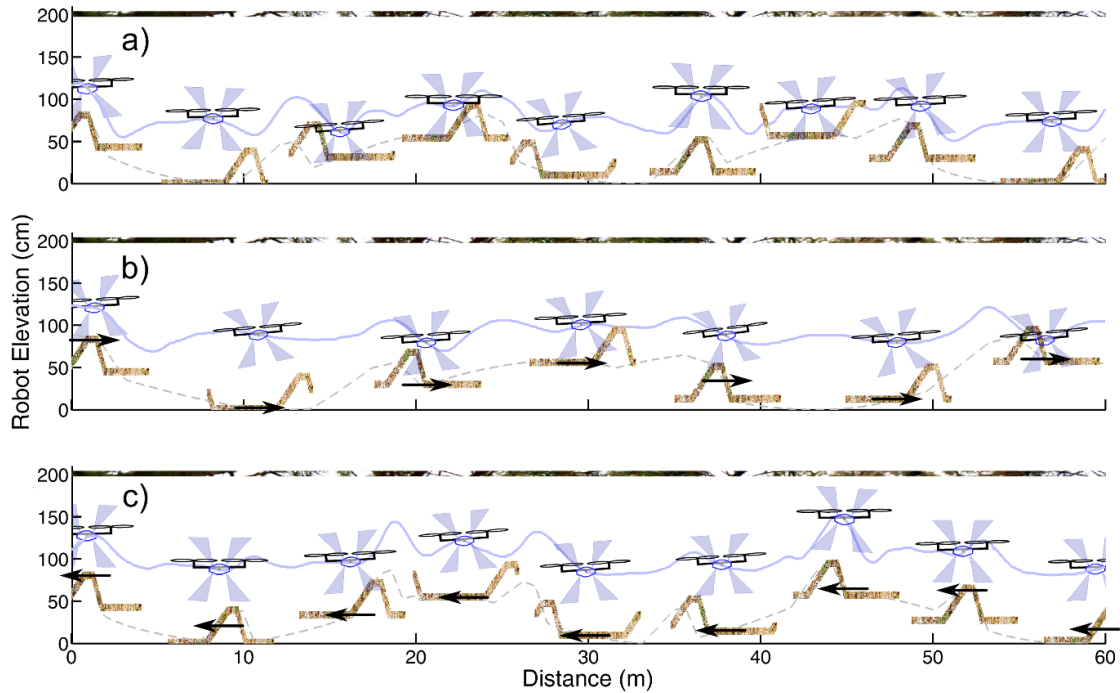


Figure 4.10: Automatic ground following under optic flow regulation with a moving and oscillating floor. Each curve shows the altitude of the aircraft during a 60-m long flight. In any case, the aircraft is represented oriented according to its pitch angle every 6s with the overflown ground. The dashed lines represent the altitude of the ground for each position considering the oscillations and the rotation of the ground and the relief. **a)** Altitude of the aircraft flying above the ground oscillating from 0 to 64cm with a 0.1Hz frequency. Despite the very strong perturbations on the measured optic flow due to the relief and the oscillations, the aircraft was still able to fly autonomously and avoid the obstacle while adjusting its forward speed to the constantly changing size of the tunnel. **b)** Altitude of the aircraft flying above the ground oscillating from 0 to 64cm with a 0.1Hz frequency with a ground moving at 50cm/s in the same direction than the aircraft. Again, the rotorcraft perfectly avoided the relief but at a higher speed and a smaller altitude relatively to the ground. **c)** Altitude of the aircraft flying above the ground oscillating from 0 to 64cm with a 0.1Hz frequency with a ground moving at 50cm/s in the opposite direction of the aircraft. This time, the perceived optic flow was greater due to the motion of the floor and the aircraft then automatically flew at a higher altitude and lower speed.

same direction than the aircraft (Figure 4.9b) navigating really close to the relief. Indeed, the perceived optic flow was reduced due to the motion of the ground and the altitude feedback loop decreased the mean speed of the propellers in order to compensate the decrease of the optic flow. On the other hand, when the floor was rotating in the opposite direction (Figure 4.9c), the perceived optic flow was greater and the aircraft altitude increased to maintain its optic flow to the setpoint value.

For each trajectory, the aircraft is represented every 6s. Due to the variations of the perceived optic flow caused by the ground motion, the sum of the ventral and dorsal optic flows varied. This led to an increase of the forward speed of the aircraft when the ground was moving in the same direction than the aircraft because the sum of the optic flows decreased and vice versa.

Figure 4.10 shows the altitude of the aircraft in a deeply changing environment where the ground altitude was oscillating while the ground was rotating in a forward or backward direction. In Figure 4.10a is represented the altitude of the aircraft while flying over a floor moving up and down with the position of the aircraft represented every 6s according to its

pitch orientation with $\omega_{setMaxOF} = 180^\circ/s$ and $\omega_{setSumOF} = 220^\circ/s$. The ground altitude was oscillating between 0 and 64 cm with a 0.1Hz frequency strongly disturbing the perceived ventral optic flow. Despite this important disturbance, the aircraft followed the ground and avoided the relief autonomously. Besides, the forward speed of the aircraft was constantly changing due to the variations in the tunnel size. In particular, we can notice that the aircraft flew at a higher speed when the altitude of the ground was minimal which explains why the rotorcraft altitude did not decrease as much as the ground altitude because the altitude feedback loop acted on the propellers' speed in order to maintain its ventral optic flow equals to the Maximum optic flow setpoint value.

The same experiment has been reproduced with the ground rotating at 50cm/s in the same direction as the aircraft with $\omega_{setMaxOF} = 125^\circ/s$ and $\omega_{setSumOF} = 280^\circ/s$ (Figure 4.10b) and with the ground rotating at 50cm/s in the opposite direction with $\omega_{setMaxOF} = 175^\circ/s$ and $\omega_{setSumOF} = 250^\circ/s$ (Figure 4.10c). In any case, the aircraft was able to automatically adjust its altitude and forward speed based on the measured optic flow and avoid the relief. The aircraft flew at a lower altitude and higher speed when the ground was rotating in the same direction because the perceived optic flow was smaller. On the other hand, the aircraft flew at a higher altitude and lower speed with the regressive floor.

4.1.5.4 Rejection of pitch disturbances

To assess the robustness of the autopilot embedded onboard the BeeRotor robot, we applied manually strong perturbations to the pitch angle of the aircraft while automatically following the stationary ground with $\omega_{setMaxOF} = 150^\circ/s$ and $\omega_{setSumOF} = 250^\circ/s$. Figure 4.11a shows a 25m-long trajectory of the aircraft where we imposed a strong negative step on the pitch angle of the robot around 8m and a positive step on the pitch angle after 20m. The pitch angle of the robot is represented in Figure 4.11c and we can clearly distinguish the negative pitch step of almost -20° and the positive pitch step of more than 10° whereas the pitch angle of the aircraft during autonomous flight generally lies around 5° . Although these perturbations clearly affected the trajectory of the rotorcraft, it was still able to avoid the relief and regain its altitude after a few meters. As the pitch angle directly affects the forward speed of the aircraft, the negative step of the pitch angle strongly reduced its forward speed (see Figure 4.11b) whereas the positive step was immediately rejected by the aircraft feedback loops almost without affecting the altitude or the forward speed of the robot.

4.1.6 Beerotor autopilot without any need for an accelerometer and an airspeed sensor

As we have discussed in the introduction, in the fly, antennae seem to play an important role in the regulation of flight speed. In our robotic implementation, the airspeed sensor could be compared with the insects antenna. However, on the fly, the position of the antennae is actively controlled and adjusted during flight in the "antennal positioning reaction" which enhances the ability of insects to sense changes in airspeed (Mamiya et al., 2011). This could indicate that the antennae are only sensitive to the air acceleration which could be used in a nested feedback loop. With our custom-made airspeed sensor, we tried to use the changes in airspeed but, due to the noise on the signal, this measurement was not satisfactory to be used onboard the aircraft.

However, it seemed interesting to test the ability of the BeeRotor robot to fly in its

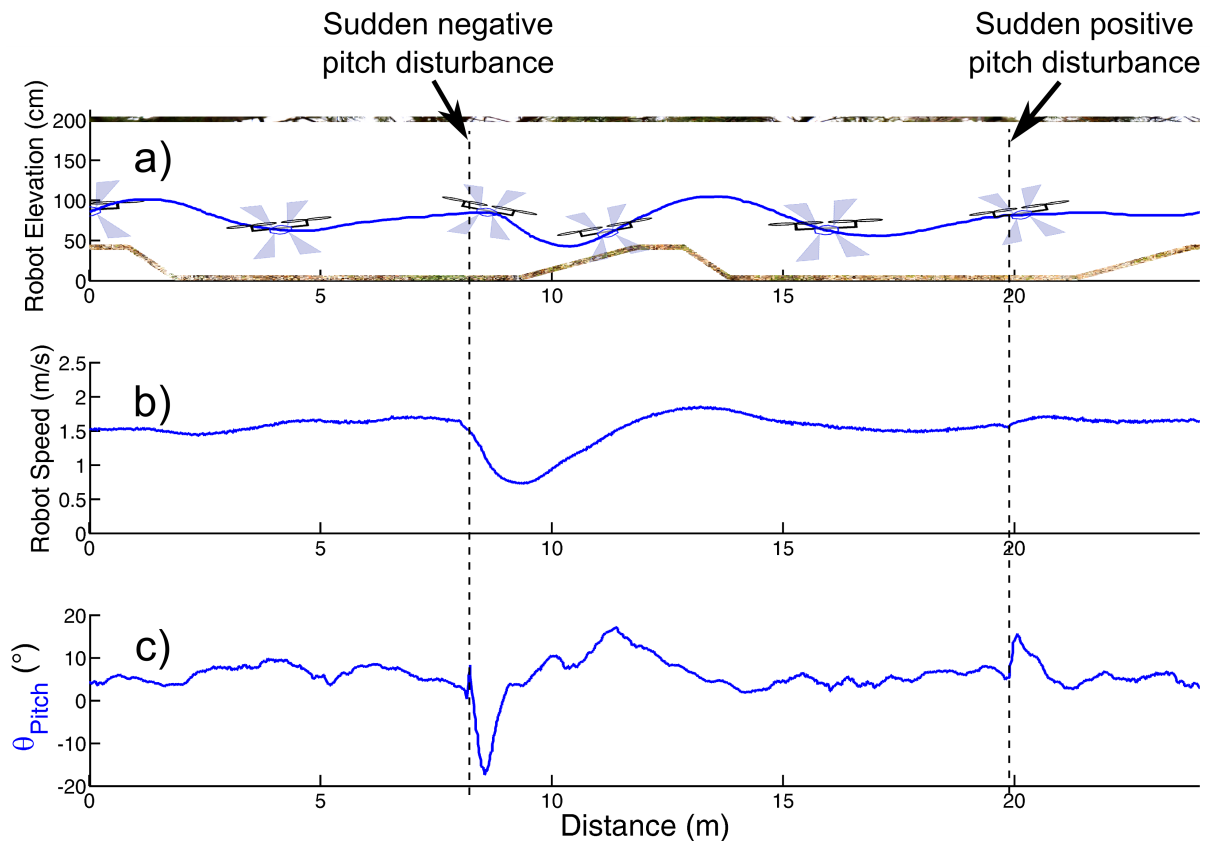


Figure 4.11: Robustness of the BeeRotor robot autopilot to strong perturbations of its pitch angle. **a)** Altitude of the aircraft flying autonomously with $\omega_{setMaxOF} = 150^\circ/s$ and $\omega_{setSumOF} = 250^\circ/s$. We manually imposed a strong negative step on the pitch angle of the robot around 8m and a positive step on the pitch angle one turn after. Despite the strong perturbations on the pitch angle, the aircraft was still able to fly autonomously while avoiding the relief and recovered its altitude quickly after the perturbation. The position and the orientation of the robot are represented regularly and we can clearly see the strong perturbations on the pitch angle right after the perturbation. **b)** Speed of the BeeRotor robot during the perturbation experiment. As we can see, the forward speed was strongly affected by the pitch perturbations but then quickly recovered to its steady state. **c)** Pitch angle of the robot measured thanks to the complementary filter but not used by the autopilot to control the aircraft. We clearly see the strong perturbations imposed on the aircraft up to -20° whereas the aircraft pitch angle normally lies around 5° .

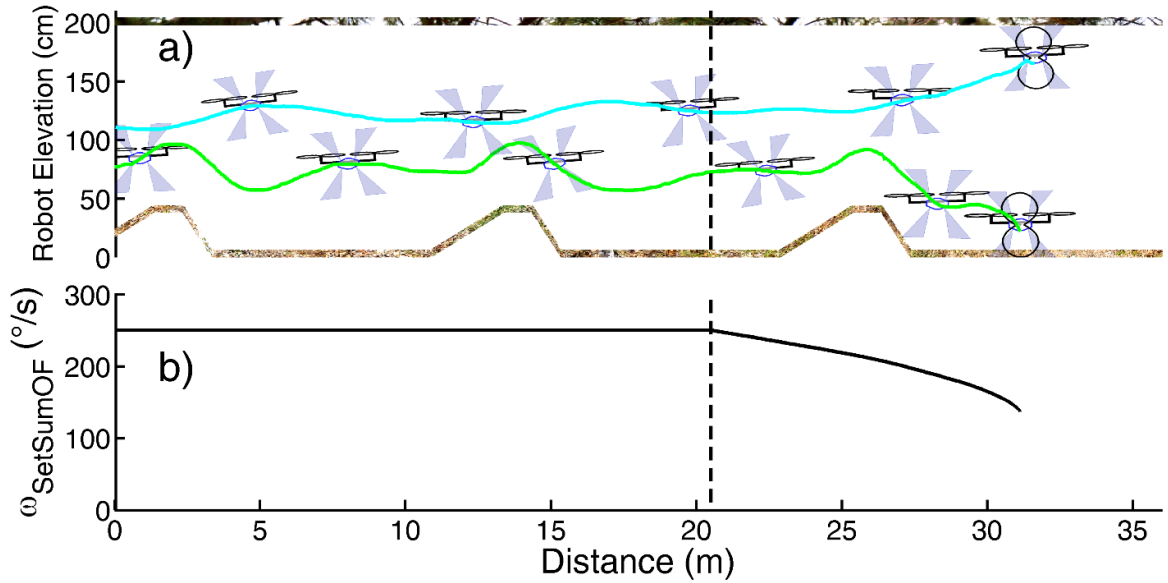


Figure 4.12: Automatic surface following and landing or docking of the aircraft respectively on the ground and on the ceiling achieved by dynamically changing the Sum OF setpoint $\omega_{setSumOF}$. The dotted line indicates the moment we started the landing procedure. **a)** Altitude of the BeeRotor robot in the 12-m long naturally contrasted environment during automatic surface following and landing or docking. The altitude is plotted in cyan when the nearest wall detected is the ceiling and in green when the nearest wall detected is the ground. Automatic landing or docking was induced by decreasing the Sum OF setpoint $\omega_{setSumOF}$, which decreased the horizontal speed V_x while keeping the Maximum OF setpoint $\omega_{setMaxOF}$ constant. The BeeRotor robot therefore adjusted its altitude to compensate for the decrease in the optic flow due to the deceleration and moved closer to the floor or the ceiling depending on the closest surface detected, which resulted in automatic landing or docking at a horizontal speed of almost zero. The BeeRotor robot is represented at the end of the landing procedures with its protection archs to show that the aircraft reached touchdown. **b)** Optic flow setpoint of the forward speed feedback loop $\omega_{setSumOF}$. Before starting the landing procedure at a distance of around 20m, this setpoint was kept constant and therefore the aircraft automatically followed the closest surface. After 20m, we decreased $\omega_{setSumOF}$ rampwise from 250 $^{\circ}/s$ to 100 $^{\circ}/s$ (in a 10 $^{\circ}/s$ ramp) inducing the landing.

environment without the feedback loop controlling the airspeed as it has been observed in insects that antennae amputation led to a degradation of the flight performances. This is why the autopilot embedded in the BeeRotor robot has been modified and the feedback loop based on the airspeed sensor has been removed (see Figure 4.3). In this configuration, the aircraft only relies on the measurements of the optic flow sensors and the rate gyro to control its forward speed, its clearance from the walls and to automatically orient its eye relatively to the closest surface. Only the blue feedback loop controlling the forward speed of the aircraft has been modified and the surge controller (which is in that case a Proportional Derivative controller) output is now directly used as a setpoint by the nested feedback loop controlling the pitch rate.

4.1.6.1 Surface following without any need for an accelerometer and an airspeed sensor

Despite the suppression of the airspeed feedback loop, we can see in Figure 4.12a that the aircraft can still follow a terrain and control its forward speed based on the ventral and dorsal optic flows while robustly avoiding obstacles. With the same setpoint values

$\omega_{setMaxOF} = 150^\circ/s$ and $\omega_{setSumOF} = 250^\circ/s$, the altitude of the aircraft is represented while following the ground (green curve) and the ceiling (cyan curve).

Whereas the aircraft can still control its forward speed thanks to the sum of the ventral and dorsal optic flows without the inner feedback loop regulating the airspeed, we noticed that, despite the constriction of the tunnel due to the relief, the forward speed did not decrease when flying over the obstacle. On the contrary, the forward speed was mainly increasing when flying over the obstacle due to the altitude control loop. Indeed, when the relief was detected by the ventral optic flow sensor, the altitude control loop increased the robot's thrust in order to avoid the obstacle. Due to the robot pitch angle, the thrust can be decomposed in two components acting respectively on the surge and the heave. When the mean speed of the propellers Ω_{Rotors} increased, this automatically resulted in an increase of the altitude and the forward speed of the aircraft. With the airspeed sensor, this forward speed increase was immediately detected and compensated by the airspeed feedback loop. We can conclude from this experiment that, similarly to the flying insects, the BeeRotor robot can still fly autonomously without sensing the airspeed but not without degrading its flying performances.

4.1.6.2 Automatic landing without any need for an accelerometer and an airspeed sensor

Biological inspiration From behavioral experiments performed on honeybees and by recording how these insects can land at a constant speed on a flat surface, Srinivasan et al. (Srinivasan et al., 2000) presented two main characteristics explaining flying insects smooth landings:

- “flying insects tend to hold constant the angular velocity of the image of the surface as they approach it,
- the instantaneous speed of descent is proportional to the instantaneous forward speed”.

Inspired by these experiments, a landing strategy is proposed here holding constant the OF of the image of the nearest wall while reducing the forward speed of the aircraft leading to a smooth landing or docking with almost no speed at touchdown. However, this strategy does not insure that the descent angle is kept constant throughout the whole landing and therefore that the speed of descent is proportional to the instantaneous forward speed.

Results In order to induce an automatic landing, after a little more than 20m (dotted line), we decreased the Sum OF setpoint $\omega_{setSumOF}$ rampwise from $250^\circ/s$ to $100^\circ/s$ in a $10^\circ/s$ ramp (see Figure 4.12b) so as to gradually decrease the horizontal speed V_x . In order to keep the maximum optic flow constant, the altitude control loop gradually decreased the distance between the nearest wall detected and the aircraft, so that the latter eventually landed or docked with a negligible forward speed at touchdown. The duration of the landing was directly determined by the slope of the ramp imposed to the Sum OF setpoint.

Using only 4 feedback loops based on the pitch rate measured thanks to a rate gyro and on the optic flow measured thanks its quasi-panoramic eye, the BeeRotor rotorcraft proved to be able to navigate autonomously and smoothly land or dock in an unknown environment using simple strategies borrowed from flying insects.

4.1.7 The vertical OF: an additional cue for the Beerotor autopilot

4.1.7.1 Definition of the Vertical OF

During experiments on *Drosophila* freely flying in a 3D virtual reality environment, Straw et al. have shown that a ventral expansion avoidance reflex is used by insects to control their altitude as they measured an increasing climb rate when flying over an expanding stimulus (Straw et al., 2010). Such reflex does not conflict with a ventral optic flow regulator and both could be used together with the expansion avoidance reflex only triggered by a strong stimulus overriding all others behaviors. In our case, as we are flying in translation in a tunnel with optic flow sensors looking only downward and upward, we can not measure expansion that only appears in front of the aircraft near the focus of expansion. However, we have shown in section 4.1.3.1 that the difference of the two ventral or dorsal optic flows depends on the ratio between the vertical speed V_z and the distance to the surface h (see equation (4.8)). This could then be used to control the climb rate of the BeeRotor robot or to detect the increasing proximity of an object and fly away from it. As the vertical speed is always smaller than the horizontal speed, this measurement will be most of the time a lot smaller than ω_{MaxOF} except when the aircraft comes really close to an object. Depending on the closest surface, the Vertical OF is computed using:

$$\omega_{Ventral\ VerticalOF}^{meas} = \frac{1}{\sin(2\gamma)} \cdot (\omega_{\gamma}^{median} - \omega_{-\gamma}^{median}) \quad (4.36)$$

$$\omega_{Dorsal\ VerticalOF}^{meas} = \frac{1}{\sin(2\gamma)} \cdot (\omega_{180^\circ+\gamma}^{median} - \omega_{180^\circ-\gamma}^{median}) \quad (4.37)$$

where ω_{γ}^{median} is the median optic flow of the local motion sensor looking in the direction γ .

Coupled with a ventral optic flow regulator, the computed Vertical OF should always be close to zero as the altitude of the aircraft will always be kept constant to maintain a safe distance with the followed surface according to its forward speed. However, if the Vertical OF strongly increases or decreases, it means that the aircraft is suddenly getting respectively nearer or further to an obstacle and this information can be used to control the robot.

4.1.7.2 Feedforward control of the Vertical OF

To improve the performances of the BeeRotor robot, we added in the altitude control loop a second feedback loop based on the measured Vertical OF $\omega_{VerticalOF}^{meas}$ which was used to control the altitude of the aircraft thanks to a feedforward controller (see Figure 4.3). The output of this controller is added to the output signal of the same Altitude controller used previously. This inner loop can be said to act as a ventral or dorsal expansion avoidance reflex. Indeed, when the aircraft is flying away from obstacles, the measured Vertical OF will be low and the altitude of the aircraft will mainly be determined by the previous altitude control loop using the maximum value between the ventral and dorsal optic flows to control the thrust of the robot. On the other hand, a strong increase of the Vertical OF indicating an approaching object will cause through the feedforward controller an increase or a decrease in the vertical lift keeping the aircraft away from danger. In the same way, an important decrease of the Vertical OF will lead to a reduction or an augmentation of the mean speed of the propellers Ω_{Rotors} .

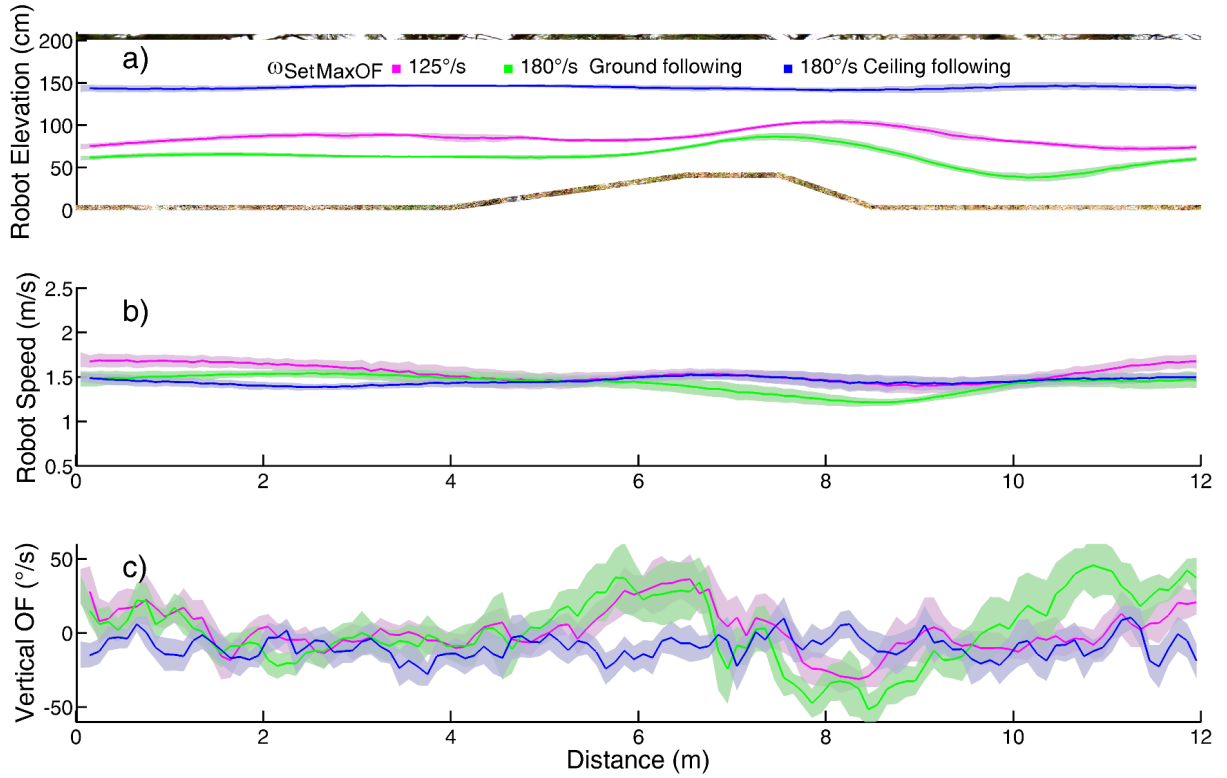


Figure 4.13: Automatic ground-hugging under optic flow regulation with a feedforward controller based on the Vertical optic flow and acting on the Vertical lift. Each curve shows the mean altitude, speed and Vertical optic flow of the aircraft with the corresponding standard dispersions during 10 consecutive turns of the aircraft on its environment with an optic flow setpoint of the speed control loop $\omega_{setSumOF} = 250^\circ/s$. **a)** Altitude of the aircraft for three different conditions: following the closest surface with $\omega_{setMaxOF} = 125^\circ/s$ (magenta), following respectively the ground (green) and the ceiling (blue) with $\omega_{setMaxOF} = 180^\circ/s$. As expected, the aircraft perfectly avoided the slanted relief thanks to the altitude control loop. When we increased the Maximum optic flow setpoint, the aircraft immediately came closer to the closest surface in order to reach the setpoint value. Thanks to the feedforward controller on the Vertical OF, the oscillation after the obstacle was reduced. **b)** Forward speed of the rotorcraft in the three conditions. The steady-state forward speed was the same in the three experiments as the Sum OF setpoint was the same. **c)** Vertical OF of the aircraft. When following the ceiling, $\omega_{VerticalOF}^{meas}$ was always close to $0^\circ/s$ whereas it increased during the ascending ramp and decreased during the descending ramp of the relief while the aircraft followed the ground.

The figure 4.13 shows the BeeRotor robot while automatically following the terrain for several initial conditions and values of the Maximum OF setpoint $\omega_{setMaxOF}$ during ten consecutive turns with an optic flow setpoint of the speed control loop $\omega_{setSumOF} = 250^\circ/s$. Regardless of the value of the Max OF setpoint, the autopilot incorporating a feedforward controller based on the Vertical OF avoided the relief. In the bottom part is represented the value of the Vertical OF which was most of the time around $0^\circ/s$. In particular, when following the ceiling at a constant altitude, the Vertical OF did not significantly differ from $0^\circ/s$ having no influence on the behavior of the aircraft. On the other hand, when following the ground with the slanted relief and in particular when the Max OF setpoint increased (green curve), the robot flew closer to the objects leading to variations of the Vertical OF that helped the rotorcraft to avoid the obstacle. In particular, we noticed that the Vertical OF decreased after the relief when the aircraft was flying down to restore its ventral optic flow leading to an increase in the speed of the propellers thanks to the feedforward controller. This is particularly interesting as it limited the amplitude of the aircraft's bounce of altitude after the relief.

Although not affecting deeply the behavior of the aircraft with our experimental setup, such strategy would allow freely flying aircraft or insects to more robustly avoid obstacles and therefore navigate collision-free in an unknown environment.

4.1.7.3 Regulation of the Vertical OF during landing

As we have seen in section 4.1.3.1, the Vertical optic flow is proportional to the ratio between the vertical speed V_z and the distance h to the surrounding objects. Thanks to the altitude control loop regulating the ventral or dorsal optic flow, the distance h to the objects is theoretically always kept constant. By coupling the altitude control loop with a feedback loop controlling the forward speed of the aircraft based on the vertical OF, we can induce an automatic landing. Indeed, by taking the difference between a positive setpoint value $\omega_{setVerticalOF}$ and the measured Vertical OF and use it to drive a lead phase regulator controlling the robot forward speed thanks to the two already presented nested feedback loops acting on the airspeed and the pitch rate, the aircraft will automatically reduce its forward speed in order to generate a non null vertical speed thanks to the altitude control loop.

Such strategy leads to a smooth landing with almost no speed at touchdown where the duration of the landing depends on the chosen setpoint $\omega_{setVerticalOF}$. The proposed autopilot is presented in figure 4.14 with the altitude control loop (in red) using the maximum value between the ventral or the dorsal optic flow compared with a setpoint value to act on the vertical lift of the aircraft and therefore its altitude. Contrary to the previous experiments, the speed control loop (in blue) is here based on the difference between a fixed setpoint and the measured Vertical OF $\omega_{VerticalOF}^{meas}$ which is used to control the forward speed of the BeeRotor robot. The Vertical OF controller is in that case a simple phase lead controller increasing the damping of the system and hence its stability.

Figure 4.15 shows the automatic landing of the aircraft obtained when the forward speed of the aircraft was controlled by the vertical OF for two different values of the Vertical OF setpoint: $50^\circ/s$ and $35^\circ/s$. In any case, the aircraft immediately decreased its forward speed and therefore came nearer to the ground as the altitude control loop decreased the vertical lift to maintain its ventral optic flow constant. As expected, the slope of the deceleration increased with the setpoint value allowing to control the descent speed of the aircraft or the duration of the landing procedure. In both cases, the aircraft is represented with the fields of view of the 4 visual motion sensors. In conclusion, the Vertical OF can not only be used as a ventral expansion reflex but also to control the vertical speed of the aircraft leading to a smooth landing on the ground at a forward speed close to 0.

4.1.8 Discussion

Following the early results obtained with the BeeRotor robot (Expert & Ruffier, 2012), we have shown here and for the first time, the autonomous flight of a bio-inspired tandem rotorcraft in a complex and unstationary environment without accelerometer and based on an autopilot relying exclusively on measurements defined in a frame of reference attached to the aerial robot's eye. The autopilot onboard the aircraft uses almost exclusively the optic flow generated by the robot own motion inside a high-roofed tunnel where the ground and ceiling are covered with natural patterns to adjust the speed of the propellers and automatically reach a "safe height and forward speed". Based on three feedback loops regulating the maximum between the ventral and dorsal optic flows and the sum of these optic flows and orienting the robot's eye, the aircraft was able to autonomously follow a terrain, adjust its forward speed to the size of the tunnel and avoid obstacles.

To do so, the aircraft is equipped with a quasi-panoramic eye processing the optic flow generated by the ground and the ceiling which is automatically kept parallel to the closest surface thanks to a Least Squares approximation based on the optic flow pattern formed by the array of Elementary Motion Detectors (EMDs). This reorientation increases the ability of the BeeRotor aircraft to avoid obstacles while eliminating the need for an absolute reference indicating the vertical direction like an accelerometer which is commonly used on flying aircraft nowadays. As we have observed, the eye reorientation is quite slow to avoid the addition of an important rotational optic flow to the measurement of the eye disturbing the computation of the reorientation angle. With a fixed panoramic eye measuring the optic flow from every direction, the eye of the angle respectively to the surface could be determined faster and reflect with more accuracy the optic flow generated by the followed surface increasing the ability of the aircraft to follow a terrain at short range while avoiding important reliefs.

In addition to its eye which can be compared to the compound eye of flying insects, the

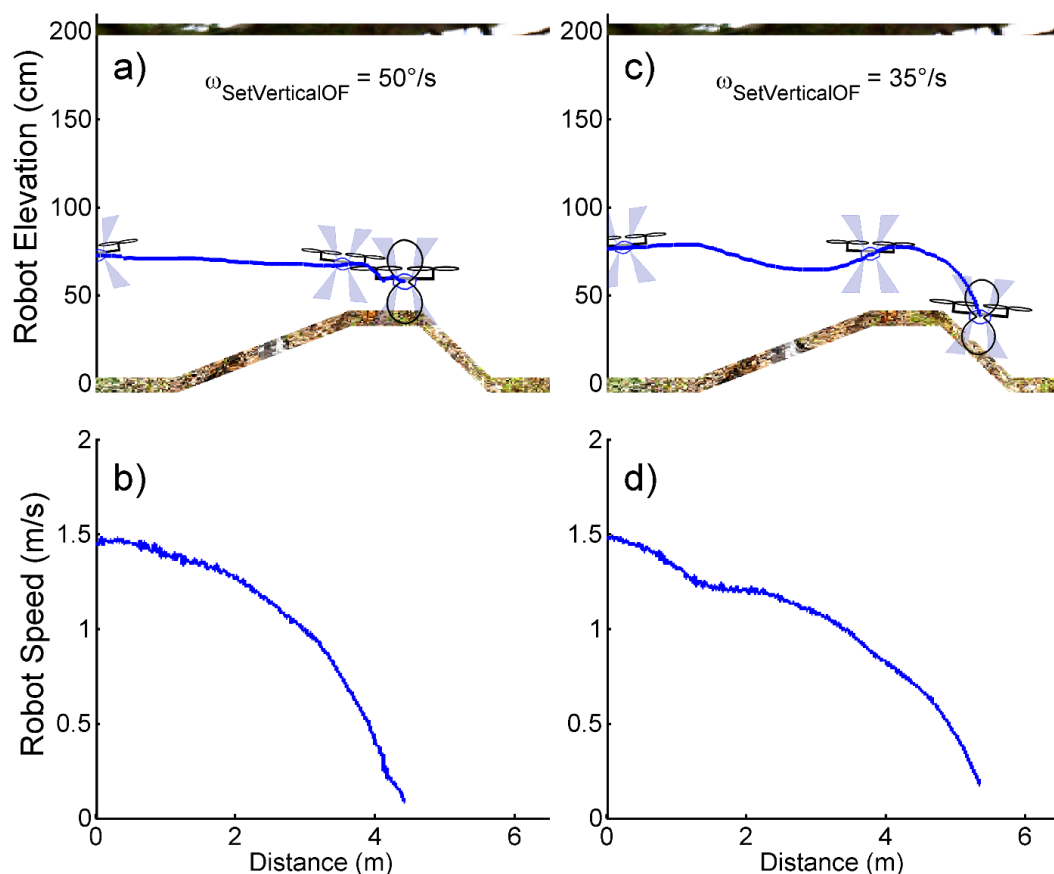


Figure 4.15: Automatic landing of the aircraft on the ground achieved by controlling the forward speed feedback loop with the Vertical optic flow. **a-c)** Altitude of the BeeRotor robot during automatic landing with $\omega_{setMaxOF} = 150^\circ/s$ and two different values of the Vertical OF setpoint $\omega_{setVerticalOF} = 50^\circ/s$ and $\omega_{setVerticalOF} = 35^\circ/s$. In both cases, the aircraft successfully landed and the duration of the landing increased when the Vertical OF setpoint $\omega_{setVerticalOF}$ decreased. **b-d)** To reach the setpoint value $\omega_{setVerticalOF}$, the rotorcraft reduced its forward speed leading to a loss of altitude induced by the feedback loop regulating the ventral optic flow and hence a smooth landing with almost no speed at touchdown.

aircraft is equipped with a rate gyro sensitive to the inertial forces similarly to the halteres of Diptera which have been found to be sensitive to the Coriolis forces (Fraenkel & Pringle, 1938) and with a custom-made anemometer sensing the airspeed like the hairs and antennas of flying insects (Campan, 1964; Gewecke & Schlegel, 1970). However, it is not clear if these organs detect airspeed or changes in airspeed. In simulation, we showed that we could control the robot with an inner feedback loop controlling the changes of airspeed instead of the airspeed but the noise on the derivated signal of our custom-made airspeed sensor destabilized the real system.

The BeeRotor robot also proved to be able to land or dock automatically thanks to the optic flow using bio-inspired strategies inspired from recordings of the honeybees grazing landings (Srinivasan et al., 2000). By always regulating its ventral or dorsal optic flow while decelerating by decreasing its Sum OF setpoint or by regulating its Vertical OF, the aircraft automatically flew closer to one of the surrounding walls, thus maintaining a “safe height” that suitably matches its speed V_x by keeping the ratio between these two variables constant. These simple strategies led to automatically land or dock depending on the closest surface with a negligible forward speed at touchdown without necessitating any equipment or extra sensor in the aircraft or on the ground. Although not shown here, the aircraft was also able to automatically take-off in closed loop thanks to its three feedback loops with only a slew rate on the setpoint inner feedback loop controlling the pitch rate to insure that the aircraft did not accelerate too much before measuring relevant optic flow.

Similarly to the ventral expansion avoidance reflex discovered recently on freely-flying flies (Straw et al., 2010), the BeeRotor autopilot also relied on a measurement of the Vertical OF which depends on the ratio between the vertical velocity V_z and the distance to objects which was here used to increase the ability of the aircraft to avoid obstacles. Due to the limitation of the experimental setup, the major beneficial effect of the feedforward controller based on the Vertical OF to control the altitude was hard to demonstrate as the involved vertical velocities were lows limiting the range of the Vertical OF.

It has been shown that flying insects ascend under tailwind and descend under headwind (Kennedy, 1951) which is consistent with the behavior observed on the OCTAVE robot equipped with a ventral optic flow regulator (Ruffier & Franceschini, 2005; Franceschini et al., 2007). On the BeeRotor robot, as we also control the forward speed on the basis of the sum of the ventral and dorsal optic flows, in presence of wind, the speed or altitude of the aircraft would only be affected transiently before the autopilot would correct the trajectory and reach back its steady state. We can hypothesize that the control of forward speed by holding constant the global optic flow which has been proven during experiments on honeybees in several tunnels presenting visual contrasts in at least two opposite directions do not apply when the insect is flying in a landscape where mainly the ground offers visual features.

The autonomous BeeRotor aircraft inspired by the insect world in terms of its visual processing system and its sensory modalities has shown great performances in a complex and unstationary environment although it requires remarkably few resources. By taking inspiration from flying insects which have polished their flying strategies through millions of years of evolution, we can endow MAVs embedding a very small payload with reliable alternative means of performing complex flying maneuvers adapted to any environment.

In the near future, the BeeRotor robot will be equipped with the recently developed CurvACE sensor (Floreano et al., 2013) which is the first Curved Artificial Compound Eye able to process the angular speed over a very wide field of view and range of illuminance

background. Thanks to its semi cylindrical field of view, several regions of interest could be chosen to extract optic flow and the reorientation of the eye could be replaced by a dynamic change of the regions of interest.

APPENDIX 1: IDENTIFIED TRANSFER FUNCTIONS

$G_{propeller}(s)$	$\frac{4.116}{0.1398s+1}$
$G_{Speed}(s)$	$\frac{0.10498}{5.4312s+1}$
$G_{PitchRate}(s)$	$\frac{-0.042s-0.02683}{0.001742s^2+0.05445s+1}$
$G_{FwdSpeed}(s)$	$G_{Speed}(s) \cdot \frac{1}{s} \cdot G_{Pitchrate}(s)$
$G_{speedCL}(s)$	$\frac{1.0395}{1.62s^2+0.994s+1}$
$G_{SumOF}(s)$	$C_{Forward}(s) \times G_{speedCL}(s) \times \frac{d}{dVx}(\omega_{Vtrl} + \omega_{Drsl})$
$G_{Alt}^{\Theta_{pitch}}(s)$	$\frac{K_{alt}}{s^2+2\zeta_{alt}\omega_0s+\omega_0^2}$
$G_{Alt}^{3.5^\circ}(s)$	$\frac{0.1202}{0.8616s^2+0.33s+1}$
$G_{Alt}^{15.3^\circ}(s)$	$\frac{0.419}{3.8852s^2+1.833s+1}$
$G_{MaxOF}(s)$	$C_{Altitude}(s) \cdot G_{Alt}(s) \cdot \frac{d}{dh}(\frac{1}{h})$

Table 4.1: Transfer functions of the BeeRotor robot.

APPENDIX 2: CONTROLLERS IMPLEMENTED ONBOARD BEEROTOR

$C_{Propeller}(s)$	$\frac{0.5s+5}{s}$
$C_{PitchRate}(z)$	$\frac{0.1057z^2-0.2056z+0.1}{0.005z^2+0.005z}$
$C_{Airspeed}(z)$	$\frac{0.0626z-0.06}{0.01z}$
$C_{Forward}(s)$	$5 \times \left(\frac{9s+26}{s+8.665}\right) \times \left(\frac{9s+26}{s+8.665}\right) \times \left(\frac{1}{0.6s+1}\right)$
$C_{Feedforward}(s)$	$\frac{0.05874s^2+0.002335s-0.1104}{s^2+20s+96.07}$
$C_{VerticalOF}(s)$	$\frac{450s+1300}{s+8.665}$
$C_{Altitude}(s)$	$\left(\frac{1.5s+0.3}{s}\right) \times \left(\frac{1.866s+1}{0.134s+1}\right) \times \left(\frac{1.866s+1}{0.134s+1}\right) \times \left(\frac{1}{0.6s+1}\right)$
$C_{Eye}(s)$	$\frac{0.0375s+0.5003}{s+0.5013}$

Table 4.2: Transfer functions of the controllers embedded onto the BeeRotor robot.

4.2 Fully cylindrical CurvACE on the BeeRotor robot

As we have seen, the BeeRotor robot equipped with only Local Motion Sensors, a rate gyro and a custom-made airspeed sensor is able to automatically control its clearance from the walls while adjusting its forward speed to the size of the tunnel it is traveling in by using simple control strategies borrowed from flying insects. However, as the aircraft mainly relies on optic flow to control its flight, its performances are directly linked to the capacity of the robot to extract visual features thanks to its eye. As soon as the illuminance is too high, thus saturating the pixels, or too low, preventing the system from detecting any contrast, the BeeRotor robot will inexorably crash after a few seconds into one of the walls. This is the reason why we equipped the robot with the CurvACE sensor presented in chapter 3 which, with its pixels automatically adapting to the background illuminance and its very wide field of view, perfectly suits the needs of the autopilot embedded into the BeeRotor robot.

4.2.1 Mechanical assembly of fully cylindrical CurvACE and BeeRotor

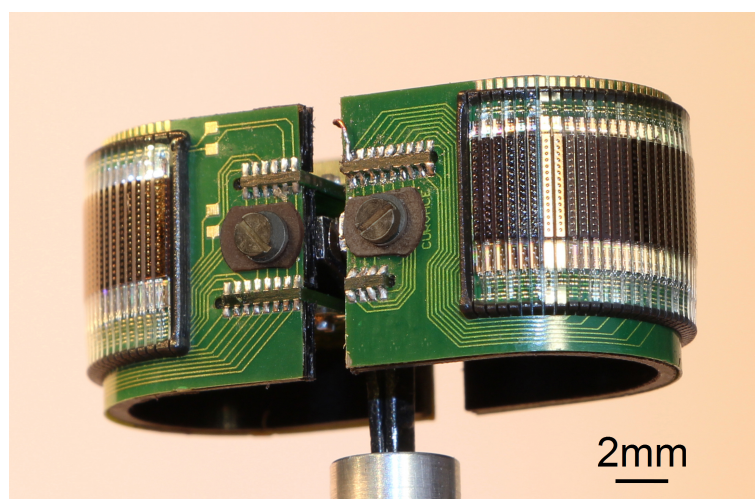


Figure 4.16: Photograph of the fully cylindrical CurvACE composed of two cylindrical CurvACE sensors mounted back to back offering a Field of View of $360^\circ \times 60^\circ$.

The fully cylindrical CurvACE, which is displayed in Figure 4.16, has been embedded into the BeeRotor robot (see Figure 4.17). This sensor is composed of two cylindrical CurvACE sensors mounted back to back offering a Field of View of 360° . Thanks to its wide FoV, the rotorcraft can assess the angular speed in several Regions of Interest with a great sampling. Similarly to the processing embedded in the previous version, the angular speeds measured

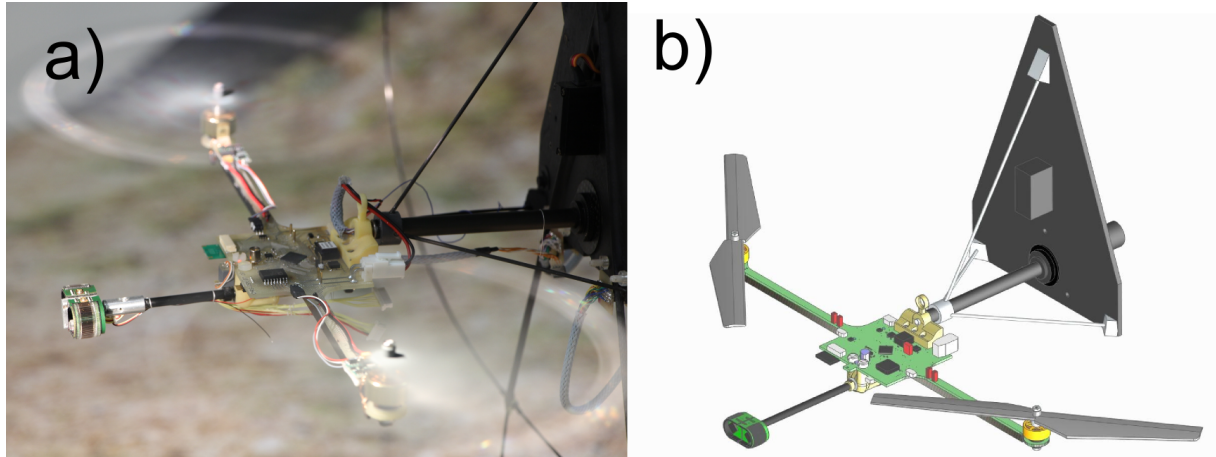


Figure 4.17: a) Photograph of the BeeRotor robot equipped with the fully cylindrical CurvACE sensor. b) CAD drawing of the BeeRotor robot equipped with a fully cylindrical CurvACE. Again, the eye has been placed 7cm away from the body of the robot to avoid being occluded by the propellers.

by 2-pixel LMSs are fused to compute a robust and frequently refreshed ventral and dorsal optic flow. Thanks to its wide Field of View, the robot is able to take into account the increase in optic flow due to the presence of any obstacles into its path, and therefore, adjust autonomously its altitude to navigate collision-free. At the same time, the aircraft adjusts its forward speed via the differential speed of the two propellers to the height of the tunnel it is traveling in.

4.2.2 BeeRotor autopilot

As can be seen in Figure 4.17, the two CurvACE sensors are looking respectively forward and backward. As a first step, we chose fixed regions of interest analogous to the ones covered in the previous studies. Each visual motion sensor having a field of view $24^\circ \times 20^\circ$ has then been replaced by a region of interest of 6×3 pixels of the CurvACE sensor from which 15 LMSs are computed (see Figure 4.18). The median value of these 15 measurements is then used by the BeeRotor autopilot to control both its altitude and forward speed.

The visuomotor control loops used on the robot equipped with the fully cylindrical CurvACE are presented in Figure 4.19. Like previously discussed, these two feedback loops guarantee that the BeeRotor robot will always keep a safe distance from both walls while adapting its forward speed to the size of the tunnel without any measurements of distance or groundspeed. However, in these first experiments, the eye of the robot was fixed instead of being continuously oriented parallel to the followed wall.

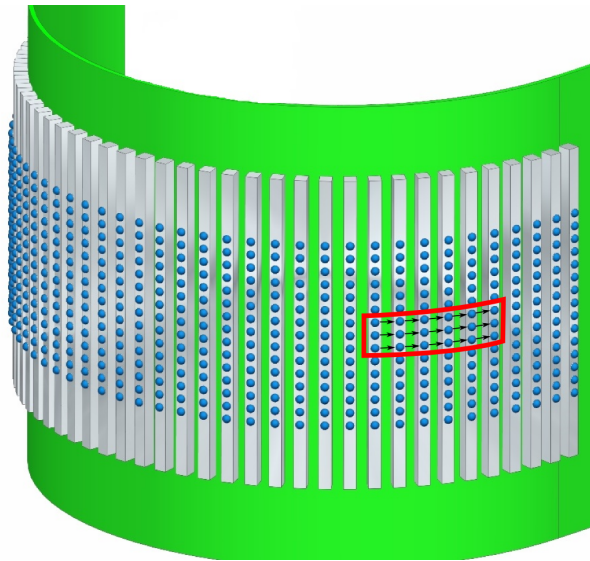


Figure 4.18: Simplified CAD drawing of one cylindrical CurvACE sensor with a red box representing one region of interest composed of 6×3 pixels. A similar region of interest (not shown here) was selected on each cylindrical CurvACE on the opposite side.

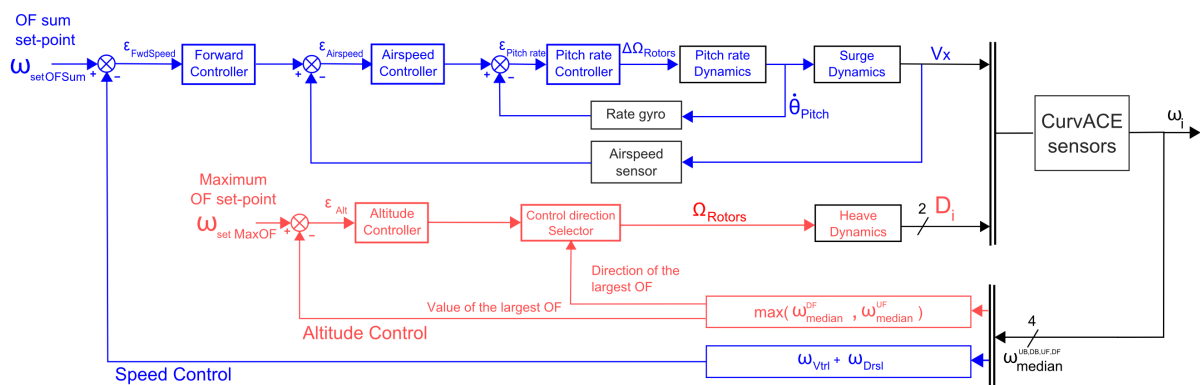


Figure 4.19: Equipped with a fully cylindrical CurvACE, the BeeRotor autopilot controls the forward speed and the altitude of the aircraft thanks to the two feedback loops previously described. These two intertwined feedback loops control the vertical lift of the aircraft and therefore its altitude to safely follow the closest surface and the differential thrust of the propellers and therefore its forward speed which is adjusted according to the size of the tunnel. In this experiment, the eye of the robot is fixed and do not always line up with the followed surface.

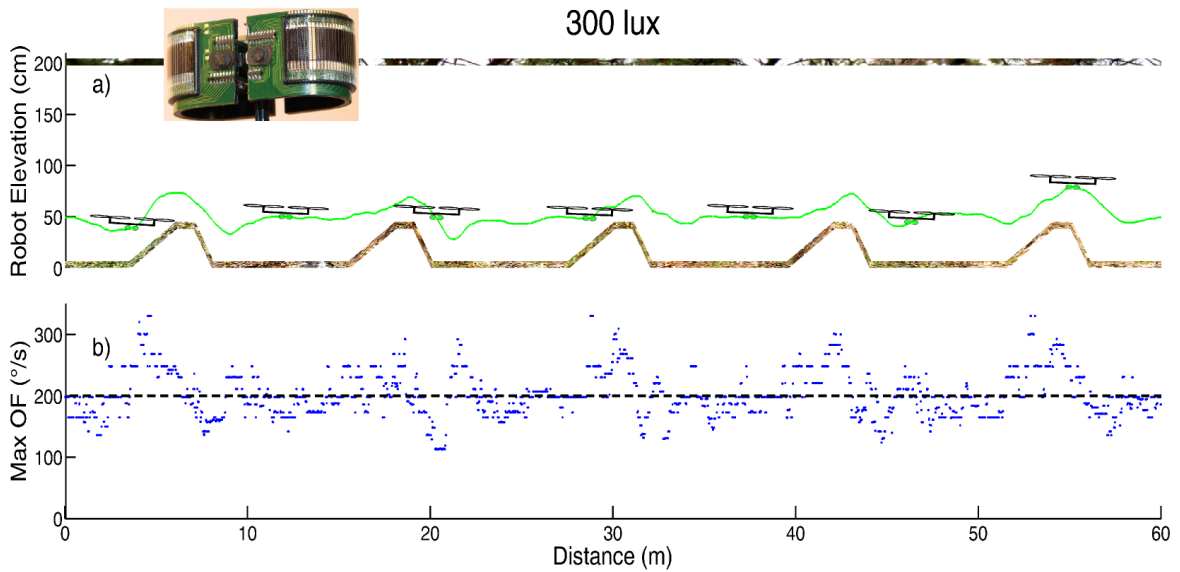


Figure 4.20: Automatic terrain following under optic flow regulation on the BeeRotor robot equipped with the fully cylindrical CurvACE sensor at 300 lux with $\omega_{setMaxOF} = 200^\circ/s$ and $\omega_{setOFSum} = 250^\circ/s$. **a)** Altitude of the aircraft following the ground and avoiding the slanted relief thanks to the altitude control loop. **b)** Maximum Optic Flow measured onboard the aircraft thanks to the CurvACE sensor. As expected, the measurement was frequently refreshed and accurately reflected the ventral angular speed.

4.2.3 Experimental results

The trajectories of the BeeRotor robot flying autonomously in the tunnel with a relief on the ground and a background illuminance of 300 lux are presented in Figure 4.20. As we can observe, the altitude control loop was still able to accurately detect the vicinity of obstacles and drive the aircraft away from them. When the aircraft was close to the relief, the altitude controller acted positively on the mean rotors' speed to fly away from the floor. The Maximal optic flow computed onboard BeeRotor thanks to the CurvACE sensor is represented in Figure 4.20b. As the chosen setpoint for the altitude control loop was $200^\circ/s$, we can see that the aircraft acted upon its altitude to maintain its ventral optic flow constant. When the aircraft was overflying the obstacle, the ventral optic flow increased due to the relief: this perturbation was rejected by the controller by flying away from the obstacle to reach back its Max OF setpoint. The aircraft is represented every 10 seconds oriented according to its pitch angle and with the field of view of the 4 regions of interest that have been chosen. Due to the speed control loop regulating the sum of the ventral and dorsal optic flows, the pitch angle of the aircraft was constantly varying. In particular, the aircraft pitched backward and therefore reduced its forward speed when flying over the obstacle due to the constriction of the tunnel. After the relief, the aircraft pitched forward to accelerate as the sum of the ventral and dorsal optic flows decreased.

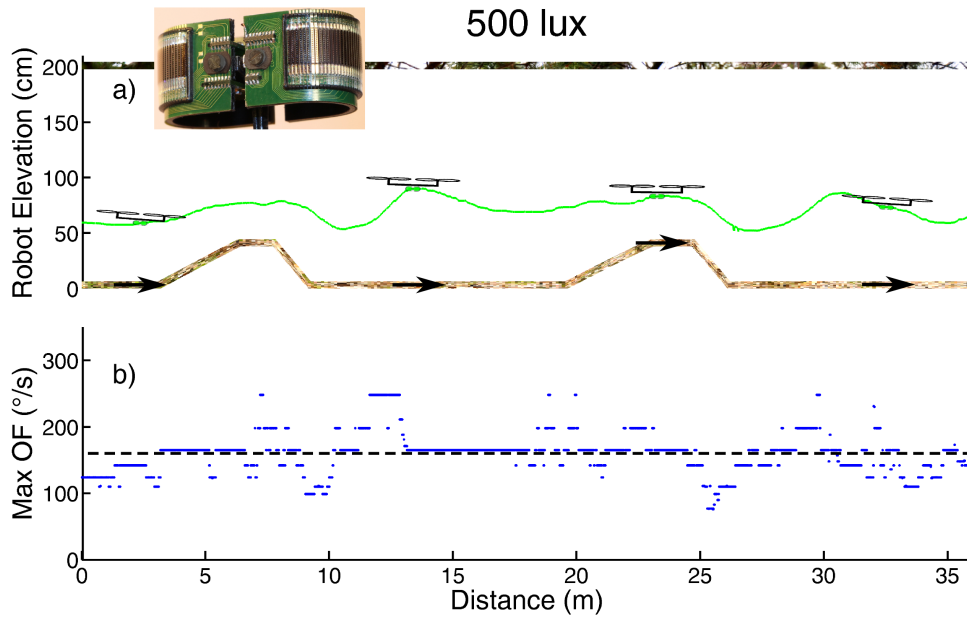


Figure 4.21: Automatic ground following in a rugged non stationary environment. Altitude of the aircraft flying above the ground moving at 30cm/s in the same direction than the aircraft at 500 lux with $\omega_{setMaxOF} = 160^\circ/s$ and $\omega_{setOFSum} = 250^\circ/s$. The Maximum optic flow setpoint was decreased as the perceived optic flow is smaller when the ground is moving forward. Again the aircraft was able to avoid the relief by acting on the propellers' thrust.

As previously presented, the floor of the experimental tunnel can be rotated thanks to an actuator in order to assess the performances of the BeeRotor robot in an unstationary environment. Figure 4.21 shows the altitude and the measured maximal optic flow of the rotorcraft when following the ground moving at 30cm/s in the same direction than the robot. Despite the perturbation on the ventral optic flow due to the motion of the floor, the aircraft was still able to control its altitude and forward speed and robustly avoid the obstacle. As the sum of the optic flows decreased due to the ground motion, the forward speed of the aircraft increased.

4.2.4 Robustness to the background illuminance changes

One key characteristic of the CurvACE sensor is to be composed of adaptive pixels automatically adapting to the background illuminance able to measure optic flow under several decades of illuminance. To assess the robustness of the CurvACE sensor to extract optic flow over a wide range of illuminance values (from 3 lux to 1000 lux), we performed a similar experiment with a background illuminance of 3 lux. As we can see in Figure 4.22, the aircraft was still able to control its altitude and its forward speed thanks to the measured optic flow. In particular, we can notice an important increase of the maximal optic flow

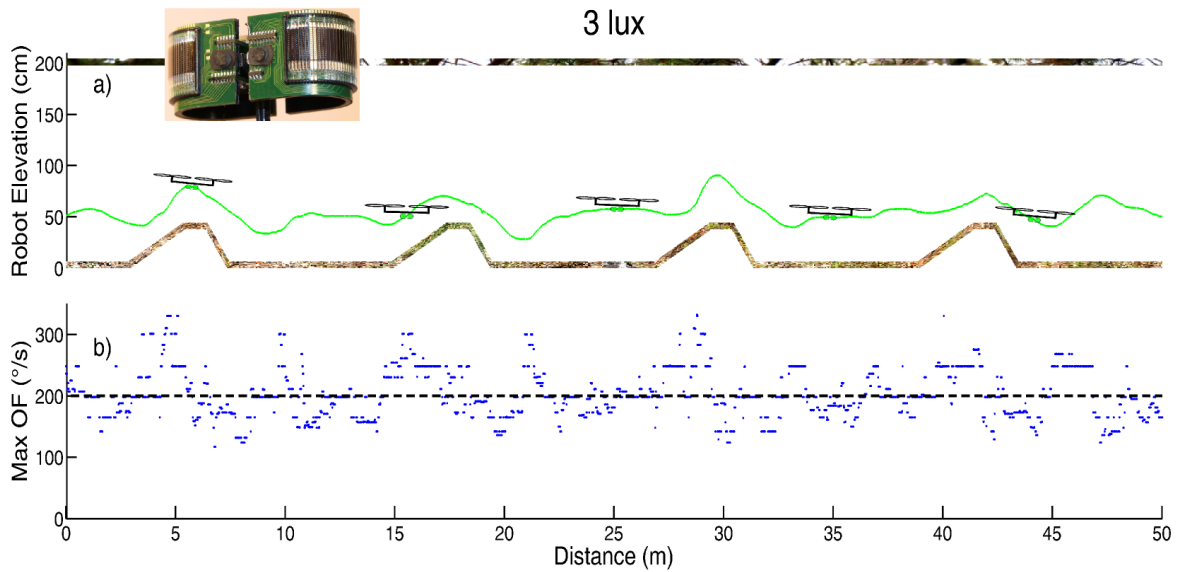


Figure 4.22: Automatic terrain following under optic flow regulation on the BeeRotor robot equipped with the fully cylindrical CurvACE sensor at 3 lux with $\omega_{setMaxOF} = 200^\circ/s$ and $\omega_{setOFSum} = 250^\circ/s$. **a)** Altitude of the aircraft following the ground and avoiding the slanted relief thanks to the altitude control loop. **b)** Maximum Optic Flow measured onboard the aircraft thanks to the CurvACE sensor.

when the aircraft was flying over the obstacle during the time the distance to the ground was decreasing.

4.3 Conclusion

In this chapter, we presented the BeeRotor robot which is a lightweight tandem rotorcraft equipped with sensors and control strategies mimicking the ones discovered in flying insects. Based on the optic flow measurements of its quasi-panoramic eye, the robot proved to be able to automatically:

- orient its eye in parallel with the followed surface thanks to a Least Squares approximation minimizing the difference between the obtained and theoretical patterns of optic flow measurements,
- hug the ground or the ceiling of a rugged or non stationary environment while robustly avoiding obstacles,
- adjust its forward speed to the size of the tunnel and therefore autonomously fly at a safe height and safe forward speed without any measurement of speed or distance.

This rotorcraft is the first one to perform such complex maneuvers without accelerometer and without any estimation in the inertial frame of its pitch, its altitude or its forward

speed. Finally, equipped with the fully cylindrical CurvACE sensor, we have shown that the rotorcraft can still fly autonomously in its environment even at very low illuminance thanks to the adaptive pixels and the wide field of view of the CurvACE sensor.

Chapter 5

Conclusion

5.1 Accomplished work

In this thesis, three main connected topics have been addressed. In all this work, the constant idea was to extract important characteristics of existing solutions from Nature to develop simple sensors and control strategies allowing a robot to autonomously navigate in complex environments. By taking inspiration from flying insects like flies and bees which are capable of navigation prowess with very limited processing resources, we strongly differ from classical robotics approach where the main idea is that we can do more if we have more sensors and more computational power.

In the first part of this thesis, we presented several implementations of optic flow sensors based on the “time of travel” scheme measuring accurately the angular speed both indoors and outdoors. In particular, we first compared the robustness of such sensors between linear pixels and pixels which automatically adapt to the background illuminance. Of course, the latter proved to work under a wider range of illuminance values but their accuracy was slightly smaller due to the well-known mismatch problem with aVLSI circuits. Our sensor with its bio-inspired processing has also been compared with a mouse sensor which has proven to be very accurate outdoors and inadequate to process the angular speed indoors. Optimizations of the processing scheme have also been proposed allowing:

- to compute several 2-pixel Local Motion Sensors that were fused in order to obtain a more accurate and frequently refreshed measurement of the angular speed,
- to detect the direction of motion thanks to a really simple decision strategy,
- to strongly reduce the computational burden of the processing unit by linearly interpolating the visual signals acquired at a smaller sampling rate.

This work has been a preliminary step toward the design of the first Curved Artificial Compound Eye developed in the framework of the European project CurvACE by 4 European research labs. This sensor is composed of three planar layers, a microlens array, a photodetector array with pixels automatically adapting to the background illuminance and a flexible Printed Circuit Board. These layers have been diced, precisely aligned and bent in order to endow this sensor with a very wide field of view ($180^\circ \times 60^\circ$) with almost no distortion. This sensor is not an imager but it has been tuned to sense visual motion thanks to a high temporal resolution and neuromorphic photodetectors. Particularly invested in the specifications of the electronic architecture and the characterization of the device, we have strongly contributed to show the ability of the sensor to extract motion with several optic flow algorithms.

The culmination of this thesis is the development of the BeeRotor robot which is a tandem rotorcraft endowed with sensors and control strategies borrowed from the flying insects. Thanks to a quasi-panoramic eye processing the optic flow in several regions of the environment, the aircraft is able to automatically control its forward speed and its clearances from the floor and ceiling based only on sensors similar to the ones known to exist in flying insects. This rotorcraft has proven that a robot can autonomously fly in an unstationnary rugged environment thanks to bio-inspired reflexes without any knowledge of attitude, altitude and speed in the absolute frame of reference. To do so, the BeeRotor robot needs to extract relevant information from its optic flow sensors. This is accomplished by constantly reorienting the eye of the robot parallel to the closest surface thanks to the pattern of angular speed measurements and a Least Squares approximation.

5.2 Toward optic flow sensors of the future

Although important improvements have occurred in the past years in the development of optic flow sensors, none of them have proven to be as efficient as their natural counterparts from whom they took inspiration and which are able to cope with any situation that can happen in natural environments. Here, we present four trails that still have to be studied to increase the performances of optic flow sensors.

5.2.1 Global optic flow processing vs fusion of local motion sensors

As we have described in the introduction, many algorithms have been proposed to process optic flow. Among them, we can discriminate between algorithms processing the whole optic flow vector field which are generally more complex but give more information about the environment and are not sensitive to the aperture or the correspondence problems and the schemes based on LMSs processing the local optic flow in specific regions of interest of the field of view. Although cameras coupled with complex algorithms will be more efficient for specific applications like movement detection, they do not seem suitable for Micro Aerial Vehicles due to the important quantity of data to process and the variety of situations that will arise in real environments. Schemes processing the local angular speed from adjacent pixels are generally lighter in terms of computational power and therefore can suit the very strong constraints in terms of size and available power available onboard flying robot. However, the fusion of an important number of local measurements is still an ongoing issue in particular to determine the direction of motion. Krapp et al. (1998) have helped us understand how such integration is performed in flies by studying at the dendritic structures of interneurons. Plett et al. (2012) successfully implemented on a FPGA a fly-inspired system based on Reichardt detectors able to visually sense rotations around different body axes but there is still a long way to go before embedding in microcontrollers or dedicated chips sophisticated systems able to compete with the performances of the visual system of flying insects.

5.2.2 Interesting regions of interest for insects and robots

One main issue in conventional machine vision systems is the difficulty to extract only the relevant information for a specific application. The same question arises when we consider optic flow. Do we really need to extract the whole vector field or concentrate on specific regions of interest ?

In insects, Portelli et al. (2011) recently shown that honeybees regulate their forward speed using optic flow cues from the ventral, dorsal and lateral fields of view.

However, to reduce the complexity, it seems interesting in robots to only focus on regions of the environment with useful information. Our very lightweight, cheap and low power optic flow sensors could therefore be highly suitable to extract optic flow from a specific region of the environment and fuse several of them to control an autonomous aircraft. Such a strategy has been adopted by Beyeler et al. (2009) who used 7 mouse sensors looking mostly down forward in a fixed wing aircraft and proved how these positions were suitable for obstacle

avoidance with such platform. In a same way the BeeRotor robot is equipped with ventral and dorsal optic flow sensors allowing to control its flight in the vertical plane. In simulation, the ALIS autopilot has shown how by relying only on four optic flow sensors (ventral, dorsal and laterals), we could control the position and forward speed of a flying agent in a 3D environment (Portelli et al., 2010). However, ALIS was not simulated with frontal optic flow sensors to detect frontal obstacles. But, the ALIS simulations show that only a few optic flow sensors could be enough for a MAV navigating in an unknown environment.

5.2.3 Light adaptation mechanisms

As we have seen, a large number of motion chips are equipped with photodetectors automatically adapting to the background illuminance like the APIS and CurvACE retinas. Such characteristic seems a key point toward the development of vision sensors adapted to be used on the field where the illuminance can strongly change with the weather and the surrounding objects. However, all these chips suffer from the mismatch that is a well-known problem in microelectronics. Indeed, it is really difficult to obtain adjacent processing circuits with exactly the same characteristics which leads to small differences in the output signals of neuromorphic pixels which have a strong influence on the measured optic flow between adjacent pixels. Besides, the adaptive pixels of the CurvACE or the APIS sensors have a limited voltage range due do the electronic circuit. By increasing this range, we could fully use the Analog to Digital Converter resolution increasing the accuracy of the visual signals. In particular, the circuit proposed by Delbrück and Mead (Delbrück & Mead, 1994) can be schematized into two gains: a very small static gain and an important transient gain enhancing the visual contrasts. For our application, the static information is completely disregarded and filtered out by the high-pass filter of the OF processing whereas this static gain reduced the output range of the pixels. Other implementations of adaptive circuits only responding to transient signals like the insect or the turtle retinas (Normann & Perlman, 1979; Matic & Laughlin, 1981) are therefore probably worth being studied in more detail to increase the accuracy of aVLSI-based motion detectors.

5.2.4 Event-based chip in the future

As pointed out already, processing the angular speed from every directions with the limited computational power of Micro Aerial Vehicles is still a challenging issue. In order to strongly reduce the computational burden of the processing units, one lead would be to design event-

based chip generating pulses corresponding to illumination changes in a scene in the field of view of the associated pixel like the chip described in (Weikersdorfer & Conradt, 2012). These chips seem particularly suitable to process the angular speed using the “time of travel” scheme because the early stages of the processing like filtering and thresholding would be realized analogically and the processing unit would only have to deal with digital signals occurring asynchronously. Such implementation would require a lot less processing power and data memory allowing to multiply the number of 2-pixel LMSs that could be coupled with a smart fusion algorithm extracting important parameters of the environment. In addition to the chip, the control of the aircraft may also be triggered only by events as the “time of travel” scheme output is only refreshed when a feature is detected and belongs to the range of measured velocity.

5.3 Toward curved compound eyes of the future

During this thesis, a major breakthrough has been accomplished in the design of a curved compound eye thanks to the cylindrical CurvACE sensor which is the first functional and programmable curved compound eye covering a wide field of view and extracting the optic flow. As already discussed, this compound eye offers a very wide field of view with no distortion and no aberrations while it processes the visual motion at high speed and automatically adapts to the background illuminance as it has been demonstrated on the BeeRotor robot.

5.3.1 Dynamically changing regions of interest

However, during the experiment on the BeeRotor robot, the optic flow was computed from 4 fixed regions of interest regardless of the aircraft pitch angle and the environment. We proved that by always reorienting the eye parallel to the followed surface, we could increase the performances of the BeeRotor rotorcraft in particular to avoid big obstacles. Due to the very wide of field of the CurvACE sensor, it does not seem useful to rotate the eye which generates an undesired rotational optic flow if we can instead dynamically adjust the regions of interest based on the measured optic flows. A simple strategy based on this idea has been tested in simulation by Lippiello et al. (2011) where they moved their region of interest more forward when the simulated vehicle was accelerating (this acceleration was detected thanks to the IMU) as, the faster you go, the earlier you need to detect an obstacle.

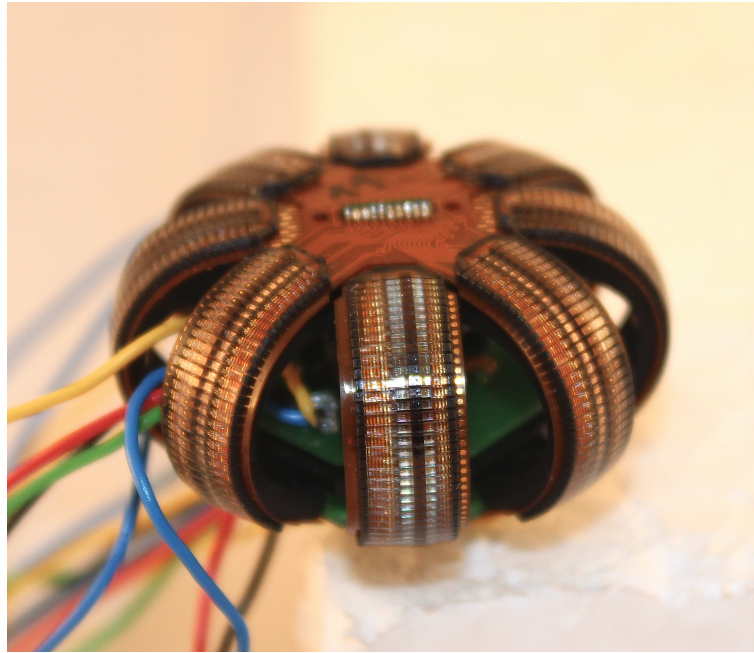


Figure 5.1: Picture of the spherical CurvACE composed of several 1-D flexible motion sensors arranged in order to obtain an omnidirectional field of view (www.curvace.org).

5.3.2 Various shapes for different applications

To demonstrate the performances of the CurvACE sensor, the first prototype has been shaped into a semi cylindrical sensor which best fit the need of Micro Aerial Vehicles to fly autonomously and avoid obstacles. We have shown how, by coupling two such sensors back to back, we could easily obtain a fully cylindrical sensor. However, as the sensor is made up of three flexible layers, the sensor could be shaped in any geometry that fit a specific application. In particular, columns of flexible ommatidia have been designed and bent along the meridians of a sphere offering to the sensor called spherical CurvACE an omnidirectional field of view (see Figure 5.1) which is particularly adapted for egomotion estimation. These columns of flexible ommatidia can find a lot of potential applications as they can be shaped arbitrarily and therefore be used on any surface where collision detection is required.

5.4 Toward smarter bio-inspired robots of the future

Nature is an endless source of inspiration for roboticists to imagine new sensors or control strategies by looking at solutions which have been selected through million of years of evolution. However, translating results of biological experiments into man-made devices is a very complex process where we always have to tackle masses of problems. For example, the

CurvACE sensor, although a major achievement, is not of the same size as the compound eyes of flying insects despite the use of state-of-the-art technologies. Although the BeeRotor robot performances do not entirely compare with the natural counterparts it is inspired from, this aircraft shares several common points with flying insects which are of great importance toward the autonomous navigation of flying aircrafts.

5.4.1 BeeRotor's commonalities with flying insects

5.4.1.1 Similar sensory modalities

Although not exactly a flying insect in particular in terms of size and propulsion system, the BeeRotor robot shares several characteristics with its natural counterparts in particular in the sensors embedded onboard the robot. It is now well known that navigation of flying insects relies heavily on optic flow cues (Gibson, 1950; Kennedy, 1951) measured thanks to their compound eye. Although even in Nature others sensors are used to estimate proximity like the echo-location ability of bats, the main advantage in using optic flow is the limited power required as it is based on a passive sensor only collecting the photons coming from the environment without any signal emission. Diptera are also sensitive to inertial forces, thanks to their halteres. In other orders of insects, as discussed in (Taylor & Krapp, 2007), similar sensors have been found that could also be sensitive to Coriolis forces like the forewings of male Strepsiptera or the antennae of the hawkmoth *Manduca*. However, no evidence of any inertial sensor has been found so far in honeybees. Finally, thanks to their hairs and antennae, flying insects can estimate the airspeed or the variations of airspeed and use it to control their flight (Campan, 1964; Taylor & Krapp, 2007).

In a similar way, the BeeRotor robot has been equipped with two compound eyes: a quasi-panoramic eye composed of 4 planar local motion sensors and a curved compound eye covering a field of view of $360^\circ \times 60^\circ$. Although inferior to the Field of View of insects, it is adequate to detect motion from several relevant regions of the environment. The robot has also been equipped with a rate gyro sensor measuring the angular velocity along the pitch axis. Without this high-speed sensor coupled with a fast feedback loop regulating the pitch rate, the tandem rotorcraft was not controllable. Similarly to the head of insects which is controlled actively by no less than 23 pairs of muscles (Strausfeld et al., 1987) and of which the orientation is sensed by a pair of mechanosensitive hair fields located in the neck (Preuss & Hengstenberg, 1992), the quasi-panoramic eye of the robot is decoupled from its body and its orientation is known thanks to a contactless magnetoresistive sensor measuring the

orientation of the eye relative to the head. Finally, the airspeed was sensed on the robot thanks to a custom-made airspeed sensor.

5.4.1.2 Similar flying strategies

Altitude control

Inspired by observations on the locusts (Kennedy, 1951), a control strategy based on the regulation of the ventral optic flow has been proposed (Ruffier & Franceschini, 2005; Franceschini et al., 2007) and successfully embedded into the BeeRotor robot to autonomously follow the ground or the ceiling while automatically avoiding obstacles in the environment. Although neither the distance to the surface or the forward speed is known with an optic flow regulator if the measurement is not disambiguated thanks to a ground speed sensor or a distance sensor like a range finder, we have shown that the aircraft automatically flies at a safe height in the high-roofed tunnel.

Straw et al. (2010) have shown with *Drosophila* flying in a 3D virtual environment that their altitude control strategy actually results from several reflexes and among them an expansion avoidance reflex in the vertical plane like the one already known in the horizontal plane. Inspired by these results, we endow the BeeRotor robot with a similar behavior based on the vertical OF (measuring the downward or upward OF expansion) generated by the closest surface during translational motion.

Speed control

Based on experiments performed by Srinivasan et al. (1996) showing that bees “control their speed by holding constant the average image velocity as seen by the two eyes” which has since then been confirmed to be true in the vertical and the horizontal planes (Portelli et al., 2011), the BeeRotor robot adjusts its forward speed based on the sum of the ventral and dorsal optic flows. This strategy coupled with a ventral or dorsal optic flow regulator results in an automatic regulation of the forward speed according to the size of the tunnel. However, it has been shown that flying insects ascend under tailwind and descend under headwind (Kennedy, 1951) which is consistent with the behavior observed on the OCTAVE robot equipped with a ventral optic flow regulator (Ruffier & Franceschini, 2005; Franceschini et al., 2007). On the BeeRotor robot, as we also control the forward speed on the basis of the sum of the ventral and dorsal optic flows, in presence of wind, the speed or altitude of the aircraft would only be affected transiently before the autopilot would correct the trajectory and reach back its steady state. We can hypothesize that the control of forward speed by

holding constant the global optic flow which has been proven in several tunnels presenting visual contrasts in at least two opposite directions do not apply when the insect is flying in a landscape where only the ground offers visual features. These two competitive behaviors discovered in flying insects should be analyzed simultaneously by performing experiments in specifically designed tunnels with changes on the global perceived optic flow in the presence of tail or head winds.

Automatic landing

By recording flying honeybees, Srinivasan et al. (2000) noticed that the angular velocity of the image in the ventral field of view is held constant during landing on a flat surface. As soon as the insect reduces its forward speed, its altitude will be decreased until reaching the ground with almost no speed.

On the BeeRotor robot, two strategies have been tested allowing the aircraft to land by regulating the ventral or dorsal optic flow at a constant value. Firstly, by decreasing the setpoint value of the forward speed feedback loop, we imposed to the aircraft to slow down triggering a landing. Secondly, by regulating the Vertical optic flow depending on the vertical speed of the aircraft coupled with a ventral or dorsal optic flow regulator, the robot reduced its speed to lose altitude and therefore generated a Vertical OF. These two strategies have allowed to perform smooth landing on uneven terrains based on optic flow regulation without any knowledge of the attitude of the robot and without requiring any external structure on the landing site.

Automatic light adaptation

As already discussed previously, automatic light adaptation is a key characteristic for visual motion sensors (as it is for compound eyes or mammalian eyes) as it will allow MAV of the future to travel in changing environments and in particular to navigate both indoors and outdoors which is still challenging. Equipped with the CurvACE sensor, the BeeRotor robot can navigate autonomously under several decades of illuminance even with illuminance as low as 3 lux. Due to the experiment, it was not possible to test the performances of the BeeRotor robot outdoors but the results of the CurvACE sensor during the characterization process lead us to believe it would still be able to fly autonomously and rely on its optic flow measurements.

No state estimation

In many species of flying insects, the ocelli are thought to act as horizon detectors and to be responsible of the dorsal-light response which compensates for attitude changes by fast head and body movements like it has been demonstrated on *Diptera* by Schuppe & Hengstenberg (1993). A similar behavior has been successfully tested on an aircraft equipped with two cameras associated with specially-shaped reflective surfaces offering a wide field of view by Thurrowgood et al. (2009) which are currently trying to develop a freely-flying aircraft relying exclusively on vision. Fuller et al. (2013) also equipped their 100mg Robobee with light-sensing ocelli allowing to estimate and control the pitch angle of a flapping-wing robot. Besides, the dorsal rim area of the compound eye of the dragonfly is known to be sensitive to sky light polarization and be used as a natural compass. Very recently, Chahl & Mizutani (2012) proposed two biomimetic sensors mimicking respectively the ocelli and the polarization compass of flying insects which were used to stabilize the roll angle and the heading of a robotic demonstrator. Although these two behaviors enabling flying insects to determine their attitude or absolute orientation are probably helpful to control their flight outdoors, insects are still able to fly in indoor environments where no horizon can be detected and the polarization of light can not be used to determine its orientation relative to the sun. Except for these two reflexes, no behavior in flying insects seem to indicate that they estimate their attitude, altitude or ground speed to control their flight. In particular, no sensor like accelerometers have been found in insects allowing them to sense their own body orientations and no evidence has been found that flying insects are sensitive to gravity.

In the visuomotor control loops used on the BeeRotor robot, neither the distance to any objects or the speed relative to the ground is determined as we rely only on a rate gyro measuring the angular velocity along the pitch axis, an airspeed sensor measuring only the forward speed relatively to the air and optic flow measurements from which we can not extract any speed or distance. This robot is the first one, as far as we know, which is able to fly in an unknown environment without any estimation of states like its attitude (pitch, roll and yaw orientation), its altitude or its ground speed. The aircraft is however able to fly autonomously only by reacting to the environment. Of course, as the degrees of freedom of the aircraft are limited (no roll and yaw rotations), we can not conclude if the used strategy would be successful on a free-flying aircraft but, theoretically, an aircraft equipped with the APIS autopilot which is an extension of the two visuomotor control loops presented here for a 3D environment and with an eye reoriented to the closest followed surface could navigate in an unknown environment without any knowledge of distance, speed, altitude or orientation.

5.4.2 Limitations of the BeeRotor autopilot

5.4.2.1 Featureless environment

Similarly to the flying insects which can not avoid drowning when flying over mirror-smooth water (Heran & Lindauer, 1963), the BeeRotor robot will not be able to control its altitude and forward speed without any contrast on the ground or the ceiling. Although this is generally acceptable for flying insects that will immediately take-off again after a crash, it will be fatal for any flying robot except those specifically designed to recover after a crash (Briod et al., 2012).

In natural environments, it has been shown that the image power spectrum behaves approximately as $S(k) = k^{-2+\nu}$ where k is the modulus of the spatial frequency and ν is a small number (Ruderman & Bialek, 1994). This property is fundamental as it shows that any natural image will be composed of various frequencies allowing to detect contrasts regardless of the scale of the image and therefore regardless of the distance between the aircraft and the environment. However, in urban environments composed of man-made buildings, this property does not apply and contrasts can generally only be distinguished at several meters of distance from the edges of the buildings or at a few centimeters range thanks to the bumps of the buildings.

5.4.2.2 Detection of small objects

To extract an accurate optic flow from the Visual Motion Sensors equipping the BeeRotor robot, we have chosen to take the median value of a specific region of the field of view which has proven to be a more robust and frequently refreshed measurement of the angular speed. However, if the aircraft flies over really small obstacles, this will probably be detected by only one LMS at the same time and it will therefore be discarded by the median operator. In flies, it has been proven that by simulating only two adjacent photoreceptors, the firing rate of the H1 neuron which integrates the output of an important number of EMD neurons increased if the simulation was in the preferred direction (Franceschini et al., 1989). This shows that flying insects have a different strategy to fuse the measurements of the local EMD neurons as only one EMD neuron can trigger a response of the neuron of the lobula plate. Alternative solutions have been tested during the development of the optic flow sensors to reflect at the same time the mean angular speed measured by the 2-pixel LMSs or one specific stronger measurement indicating an immediate danger. However, the performances of the optic flow

sensor was greatly degraded due to the occurrence of false measurements.

5.4.2.3 Avoidance of frontal obstacles

One obvious limitation of the BeeRotor autopilot is the lack of visual sensor in the frontal region of the robot preventing it to detect and avoid frontal obstacles. Even with a visual sensor looking in the forward direction, the optic flow generated in the direction of the translation would be too small to be measured early enough to avoid a frontal obstacle. In insects, it has been found during experiments of freely-flying flies that the generated saccades do not always correspond with the presence of a close obstacle (Boeddeker et al., 2005). This behavior maybe allows the insect to change the position of the focus of expansion and therefore greatly reduces the probability of missing the detection of an obstacle in the flight path.

To cope with this issue, one solution could be to equip the BeeRotor robot with a frontal motion sensor specifically designed to sense low angular speed like the one described in (Sabiron et al., 2013). Thanks to this, even obstacles close to the focus of expansion and generating low optic flow could be detected. Another strategy, which has been demonstrated on the “robot mouche” (Franceschini et al., 1992), was to equip the robot with two off-centered sets of 2-pixel LMSs spatially arranged to measure the optic flow in a $\pm 10^\circ$ around the focus of expansion. However, this specific layout was adapted to detect obstacles at a given distance from the aircraft which could be inadequate for an aircraft flying at strongly varying forward speeds. Finally, one possibility that could be tested would be to take inspiration from insects and regularly change the direction of flight with an aircraft zigzagging similarly to the peering behavior of honeybees. However, performing saccades would also probably complexify the altitude and speed control of the aircraft.

5.4.3 Possible applications

Although presented here as a proof of concept limited to the vertical plane, a Micro Aerial Vehicle equipped with similar sensors and control strategies than the BeeRotor robot could fly autonomously in any environment without relying on traditional bulky and power consuming sensors like:

- a 6 Degrees of Freedoms (DoFs) Inertial Measurement Unit that can be used to estimate the attitude of the aircraft,
- a Global Positioning System (GPS) giving the position,

- a Doppler-radar which is used to measure the ground speed (which is generally coupled on military aircraft with a Pitot tube measuring the airspeed to determine the wind speed and perform dead reckoning),
- a radar altimeter which measures the altitude above ground,
- a barometric altimeter which provides the absolute altitude above a defined datum, usually the sea level.

In particular, such flying strategies are particularly adapted to equip planetary landers as they will meet the strong constraints in terms of size and power consumption of such vehicles. Besides, most of the previously presented sensors could not be used on other planets (GPS, barometric altimeter, IMU ...). This explains the strong interest of the European Space Agency (ESA) to perform planetary landing based on optic flow (Valette et al., 2010; Izzo et al., 2011).

5.5 Feedback to biology

In the Biorobotics team, the main thrust is always to learn from biology and apply it to develop out-of-the box sensors and robots. In particular, the optic flow sensors presented here feature several aspects of the visual system of flying insects: Gaussian sensitivity, automatic adaptation to the background illuminance, wide field of view and fast detection of motion thanks to a bio-inspired scheme... The flying strategies used onboard BeeRotor to follow a terrain, avoid obstacles, automatically adjust its altitude and speed and land are also derived from the results of behavioral experiments performed on bees and flies during the past decades.

Based on the performances of the developed robot, new questions arise on the information available for the flying insects and how they use them to perform such prowess to control their flight.

- As we have seen, the BeeRotor autopilot relies on an inner feedback loop controlling the pitch rate of the aircraft to avoid crashing due to an uncontrolled fast change of attitude. Contrary to the fly which is equipped with halteres sensitive to Coriolis force; in honeybees, no evidence has been found that these insects are sensitive to inertial forces. Does the natural stability of these insects allow them to do without such sensory modality or does an organ sensitive to Coriolis forces exist in honeybees?

- In simulation, we have found that a forward speed feedback loop based on an inner loop regulating the changes in airspeed instead of the airspeed allowed the aircraft to control its forward speed based on the sum of the ventral and dorsal optic flows. Such strategy could not be tested however on the aircraft due to the noise on the measurement of the changes in airspeed but prompts us to wonder which information is used by the flying insects to regulate their forward speed.
- We may wonder from this work whether flying insects actively control their head relatively to their body in a similar way to the BeeRotor. Due to the difficulty to record the head orientation relatively to the body during real flights, only van Hateren and Schilstra (van Hateren & Schilstra, 1999) succeeded to do it but they did not focus on the rotations along the pitch axis. Although they noticed that the head pitch is slightly more stable than the thorax pitch, no hypothesis has been done so far on this active control of the head pitch of the fly and if it is mediated by vision or others sensors.
- The neurons of the lobula plate have proven to be able, at the same time, to detect important patterns of optic flow over their whole field of view and be sensitive to a change of angular speed in a very specific region. This is the reason why the process used to fuse the data of all the EMD neurons still need to be investigated.
- For the altitude control, several strategies have been discovered in flies and honeybees: lateral edge fixation, ventral expansion avoidance, ventral optic flow regulation. On the BeeRotor robot, two of them were implemented together but it is still not clear how these behaviors can intervene jointly during insect flight.

The motivation lying behind the work presented during this thesis is therefore to use the results of our robotic demonstrator to better understand how flying insects with their limited computational power and sensors can fly so gracefully forming a virtuous loop between biology and robotics: try to reproduce on new robots theories borrowed from experiments on flying insects and use these robots to propose new experiments to assess the capabilities of flying insects.

Appendix A

Additional information about CurvACE

In this section, more details not published on the PNAS paper are given on the CurvACE sensor focusing on my contribution to the CurvACE project.

Description of the readout protocol

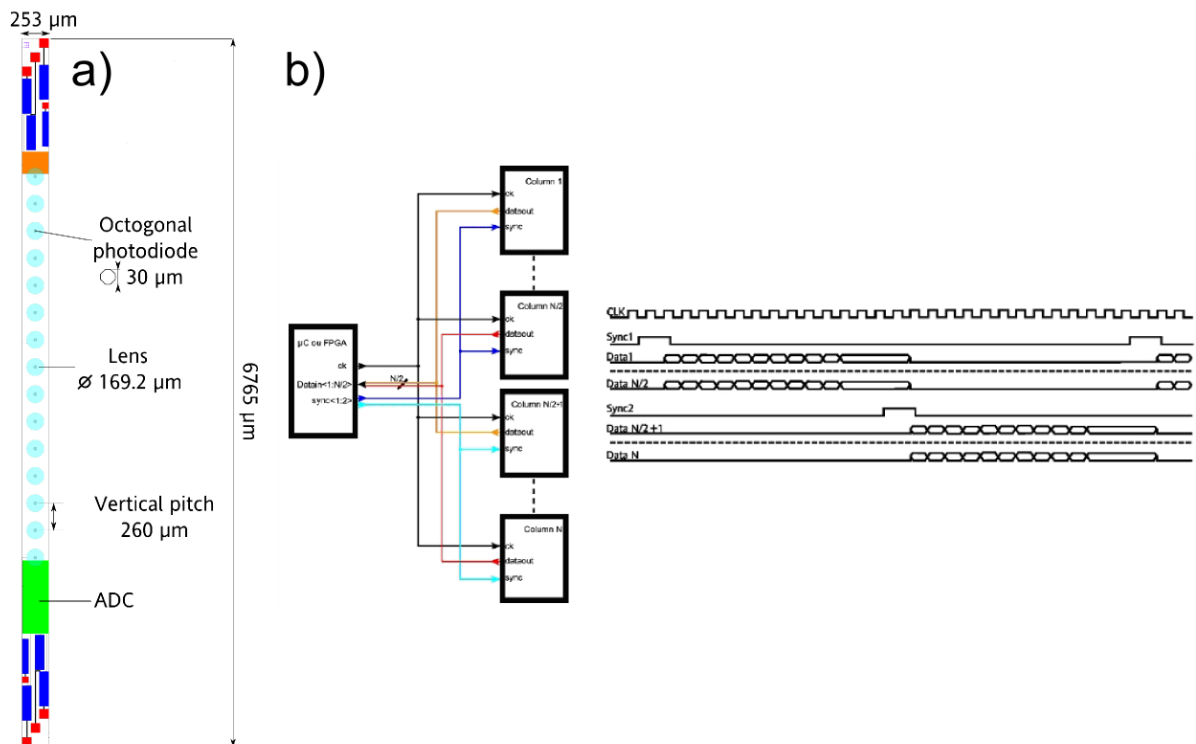


Figure A.1: a) Structure of one column of the CurvACE sensor. Each column is composed of 15 pixels separated by a distance of 260 μm . At the bottom of the column, an Analog to Digital Converter digitizes the output signals of the photodiodes. b) Functional Schematic of the direct connection protocol (left) and Chronogram of the direct connection protocol (right).

As previously presented, the CurvACE sensor is composed of 42 columns; each of them being composed of 15 pixels and an Analog-to-Digital (ADC) converter digitizing the photodiode signals (see Fig. A.1a). It was then necessary to develop a read-out protocol able to

	Direct connection protocol (CurvACE choice)	UART	SPI	I ² C	CAN	Parallel to Serial	oneWire
Maximum bit rate	Main μC quartz	115 kbits	40 Mbits	400 kbits	1 Mbits	2 Mbits	140 kbits
Nr. of pads on each column for R/O	3	2	4	2	2	3	1
Nr. of tracks on the flex PCB	$N + 2$	$N + 1$	$N + 3$	2	2	$N + 2$	1

Table A.1: Characteristics of the protocols first considered to communicate with the CurvACE sensor with respect to the number of tracks and pads as well as the bitrate.

transfer the values of the 630 pixels to the microcontrollers driving CurvACE at high speed. Different possible protocols have been considered to be used in CurvACE, and their main characteristics are summarized in Table A.1.

The selected communication protocol called “direct connection protocol” consists of:

- A unique clock signal sent to each column,
- A sync signal used to start the conversion of the associated columns,
- A digital-out (Dout) signal per column used for the serial transfer of each pixel output signal.

The main advantages of this protocol are its simplicity and the fact that we do not need any address (stored in an EEPROM memory for example) to communicate with a column. Besides, the refresh rate is independent of the number of columns and the readout protocol adds only 3 pads per column, which makes the total number of pads equal to 6:

- 3 pads on top for digital (Dvdd) and analog power source (Avdd) and for ground (Gnd),
- 3 pads on base for readout protocol (Clock, Sync, Dout).

The main drawback of the direct connection protocol is the relative important number of wires on the flexible PCB needed between the main controller and the CurvACE sensor. In order to reduce the number of wires, we can use several sync signals which reduces the total rate but also the number of wires for connecting the chip to a microcontroller. We chose to

use two sync signals which requires only 27 wires but divides the total rate by two as the refresh rate is given by:

$$\text{Sampling rate} = \frac{10^6}{16 \times 15 \times N} \quad (\text{A.1})$$

with N synchronization signals and a 1MHz clock. Figure A.1b illustrates the schematic and the chronogram of the protocol with 2 sync signals used to reduce the total number of wires.

Optic Flow characterization of the cylindrical CurvACE

I detail here the optic flow characterization in which I have been particularly involved during the CurvACE project.

The CurvACE sensor chip has been designed to compute motion over several decades of illuminance in an unknown environment. A setup has therefore been developed to assess the performances of the CurvACE sensor as an optic flow sensor during controlled motions in a still environment. These experiments have been conducted in a controlled environment where the whole field of view of the cylindrical CurvACE was stimulated by images of real scenes placed in front of the sensor surrounded by a cylindrical arena. For the optic flow characterization, we wanted to demonstrate the performance of the cylindrical CurvACE as an optic flow sensor:

- during specific controlled motions (translation and rotation),
- in front of real scenes corresponding to an outdoor environment stimulating the 180° field of view of the cylindrical CurvACE,
- at a high frame rate (300fps).

Description of the optic flow characterization setup

A generic electronic test board (see Figure A.2) has been developed for optic flow characterization to:

- Determine the optic flow generated by specific motions over the whole field of view of the cylindrical CurvACE,
- Assess the performances of several optic flow algorithms,
- Demonstrate the robustness of the CurvACE sensor to illuminance variations,
- Simultaneously compare several optic flow sensors.

This board is equipped with a dsPIC33FJ128GP802 microcontroller and can communicate through SPI with the two microcontrollers inside CurvACE. The data can also be collected through SPI from an external unit. This board is also equipped with:

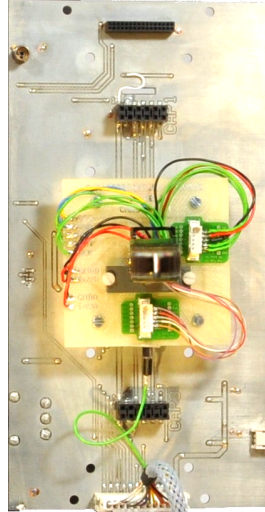


Figure A.2: CurvACE test board for optic flow characterization.



Figure A.3: FT2232H Mini Module with the FTDI chip.

- A rate gyro (ADIS16100), which has a range from $-300^\circ/s$ to $300^\circ/s$, and which can be used as a reference for the optic flow computation during a rotation of the sensor.
- An illuminance sensor based on a BPX65 photodiode, which gives an overview of the global illuminance over the whole field of view of the cylindrical CurvACE sensor. This sensor could be used to assess the robustness of the CurvACE chip to illuminance variations over several decades.
- A Bluetooth module for wireless communication (ALA module from freetomove).

High frame rate data acquisition

The acquisition of the data from the CurvACE sensor to a computer running under Windows is achieved at high speed thanks to a FTDI 2232H mini module (Figure A.3). This mini module is equipped with a FT2232H chip from FTDI, which is used as a bridge between the SPI bus of the CurvACE sensor and the USB port on the computer. The acquisition program can collect CurvACE data on a Windows-based computer through a classical USB port, and save the data in a text format for analysis. The architecture of the data acquisition and the experimental setup can be seen in Figure A.4.

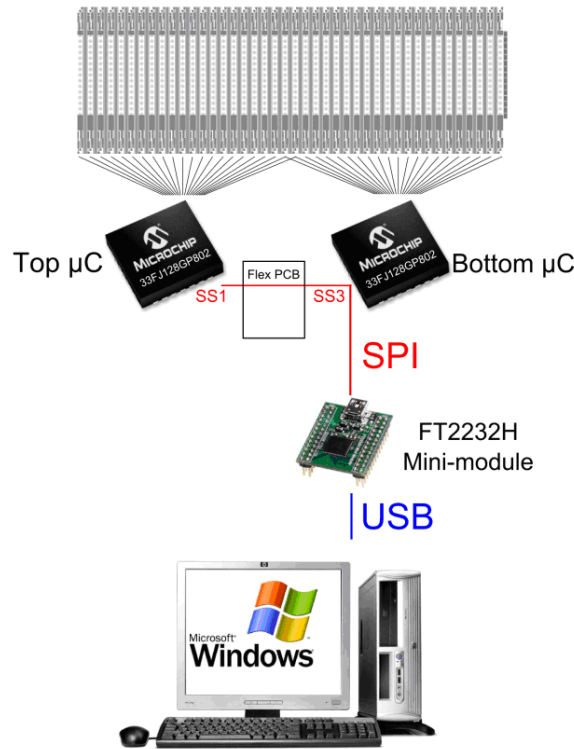


Figure A.4: Architecture of the data acquisition.

Although the data are acquired using Windows-based computer (which is not a Real Time OS), more than 99.5% of the frames are correctly acquired in our computer. Unfortunately, the time between two frames can not be controlled with perfect accuracy and a few frames (0.5%) can be lost during acquisition.

Optic flow expansion experiment

The expansion experiment is performed on an electronic board translating at a constant speed toward a curved wall (see Figure A.5) by means of a motorized linear slide system. The electronic board is equipped with a CurvACE sensor and communicates using SPI and USB protocols with a host computer. The control of the stepper motor is achieved using dSpace Control Desk whereas data acquisition is achieved using the FT2232H Mini Module.

The electronic board is translating toward a curved wall covered with a natural panorama at 15 cm/s from 55 cm to 10 cm ahead of the wall. The optic flow over the whole field of view is computed using the Lucas-Kanade algorithm and represented using a Mercator projection.

Figure A.6 is a Mercator projection of the measured optic flow pattern during the expansion experiment at a translational speed of 1.4 m/s with an irradiance of $5.10^{-4}W/cm^2$. As expected, the optic flow is really small close to the focus of expansion (FOE at the center of the image) and increases when the point of interest moves away from the FOE. However, Figure A.6 shows a slight asymmetry in the distribution of the optic flow vectors with respect to the FOE. This asymmetry or deviation could be due to the use of natural contrasts and

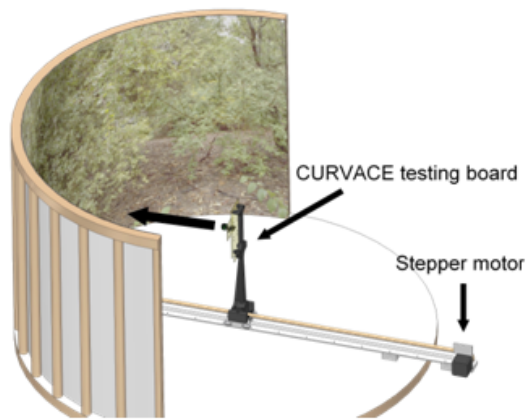


Figure A.5: Mechanical assembly including a panoramic visual environment used for the expansion experiment.

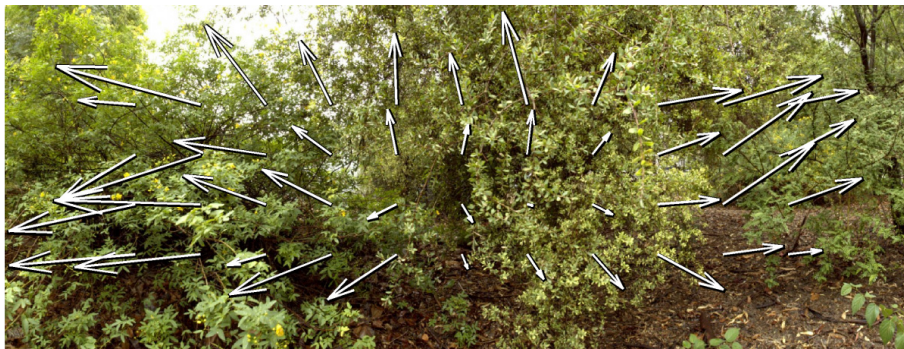


Figure A.6: Measured optic flow pattern during the expansion experiment. The Lucas-Kanade algorithm was used to compute the optic flow from the images taken by CurvACE at 300fps.

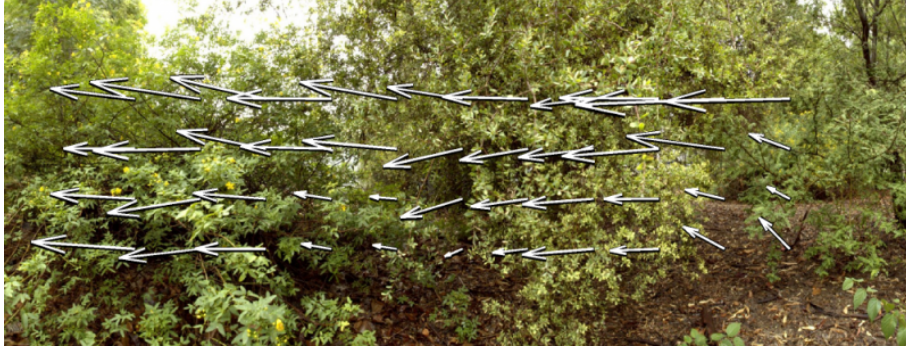


Figure A.7: Measured optic flow pattern during the yaw rotation experiment. The Lucas-Kanade algorithm was used to compute the optic flow from the images taken by CurvACE at 300fps.



Figure A.8: Electronic board in its circular arena covered by the CurvACE logo.

natural, non-homogeneous lighting conditions.

Optic flow yaw rotation experiment

The yaw rotation optic flow characterization of the cylindrical CurvACE is performed on the same electronic board rotating along its yaw axis at an angular speed controlled thanks to a stepper motor. The control of the stepper motor is achieved using dSpace Control Desk whereas the data acquisition is achieved using the FT2232H Mini Module. The optic flow over the whole field of view is computed using the Lukas-Kanade algorithm at 300Hz and represented using Mercator projection (see figure A.7). We obtain a clear pattern of rotation along the yaw axis with optic flow vectors all pointing to the left with the same amplitude for a given angle of elevation.

Visualization of images

Even though the CurvACE sensor has been developed to extract motion, it is possible to visualize the environment when it is moving like on a classical imager. To characterize the image rendering, we covered our arena with the CurvACE logo (see FigureA.8) printed in black on a 330cm x 75cm white paper as pattern to visualize. Figure A.9 shows the image

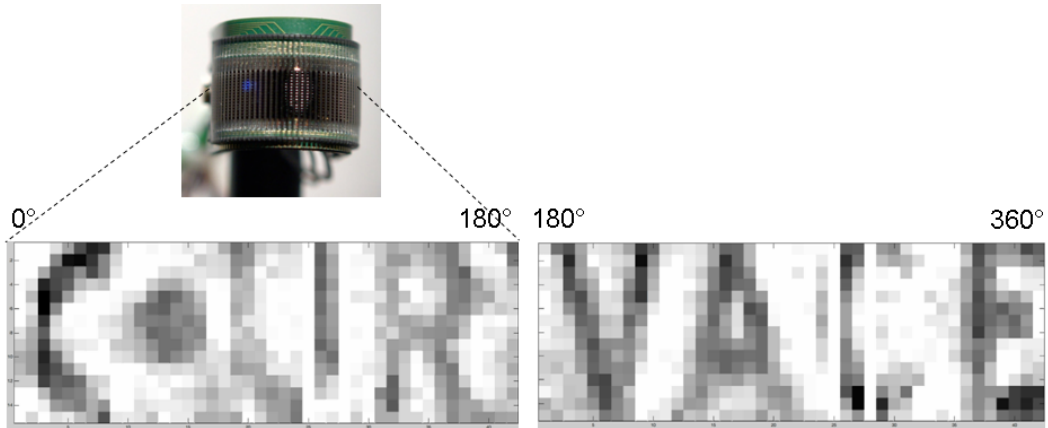


Figure A.9: Images of the CurvACE logo rendered by the cylindrical prototype. As the CurvACE sensor covers a field of view of 180° in the horizontal plane, two images taken from opposite directions were necessary to reconstruct the pattern seen by the sensor during a rotation (www.curvace.org).

rendered by the CurvACE prototype when rotating the CurvACE sensor at an angular speed of $125^\circ/s$ and acquiring the images at 25fps. Of course, the CurvACE sensor has not been designed to be an imager able to recognize a pattern and we can see here the coarse resolution of the sensor. We repeated this experiment for several background illuminances ranging from 0.5 lux to 1500 lux to assess the robustness of the CurvACE sensor to the variations of illuminance. There was no significant difference in the obtained images.

Appendix B

Description of the BeeRotor aircraft

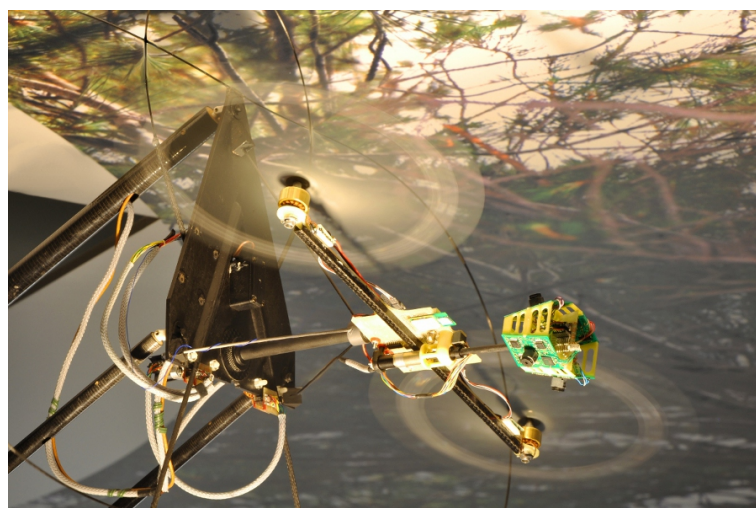


Figure B.1: Photograph of the 80g BeeRotor robot in the experimental environment. (Expert & Ruffier, 2012)

Figure B.1 is a picture of the BeeRotor robot. It is composed of a main electronic board called the body, which carries most of the sensors and actuators, performs all the data processing and controls the rotorcraft. The pantographic arm to which this board is connected simply provides the aircraft with its power requirements. The main electronic board is composed of two elongated arms connected to two propellers controlled by Brushless outrunner motors. The robot's eye, which is set apart from the main board to prevent the visual field from being occluded by the propellers, is composed of 4 custom-made optic flow sensors based on an off-the-shelf photosensor array combined with the "time of travel" scheme and an anemometer to measure the airspeed. The eye can rotate independently from the body of the aircraft thanks to the presence of a stepper motor. This robot mainly relies on optic flow to control both its clearance from the environment and its forward speed without any measurements of distance or speed. The aircraft is placed at the end of a counter-weighted pantographic arm and can travel in a 12m long high-roofed tunnel where the ground and ceiling are covered by natural patterns.

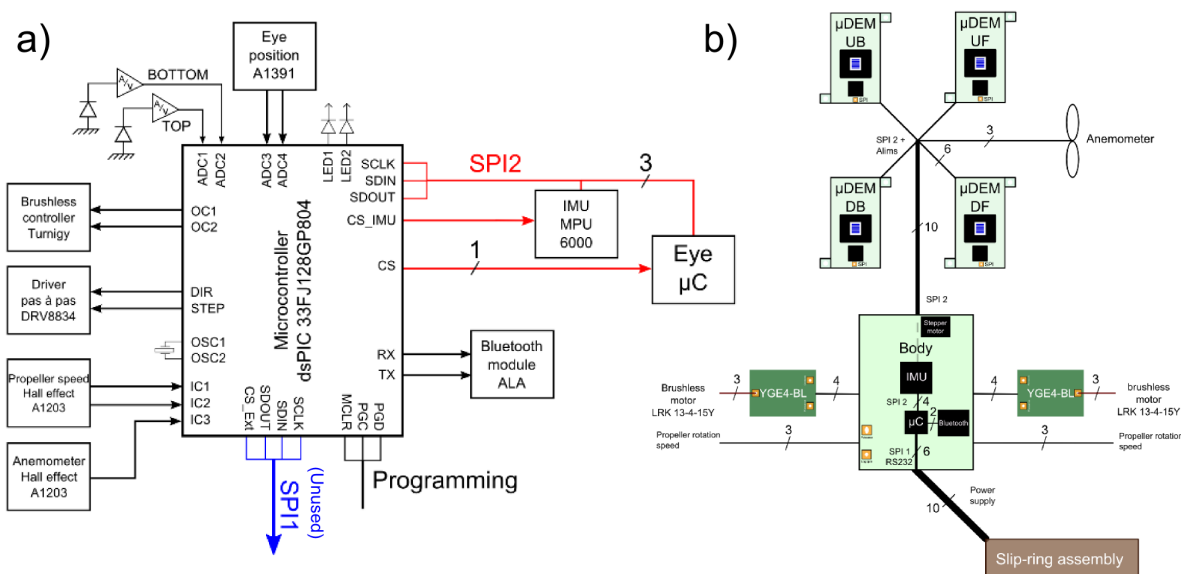


Figure B.2: a) Schematics of the electrical connections of the main microcontroller of the BeeRotor board. This microcontroller collects the data coming from all the sensors (eye, airspeed sensor, IMU, eye position sensor and propeller speed sensors) and control the rotation of the eye and the speed of the two propellers. It also communicates with a host computer through a Bluetooth module. b) Schematics of the two electronic components of the BeeRotor robot. The aircraft is supplied externally through a slip ring assembly. The main board of the robot communicates with the 4 6-pixel Visual Motion Sensor thanks to a SPI bus and send commands to the two Brushless controllers (YGE 4-BL) driving the Brushless outrunners.

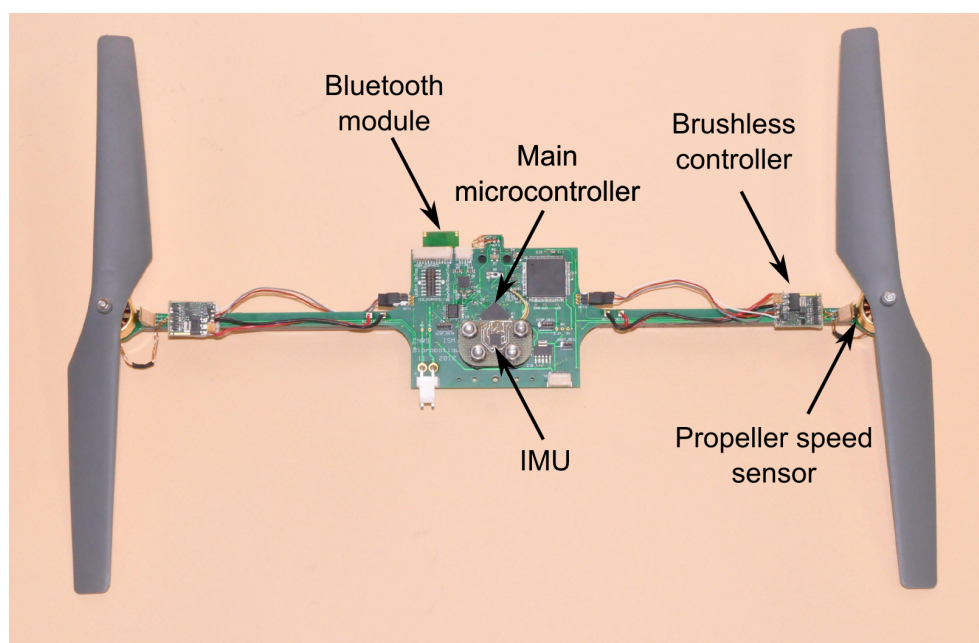


Figure B.3: Photograph of the BeeRotor robot main electronic board. The main microcontroller of the robot is placed in the center. We can clearly distinguish the two Electronic Speed Control (ESC) modules driving the Brushless motors and the two propeller's speed sensors. Isolated from the vibration of the aircraft, the IMU has been placed on top of four vibration isolators on a dedicated electronic board.

The body of the rotorcraft is composed of a custom-designed electronic board (see Figure B.3), on which all the main sensors and actuators are set around a dsPIC microcontroller 33FJ128GP804 (see Figure B.2a). This microcontroller embeds the autopilot processing the data provided by the visual motion sensors and controls the actuators of the robot. This microcontroller communicates with the 4 visual motion sensors through a SPI bus and receives the outputs from the 20 1-D Local Motion Sensors (LMS) computed at a rate of 1kHz (see Figure B.2b). The main electronic board is also equipped with:

- a tiny Bluetooth module (ALA from Free2move company) mediating information between the robot and a host computer,
- a custom-made positioning sensor, based on 2 tiny magnets with their orientation separated by an angle of 25° and an A1391 Hall effect sensor, which determines the orientation of the eye with respect to the body.
- a 6-axis Inertial Measurement Unit MPU 6000 from Invensense communicating with the main microcontroller through a SPI bus.

Eye of the robot

The BeeRotor robot needs to extract the optic flow from several regions (see section 4.1.3). In a first version of the BeeRotor robot, the eye is composed of 4 6-pixel Visual Motion Sensors (VMSs) (Figure B.4) processing the angular speed using the implementation of the “time of travel” scheme described in section 2.3.3. Among these 4 VMSs, 2 are looking Upward respectively Forward (UF) and Backward (UB) and two are looking Downward respectively Forward (DF) and Backward (DB) with a 22.8° angle from the horizontal direction (see Figure B.5). Each VMS is composed of a 6 pixel retina IC-Haus LSC and processes on a dsPIC microcontroller 5 optic flows over a field of View of 24° in one direction since the direction of the aircraft is known. These 4 VMSs communicate with the main microcontroller using SPI bus. The details about the description of the electronic board and the processing of each VMS have been given in section 2.3.3. Due to the limited number of pixels, linearly interpolating the signals was not necessary and the processing was performed at 1kHz.

Sensors of the Micro Aerial Vehicle

Ground and ceiling luxmeters

In order to assess the robustness of the BeeRotor robot with the variations of the background illuminance, we equipped the aircraft with two luxmeters looking respectively upward and downward and based on a BPX65 photodiode connected in photovoltaic mode to an OPA2342 operational amplifier. The current through the photosensor is linked to the output voltage according to the following equation:

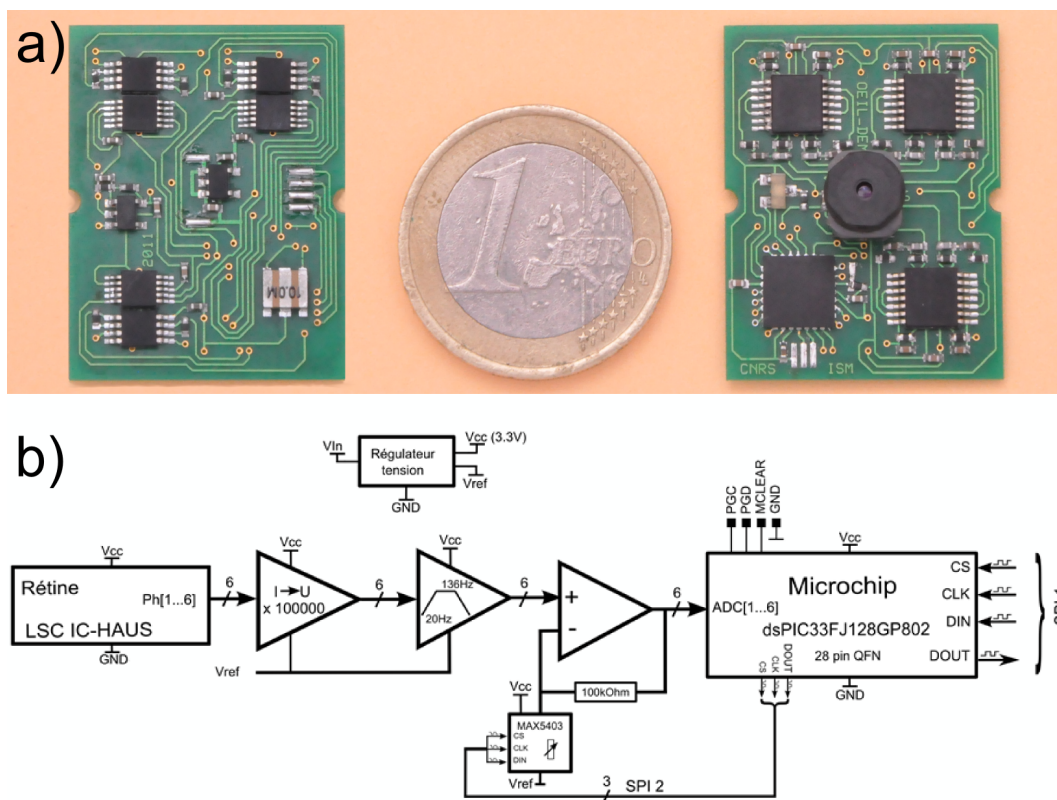


Figure B.4: a) Bottom and top views of one of the four 2-gram microcontroller-based visual motion sensors with its lens (focal length: 2 mm) mounted on the one-dimensional 6-photosensor array. b) Synoptic of one 2-pixel Local Motion Sensor. The processing embedding in each 2-pixel LMS is similar to the one described in 2.3.3 and the 6 pixels of the LSC retina are used to compute 5 angular speeds from which the median value is extracted. To increase the working illuminance range of the sensor, the gain applied to the visual signals can be adjusted electronically through a MAX5403 digital potentiometer controlled by a SPI bus.

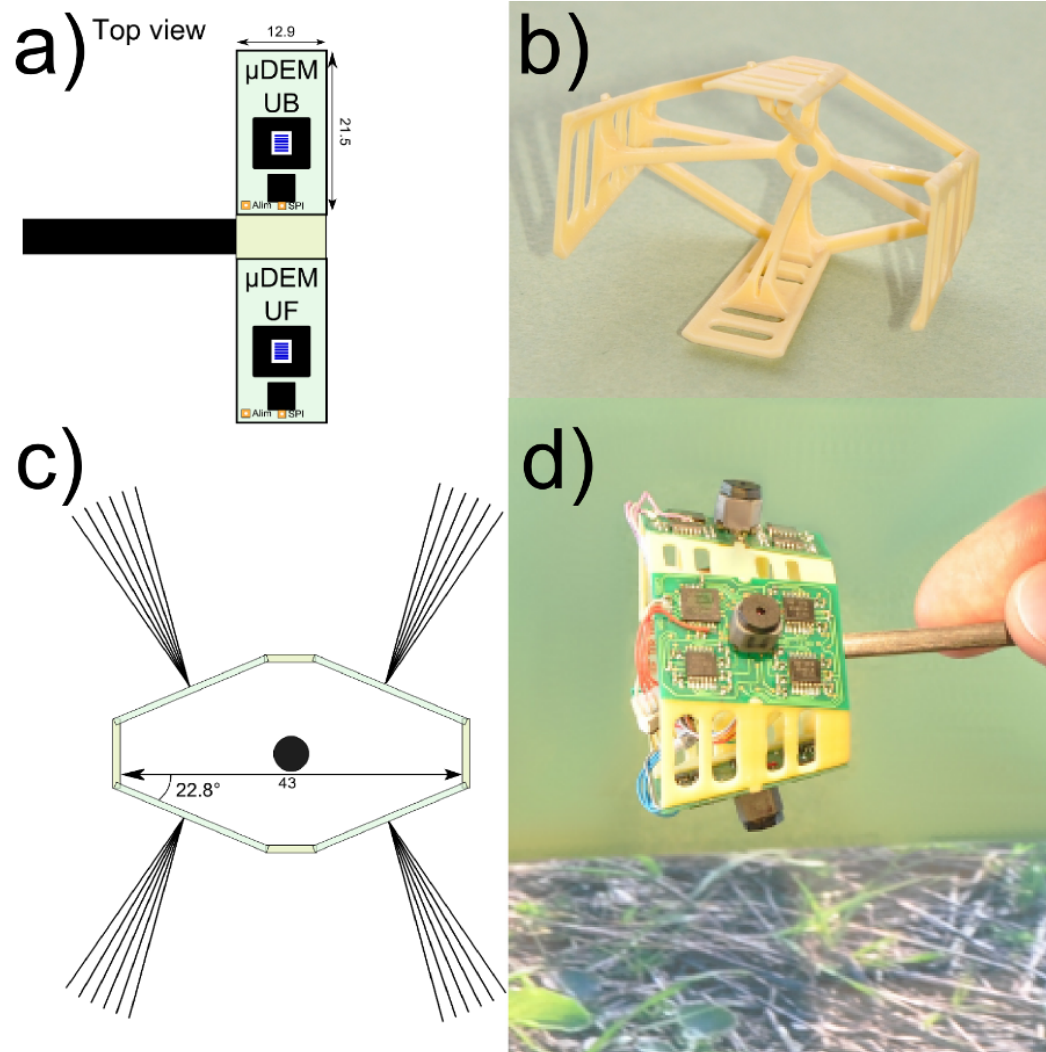


Figure B.5: Eye of the BeeRotor robot. **a-c)** The eye is composed of four 6-pixel VMSs looking respectively Up Forward (UF), Up Backward (UB), Down Forward (DF) and Down Backward (DB) with an angle of 22.8° with the horizontal direction. Each VMS processes the optic flow from a 6 pixel retina and has a Field of View of around 24° . **b)** Mechanical support of the 4 Visual Motion Sensors manufactured using 3D printing. **d)** Photograph of the BeeRotor's eye with its four electronic boards.

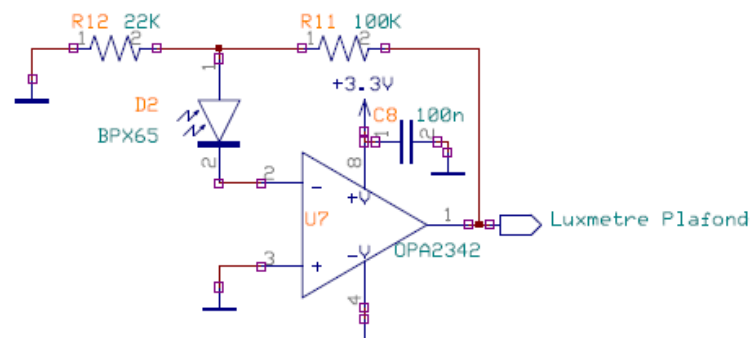


Figure B.6: Schematics of the luxmeter based on a BPX65 photodiode. The signal of the photodiode is then amplified by 100000 thanks to a transimpedance amplifier which converts the current in the photodiode into a voltage captured by one Analog Digital Converter of the microcontroller of the main board.

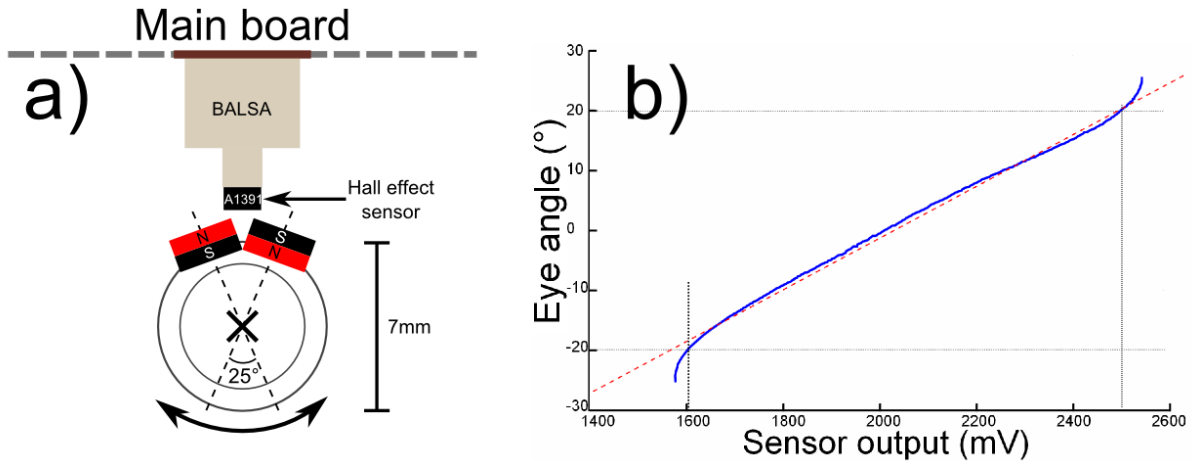


Figure B.7: **a)** Mechanical principle of the eye position sensor. Two magnets with reverse polarities and separated by an angle of about 25° have been placed on the carbon tube of the eye of the robot. A fixed Hall effect sensor sensitive to the magnetic field is placed a few millimeters away from these two magnets and measures the variations of the magnetic field when the eye rotates. **b)** Evolution of the output of the Eye orientation sensor with the angle. The output of the sensor is monotonically increasing between -20° and $+20^\circ$

$$I_{ph} = I_{dark} \times \left(e^{\frac{V_{out} \times q \times R_{12}}{K_b \times T \times R_{11}}} - 1 \right) \quad (\text{B.1})$$

where $I_{dark} = 0.1nA$ is the photodiode dark current, T the temperature in K, K_b the Boltzmann constant $K_b = 1.38 \cdot 10^{-23} m^2 \cdot kg \cdot s^{-2} \cdot K^{-1}$ and q the elementary charge $q = 1.6 \cdot 10^{-19} C$.

$$I_{ph} \approx 1.10^{-10} \times e^{\frac{V_{out}}{0.025 \times 4.54}} \quad (\text{B.2})$$

Position of the eye relative to the body

The position of the eye relative to the body of the robot is determined thanks to a Hall effect sensor placed a few millimeters away from two magnets with reverse polarities (see Figure B.7a). Indeed, as it was not possible to place this magnetic sensor along the axis of rotation in front of one single magnet, we placed two magnets on the carbon tube carrying the eye. Of course, with this principle, we can not measure the orientation of the eye over 360° of rotation but we were able to obtain a monotonic analog output of the sensor over 40° as can be seen in Figure B.7b. A look-up table was used to determine the eye angle from the output of the sensor.

Measurement and regulations of the propellers' speed

In order to precisely adjust the thrust of both propellers, it is necessary to control the speed of the propellers. To measure the propellers' speed, we used a digital Hall effect sensor A1203 placed a few millimeters away from the motor shaft containing 16 magnets. The

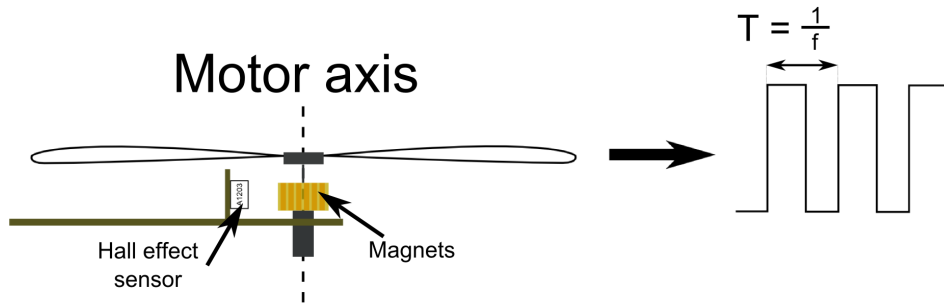


Figure B.8: Mechanical principle of the propeller speed sensor. A digital Hall effect sensor is placed a few millimeters away from the shaft of the outrunner composed of 16 magnets. When rotating, the variations in the magnetic field are detected by the magnetic sensor generating a square signal with a frequency depending on the rotational speed of the propellers.

digital output of the sensor switches each time the sensor is in front of a magnet (Figure B.8). By computing the frequency of the output signal thanks to an input capture of the microcontroller, we determine the speed of the propellers with a good accuracy.

Regulation of the rotational speed of the propellers (1st feedback loop)

Identification of the transfer function between the propellers' command and the rotational speed of the propellers

In order to identify the transfer function between the propellers' control signal and the rotational speed of the propellers measured thanks to a Hall effect sensor, we applied a series of steps on the propellers' command (see Figure B.9).

We identified a first order system with the following transfer function:

$$G_{propeller}(s) = \frac{\Omega_{rotor}(s)}{u_{rotor}(s)} = \frac{K_{rotor}}{\tau_{rotor}s + 1} = \frac{4.116}{0.1398s + 1} \quad (\text{B.3})$$

After a discretization at 200Hz, we obtained the following system:

$$G_{propeller}(z) = \frac{0.1446}{z - 0.9649} \quad (\text{B.4})$$

Results of the regulation of the speed of the propellers by a PI controller

We chose to include in the closed loop system (Figure B.10) a Proportional Integral (PI) controller in order to cancel the static error of the system. This PI controller has been adjusted in order to have a response time at 5% smaller than 0.1s and an overshoot smaller than 10%. The results of the close loop system are given in Figure B.11 for the simulated and the real system.

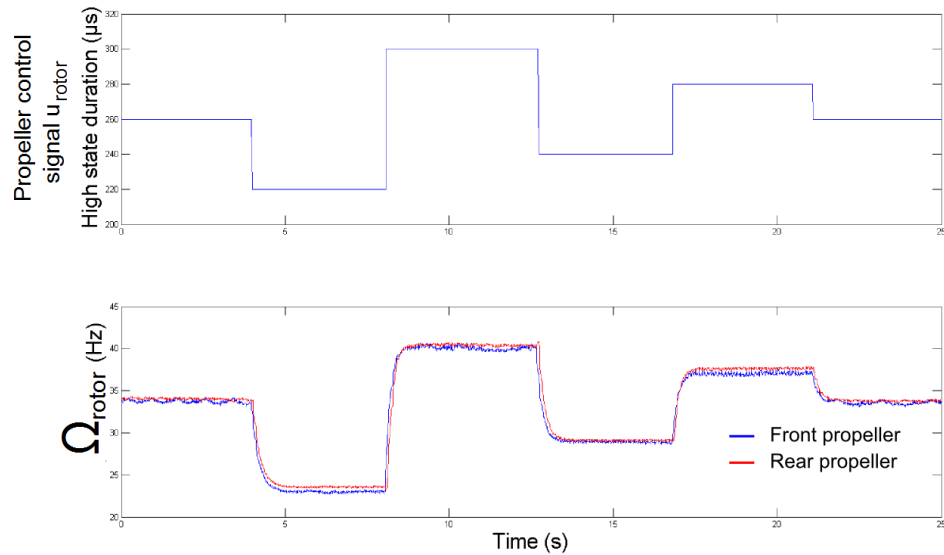


Figure B.9: Propellers' speed when applying a series of steps on the duty cycle of the signals send to the Brushless controllers. We notice that the speed of the propellers is very similar for both propellers and adapt to a new setpoint value with no overshoot and no delay.

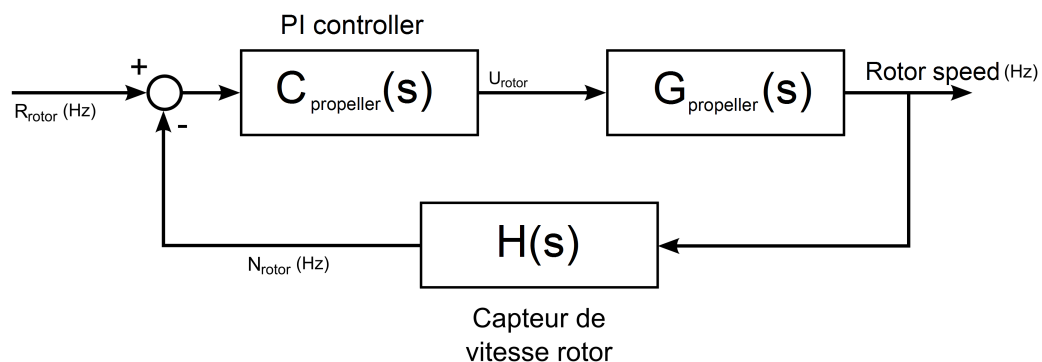


Figure B.10: Feedback loop including a Proportional Integral controller to control the speed of the propellers. The controller has been adjusted to have a very small response time and no static error.

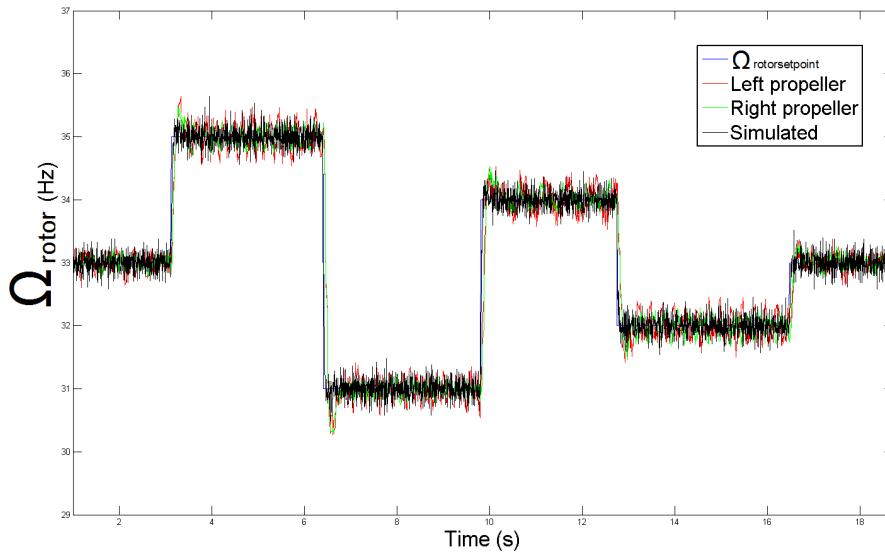


Figure B.11: Results of the feedback loop regulating the speed of the propellers when applying a series of steps on the setpoint of the speed of the rotors. In blue, is represented the speed command and the red and blue curves show the speed of the left and right propellers measured thanks to the sensors. As expected thanks to the PI controller, the closed loop system has a very short settling time (0.1s) and no static error. The measured speed is very consistent with the simulation of the feedback loop in black.

Airspeed sensor

The airspeed of the aircraft is measured thanks to a custom-made sensor based on a digital Hall effect sensor A1203 placed in front of a magnet attached to the axis of a freely rotating propeller (Figure B.12). The total weight of this tiny airspeed sensor is smaller than 0.5g.

In order to assess the quality of the measurements of the airspeed sensor, we placed it on the aircraft flying at a varying speed. The speed of the aircraft is measured thanks to an azimuthal position sensor placed on the pantographic arm that will be described in section B.

Figure B.13 shows in red the speed of the aircraft and in blue the airspeed measured by our airspeed sensor. To scale both measurements, we divided by 600 the output of the airspeed sensor. We can see that the airspeed sensor output precisely reflects the groundspeed of the BeeRotor robot as there was no wind.

Inertial Measurement Unit

The aircraft is equipped with a 6-axis Invensense MPU 6000 Inertial Measurement Unit communicating with the main microcontroller by SPI bus. As the aircraft can not perform any yaw or roll rotations, we only collect the rate gyro corresponding to the pitch angle of the robot. In order to be less sensitive to the aircraft's vibrations, the IMU has been placed on a specific electronic board mounted on 4 bushings (vibration isolators).

Although the aircraft while flying autonomously only use the information of the rate

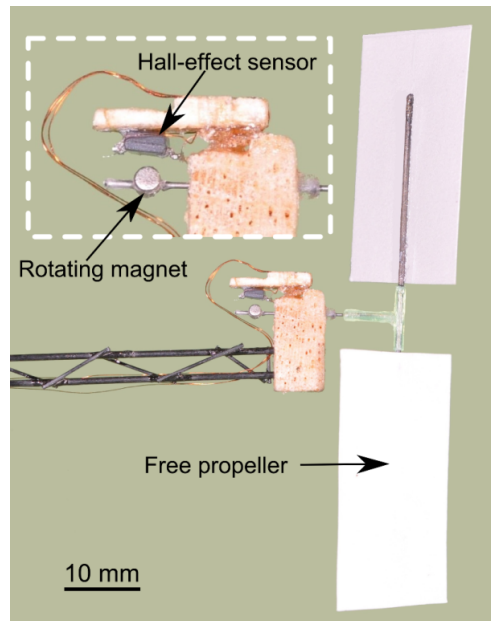


Figure B.12: Picture of the airspeed sensor. This custom-made sensor is composed of a freely rotating propeller dragging along a magnet placed a few millimeters away from a Hall effect sensor. When moving forward or with wind, the freely rotating propeller will rotate at a speed depending on the airspeed that will generate a square signal at the output of the Hall effect sensor with a frequency depending on the airspeed.

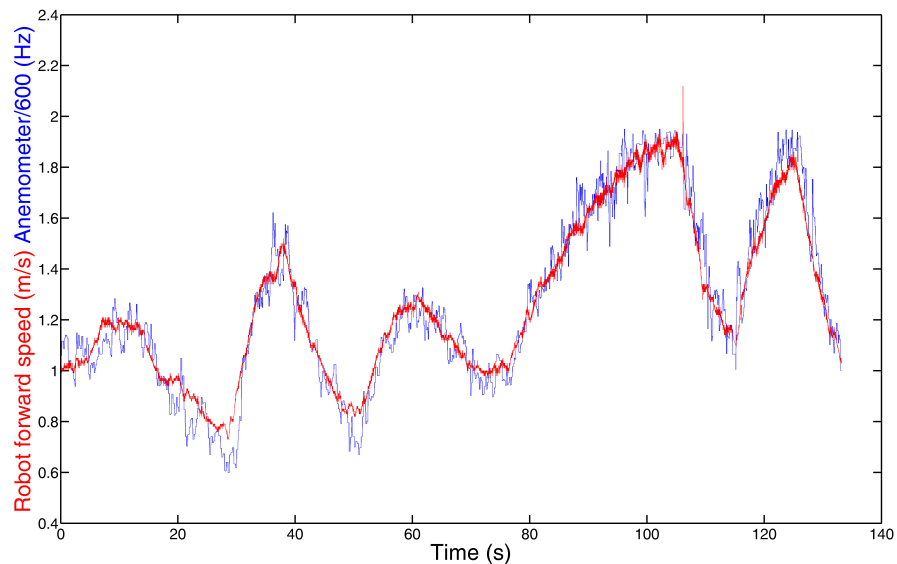


Figure B.13: Airspeed sensor output measured during a flight of the aircraft. In blue is represented the speed measured by the airspeed sensor and in red the speed of the aircraft measured by the pantographic arm. The two measurements have been scaled for clarity and we can see a strong correlation between the two signals.

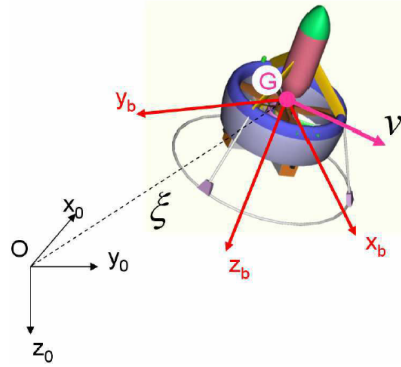


Figure B.14: Representation of the inertial coordinate system in black and the body coordinate system in red. Reprinted from (Pflimlin, 2007).

gyro to control its pitch rate, it is very useful to be able to measure with precision the pitch angle of the robot to monitor it during the flights. In some situations, an accelerometer can be used as an inclinometer but not on a moving and vibrating aircraft to estimate its attitude directly. This is the reason why we implemented a complementary filter fusing the information from the accelerometer and the rate gyro to compute accurately the pitch angle.

Complementary filter for monitoring purpose

Coordinate systems

In order to monitor offline the pitch angle of the robot, we first have to define two coordinate systems: the inertial coordinate system $(0, x_0, y_0, z_0)$ and the body coordinate system (G, x_B, y_B, z_B) (see Figure B.14). The change-of-basis matrix R between the inertial coordinate system and the body coordinate system can be decomposed as a succession of rotations.

- a rotation of the angle $\varphi \in [-180 \text{ deg}, 180 \text{ deg}]$, called the yaw angle, in the horizontal plane (x_0, y_0) ,
- a rotation of the angle $\theta \in]-90 \text{ deg}, 90 \text{ deg}[$, called the pitch angle, in the longitudinal plane (x_B, z_B) ,
- a rotation of the angle $\psi \in [-180 \text{ deg}, 180 \text{ deg}]$, called the roll angle, around the (x_B) axis.

The R matrix can be expressed:

$$R = \begin{pmatrix} c\theta c\psi & s\theta s\phi c\psi - s\psi c\phi & s\theta c\phi c\psi + s\phi s\psi \\ c\theta s\psi & s\theta s\phi s\psi + c\psi c\phi & s\theta c\phi s\psi - s\phi c\psi \\ -s\theta & c\theta s\phi & c\theta c\phi \end{pmatrix} \quad (\text{B.5})$$

Equations of the complementary filter

We can see that the vertical direction can be determined in terms of Euler angles by estimating the roll and the pitch angles. We call x the vertical direction.

$$\text{We can see that } x = -z_0 = -R^T e_3 = \begin{pmatrix} s\theta \\ -c\theta s\phi \\ -c\theta c\phi \end{pmatrix}$$

The dynamical equation between the vertical direction $x(t)$ and the angular speed $\Omega(t)$ is:

$$\dot{x} = -\dot{R}^T e_3 = -(-\Omega \times R^T) e_3 = -\Omega \times x$$

Thanks to the IMU, we know the measurements of the accelerations ($x_m \simeq x$) and the angular speeds which are affected by a bias ($\Omega_m = \Omega + b$). In our case, we are only interested

in monitoring the pitch angle. $\Omega_m = \begin{pmatrix} 0 \\ \theta_m \\ 0 \end{pmatrix}$, $b = \begin{pmatrix} 0 \\ b \\ 0 \end{pmatrix}$ where b is an unknown bias

estimated by the complementary filter.

Pflimlin (2007) proposed a filter described by the following equations:

$$\begin{cases} \dot{\hat{x}} = -(\Omega_m - \hat{b} - k_x(\hat{x} \times x_m)) \times \hat{x} \\ \dot{\hat{b}} = k_b(\hat{x} \times x_m) \end{cases}$$

They proved that, as soon as the coefficients k_x and k_b verify several inequalities, this filter converges $\hat{x} \rightarrow x$. Besides, the error of the bias estimation $\tilde{b} = b - \hat{b}$ also converges to 0.

In order to determine the values of these parameters k_x and k_b , the complementary filter has first been tested in simulation before being implanted onto the main microcontroller of the robot after discretization.

$$\begin{cases} x[k+1] = -(\Omega_m - b[k] - k_x(x[k] \times x_m)) \times x[k] \times T_e + x[k] \\ b[k+1] = k_b(x[k] \times x_m) \times T_e + b[k] \end{cases}$$

Output of the complementary filter $\hat{\theta}_{onboard}$

Figure B.15 shows the angle estimated by the onboard discrete complementary filter (green) and the simulated continuous complementary filter (blue) superimposed with the output of the accelerometer in red which is really noisy due to the vibrations of the aircraft while flying. We can see that, thanks to the complementary filter, we obtain a really accurate measurement of the pitch angle and the complementary filter quickly follows any changes of the pitch angle. Of course, as we do not possess an absolute angular sensor on the robot, it is really hard to evaluate the accuracy of this measurement and in particular if the oscillations visible on the various steps really match the oscillations of the aircraft. The convergence time of the filter directly depends on the choice of the parameters k_x and k_b .

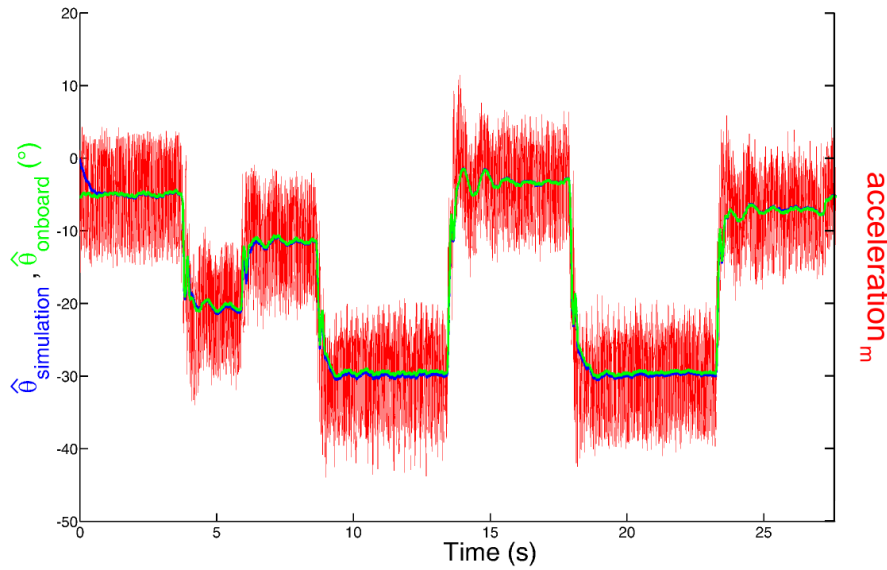


Figure B.15: Comparison between the pitch angle estimated onboard and in simulation with the measurement of the accelerometer alone. Thanks to the complementary filter, the dispersion on the estimated pitch angle is very small both in simulation and onboard the aircraft.

Bluetooth communication to a host computer

The aircraft can communicate to a host computer using a Bluetooth module FM03ALA creating a UART link between the main microcontroller of the robot and the host computer. A specific C sharp (C#) interface has been developed to communicate with the aircraft to monitor data and send high level commands. This interface also handles the UART link between the computer and the dSpace card controlling the motion of the ground and collecting the data coming from the pantographic arm.

Actuators of the BeeRotor robot

Selection of the propellers and Brushless motors

During the specifications of the aircraft, we assumed a final weight of the robot around 80g. We needed to select the lightest propellers and Brushless motors allowing to generate the maximal thrust. In order to control the robot and be able to perform aggressive maneuvers, we wanted to be able to propel at least 1.5 times the aircraft weight with a maximal current of 4A.

After some research, we decided to test two Brushless motors and 3 propellers:

- The LRK 13-4-15Y motor (6g, 3A, 11V) and the LRK13-6-11Y motor (7.8g, 4A, 12V),
- The X-UFO propellers (8 inches, 3.8° twist angle), the APC propellers (8 inches, 3.8° twist angle) and the DF propellers (8 inches, 4.5° twist angle).

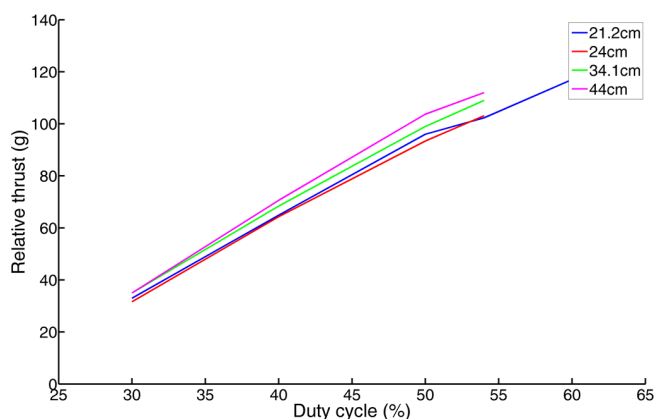


Figure B.16: Influence of the distance between the two propellers on the generated thrust. The distance between the two propellers has almost no influence on the generated thrust.

In order to measure the thrust generated, we built a set-up to measure the thrust generated in grams thanks to a weighing scale. We could also monitor the current and the rotation speed of the propellers.

Influence of the distance between the two propellers

The first thing we checked was how the thrust was affected by the distance between the two propellers. Figure B.16 shows the evolution of the relative thrust with the duty cycle for four different spacings between the two propellers. The relative thrust is the difference between the thrust generated and the weight of the propellers and motors. We can see that the thrust only slowly decreases when we increase the spacing between the two propellers from 21.2cm to 44cm. This is the reason why we chose to put the propellers as close as possible in order to decrease the wingspan of the aircraft.

Selection of the motors

Figure B.17 shows the evolution of the relative thrust with the current for the two Brushless motors. We can see that the LRK 13-6-11Y is clearly more efficient as the thrust is always greater for the same current drawn.

Selection of the propellers

In figure B.18 is shown the evolution of the relative thrust with the current for the three types of propellers. We can see that the X-UFO propellers are the ones generating the more thrust for a given current drawn. As this last experiment has been performed with the LRK 13-6-11Y Brushless motors and with a distance of 22cm between the two propellers which is the distance chosen for the aircraft, we can see that one propeller is able to generate a

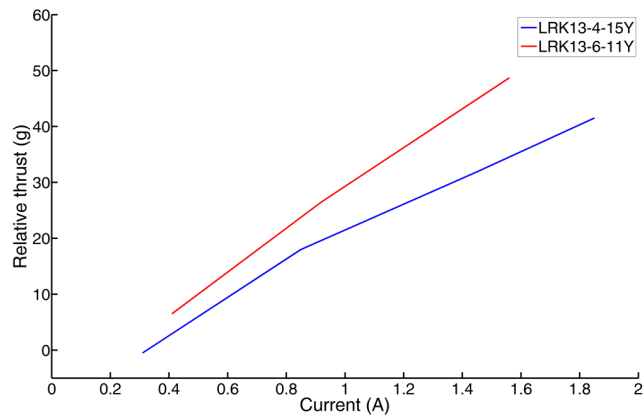


Figure B.17: Evolution of the relative thrust with the current for the two Brushless motors. The LRK 13-6-11Y motor generates a more important thrust for a given current drawn.

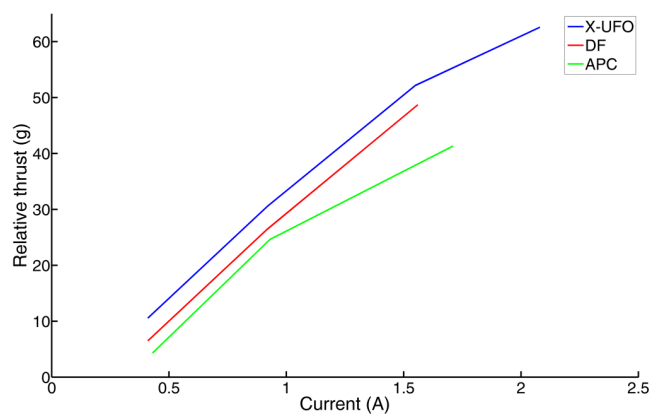


Figure B.18: Evolution of the relative thrust with the current for the three propellers. The X-UFO propeller generates a more important thrust for a given current drawn.

relative thrust of around 60g under 2A which is the value we were expecting when we started the specifications.

This propeller/motor pair is generating the thrust of the aircraft. This thrust F_N varies monotonically with the speed of the propeller according to the following equation:

$$F_N = \frac{1}{2}\rho C_N \left(\frac{2}{3} \times R \times N_{Rotor}\right)^2 = \alpha \times N_{Rotor}^2 \quad (\text{B.6})$$

where ρ is the density of air, C_N is the lift coefficient, R is the rotor radius and N_{Rotor} is the rotor speed. For the control, we chose to consider the rotational speed of the propeller instead of the generated thrust for simplicity.

Eye rotation

The eye is commanded by a stepper motor AM0820_V_5_56 with 20 steps followed by a 1/120 reductor. This motor is commanded by a A3967 driver motor in eighth of steps which gives a resolution of $\frac{360}{20 \times 120 \times 8} = 0.0187^\circ$. The eye is oriented to a specific position thanks to the measurement of the Eye orientation sensor. The mass balance of the aircraft equipped with the sensors and actuators presented previously is presented in Table B.1. The total mass is slightly smaller than 80g which was the objective when we started the specifications.

Parts	Mass (g)
Main board (density 0.31 g/cm ²)	13
Electrical components	9.1
Brushless motors	8.2*2
Propellers	3.6 * 2
Stepper motor + reductor	9.1
Stepper motor frame	1.7
Eye tube	0.6
Carbon fiber	2.4
Robot frame	2.7
Eye	13.54
Airspeed sensor	0.52
Brushless controllers	1.5*2
Total	79.26

Table B.1: Mass balance of the BeeRotor robot

Description of the pantographic arm

As can be seen in Figure B.19, the BeeRotor robot is tethered to the end of a light, counter-balanced whirling pantographic arm. The BeeRotor robot is travelling along a circular high-roofed 12-m long tunnel, the floor and ceiling of which are covered with printed discs (inner

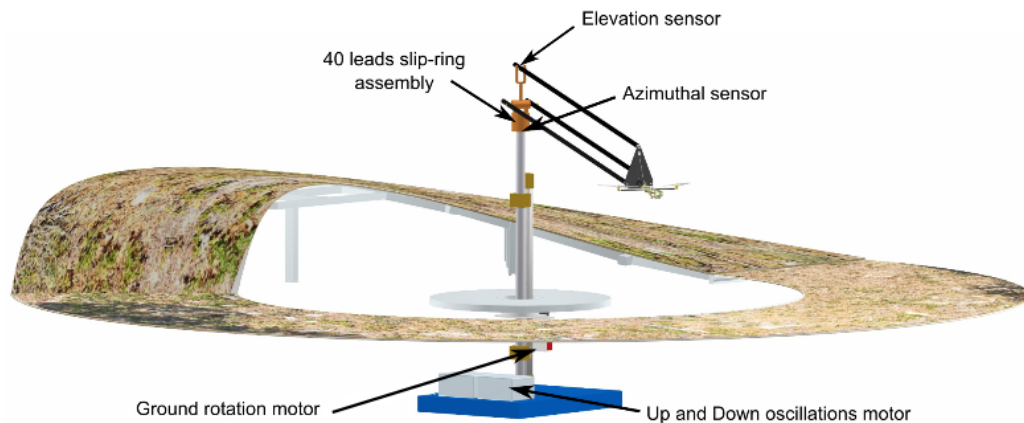


Figure B.19: Simplified CAD drawing of the test bench of the BeeRotor experiment. The aircraft is at the end of a rotating pantographic arm and travels along a 12-m long high roofed tunnel where the ground and ceiling are covered by natural patterns (only the ground is represented here for clarity). The ground has a 38-cm high obstacle and can rotate and perform up and down movements thanks to two motors.

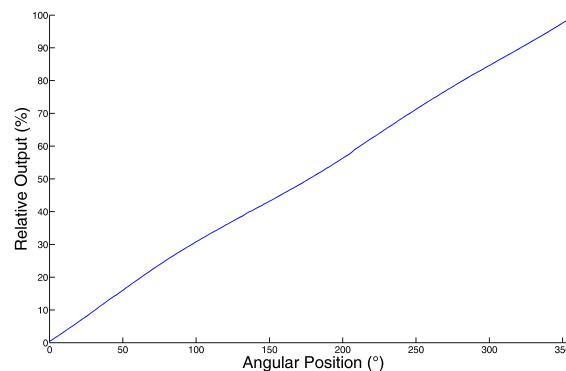


Figure B.20: Evolution of the magnetic compass output during a 360° rotation of the sensor placed on an accurate 2D goniometer.

diameter 2.4m, outer diameter 4.5m) depicting natural scenes. The altitude of the ground of the tunnel can be actively controlled over a 64cm range using a servomotor (DBL2 from Kollmorgen) coupled with a Servostar 300 modifying the height of the tunnel from 200cm to 140cm. The ground can also rotate in both directions thanks to a 30W Brushless DC geared motor (80 149 606 from Crouzet) altering the ground speed and therefore disturbing the perceived optic flow. These two motors are controlled using dSpace controller board (RT1104).

Sensors embedded on the pantographic arm

The pantographic arm is equipped on the elevation axis with a servo-potentiometer giving the robot's altitude. It is also equipped on the travel axis, with an incremental optical encoder (500 pulses per revolution) placed inside the pivot joint and giving the robot's azimuth angle, and hence the horizontal distance travelled and the robot's forward speed. A second optical

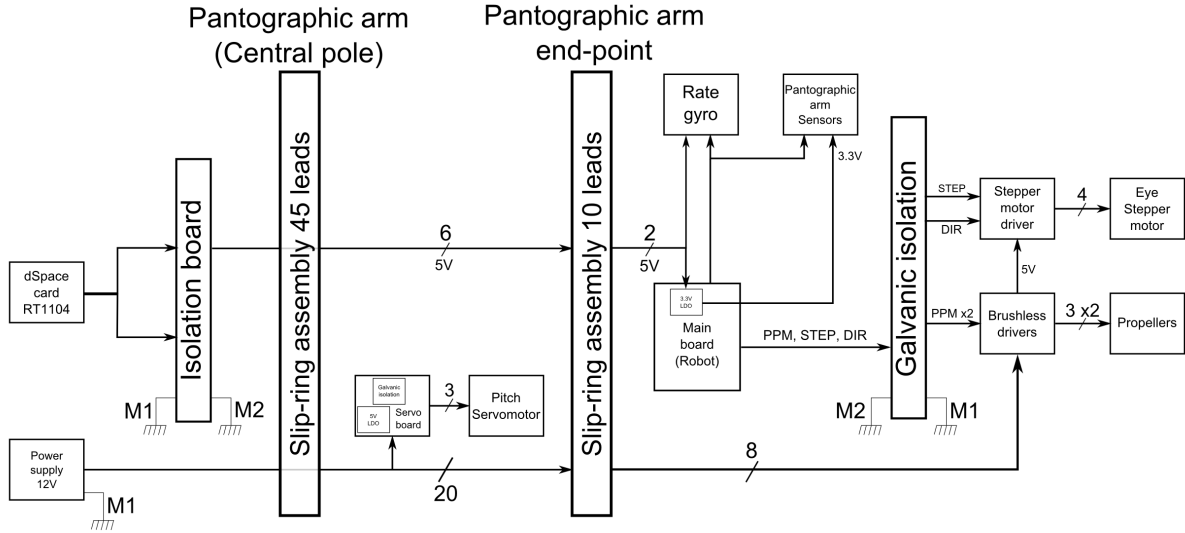


Figure B.21: Schematics of the power supply of the aircraft. The aircraft is supplied by a 11V power supply driving the Brushless outrunners and which is used to generate the 5V controlling the stepper motor rotating the eye and a 7V logic supply for the sensors and the microcontrollers.

sensor is used as a reference of the azimuthal orientation and give one pulse per revolution.

The height of the ground is known directly from the command of the Up and Down motor as the motor's position is regulated. As can be seen in Figure B.20, the azimuthal position of the ground is sensed using a magnetic compass giving the orientation of the sensor relative to the magnetic North. These data are collected on the host computer using an UART link between the dSpace card and the C sharp interface of the aircraft.

Electrical connections and power supply of the test bench.

Although the aircraft is fully autonomous in terms of computational power, it is not autonomous in terms of power supply which is carried into the aircraft through two slip-sing assemblies (see Figure B.21):

- a 45-leads slip ring assembly situated inside the pantographic arm,
- a 10-leads slip ring assembly placed inside the tube linking the aircraft at the end-point of the pantographic arm.

In order to decrease the noise generated by the actuators, two power sources are used to supply the aircraft:

- One 11V power supply for the Brushless drivers. Due to the size of the test rig (4.5m diameter), the distance between the power supply and the robot is greater than 5m and the voltage drops to close to 9V on the aircraft. As we chose a 5V stepper motor to drive the eye orientation, we used the Beck output of the Brushless drivers to supply this motor.

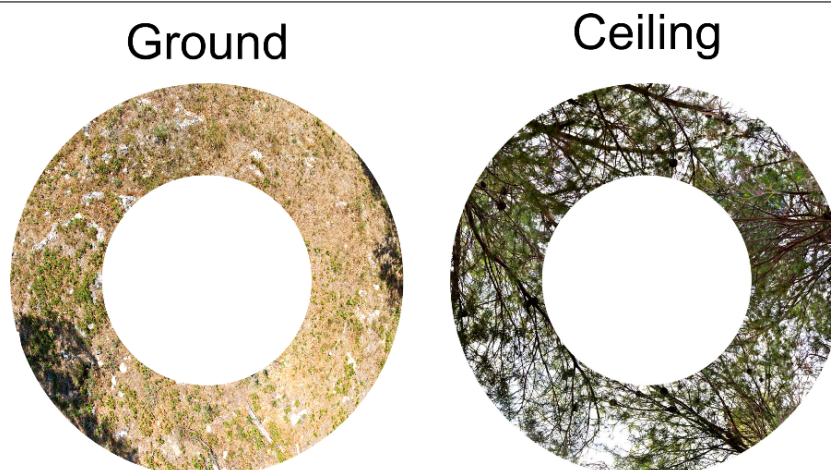


Figure B.22: Photographs of the ground and the ceiling.

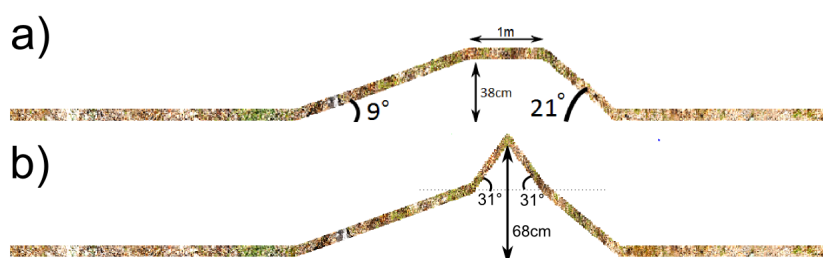


Figure B.23: a) Side view of the ground altitude with the first relief. The ground is composed of a 4.5m-long obstacle with a 2.5m-long ascending ramp, a 1m-long flat and a 1m-long descending ramp. b) Side view of the ground altitude with the second relief. The 1m-long flat part has been replaced by a 30cm-high obstacle with an ascending and descending ramp of 31° .

- One 7V logic voltage supply for the sensors and the microcontrollers. Again, due to the power line distance, the voltage drops to a little more than 5V.

A galvanic isolation is used on the aircraft to clearly separate the analog and digital signals from the power motor signals.

The environment of the BeeRotor robot.

Figure B.22 shows the natural patterns covering the ground and the ceiling which are used to stimulate the aircraft. These patterns have been printed on wide discs (inner diameter 2.4m, outer diameter 4.5m) in order to be sure that the quasi-panoramic eye of the BeeRotor robot is always looking at these contrasts regardless of its height or its pitch angle.

In order to assess the performances of the BeeRotor autopilot and in particular its ability to avoid collisions, we added two 450-cm long obstacles to the ground. The first obstacle is 38 cm high and is composed of a 9° ascending ramp, a 1-m long flat part and a 21° descending ramp (see Figure B.23a). With the second obstacle, the 1-m long flat part has been replaced by a 30cm-high supplementary relief with an ascending and descending ramp of 31° (see Figure B.23b).

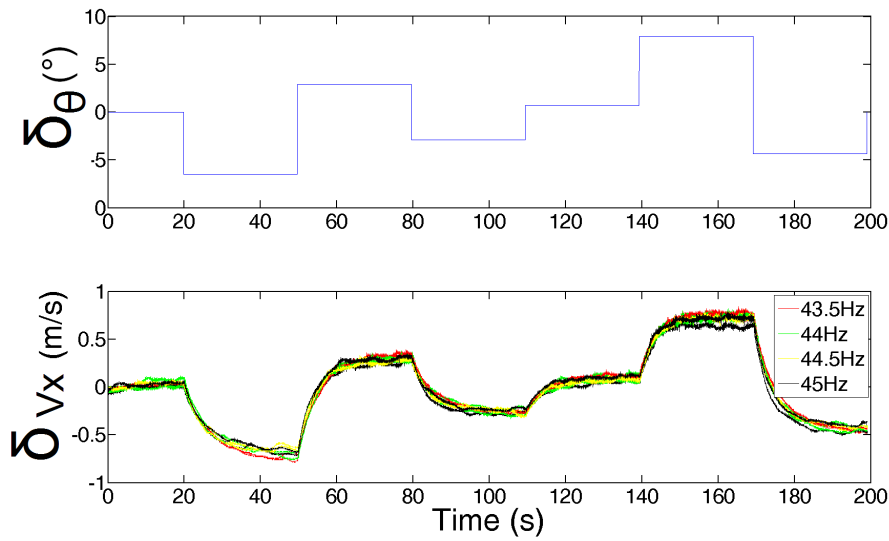


Figure B.24: Speed response of the BeeRotor aircraft when applying a series of steps on its pitch angle from several operating points with an initial pitch angle equals to 6° .

Although it introduced some inertial forces (more details are given on the influence of the pantographic arm onto the aircraft in (Ruffier, 2004)), the pantographic arm enabled us to reliably and reproducibly test the performances of the BeeRotor robot under safe flying conditions, while making the parameter monitoring simpler.

Identification and control of the dynamics of the aircraft

Although it would be easier to model accurately the aircraft's dynamics from the physical equation if it was freely flying, the pantographic arm plays in our case a very important part in the altitude and forward speed dynamics and this is the reason why we chose to identify the dynamics of the aircraft as a black box based on real data captured onboard the aircraft while flying. Besides, for simplification, we have chosen to identify separately the altitude dynamics and the forward speed dynamics and we consider these two dynamics are independent. If this is the case, the altitude of the aircraft will then depend only on the mean speed of the propellers Ω_{Rotors} whereas its forward speed will depend only on the propellers differential speed $\Delta\Omega_{Rotors}$ with the speed of the Left propeller $\Omega_{Left} = \Omega_{Rotors} - (\Delta\Omega_{Rotors})/2$ and the speed of the Right propeller $\Omega_{Right} = \Omega_{Rotors} + (\Delta\Omega_{Rotors})/2$

Forward speed control

Identification of the dynamics between the pitch angle and the forward speed of the BeeRotor robot.

We identified the dynamics between the forward speed of the robot and its pitch angle by applying a series of steps on the pitch angle of the BeeRotor robot which was controlled

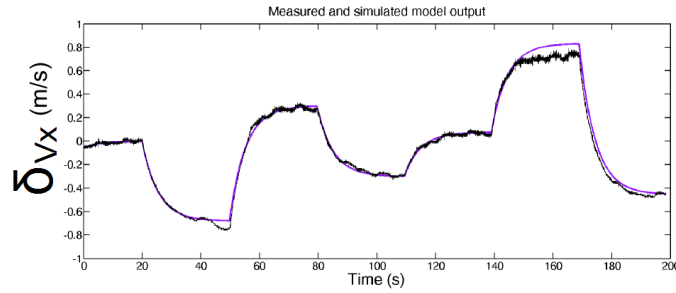


Figure B.25: Comparison between the output of the identified model and one typical response of the aircraft when applying a series of steps on the pitch angle of the robot.

using a servomotor for several operating points (Initial pitch = 6° which corresponds to a forward speed of 1.3m/s with a rotational speed of the propellers between 43.5Hz and 45Hz).

Figure B.24 shows the speed response of the rotorcraft when applying a series of steps on the pitch angle of the robot. We can see that, regardless of the speed of the propellers, the speed response is identical which proves that the forward speed dynamics is independent from the speed of the propellers and depends only on the pitch angle of the robot. We identify in any case a first order system with the transfer function:

$$G_{Speed}(s) = \frac{\delta V_x(s)}{\delta \theta(s)} = \frac{K}{\tau s + 1} = \frac{0.10498}{5.4312s + 1} \quad (\text{B.7})$$

The correlation between the identified model and the 7 other curves of validation is greater than 85%. Figure B.25 shows the correlation between the response of the identified model and one validation curve.

Dynamics between the propellers differential and the pitch rate of the aircraft

Closed loop identification

In order to identify the dynamics between the propellers differential and the pitch rate of the rotorcraft after removing the servomotor used previously (Expert & Ruffier, 2012), we first implemented a basic Proportional Derivative regulator on the pitch angle of the robot to roughly stabilize the pitch angle of the robot because, without this feedback loop, the robot always starts to oscillate and reaches its mechanical stops. This feedback loop uses the fused information from the accelerometer and the rate gyro to stabilize the pitch angle to a setpoint as can be seen in figure B.26. We then want to identify the transfer function $G_{PitchRate}(s)$ between the propellers differential speed $\Delta\Omega_{Rotors}$ and the pitch rate of the aircraft $\dot{\theta}$.

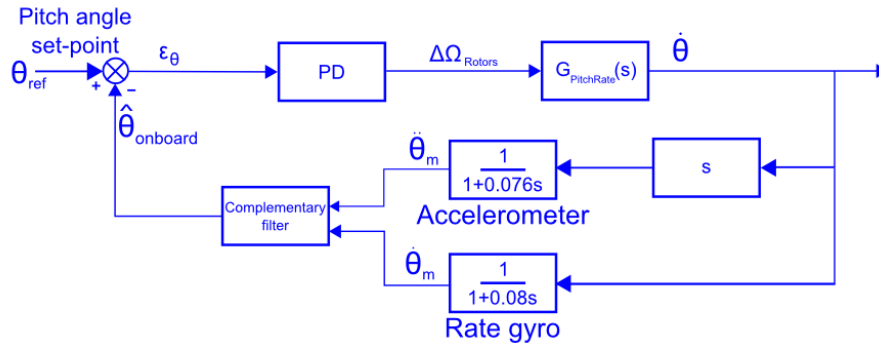


Figure B.26: Closed loop implemented on the BeeRotor aircraft solely used to identify the dynamics between the propellers differential speed $\Delta\Omega_{Rotors}$ and the pitch rate of the aircraft $\dot{\theta}$ measured thanks to a rate gyro. The pitch angle of the robot is determined thanks to a complementary filter fusing the information coming from the accelerometer and the rate gyro.

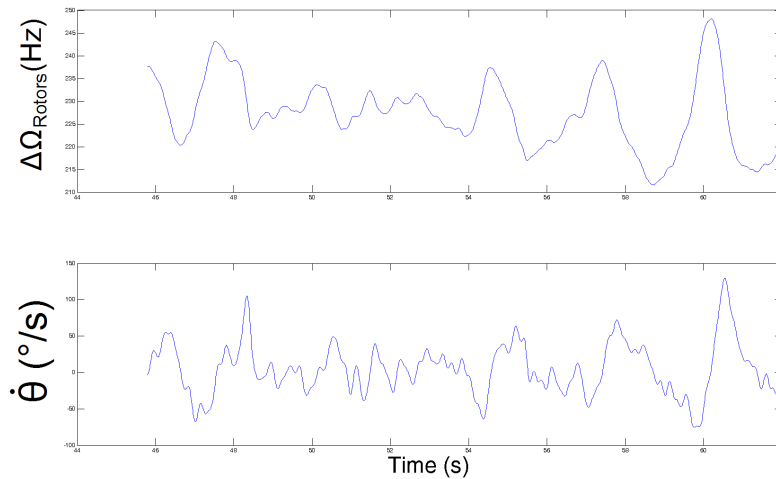


Figure B.27: Pitch rate response of the aircraft to a varying command to the propellers differential thrust. During this experiment, we applied a series of steps on the pitch angle setpoint θ_{ref} of the aircraft to identify the pitch rate dynamics.

Identification of the dynamics between the propellers differential and the pitch rate of the aircraft

To identify the dynamics between the propellers differential and the pitch rate of the aircraft, we applied a series of steps on the pitch angle of the rotorcraft (see Figure B.27). Due to the feedback loop, we can not obtain exactly the same set of $\Delta\Omega_{Rotors}$ signals from one experiment to another. However, we noticed that, regardless of the speed of the propellers Ω_{Rotors} , the pitch rate response was identical. We identified the transfer function between the propellers differential and the pitch rate to be a second order function with a zero.

$$G_{PitchRate}(s) = \frac{\dot{\theta}(s)}{\Delta\Omega_{Rotors}(s)} = \frac{-0.042s - 0.02683}{0.001742s^2 + 0.05445s + 1} \quad (\text{B.8})$$

Figure B.28 shows the correlation between the response of the identified model and one

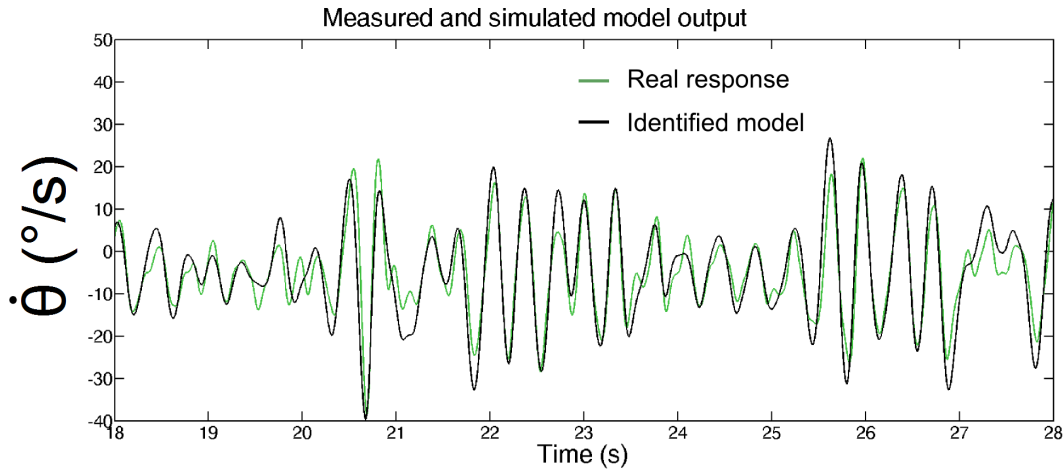


Figure B.28: Comparison between the output of the identified model and one typical response of the aircraft's pitch rate when applying a series of steps on the pitch angle of the robot.

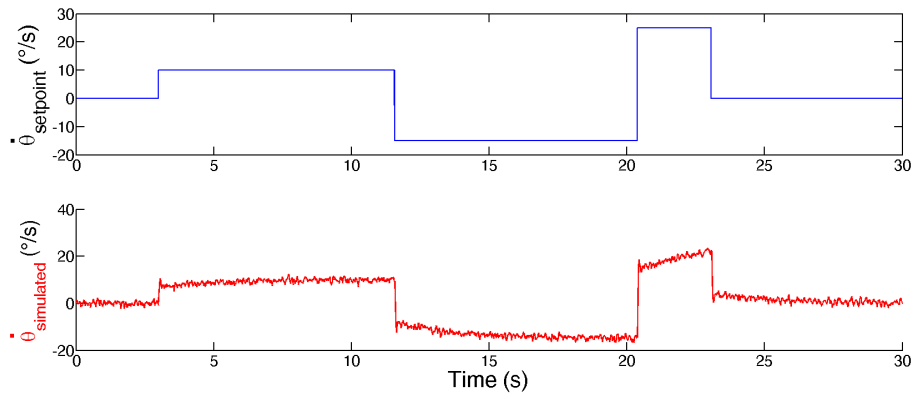


Figure B.29: Pitch rate response in simulation when applying a series of steps on the setpoint of the pitch rate feedback loop. The PID controller regulating the pitch rate has been adjusted in order to have a very short settling time.

validation curve.

Inner pitch rate regulation (2nd feedback loop)

In order to regulate the pitch rate based on the information of the rate gyro, we synthesized a Proportional Integral Derivative (PID) controller. This controller has been adjusted in order to have a very short settling time ($< 200\text{ms}$) because this feedback loop needs to be very fast in order to be able to control the rotorcraft. The output response of the system simulated with noise and with the PID controller is shown in Figure B.29. We can see that the system quickly responds to a step on the setpoint value without overshooting. The integral coefficient is quite low which explains the long time necessary to cancel the static error but the system was not stable when this coefficient was increased due to the constant slight oscillations of the tandem rotorcraft.

Again, due to the same oscillations of the robot measured by the MEMS rate gyro when

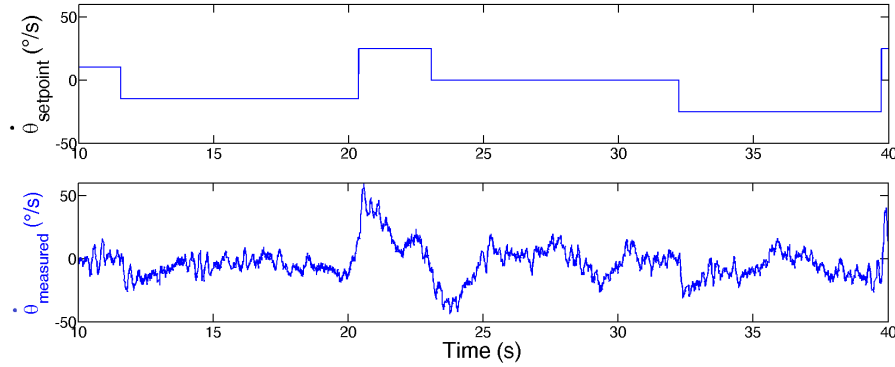


Figure B.30: Pitch rate response measured on the rotorcraft flying when applying a series of steps on the setpoint of the pitch rate feedback loop.

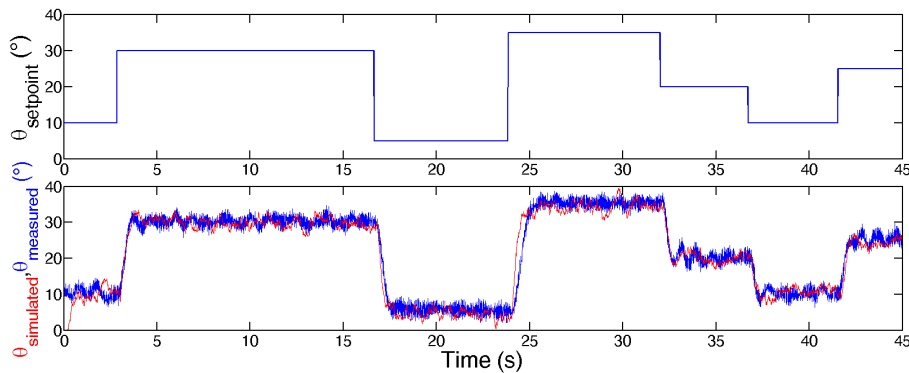


Figure B.31: Pitch angle response in simulation and measured on the rotorcraft flying when applying a series of steps on the setpoint of the pitch angle feedback loop. We can see that the real system response faithfully followed the simulated one. The pitch angle oscillates slightly around its setpoint value due to the vibrations of the aircraft.

the aircraft was flying, when regulated, the system was not able to stay at the setpoint value with as much accuracy as the simulation (see Figure B.30). Nevertheless, the settling time of the feedback loop is as low as expected and the controller is able to robustly reject perturbations.

Dynamics between the propellers differential and the pitch angle of the aircraft

Although the information from the accelerometer are not used on the robot when flying autonomously, it was useful to be able to control the pitch angle of the aircraft during the early stages of the development and the identification process. This is the reason why we implemented a feedback loop to regulate the pitch angle of the aircraft nesting the fast feedback loop on the pitch rate. The value of the pitch angle was estimated using the complementary filter. As this feedback loop's performances were not critical, we only implemented a Proportional regulator as the static error of the closed loop system was already null.

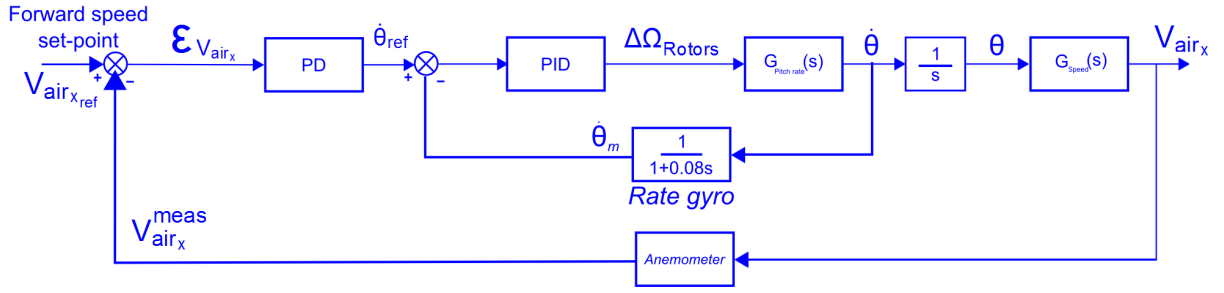


Figure B.32: Schematic representation of the feedback loop controlling the forward speed of the rotorcraft. This feedback loop is composed of a fast nested loop regulating the pitch rate of the aircraft and a Proportional Derivative Controller regulating the forward speed of the robot based on the information of the anemometer.

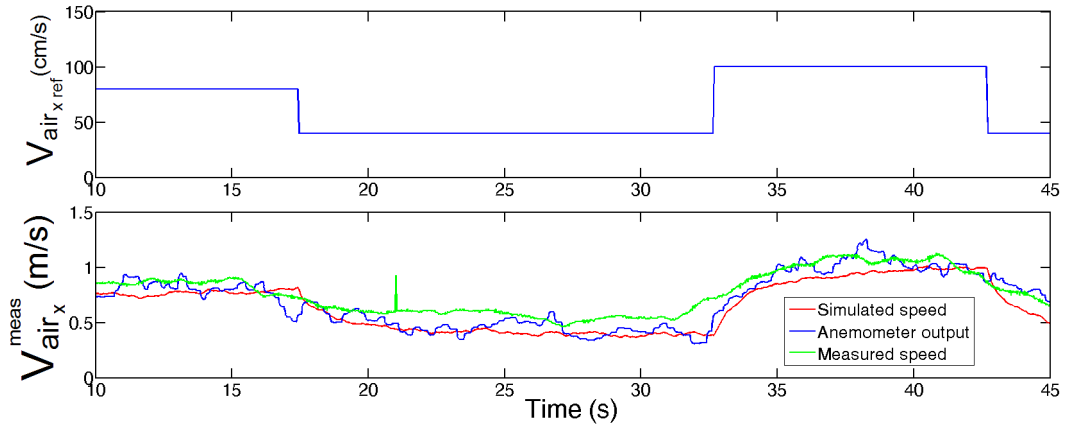


Figure B.33: Real and simulated output of the forward speed feedback loop. Although the absolute speed of the aircraft was always quite greater than the simulated speed, we can see that the speed of the aircraft accurately followed the setpoint value despite the variations on the anemometer measurements.

Airspeed regulation (3rd feedback loop)

The complete feedback loop acting on the propellers' differential speed to regulate the forward speed of the robot is shown in Figure B.32. This loop is composed of a nested and very fast feedback loop regulating the pitch rate of the aircraft and a Proportional Derivative (PD) controller using the measurement of the airspeed sensor. Although all the dynamics G_{Speed} and $G_{Pitchrate}$ were known, we chose to identify the dynamics between the pitch rate setpoint $\dot{\theta}_{ref}(s)$ and the forward speed of the aircraft $V_{air_x}(s)$ based on real measurements performed on the aircraft while flying. This identification includes the nested feedback loop controlling the pitch rate of the aircraft. We obtained a third order system with one zero and one integrator with the following transfer function:

$$G_{PitchRate_{CL}}(s) = \frac{V_{air_x}(s)}{\dot{\theta}_{ref}(s)} = \frac{7.44s - 0.057904}{s(55.1s^2 + 29.15s + 1)} \quad (\text{B.9})$$

As the closed loop system static error was null, we chose to implement a Proportional

Derivative controller in order to reduce as much as possible the response time of the whole system. The output of the forward speed feedback loop when applying a series of steps on the setpoint of the feedback loop is shown in Figure B.33. Thanks to the proportional gain, we reduced the settling time of the system while the derivative coefficient decreases the overshoot and the oscillations. The simulated (red) and measured (blue) speeds faithfully followed the setpoint value.

$$G_{Speed_{CL}}(s) = \frac{V_{air_x}(s)}{V_{air_{ref}}(s)} = \frac{1.0395}{1.62s^2 + 0.994s + 1} \quad (B.10)$$

Dynamics between the propellers' differential speed and the sum of the ventral and dorsal optic flow ω_{SumOF}

We identified experimentally the dynamics between the propellers' differential speed and the airspeed with the two nested loops regulating the pitch rate and the airspeed $G_{speed_{CL}}$. As expected, the static gain is very close to 1. We linearized the open-loop transfer function which can be written:

$$\begin{aligned} G_{SumOF}(s) &= G_{surge}(s) \times G_{speed_{CL}}(s) \times \frac{d}{dVx}(\omega_{Vtrl} + \omega_{Drsl}) \\ &= G_{surge}(s) \times G_{speed_{CL}}(s) \times \frac{D_{Up} + D_{Down}}{D_{Up} \cdot D_{Down}} \end{aligned} \quad (B.11)$$

where G_{surge} is the controller regulating the sum of the optic flow and D_{Down} and D_{Up} are respectively the distances between the aircraft and the ground and the ceiling. Assuming, we fly at 1m from the followed surface $\frac{D_{Up} + D_{Down}}{D_{Up} \cdot D_{Down}} \sim 2rad.s^{-1}/(m/s)$.

Synthesis of the forward controller (4th feedback loop) for the regulation of the OF sum

The forward controller has been designed in the frequency domain to increase the phase margin of the system. A double phase lead controller has been implemented strongly reducing the response time of the system. This controller is cascaded with a low-pass filter reducing the noise on the optic flow measurements. Figure B.34 shows the step responses of the closed loop system (blue) and the $G_{speed_{CL}}$ transfer function (red). As we can see, the proposed controller reduces the response time of the system. Of course, the static gain of the system is smaller to 1 but the static error is small and increasing the gain destabilizes the system.

Figure B.35 shows the evolution of the sum of the ventral and dorsal optic flows during an autonomous flight of the aircraft following the ceiling. As expected thanks to the forward controller, the value of the Sum OF is regulated around the chosen setpoint value $\omega_{setSumOF} = 250^\circ/s$.

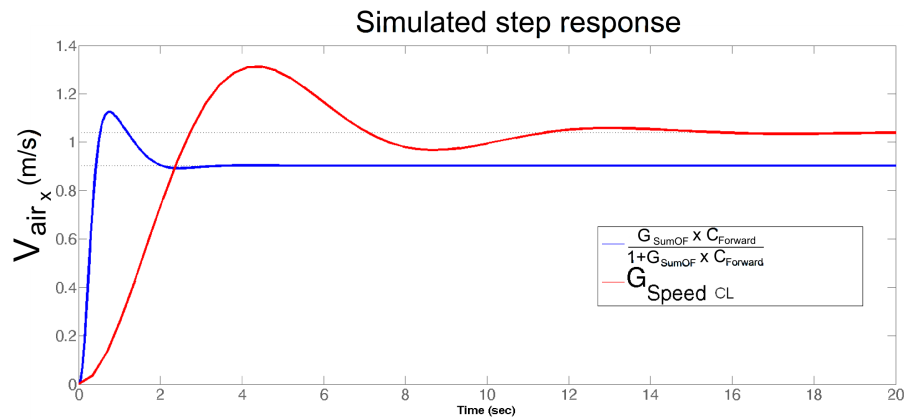


Figure B.34: Simulated step response of the forward speed feedback loop (blue) and the $G_{speedCL}$ transfer function (red). We show here in simulation that the settling time is much smaller thanks to the Forward controller $C_{Forward}(s)$

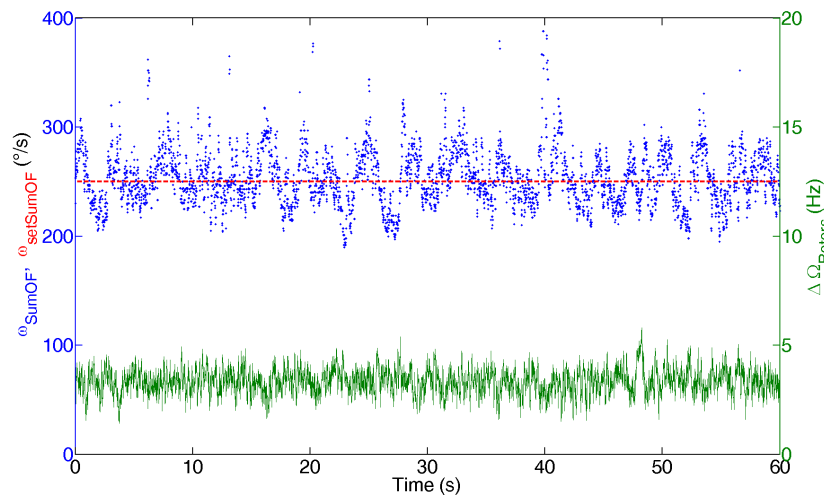


Figure B.35: Evolution of the sum of the ventral and dorsal optic flows during a 60m-long flight when the aircraft was flying autonomously following the ceiling and regulating the optic flow to control its altitude and forward speed with $\omega_{setMaxOF} = 180^{\circ}/s$ and $\omega_{setSumOF} = 250^{\circ}/s$. By acting on the differential speed of the propellers, the aircraft maintains its Sum OF around the setpoint value.

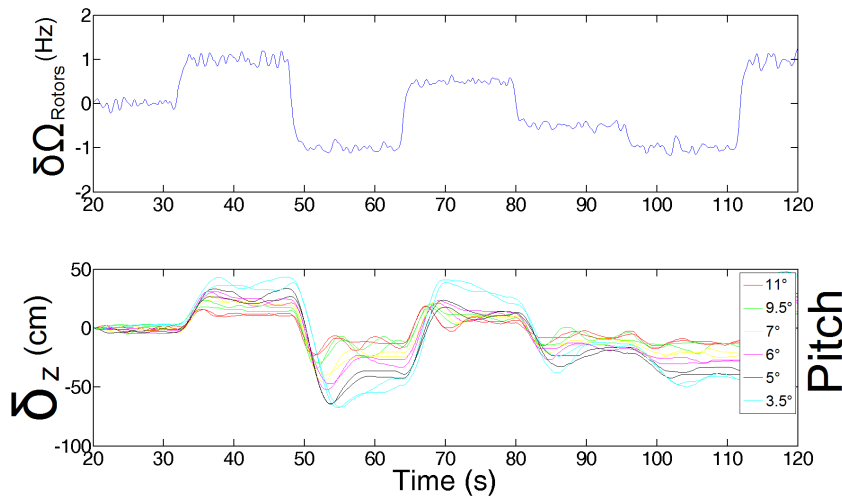


Figure B.36: Altitude variations of the BeeRotor aircraft when applying a series of steps on its propellers' speed from several operating pitch angles (forward speeds) with an initial propeller speed of 44.5Hz.

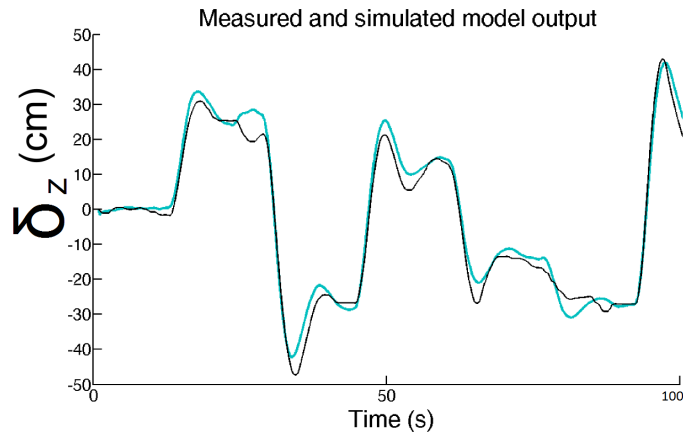


Figure B.37: Comparison between the output of the identified model and one typical response of the aircraft's altitude when applying a series of steps on the propellers' thrust.

Altitude control

Identification of the dynamics between the propellers' speed and the altitude of the aircraft

We then identified the heave dynamics by applying a series of steps on the speed of the propellers for several operating points (Initial propeller frequency 44.5Hz with a pitch angle between 3.5° and 15.3°).

Figure B.36 shows the altitude response of the rotorcraft when applying a series of steps on the propellers' speed. We can see that, contrary to the forward speed dynamics, the altitude response does not depend only on one parameter. Indeed, the altitude of the aircraft depends not only on the propellers' speed but also on the pitch angle of the aircraft. We identified for each pitch angle value the transfer function between the propellers' speed and

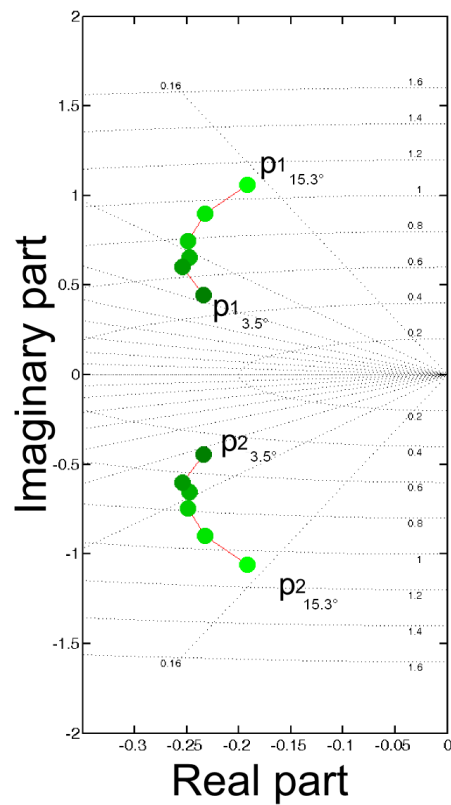


Figure B.38: Evolution of the system's poles (p_1, p_2) of $G_{alt}(s)$ according to the forward speed of the robot. Although the forward speed of the robot affects the transfer function between the propellers' speed and the altitude of the aircraft, the system always behaves as an underdamped second order system with a damping ratio increasing from $\zeta_{alt} = 0.17$ for a pitch angle of 3.5° to $\zeta_{alt} = 0.47$ for a pitch angle of 15.3°

the altitude of the aircraft $G_{alt}^\theta(s)$. The output of one identified model compared to one validation curve for one of these transfer functions is shown in figure B.37.

In order to control our system, we determined the poles of the identified models for each value of the pitch angle of the aircraft (see figure B.38). We can see that the system always behave like an underdamped second order system with a damping ratio ranging from $\zeta_{alt} = 0.17$ for a pitch angle of 3.5° to $\zeta_{alt} = 0.47$ for a pitch angle of 15.3° whereas the gain varies between 0.12 et 0.42 on the same range.

$$G_{alt}^\theta(s) = \frac{K_{alt} \times \omega_n}{s^2 + 2\zeta_{alt}\omega_0s + \omega_0^2} \quad (\text{B.12})$$

In order to control the system, as we do not use the information of the accelerometer and we therefore do not know the pitch angle of the aircraft, we synthesized an altitude controller $C_{Altitude}(s)$ guaranteeing the stability of the system for any value of the pitch angle, i.e. the robot forward speed.

Control of the altitude of the aircraft

Linearization of the dynamics between the propellers' speed and the Maximal OF ω_{MaxOF}

As we have seen, several transfer functions have been identified between the propellers' speed and the altitude G_{Alt} depending on the forward speed of the aircraft. On the robot, we want to use the Maximal optic flow to control the speed of the propellers Ω_{Rotors} which is a nonlinear system as the optic flow is inversely proportional to the altitude. We therefore chose to linearize the transfer function for an altitude $h = 1m$ between the robot and the closest wall. The linearized transfer functions between the propellers' speed and ω_{MaxOF} for each forward speed can therefore be written:

$$\begin{aligned} G_{MaxOF}(s) &= C_{Altitude}(s) \cdot G_{Alt}(s) \cdot \frac{d}{dh} \left(\frac{1}{h} \right) \\ &= C_{Altitude}(s) \cdot G_{Alt}(s) \cdot \left(-\frac{1}{h^2} \right) \\ &= -C_{Altitude} \cdot \frac{K_{alt} \times \omega_n}{s^2 + 2\zeta_{alt}\omega_0s + \omega_0^2} \end{aligned} \quad (\text{B.13})$$

where $K_{alt} \in [0.12, 0.42]$ and $\zeta_{alt} \in [0.17, 0.47]$ depending on the forward speed of the aircraft.

Synthesis of the altitude controller for Maximum optic flow regulation (5th feedback loop)

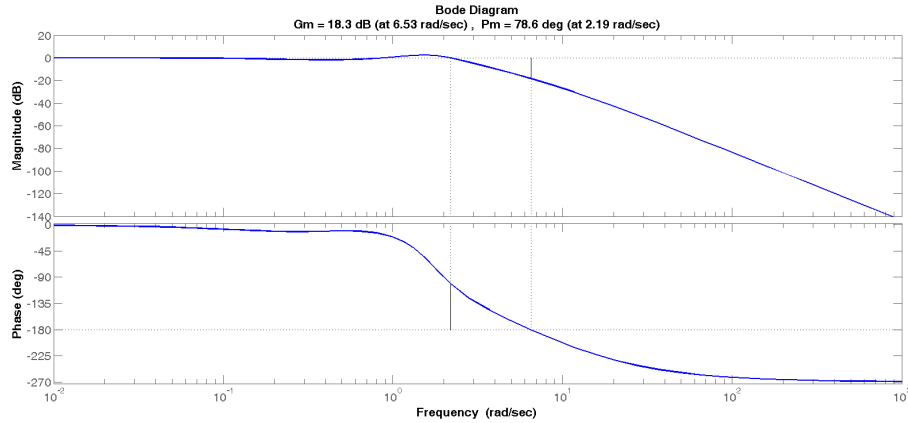


Figure B.39: Bode diagram of the closed loop system between the propellers' speed and the measured Maximal OF for a forward speed of 1.5m/s. Thanks to the Integral controller, the static gain of the system is 1. The double phase lead controller has been chosen to strongly increase the phase margin (78.6°) and the gain margin ($18.3dB$) of the system. These important margins are necessary to guarantee the good performances of the system regardless of the forward speed.

The goal of the BeeRotor robot is to follow the ground or the ceiling depending on the closest surface. In order to be able to follow both surfaces at an equal distance for a same forward speed, it is necessary to add an integral controller in the feedback loop. We therefore implemented a Proportional Integral (PI) Controller eliminating the static error even if it added a phase difference of -90° . The Integral coefficient was chosen quite small to avoid being too sensitive to disturbances as obstacles. To increase the phase margin and the damping of the system, this PI controller was cascaded with a double phase lead controller followed by a low pass filter smoothing the measured optic flow. The obtained surge controller can be written:

$$\begin{aligned}
 C_{Altitude}(s) &= PI(s) \times \left(\frac{\tau_1 s + 1}{\tau_2 s + 1}\right) \times \left(\frac{\tau_1 s + 1}{\tau_2 s + 1}\right) \times \left(\frac{1}{\tau_3 s + 1}\right) \\
 &= \left(\frac{1.5s + 0.3}{s}\right) \times \left(\frac{1.866s + 1}{0.134s + 1}\right) \times \left(\frac{1.866s + 1}{0.134s + 1}\right) \times \left(\frac{1}{0.6s + 1}\right)
 \end{aligned} \tag{B.14}$$

Figure B.39 shows the Bode diagram of the closed loop system corresponding to a forward speed of 1.5m/s. This controller has proven to guarantee the stability and the robustness of the system to disturbances for every identified transfer functions.

Figure B.40 shows the evolution of the Maximum optic flow during an autonomous flight of the aircraft following the ceiling. As expected thanks to the altitude controller, the value of the Max OF is regulated around the chosen setpoint value $\omega_{setMaxOF} = 180^\circ/s$.

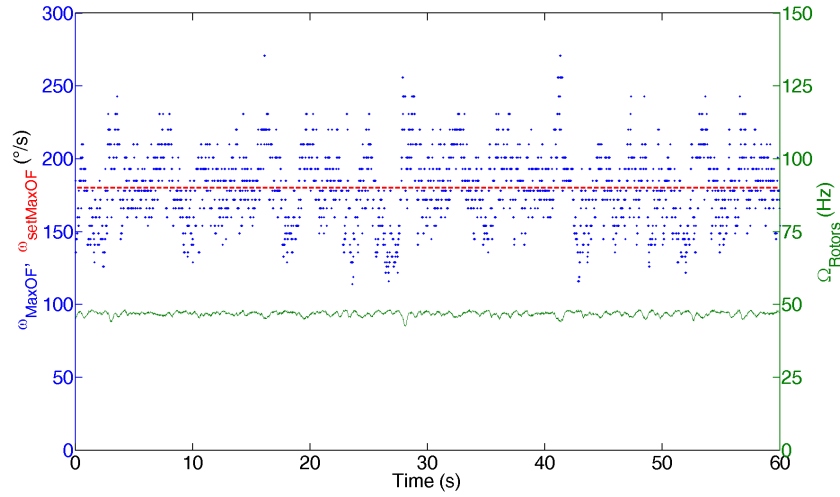


Figure B.40: Maximum optic flow value during a 60m-long flight when the aircraft is flying autonomously following the ceiling and regulating the optic flow to control its altitude and forward speed with $\omega_{setMaxOF} = 180^\circ/s$ and $\omega_{setSumOF} = 250^\circ/s$. By acting on the speed of the propellers, the aircraft maintains its Maximum optic flow around the setpoint value.

$G_{propeller}(s)$	$\frac{4.116}{0.1398s+1}$
$G_{Speed}(s)$	$\frac{0.10498}{5.4312s+1}$
$G_{PitchRate}(s)$	$\frac{-0.042s-0.02683}{0.001742s^2+0.05445s+1}$
$G_{FwdSpeed}(s)$	$G_{Speed}(s) \cdot \frac{1}{s} \cdot G_{Pitchrate}(s)$
$G_{PitchRate_{CL}}(s)$	$\frac{7.44s-0.057904}{s(55.1s^2+29.15s+1)}$
$G_{speed_{CL}}(s)$	$\frac{1.0395}{1.62s^2+0.994s+1}$
$G_{SumOF}(s)$	$C_{Forward}(s) \times G_{speed_{CL}}(s) \times \frac{d}{dVx}(\omega_{Vtrl} + \omega_{Drsl})$
$G_{Alt}^{\Theta_{pitch}}(s)$	$\frac{K_{alt}}{s^2+2\zeta_{alt}\omega_0s+\omega_0^2}$
$G_{Alt}^{3.5^\circ}(s)$	$\frac{0.1202}{0.8616s^2+0.33s+1}$
$G_{Alt}^{15.3^\circ}(s)$	$\frac{0.419}{3.8852s^2+1.833s+1}$
$G_{MaxOF}(s)$	$C_{Altitude}(s) \cdot G_{Alt}(s) \cdot \frac{d}{dh}(\frac{1}{h})$

Table B.2: Transfer functions of the BeeRotor robot.

$C_{Propeller}(s)$	$\frac{0.5s+5}{s}$
$C_{PitchRate}(z)$	$\frac{0.1057z^2-0.2056z+0.1}{0.005z^2+0.005z}$
$C_{Airspeed}(z)$	$\frac{0.0626z-0.06}{0.01z}$
$C_{Forward}(s)$	$5 \times \left(\frac{9s+26}{s+8.665}\right) \times \left(\frac{9s+26}{s+8.665}\right) \times \left(\frac{1}{0.6s+1}\right)$
$C_{Feedforward}(s)$	$\frac{0.05874s^2+0.002335s-0.1104}{s^2+20s+96.07}$
$C_{VerticalOF}(s)$	$\frac{450s+1300}{s+8.665}$
$C_{Altitude}(s)$	$\left(\frac{1.5s+0.3}{s}\right) \times \left(\frac{1.866s+1}{0.134s+1}\right) \times \left(\frac{1.866s+1}{0.134s+1}\right) \times \left(\frac{1}{0.6s+1}\right)$
$C_{Eye}(s)$	$\frac{0.0375s+0.5003}{s+0.5013}$

Table B.3: Transfer functions of the controllers embedded onto the BeeRotor robot.

Bibliography

- Amic, S. (2002). Intégration des fonctions de détection de mouvements par le traitement parallèle des signaux visuels. Master's thesis, École National Supérieure d'Électronique et de Radioélectricité de Grenoble (ENSERG/INPG), Grenoble.
- Argyros, A., Tsakiris, D., & Groyer, C. (2004). Biomimetic centering behavior [mobile robots with panoramic sensors]. *Robotics & Automation Magazine, IEEE*, 11, 21–30.
- Aubépart, F. & Franceschini, N. (2007). Bio-inspired optic flow sensors based on FPGA: Application to micro-air-vehicles. *Microprocessors and Microsystems*, 31, 408–419.
- Aubépart, F., Ménouni, M., Loubignac, T., Dinkelspieler, B., & Franceschini, N. (2007). Capteur de flux optique basé sur une rétine intégrée et un FPGA. In *Colloque Interdisciplinaire en Instrumentation*, (pp. 508–520). Hermes.
- Baird, E., Kornfeldt, T., & Dacke, M. (2010). Minimum viewing angle for visually guided ground speed control in bumblebees. *The Journal of Experimental Biology*, 213, 1625–1632.
- Baird, E., Srinivasan, M., Zhang, S., Lamont, R., & Cowling, A. (2006). Visual control of flight speed and height in the honeybee. In S. Nolfi, G. Baldassarre, R. Calabretta, J. Hallam, D. Marocco, J.-A. Meyer, O. Miglino, & D. Parisi (Eds.), *From Animals to Animats 9*, volume 4095 (pp. 40–51). Springer Berlin / Heidelberg.
- Barron, A. & Srinivasan, M. (2006). Visual regulation of ground speed and headwind compensation in freely flying honey bees (*Apis mellifera* L.). *Journal of Experimental Biology*, 209 (5), 978–984.
- Barron, J., Fleet, D., & Beauchemin, S. (1994). Performance of optic flow techniques. *International Journal of Computer Vision*, 12, 43–77.
- Barrows, G. & Neely, C. (2000). Mixed-mode VLSI optic flow sensors for in-flight control of a Micro Air Vehicle. In *SPIE : Critical technologies for the future of computing*, volume 4109, (pp. 52–63), San Diego, CA, USA.
- Benson, R. & Delbrück, T. (1992). *Advances in Neural Information Processing Systems*, chapter Direction selective silicon retina that uses null inhibition, (pp. 756–763). D. S. Touretzky, Ed. San Mateo, CA: Morgan Kaufman,.
- Bermudez, F. G. & Fearing, R. (2009). Optical flow on a flapping wing robot. In *IEEE International Conference on Intelligent Robots and Systems (IROS)*, St Louis, USA.

- Beyeler, A., Zufferey, J., & Floreano, D. (2009). optiPilot: control of take-off and landing using optic flow. In *European Micro Aerial Vehicle Conference*, Delft, Netherlands.
- Beyeler, A., Zufferey, J. C., & D., F. (2009). Vision-based control of near-obstacle flight. *Autonomous robots*, *27*, 201–219.
- Beyeler, A., Zufferey, J.-C., & Floreano, D. (2007). 3d vision-based navigation for indoor microflyers. In *IEEE International Conference on Robotics and Automation (IROS)*, (pp. 1336 – 1341)., San Diego, USA.
- Blanchard, M., Rind, F., & Verschure, P. (2000). Collision avoidance using a model of the locust LGMD neuron. *Robotics and Autonomous Systems*, *30(1-2)*, 17–38.
- Blanes, C. (1986). *Appareil visuel élémentaire pour la navigation a vue d'un robot mobile autonome*. Marseille: Master thesis in Neurosciences (DEA in French), Neurosciences, Univ. Aix-Marseille II.
- Blanes, C. (1991). *Guidage visuel d'un robot mobile autonome d'inspiration bionique*. PhD thesis, INP Grenoble.
- Boeddeker, N., Lindemann, J., Egelhaaf, M., & Zeil, J. (2005). Responses of blowfly motion-sensitive neurons to reconstructed optic flow along outdoor flight path. *Journal of Comparative Physiology A*, *191 (12)*, 1143–1155.
- Boyer, F., Ali, S., & Porez, M. (2012). Macro-continuous dynamics for hyper-redundant robots: Application to kinematic locomotion bio-inspired by elongated body animals. *IEEE Transactions on Robotics*, *28*, 303–317.
- Brinkworth, R., Shoemaker, P., & O'Carroll, D. (2009). Characterization of a neuromorphic motion detection chip based on insect visual system. In *International Conference on Intelligent Sensors, Sensor Networks and Information Processing (ISSNIP)*, (pp. 289–294)., Melbourne, Australia.
- Briod, A., Klaptocz, A., Zufferey, J., & D. Floreano, D. (2012). The airburr: A flying robot that can exploit collisions. In *International Conference on Complex Medical Engineering (CME)*, Kobe, Japan.
- Brückner, A., Duparré, J., J., Wippermann, F., Dannberg, P., & Bräuer, A. (2010). *Flying Insects and Robots*, volume 1, chapter Microoptical artificial compound eyes, (pp. 127–142). Springer Berlin Heidelberg.
- Buchner, E. (1984). *Photoreception and vision in insects*, chapter Behavioral analysis of spatial vision in insects., (pp. 561–621). Plenum Press.
- Bülthoff, H., Little, J., & Poggio, T. (1989). A parallel algorithm for real-time computation of optical flow. *Nature*, *337(6207)*, 549–553.
- Burkhardt, D. & Gewecke, M. (1965). Mechanoreception in arthropoda: the chain from stimulus to behavioral pattern. In *Cold Spring Harbor Symposia on Quantitative Biology*, volume 30, (pp. 601–614).

- Campan, M. (1964). Recherches sur la fonction dynamogène de l'antenne des insectes. expériences sur la géotaxie ascensionnelle et la phototaxie positive de *Drosophila melanogaster* Meigen. *Comptes rendus des séances de la Société de biologie*, 158, 2189–2194.
- Camus, T. (1995). Real-time quantized optical flow. *Computer Architectures for Machine Perception*, 1, 126 – 131.
- Chahl, J. & Mizutani, A. (2012). Biomimetic attitude and orientation sensors. *IEEE Sensors Journal*, 12 (2), 289–297.
- Chahl, J., Srinivasan, M., & Zhang, S. (2004). Landing strategies in honeybees and applications to uninhabited airborne vehicles. *The International Journal of Robotics Research*, 23, 101–110.
- Chan, R., Mulla, A., & Stol, K. (2010). Characterisation of low-cost optical flow sensors. In *Australasian Conference on Robotics and Automation (ACRA)*, volume Brisbane, Australia, (pp. 1–8).
- Chen, L., Yang, H., Takaki, T., & Ishii, I. (2012). Real-time optical flow estimation using multiple frame-straddling intervals. *Journal of Robotics and Mechatronics*, 24 (4), 686–698.
- Chown, W. & Aggarwal, J. (1977). Computer analysis of planar curvilinear moving images. *IEEE Transactions on Computers*, 26, 179–185.
- Collett, T. (1980). Some operating rules for the optomotor system of a hoverfly during voluntary flight. *Journal of Comparative Physiology A*, 138, 271–282.
- Collett, T. S. & Land, M. (1975). Visual control of flight behavior in the hoverfly, *Syrphoctonus pipiens* L. *Journal of Comparative Physiology A*, 99, 1–66.
- Conroy, J., Gremillion, G., Ranganathan, B., & Humbert, J. (2009). Implementation of wide-field integration of optic flow for autonomous quadrotor navigation. *Autonomous robots*, 27 (3), 189–198.
- Coutard, L., Chaumette, F., & Pfimlin, J. (2011). Automatic landing on aircraft carrier by visual servoing. In *IEEE International Conference on Intelligent Robots and Systems (IROS)*, (pp. 2843–2848)., San Francisco, USA.
- Crétual, A. & Chaumette, F. (2001). Visual servoing based on image motion. *International Journal of Robotics Research*, 20 (11), 857–877.
- Crétual, A. and Chaumette, F. (1997). Positioning a camera parallel to a plane using dynamic visual servoing. In *IEEE International Conference on Intelligent Robots and Systems (IROS)*, volume 1, (pp. 43–48)., Grenoble, France.
- Dacke, M. & Srinivasan, M. (2008). Two odometers in honeybees? *The Journal of Experimental Biology*, 211, 3281–3286.
- Dahmen, H., Millers, A., & Mallot, H. A. (2009). *Flying insects and robots*, chapter 9 : Insect inspired odometry by optic flow recorded with optical mouse chips, (pp. 115–126). Springer, Berlin, Eds : Floreano, D. and Zufferey, J. C. and Srinivasan, M. V. and Ellington, C.

- Daneshpanah, M. & Javidi, B. (2011). Three-dimensional imaging with detector arrays on arbitrarily shaped surfaces. *Optics Letters*, *36*(5), 600–602.
- David, C. (1978). The relationship between body angle and flight speed in free-flying drosophila. *Physiological Entomology*, *3*, 191–195.
- de Croon, G., de Weerd, E., de Wagter, C., Remes, B., & Ruijsink, R. (2012). The appearance variation cue for obstacle avoidance. *IEEE Transactions on Robotics*, *28*(2), 529–534.
- de Croon, G. C. H. E., Groen, M., de Wagter, C., Remes, B., Ruijsink, R., & van Oudheusden, B. (2012). Design, aerodynamics and autonomy of the delfly. *Bioinspiration and Biomimetics*, *7*(2), 1–16.
- Delbrück, T. (1993). Silicon retina with correlation-based, velocity-tuned pixels. *IEEE Transactions on Neural Networks*, *4*, 529–541.
- Delbrück, T. & Mead, C. A. (1994). Adaptive photoreceptor with wide dynamic range. In *IEEE International Symposium on Circuits and Systems (ISCAS)*, volume 4, (pp. 339–342)., London, UK.
- Deutschmann, R. (1997). *Analog VLSI Motion Sensors*. PhD thesis, Technische Universität München/Germany & California Institute of Technology/USA.
- Díaz, J., Ros, E., Agis, R., & Bernier, J. (2008). Superpipelined high-performance optical-flow computation architecture. *Computer Vision and Image Understanding*, *112*, 262–273.
- Dinyari, R., Rim, S.-B., Huang, K., Catrysse, P., & Peumans, P. (2008). Curving monolithic silicon for nonplanar focal plane array applications. *Applied Physics Letters*, *92*(9), 091114–091113.
- Dobrzynski, M., Pericet-Camara, R., & Floreano, D. (2012). Vision tape - a flexible compound camera for motion detection and proximity estimation. *IEEE Sensors Journal*, *12*(5), 1131 – 1139.
- Douglass, J. & Strausfeld, N. (1996). Visual motion-detection circuits in flies: parallel direction- and non-direction-sensitive pathways between the medulla and lobula plate. *Journal of Neuroscience*, *16* (15), 4551–4562.
- Duhamel, P.-E., Perez-Arancibia, N., Barrows, G., & Wood, R. (2012). Altitude feedback control of a flapping-wing microrobot using an on-board biologically inspired optical flow sensor. In *IEEE International Conference on Robotics and Automation (ICRA)*, Saint Paul, Minnesota, USA.
- Dumas, D., Fendler, M., Berger, F., Cloix, B., Pornin, C., Baier, N., Druart, G., Primot, J., & le Coarer, E. (2012). Infrared camera based on a curved retina. *Optics Letters*, *37* (4), 653–655.
- Duparré, J., Dannberg, P., Schreiber, P., Bräuer, A., & Tünnermann, A. (2005). Thin compound-eye camera. *Applied Optics*, *44*(15), 2949–2956.

- Eckles, M., Roubik, D., & Nieh, J. (2012). A stingless bee can use visual odometry to estimate both height and distance. *Journal of Experimental Biology*, *215*, 3155–3160.
- Egelhaaf, M. & Reichardt, W. (1987). Dynamic response properties of movement detectors : Theoretical analysis and electrophysiological investigation in the visual system of the fly. *Biological Cybernetics*, *56*, 69–87.
- Eichner, H., Joesch, M., Schnell, B., Reiff, D., & Borst, A. (2011). Internal structure of the fly elementary motion detector. *Neuron*, *70*, 1155–1164.
- Esch, H. E. & Burns, J. E. (1995). Honeybees use optic flow to measure the distance of a food source. *Naturwissenschaften*, *82*, 38–40.
- Etienne-Cummings, R. (1999). Intelligent robot vision sensors in VLSI. *Autonomous Robots*, *7*, 225–237.
- Etienne-Cummings, R., Van der Spiegel, J., & Mueller, P. (1997). A focal plane visual motion measurement sensor. *IEEE Transactions on Circuits and Systems 1*, *44*, 55–66.
- Expert, F., Roubieu, F., & Ruffier, F. (2012). Interpolation based "time of travel" scheme in a visual motion sensor using a small 2d retina. In *IEEE Sensors Conference*, (pp. 2231–2234)., Taipei, Taiwan.
- Expert, F. & Ruffier, F. (2012). Controlling docking, altitude and speed in a circular high-roofed tunnel thanks to the optic flow. In *IEEE International Conference on Robots and Systems (IROS)*, (pp. 1125–1132)., Vilamoura, Portugal.
- Expert, F., Viollet, S., & Ruffier, F. (2011a). A mouse sensor and a 2-pixel motion sensor exposed to continuous illuminance changes. In *IEEE Sensors 2011 conference*.
- Expert, F., Viollet, S., & Ruffier, F. (2011b). Outdoor field performances of insect-based visual motion sensors. *Journal of Field Robotics*, *28* (4), 529–541.
- Ferrat, P., Gimkiewicz, C., Neukom, S., Zha, Y., Brenzikofer, A., & Baechler, T. (2008). Ultra-miniature omni-directional camera for an autonomous flying micro-robot. In *Conference on Optical and Digital Image Processing (Proceedings of SPIE, Vol 7000)*.
- Fischler, M. & Bolles, R. (1981). Random sample consensus: A paradigm for model fitting with applications to image analysis and automated cartography. *Communications of the ACM*, *24*, 381–395.
- Fleet, D. & Langley, K. (1995). Recursive filters for optical flow. *IEEE Transactions on Pattern Analysis and Machine Intelligence*, *17*(1), 61–67.
- Floreano, D., Pericet-Camara, R., Viollet, S., Ruffier, F., Brückner, A., Leitel, R., Buss, W., Menouni, M., Expert, F., Juston, R., Dobrzynski, M., L Eplattener, G., Recktenwald, F., Mallot, H., & Franceschini, N. (2013). Miniature curved artificial compound eyes. *Proceedings of the National Academy of Sciences (PNAS)*, *110*, 9267–9272.
- Floreano, D., Zufferey, J.-C., & Srinivasan, M. (2009). *Flying Insects and Robots*. Springer, Berlin.

- Fortey, R. & Chatterton, B. (2003). A devonian trilobite with an eyeshade. *Science*, 301(5640), 1689.
- Fraenkel, G. & Pringle, J. W. S. (1938). Halteres or flies as gyroscopic organs of equilibrium. *Nature*, 141, 919–920.
- Franceschini, N. (1975). *Photoreceptor Optics*, chapter Sampling of the Visual Environment by the Compound Eye of the Fly: Fundamentals and Applications, (pp. 98–125). Springer, Berlin.
- Franceschini, N. (1985). Early processing of colour and motion in a mosaic visual system. *Neuroscience Research (Suppl. 2)*, 2, 17–49.
- Franceschini, N. (2003). *From fly vision to robot vision: Re-construction as a mode of discovery. I*, chapter Sensors and Sensing in Biology and Engineering, (pp. 223–235). Springer.
- Franceschini, N. (2004). Visual guidance based on optic flow: a biorobotic approach. *Journal of Physiology-Paris*, 98(1-3), 281–292.
- Franceschini, N., Hardie, R., Ribi, W., & Kirschfeld, K. (1981). Sexual dimorphism in a photoreceptor. *Nature*, 291(5812), 241–244.
- Franceschini, N. & Kirschfeld, K. (1971). In vivo optical study of photoreceptor elements in the compound eye of drosophila. *Biological Cybernetics*, 8, 1–13.
- Franceschini, N., Pichon, J. M., & Blanes, C. (1992). From insect vision to robot vision. *Philosophical Transactions of the Royal Society B: Biological Sciences*, 337 (1281), 283–294.
- Franceschini, N., Riehle, A., & Nestour, A. L. (1989). *Facets of Vision*, chapter 17 : Directionally Selective Motion Detection by Insect Neurons, (pp. 360–390). Springer, Berlin, Eds : D.G. Stavenga, R.C. Hardie.
- Franceschini, N., Ruffier, F., & Serres, J. (2007). A bio-inspired flying robot sheds light on insect piloting abilities. *Current Biology*, 17, 329 – 335.
- Franceschini, N., Ruffier, F., Serres, J., & Viollet, S. (2009). *Aerial vehicles*, chapter 35 : Optic flow based visual guidance: from flying insects to miniature aerial vehicles, (pp. 747–770). Vienna : In-Tech, Eds : T. M. Lam.
- Franz, M. & Krapp, H. (2000). Wide-field, motion-sensitive neurons and matched filters for optic flow fields. *Biological Cybernetics*, 83(3), 185–197.
- Fry, S. N., Rohrseitz, N., Straw, A. D., & Dickinson, M. H. (2009). Visual control of flight speed in drosophila melanogaster. *Journal of Experimental Biology*, 212, 1120–1130.
- Fuller, S., Sands, A., Haggerty, A., Karpelson, M., & Wood, R. (2013). Estimating attitude and wind velocity using biomimetic sensors on a microrobotic bee. In *IEEE International Conference on Robotics and Automation (ICRA)*, Karlsruhe, Germany.
- Garratt, M. & Chahl, J. (2008). Vision-based terrain following for an unmanned rotorcraft. *Journal of Field Robotics*, 25, 284–301.

- Gewecke, M. & Schlegel, P. (1970). Die schwingungen der antenne und ihre bedeutung für die flugsteuerung bei *calliphora erythrocephala*. *Zeitschrift für vergleichende Physiologie*, *67*, 325–362.
- Gibson, J. (1950). *The perception of the visual world*. New York: Boston.
- Götz, K. (1964). Optomotorische Untersuchung des visuellen systems einiger Augenmutanten der Fruchtfliege *Drosophila*. *Biological Cybernetics*, *2*, 77–92.
- Götz, K. (1965). Die optischen übertragungseigenschaften der komplexaugen von *drosophila*. *Biological Cybernetics*, *2*(5), 215–221.
- Green, W., Oh, P., & Barrows, G. (2004). Flying insect inspired vision for autonomous aerial robot maneuvers in near-earth environments. In *IEEE International Conference on Robotics and Automation (ICRA)*.
- Griffiths, S., Saunders, J., Curtis, A., Barber, B., McLain, T., & Beard, R. (2006). Maximizing miniature aerial vehicles. *Robotics & Automation Magazine, IEEE*, *13*, 34–43.
- Griffiths, S., Saunders, J., Curtis, A., Barber, B., McLain, T., & Beard, R. (2007). *Advances in Unmanned Aerial Vehicles: State of the Art and the Road to Autonomy*, chapter Obstacle and Terrain Avoidance for Miniature Aerial Vehicles, (pp. 211–244). Springer.
- Gu, Y., Oberwinkler, J., Postma, M., & Hardie, R. (2005). Mechanisms of light adaptation in *drosophila* photoreceptors. *Current Biology*, *15*(13), 1228–1234.
- Harrison, R. R. & Koch, C. (1999). A robust analog VLSI motion sensor based on the visual system of the fly. *Autonomous robots*, *7*(3), 211–224.
- Hassenstein, B. & Reichardt, W. (1956). Systemtheoretische Analyse der Zeit-, Reihenfolgen-, und Vorzeichenbewertung bei der Bewegungsperzeption des Rüsselkäfers. *Chlorophanus. Zeitschrift für Naturforschung*, *11*, 513–524.
- Hausen, K. (1982). Motion sensitive interneurons in the optomotor system of the fly, part i: the horizontal cells: structure and signals. *Biological Cybernetics*, *45*, 143–156.
- Hausen, K. (1984). The lobula-complex of the fly: structure, function and significance in visual behaviour. In Ali., M. (Ed.), *Photoreception and Vision in Invertebrates*, (pp. 523–559). New York: Plenum.
- Heisenberg, M. & Wolf, R. (1984). *Vision in Drosophila: Genetics of Microbehavior*. Springer Verlag.
- Hengstenberg, R. (1984). *Localization and Orientation in Biology and Engineering*, chapter Roll-stabilization during flight of the blowfly s head and body by mechanical and visual cues, (pp. 121–134). Heidelberg: Springer.
- Hengstenberg, R. (1988). Mechanosensory control of compensatory head roll during flight in the blowfly *calliphora erythrocephala meig*. *Journal of Comparative Physiology A*, *163*, 159–168.

- Hengstenberg, R. (1992). *Proceedings of Rhythmogenesis in Neurons and Networks, Proceedings of the 20th Gttingen Neurobiology Conference*, chapter Control of head pitch in *Drosophila* during rest and flight, (pp. 305). Thieme Verlag, Stuttgart.
- Hengstenberg, R. (2001). Pitch control of head posture in walking and flying *drosophila*. In *Proceeding of Invertebrate Vision Conference*, (pp. 224)., Bäckaskog Castle, Sweden.,
- Hengstenberg, R., Hausen, K., & Hengstenberg, B. (1982). The number and structure of giant vertical cells (vs) in the lobula plate of the blowfly *calliphora erythrocephala*. *Journal of Comparative Physiology A*, 149, 163–177.
- Heran, P. & Lindauer, M. (1963). Windkompensation und seitenwindkorrektur der bienen flug über wassen. *Zeitschrift für Vergleichende Physiologie*, 47, 39–55.
- Herisse, B., Hamel, T., Mahony, R., & Russotto, F.-X. (2010). The landing problem of a VTOL unmanned aerial vehicle on a moving platform using optical flow. In *IEEE International Conference on Intelligent Robots and Systems (IROS)*, (pp. 1600–1605)., Taipei, Taiwan.
- Herisse, B., Hamel, T., Mahony, R., & Russotto, F.-X. (2012). Landing a VTOL Unmanned Aerial Vehicle on a moving platform using optical flow. *IEEE Transactions on Robotics*, 28(1), 77–89.
- Herisse, B., Russotto, F.-X., Hamel, T., & Mahony, R. (2008). Hovering flight and vertical landing control of a VTOL unmanned aerial vehicle using optical flow. In *IEEE International Conference on Intelligent Robots and Systems (IROS)*, (pp. 801 – 806)., Nice, France.
- Higgins, C. & Shams, S. (2002). A biologically inspired modular VLSI system for visual measurement of self-motion. *IEEE Sensors Journal*, 2, 508–528.
- Honegger, D., Meier, L., Tanskanen, P., & Pollefeys, M. (2013). An open source and open hardware embedded metric optical flow CMOS camera for indoor and outdoor applications. In *IEEE International Conference on Robotics and Automation (ICRA)*, Karlsruhe, Germany.
- Horn, B. & Schunck, B. (1981). Determining optical flow. *Artificial Intelligence*, 17, 185–204.
- Horrige, G. (1978). The separation of visual axes in apposition compound eyes. *Philosophical Transactions of the Royal Society of London Series B, Biological Sciences*, 285(1003), 1–59.
- Horrige, G. A. (1977). The compound eye of insects. *Scientific American*, 237, 108–120.
- Humbert, J. (2005). *Bio-Inspired Visuomotor Convergence in Navigation and Flight Control Systems*. PhD thesis, California Institute of Technology.
- Humbert, J., Conroy, J. K., Neely, C., & Barrows, G. (2009). Wide-field integration methods for visuomotor control. In Floreano, D., Zufferey, J. C., Srinivasan, M., & Ellington, C. (Eds.), *Flying insects and robots*, (pp. 63–71). Berlin: Springer Berlin Heidelberg.

- Humbert, J. & Hyslop, A. (2010). Bioinspired visuomotor convergence. *IEEE Transactions on Robotics*, *26*(1), 121–130.
- Hyslop, A. & Humbert, J. (2010). Autonomous navigation in three-dimensional urban environments using wide-field integration of optic flow. *Journal of guidance, control, and dynamics*, *33*, 147–159.
- Ibbotson, M. (1991). Wide-field motion-sensitive neurons tuned to horizontal movement in the honeybee *apis mellifera*. *Journal of Comparative Physiology A*, *168*, 91–102.
- Ibbotson, M. (2001). Evidence for velocity-tuned motion-sensitive descending neurons in the honeybee. *Proceedings of the Royal Society London B*, *268* (1482), 2195–2201.
- Iida, F. (2001). Goal-directed navigation of an autonomous flying robot using biologically inspired cheap vision. in *Proceedings of the 32nd International Symposium on Robotics (ISR), Seoul, SK*, 1404–1409.
- Iida, F. (2003). Biologically inspired visual odometer for navigation of a flying robot. *Robotics and autonomous systems*, *44*, 201–208.
- Ijspeert, A. J., Crespi, A., Ryczko, D., & Cabelguen, J. (2007). From swimming to walking with a salamander robot driven by a spinal cord model. *Science*, *5817*, 1416–1420.
- Indiveri, G., Kramer, J., & Koch, C. (1996). System implementations of analog VLSI velocity sensors. *IEEE Micro*, *16* (5), 40–49.
- Izzo, D., Weiss, N., & Seidl, T. (2011). Constant-optic-flow lunar landing: Optimality and guidance. *Journal of Guidance, Control, and Dynamics*, *34*, 1383–1395.
- Jackson, J. D., Callahan, D. W., & Marstrander, J. (Sept, 2007). A rationale for the use of optical mice chips for economic and accurate vehicle tracking. *Proc. IEEE International Conference on Automation Science and Engineering CASE 2007, Scottsdale, AZ, USA*, 939–944.
- Jeong, K.-H., Kim, J., & Lee, L. (2006). Biologically inspired artificial compound eyes. *Science*, *312*(5773), 557–561.
- Jung, I., Xiao, J., Malyarchuk, V., Lu, C., Li, M., Liu, Z., Yoon, J., Huang, Y., & Rogers, J. (2011). Dynamically tunable hemispherical electronic eye camera system with adjustable zoom capability. *Proceedings of the National Academy of Sciences*, *108*(5), 1788–93.
- Juusola, M. & Hardie, R. (2001). Light adaptation in drosophila photoreceptors. i. response dynamics and signaling efficiency at 25 degrees c. *Journal of General Physiology*, *117*, 3–25.
- Kendoul, F., Nonami, K., Fantoni, I., & Lozano, R. (2009). An adaptive vision-based autopilot for mini flying machines guidance, navigation and control. *Autonomous robots*, *27*, 165–188.
- Kendoul, F., Yu, Z., & Nonami, K. (2010). Guidance and nonlinear control system for autonomous flight of minirotorcraft unmanned aerial vehicles. *Journal of Field Robotics*, *27*(3), 311–334.

- Kennedy, J. (1939). Visual responses of flying mosquitoes. In *Zoological Society of London*, volume 109, (pp. 221–242).
- Kennedy, J. (1951). The migration of the desert locust (*Schistocerca gregaria* forsk.) i. the behaviour of swarms. ii. a theory of long-range migrations. *Philosophical Transactions of the Royal Society of London*, 235 (625), 163–290.
- Kerhuel, L. (2009). *Capteurs optiques minimalistes et réflexes oculomoteurs biomimétiques. Applications à la robotique aérienne*. PhD thesis, University of Montpellier, France.
- Kerhuel, L., Ruffier, F., & Franceschini, N. (2009). Method and device for measuring the angular velocity of a light transition zone and steering aid system for fixing and tracking a target comprising at least one such light transition.
- Kerhuel, L., Viollet, S., & Franceschini, N. (2010). Steering by gazing : an efficient biomimetic control strategy for visually guided micro aerial vehicles. *IEEE Transactions on robotics*, 26, 307–319.
- Khang, D.-Y., Jiang, H., Huang, Y., & Rogers, J. (2006). A stretchable form of single-crystal silicon for high-performance electronics on rubber substrates. *Science*, 311(5758), 208–212.
- Kim, J., Jeong, K., & Lee, L. (2005). Artificial ommatidia by self-aligned microlenses and waveguides. *Optics Letters*, 30(1), 5–7.
- Kirchner, W. H. & Srinivasan, M. V. (1989). Freely flying honeybees use image motion to estimate object distance. *Naturwissenschaften*, 76, 281–282.
- Kirschfeld, K. (1976). *Neural Principles in Vision*, chapter The resolution of lens and compound eyes, (pp. 354–370). Springer, Berlin, Germany.
- Koenderink, J. & van Doorn, A. (1987). Facts on optic flow. *Biological Cybernetics*, 56, 247–254.
- Kramer, J., Sarpeshkar, R., & Koch, C. (1995). An analog VLSI velocity sensor. in *Proceedings of the IEEE International Symposium on Circuit and Systems (ISCAS)*, Seattle, WA, USA, 413–416.
- Kramer, J., Sarpeshkar, R., & Koch, C. (1997). Pulse-based analog VLSI velocity sensors. *IEEE transactions on circuits and systems. 2, Analog and digital signal processing*, 44, 96–101.
- Krapp, H., Hengstenberg, B., & Hengstenberg, R. (1998). Dendritic structure and receptive-field organisation of optic flow processing interneurons in the fly. *Journal of Neurophysiology*, 79, 1902–1917.
- Krapp, H. & Hengstenberg, R. (1996). Estimation of self-motion by optic flow processing in single visual interneurons. *Nature*, 384(6608), 463–466.
- Kuenen, L. & Baker, T. (1982). Optomotor regulation of ground velocity in moths during flight to sex pheromone at different heights. *Physiological Entomology*, 7, 193–202.

- Labhart, T. (1980). Specialized photoreceptors at the dorsal rim of the honeybee's compound eye: Polarizational and angular sensitivity. *Journal of Comparative Physiology A*, *141*(1), 19–30.
- Labonne, E., Sicard, G., & Renaudin, M. (2006). A 120db cmos imager with a light adaptive system and digital outputs. In *Ph. D. Research in Microelectronics and Electronics (PRIME)*, (pp. 269–272).
- Land, M. (1973). Head movement of flies during visually guided flight. *Nature*, *243*, 299–300.
- Land, M. (1997). Visual acuity in insects. *Annual Review of Entomology*, *42*, 147–17.
- Land, M. & Nilsson, D.-E. (2002). *Animal Eyes*. Oxford University Press.
- Landolt, A. & Mitros, A. (2001). Visual sensor with resolution enhancement by mechanical vibrations. *Autonomous Robots*, *11* (3), 233–239.
- Laughlin, S. (1989). The role of sensory adaptation in the retina. *Journal of Experimental Biology*, *146*(1), 39–62.
- Laughlin, S. & Weckström, M. (1993). Fast and slow photoreceptors - a comparative study of the functional diversity of coding and conductances in the diptera. *Journal of Comparative Physiology A*, *172*(5), 593–609.
- Laviana, R., Carranza, L., Vargas, S., Linan, G., & Roca, E. (2005). A bioinspired vision chip architecture for collision detection in automotive applications. In *SPIE : Bioengineered and bioinspired systems II*, volume 5839, (pp. 13–24)., Sevilla, Spain.
- Lee, J., Budanov, A., Park, E., Birse, R., Kim, T., Perkins, G., Ocorr, K., Ellisman, M., Bodmer, R., Bier, E., & M., K. (2010). Sestrin as a feedback inhibitor of tor that prevents age-related pathologies. *Science*, *327* (5970), 1223–1228.
- Lee, M., Jago, J., Garcia-Bellido, D., Edgecombe, G., Gehling, J., & Paterson, J. (2011). Modern optics in exceptionally preserved eyes of early cambrian arthropods from australia. *Nature*, *474*, 631–634.
- Lin, H.-T., Leisk, G., & Trimmer, B. (2011). Goqbot: a caterpillar-inspired soft-bodied rolling robot. *Bioinspiration and Biomimetics*, *6* (2), 1–14.
- Lippiello, V., Loianno, G., & Siciliano, B. (2011). Mav indoor navigation based on a closed-form solution for absolute scale velocity estimation using optical flow and inertial data. In *50th IEEE Conference on Decision and Control and European Control Conference (CDC-ECC)*, Orlando, FL, USA.
- Liu, S. & Usseglio-Viretta, A. (2001). Fly-like visuomotor responses of a robot using a VLSI motion-sensitive chips. *Biological Cybernetics*, *85*, 449–457.
- Lucas, B. & Kanade, T. (1981). An iterative image registration technique with an application to stereo vision. In *International Joint Conference on Artificial Intelligence (IJCAI)*, (pp. 674–679)., Vancouver, Canada.
- Lyon, R. & Haeberli, M. (1982). Designing and testing the optical mouse. *VLSI design*, *1*, 20–29.

- Ma, K., Chirarattananon, P., Fuller, S., & Wood, R. (2013). Controlled flight of a biologically inspired, insect-scale robot. *Science*, *340* (6132), 603–607.
- Mahony, R., Hamel, T., & Pflimlin, J. (2008). Non-linear complementary filters on the special orthogonal group. *IEEE Transactions*, *53* (5), 1203–1218.
- Maimon, G., Straw, A., & Dickinson, M. (2008). A simple vision-based algorithm for decision making in flying drosophila. *Current Biology*, *18*, 464–470.
- Mamiya, A., Straw, A., Tomasson, E., & Dickinson, M. (2011). Active and passive antennal movements during visually guided steering in flying drosophila. *The Journal of Neuroscience*, *31*(18), 6900–6914.
- Manecy, A., Viollet, S., & Marchand, N. (2012). Bio-inspired hovering control for an aerial robot equipped with a decoupled eye and a rate gyro. In *IEEE International Conference on Intelligent Robots and Systems (IROS)*, Vilamoura, Portugal.
- Martin, N. & Franceschini, N. (1994). Obstacle avoidance and speed control in a mobile vehicle equipped with a compound eye. In *Proceedings of the Intelligent Vehicles Symposium (IV)*, (pp. 381–386)., Paris, France.
- Matic, T. & Laughlin, S. (1981). Changes in the intensity-response function of an insect's photoreceptors due to light adaptation. *Journal of comparative physiology*, *145* (2), 169–177.
- McCarthy, C. & Barnes, N. (2012). A unified strategy for landing and docking using spherical flow divergence. *IEEE Transactions on Pattern Analysis and Machine Intelligence*, *34* (5), 1024–1031.
- Mead, C. (1989). *Analog VLSI and Neural Systems*. Addison-Wesley.
- Moeckel, R. & Liu, S. (2007). Motion detection circuits for a time-to-travel algorithm. *IEEE International Symposium on Circuits and Systems. (ISCAS)*, New Orleans, LA, USA, 3079–3082.
- Moini, A. (1999). *Vision Chips*. Kluwer academic, Norwell, MA.
- Moore, A. & Koch, C. (1991). A multiplication based analog motion detection chip. In *Visual Information processing: From neurons to chips*, volume 1473, (pp. 66–75).
- Mura, F. & Franceschini, N. (1994). *From Animals to Animats III*, chapter Visual control of altitude and speed in a flying agent, (pp. 91–99). Cambridge: MIT Press.
- Netter, T. & Franceschini, N. (1999). Neuromorphic optical flow sensing for nap-of-the-earth flight. In Gage, D. & Choset, H. (Eds.), *proceedings of SPIE, vol. 3838, Mobile Robots XIV*, (pp. 208–216.).
- Netter, T. & Franceschini, N. (2002). A robotic aircraft that follows terrain using a neuromorphic eye. *Intelligent Robots and Systems, 2008. IROS 2008. IEEE/RSJ International Conference on*, *1*, 129–134.
- Normann, R. & Perlman, I. (1979). The effects of background illumination on the photoreponses of red and green cones. *Journal of Physiology*, *286*(1), 491–507.

- Okuno, H. & Yagi, T. (2009). A mixed analog-digital vision sensor for detecting objects approaching on a collision course. *Robotics and Autonomous Systems*, 57, 508–516.
- Orchard, G., Bartolozzi, C., & Indiveri, G. (2009). Applying neuromorphic vision sensors to planetary landing tasks. *Biomedical Circuits and Systems Conference*, 1, 201–204.
- Pericet-Camara, R., Dobrzynski, M., Eplattienier, G., Zufferey, J., Expert, F., Juston, R., Ruffier, F., Franceschini, N., Viollet, S., Menouni, M., Godiot, S., Brückner, A., Buss, W., Leitel, R. and Recktenwald, F., Yuan, C., Mallot, H., & Floreano, D. (2011). CURVACE - CURVed Artificial Compound Eyes. In *2nd European Future Technologies Conference and Exhibition (FET)*, Hamburg, Germany.
- Pflimlin, J. (2007). *Commande d'un minidrone a helice carenee : De la stabilisation dans le vent a la navigation autonome*. PhD thesis, Ecole Doctorale Systèmes de Toulouse.
- Pichon, J., Blanes, C., & Franceschini, N. (1989). Visual guidance of a mobile robot equipped with a network of self-motion sensors. *Proceedings of SPIE, Mobile Robots IV*, 1195, 44–53.
- Pichon, J.-M. (1991). *Guidage visuel d'un robot mobile autonome d'inspiration bionique*. PhD thesis, INP Grenoble.
- Plett, J., Bahl, A., Buss, M., Kuehnlenz, K., & Borst, A. (2012). Bio-inspired visual ego-rotation sensor for mavs. *Biological Cybernetics*, 106(1), 51–63.
- Portelli, G., Ruffier, F., & Franceschini, N. (2010). Honeybees change their height to restore their optic flow. *Journal of Comparative Physiology A*, 196(4), 307–313.
- Portelli, G., Ruffier, F., Roubieu, F., & Franceschini, N. (2011). Honeybees' speed depends on dorsal as well as lateral, ventral and frontal optic flows. *PLOS One*, 6(5), doi:10.1371/journal.pone.0019486.
- Portelli, G., Serres, J., Ruffier, F., & Franceschini, N. (2008). A 3D insect-inspired visual autopilot for corridor-following. *2nd Biennial IEEE*, 0, 0.
- Portelli, G., Serres, J., Ruffier, F., & Franceschini, N. (2010). Modelling honeybee visual guidance in a 3-D environment. *Journal of Physiology - Paris*, 104(1-2), 27–39.
- Potter, J. (1977). Scene segmentation using motion information. *Computer Graphics and Image Processing*, 6, 558–581.
- Preiss, R. & Kramer, E. (1984). *Localization and orientation in biology and engineering.*, chapter Control of flight speed by minimization of the apparent ground pattern movement, (pp. 140–142). Springer, Berlin.
- Preuss, T. & Hengstenberg, R. (1992). Structure and kinematics of the prosternal organs and their influence on head position in the blowfly calliphora erythrocephala meig. *Journal of Comparative Physiology A*, 171 (4), 483–493.
- Prokopowicz, P. & Cooper, P. (1995). The dynamic retina : contrast and motion detection for active vision. *International journal of computer vision*, 16, 191–204.

- Pudas, M., Viollet, S., Ruffier, F., Kruusing, A., Amic, S., Leppavuori, S., & Franceschini, N. (2007). A miniature bio-inspired optic flow sensor based on low temperature co-fired ceramics (LTCC) technology. *Sensors and Actuators A: Physical*, *133*, 88–95.
- Pulsifer, D., Lakhtakia, A., Martin-Palma, R., & Pantano, C. (2010). Mass fabrication technique for polymeric replicas of arrays of insect corneas. *Bioinspiration and Biomimetics*, *5*(3), 036001.
- Qu, P., Chen, F., Liu, H., Yang, Q., Lu, J., Si, J., Wang, Y., & Hou, X. (2012). A simple route to fabricate artificial compound eye structures. *Optics Express*, *20*(5), 5775–5782.
- Radtke, D., Duparré, J., Zeitner, U., & Tünnermann, A. (2007). Laser lithographic fabrication and characterization of a spherical artificial compound eye. *Optics express*, *15*, 1.
- Reichardt, W. (1969). Movement perception in insects. In *Processing of optical data by organisms and machines*, Academic, (pp. 465–493)., New York, USA.
- Reiff, D., Plett, J., Mank, M., Griesbeck, O., & Borst, A. (2010). Visualizing retinotopic half-wave rectified input to the motion detection circuitry of drosophila. *Nature Neuroscience*, *13*(8), 973–979.
- Reiser, M. & Dickinson, M. (2010). Drosophila fly straight by fixating objects in the face of expanding optic flow. *The Journal of Experimental Biology*, *213*, 1771–1787.
- Reiser, M. & Dickinson, M. (2013). Visual motion speed determines a behavioral switch from forward flight to expansion avoidance in drosophila. *Journal of Experimental Biology*, *216*, 719–732.
- Riehle, A. & Franceschini, N. (1984). Motion detection in flies : parametric control over on-off pathways. *Experimental Brain Research*, *54* (2), 390–394.
- Riggs, J. (1983). Notes on silicon photodiode detectors. *International Amateur-Professional Photoelectric Photometry Communications*, *14*, 30–44.
- Rondon, E., Garcia-Carrillo, L.-R., & Fantoni, I. (2010). Vision-based altitude, position and speed regulation of a quadrotor rotorcraft. In *IEEE International Conference on Intelligent Robots and Systems (IROS)*, (pp. 628–633)., Taiwan, China.
- Roubieu, F., Expert, F., Boyron, M., Fuschlock, B.-J., Viollet, S., & Ruffier, F. (2011). A novel 1-gram insect based device measuring visual motion along 5 optical directions. In *IEEE Sensors 2011 conference*, Limerick, Ireland.
- Roubieu, F. L., Expert, F., Sabiron, G., & Ruffier, F. (2012). Two-directional 1-g visual motion sensor inspired by the fly’s eye. *IEEE Sensors Journal*, *13* (3), 1025–1035.
- Roubieu, F. L., Serres, J., Franceschini, N., Ruffier, F., & Viollet, S. (2012). A fully-autonomous hovercraft inspired by bees; wall-following and speed control in straight and tapered corridors. In *IEEE International Conference on Robotics and Biomimetics (RO-BIO)*, Guangzhou, China.

- Ruderman, D. L. & Bialek, W. (1994). Statistics of natural images: Scaling in the woods. *Phys. Rev. Lett.*, *73*, 814–817.
- Ruffier, F. (2004). *Pilote Automatique Biomimetique : Système générique inspiré du contrôle visuo-moteur des insectes pour : le décollage, le suivi de terrain, la réaction au vent et l'atterrissage automatiques d'un micro-aéronef*. PhD thesis, INP Grenoble.
- Ruffier, F. & Expert, F. (2012). Visual motion sensing onboard a 50-g helicopter flying freely under complex vicon-lighting conditions. In *IEEE International Conference on Complex Medical Engineering (CME)*, (pp. 634–639)., Kobe, Japan.
- Ruffier, F. & Franceschini, N. (2003). Octave, a bioinspired visuo-motor control system for the guidance of micro-air vehicles. In Rodriguez-Vazquez, A., Abbott, D., & Carmona, R. e. (Eds.), *SPIE Conference on Bioengineered and Bioinspired Systems*, volume 5119, (pp. 1–12)., Maspalomas, Spain. Bellingham, USA.
- Ruffier, F. & Franceschini, N. (2004). Visually guided micro-aerial vehicle: automatic take off, terrain following, landing and wind reaction. In *Proceeding of IEEE International Conference on Robotics and Automation (ICRA)*, (pp. 2339–2346)., New Orleans, USA.
- Ruffier, F. & Franceschini, N. (2005). Optic flow regulation: the key to aircraft automatic guidance. *Robotics and Autonomous Systems*, *50*(4), 177 – 194. Biomimetic Robotics.
- Ruffier, F. & Franceschini, N. (2008). Aerial robot piloted in steep relief by optic flow sensors. *International Conference on Intelligent Robots and Systems (IROS)*. Nice, *1*, 1266 – 1273.
- Ruffier, F., Viollet, S., Amic, S., & Franceschini, N. (2003). Bio-inspired optical flow circuits for the visual guidance of micro-air vehicles. *Proceeding of IEEE International Symposium on Circuits and Systems (ISCAS)*, *3*, 846–849.
- Sabiron, G., Chavent, P., Raharijaona, T., Fabiani, P., & Ruffier, F. (2013). Low-speed optic-flow sensor onboard an unmanned helicopter flying outside over fields. In *IEEE International Conference on Robotics and Automation*, (pp. 1734 – 1741)., Karlsruhe, Germany.
- Santos-Victor, J. & Sandini, G. (1997). Visual behaviors for docking. *Computer Vision and Image Understanding*, *67*(3), 223–238.
- Santos-Victor, J., Sandini, G., Curotto, F., & Garibaldi, S. (1995). Divergent stereo in autonomous navigation: From bees to robots. *International Journal of Computer Vision*, *14*, 159–177.
- Sarpeshkar, R., Bair, W., & Koch, C. (1993). Visual motion computation in analog VLSI using pulses. *Advances in Neural Information Processing Systems 5 (NIPS)*, Denver, CO, USA, 781–788.
- Sarpeshkar, R., Kramer, J., Indiveri, G., & Koch, C. (1996). Analog VLSI architectures for motion processing: From fundamental limits to system applications. *Proceedings of the IEEE*, *84* (7), 969–987.

- Schuppe, H. & Hengstenberg, R. (1993). Optical-properties of the ocelli of calliphora erythrocephala and their role in the dorsal light response. *Journal of Comparative Physiology A*, 173, 143–149.
- Serres, J. (2008). *De l'abeille au robot: la régulation du flux optique. Contrôle conjoint de vitesse et d'évitement d'obstacles latéraux pour véhicules totalement actionnés*. PhD thesis, Université Montpellier II.
- Serres, J., Dray, D., Ruffier, F., & Franceschini, N. (2008). A vision-based autopilot for a miniature air vehicle: joint speed control and lateral obstacle avoidance. *Autonomous robot*, 25, 103–122.
- Serres, J., Masson, G., Ruffier, F., & Franceschini, N. (2008). A bee in the corridor: centering and wall-following. *Naturwissenschaften*, 95(12), 1181–1187.
- Sicard, G., Bouvier, G., Fristot, V., & Lelah, A. (1998). A light adaptive 4000 pixel analog silicon retina for edge extraction and motion detection. In *Workshop on Machine Vision Applications (MVA)*.
- Song, Y., Xie, Y., Malyarchuk, V., Xiao, J., Jung, I., Choi, K., Liu, Z., Park, H., Lu, C., Kim, R., Li, R., Crozier, K., Huang, Y., & Rogers, J. (2013). Digital cameras with designs inspired by the arthropod eye. *Nature*, 497, 95–99.
- Srinivasan, M. (1994). An image-interpolation technique for the computation of optic flow and egomotion. *Biological Cybernetics*, 71, 401–415.
- Srinivasan, M. (2011). Honeybees as a model for the study of visually guided flight, navigation, and biologically inspired robotics. *Physiological Reviews*, 91(2), 413–460.
- Srinivasan, M., Poteser, M., & Kral, K. (1999). Motion detection in insect orientation and navigation. *Vision Research*, 39 (16), 2749–2766.
- Srinivasan, M., Zhang, S., Chahl, J., Barth, E., & Venkatesh, S. (2000). How honeybees make grazing landings on flat surfaces. *Biological Cybernetics*, 83, 171–183.
- Srinivasan, M., Zhang, S., Lehrer, M., & Collett, T. (1996). Honeybee navigation en route to the goal: visual flight control and odometry. *Journal of Experimental Biology*, 199(1), 237–244.
- Srygley, R. & Oliveira, E. (2001). *Insect movements: mechanisms and consequences.*, chapter Orientation mechanisms and migration strategies within the flight boundary layer., (pp. 183–206). CAB international.
- Stavenga, D. (2003). Angular and spectral sensitivity of fly photoreceptors. I. integrated facet lens and rhabdomere optics. *Journal of Comparative Physiology A*, 189, 1–17.
- Stocker, A. (2006). Analog integrated 2-D optical flow sensor. *Analog Integrated Circuits and Signal Processing*, 46, 121–138.
- Stowers, J., Hayes, M., & Bainbridge-Smith, A. (2011). Beyond optical flow - biomimetic UAV altitude control using horizontal edge information. In *International Conference on Automation, Robotics and Applications (ICARA)*, (pp. 372 – 377)., Wellington, New Zealand.

- Strausfeld, N., Seyan, H., & Milde, J. (1987). The neck motor system of the fly calliphora erythrocephala. 1. muscles and motor neurons. *Journal of Comparative Physiology A*, *160*, 205–224.
- Straw, A., Lee, S., & Dickinson, M. (2010). Visual control of altitude in flying *Drosophila*. *Current Biology*, *20(17)*, 1550–1556.
- Tammero, L. F. & Dickinson, M. H. (2002). The influence of visual landscape on the free flight behavior of the fruit fly drosophila melanogaster. *Journal of Experimental Biology*, *205(3)*, 327–343.
- Tammero, L. F., Frye, M. A., & Dickinson, M. H. (2004). Spatial organization of visuomotor reflexes in drosophila. *Journal of Experimental Biology*, *207*, 113–122.
- Tanner, J. & Mead, C. (1986). *VLSI Signal Processing, II*, volume 1986, chapter An integrated analog optical motion sensor, (pp. 59–76). IEEE Press.
- Tautz, J., Zhang, S., Spaethe, J., Brockmann, A., Si, A., & Srinivasan, M. (2004). Honeybee odometry: Performance in varying natural terrain. *Plos Biology*, *4*, 1.
- Taylor, G. & Krapp, H. (2007). Sensory systems and flight stability : what do insects measure and why ? *Insect Mechanics and Control*, *0*, 231–316.
- Thurrowgood, S., Soccol, D., Moore, R., Bland, D., & Srinivasan, M. (2009). A vision based system for attitude estimation of uavs. In *IEEE International Conference on Intelligent Robots and Systems (IROS)*, (pp. 5725–5730)., St Louis, USA.
- Ullman, S. (1981). Analysis of visual motion by biological and computer systems. *Computer*, *14*, 57–69.
- Valette, F., Ruffier, F., Viollet, S., & Seidl, T. (2010). Biomimetic optic flow sensing applied to a lunar landing scenario. In *IEEE International Conference on Robotics and Automation (ICRA)*, (pp. 2253–2260)., Anchorage, USA.
- van Hateren, J., Hardie, R., Rudolph, A., Laughlin, S., & Stavenga, D. (1989). The bright zone, a specialized dorsal eye region in the male blowflychrysomya megacephala. *Journal of Comparative Physiology A*, *164(3)*, 297–308.
- van Hateren, J. H. & Schilstra, C. (1999). Blowfly flight and optic flow ii. head movements during flight. *Journal of Experimental Biology*, *202*, 1491–1500.
- Viollet, S. & Franceschini, N. (1999). Biologically-inspired visual scanning sensor for stabilization and tracking. In *IEEE International Conference on Intelligent Robots and Systems (IROS)*, Kyongju, Korea.
- Viollet, S. & Franceschini, N. (2001). Super-accurate visual control of an aerial minirobot. In *Autonomous minirobots for research and edutainment (AMIRE)*, *1*, 215–224.
- Viollet, S., Ruffier, F., Ray, T., Menouni, M., Aubépart, F., Kerhuel, L., & Franceschini, N. (2010). Characteristics of three miniature bio-inspired optic flow sensors in natural environments. In *IEEE International Conference on Sensor Technologies and Applications (SENSORCOMM)*.

- von Frisch, K. (1967). *The Dance Language and Orientation of Bees*. Harvard University Press.
- Vu, N. & Caplier, A. (2009). Illumination-robust face recognition using retina modeling. In *16th IEEE International Conference on Image Processing (ICIP)*, (pp. 3289 – 3292).
- Wagner, H. (1982). Flow-field variables trigger landing in flies. *Nature*, *297(5862)*, 147–148.
- Watman, D. & Murayama, H. (2011). Design of a miniature, multi-directional optical flow sensor for micro aerial vehicles. In *IEEE International Conference on Robotics and Automation (ICRA)*, Shanghai, China.
- Webb, B. (2002). Robots in invertebrate neuroscience. *Nature*, *417(6886)*, 359–363.
- Weikersdorfer, D. & Conradt, J. (2012). Event-based particle filtering for robot self-localization. In *IEEE International Conference on Robotics and Biomimetics (ROBIO)*, (pp. 866–870), Guangzhou, China.
- Whiteside, T. & Samuel, G. (1970). Blur zone. *Nature*, *225*, 94–95.
- Williams, C. (1965). *Insect migration*. London.
- Wood, R. J. (2008). The first takeoff of a biologically inspired at-scale robotic insect. *IEEE Transactions on Robotics*, *24 (2)*, 341–347.
- Xu, P., Humbert, J., & Abshire, P. (2011). Analog VLSI implementation of wide-field integration method. *Journal of Intelligent and Robotic Systems, Online*, 1–23.
- Xu, X., Davanco, M., Qi, X., & Forrest, S. (2008). Direct transfer patterning on three dimensionally deformed surfaces at micrometer resolutions and its application to hemispherical focal plane detector arrays. *Organic Electronics*, *9(6)*, 1122–1127.
- Zeil, J. & Al-Mutairi, M. (1996). The variation of resolution and of ommatidial dimensions in the compound eyes of the fiddler crab *uca lactea annulipes* (ocypodidae, brachyura, decapoda). *Journal of Experimental Biology*, *199(7)*, 1569–1577.
- Zingg, S., Scaramuzza, D., Weiss, S., & Siegwart, R. (2010). MAV navigation through indoor corridors using optical flow. In *IEEE International Conference on Robotics and Automation (ICRA)*, (pp. 3361 – 3368), Anchorage, Alaska.
- Zufferey, J., Klaptocz, A., Beyeler, A., & Nicoud, J.D. Floreano, D. (2007). A 10-gram vision-based flying robot. *Advanced Robotics*, *21 (14)*, 1671–1684.
- Zufferey, J.-C., Beyeler, A., & Floreano, D. (2010). Autonomous flight at low altitude using light sensors and little computational power. *International Journal of Micro Air Vehicles*, *2 (2)*, 107–117.
- Zufferey, J.-C. & Floreano, D. (2006). Fly-inspired visual steering of ultralight indoor aircraft. *IEEE Transactions on Robotics*, *22(1)*, 137–146.
- Zwaan, S. & Santos-Victor, J. (1999). An insect inspired visual sensor for the autonomous navigation of a mobile robot. In *International Symposium on Intelligent Robotic Systems (SIRS)*, Coimbra, Portugal.

Résumé de thèse en français

Sommaire

I	Capteurs de flux optique	274
I.1	Performances en extérieur de capteurs de flux optique	274
I.2	Comparaison avec un capteur de souris optique	275
I.3	Réalisation d'un micro-capteur de flux optique d'un gramme	277
I.4	Réduction des ressources calculatoires en interpolant linéairement les signaux visuels	279
I.5	Conclusion	281
II	CurvACE : le premier œil composé courbe artificiel program- mable	283
III	Le robot BeeRotor	287
III.1	Description du robot BeeRotor et de son environnement	287
III.2	Navigation autonome	291
III.3	BeeRotor équipé de CurvACE	291
IV	Conclusion	295

I Capteurs de flux optique

Pour se déplacer de manière autonome dans des environnements inconnus, les animaux utilisent l'ensemble de leurs modalités sensorielles et en particulier leur vision. Lorsqu'ils se déplacent, les objets texturés vont créer sur leur rétine un champ vectoriel de vitesses angulaires que l'on appelle flux optique (Gibson, 1950). La mesure du flux optique est une information complexe étant donnée qu'elle dépend des translations et des rotations de l'animal dans son environnement ainsi que des objets mobiles de l'environnement (Koenderink & van Doorn, 1987). Cependant, elle est particulièrement intéressante pour les animaux comme pour les robots car, lors d'une translation dans un environnement stationnaire, le flux optique mesuré dépend du ratio : vitesse de déplacement de l'agent divisée par la distance entre l'agent et les objets de l'environnement. De ce fait, le flux optique de translation reflète la dangerosité des objets environnants et peut être utilisé aussi bien pour éviter les obstacles que pour contrôler sa vitesse.

Comme nous avons pu le voir dans l'introduction, de nombreux algorithmes ont été proposés permettant de mesurer ce flux optique (voir section 1.2.2) à partir de diverses rétines telles que des caméras CMOS, des capteurs de souris ou des rétines spécialisées développées en technologie VLSI (voir section 1.2.4).

Dans ces travaux, nous avons testé et amélioré un algorithme de mesure locale du flux optique 1-D appelé "temps de passage" ("time of travel") qui est inspiré d'expériences électrophysiologiques effectuées sur l'œil de mouche sur le neurone H1 (Riehle & Franceschini, 1984; Franceschini et al., 1989). En stimulant successivement deux pixels d'une même ommatidie d'un œil composé de mouche, simulant de ce fait un mouvement, ils ont observé que le taux de décharge du neurone H1 augmentait pour un mouvement dans la direction préférée et diminuait dans la direction opposée. Ce traitement a été reproduit sur un capteur visuel analogique de 2 pixels mesurant le temps de parcours d'un contraste défilant face à lui (Blanes, 1986; Pichon et al., 1989; Ruffier et al., 2003).

I.1 Performances en extérieur de capteurs de flux optique

L'idée originelle de ce traitement est encore bien présente dans la mise en œuvre actuelle des capteurs de flux optique utilisés au cours de ces travaux. La Figure B.1 illustre le traitement programmé au sein d'un microcontrôleur utilisé lors d'une première étude destinée à démontrer les performances de nos capteurs aussi bien en intérieur qu'en extérieur (Expert et al., 2011b). Deux rétines différentes ont été utilisées au cours de cette étude :

- La rétine LSC qui est composée de 2 lignes de 6 pixels linéaires possédant un étage de pré-amplification linéaire directement au niveau des pixels,
- La rétine APIS (Adaptive Pixels for Insect-based Sensors) qui est une rétine VLSI composée de 25 pixels s'adaptant automatiquement au niveau d'éclairement ambiant (Delbrück & Mead, 1994) sur une très large gamme de luminance s'étendant de 1 lux à 10000 lux.

Deux pixels de chacune de ces rétines sont reliés indépendamment au circuit électronique mettant en œuvre l'algorithme du "temps de passage" constituant ainsi deux capteurs 2-pixel de flux optique. Ces capteurs de flux optique ont été testés en intérieur et en extérieur sur une large gamme de luminance variant approximativement entre 50 lux et 10000 lux. Les

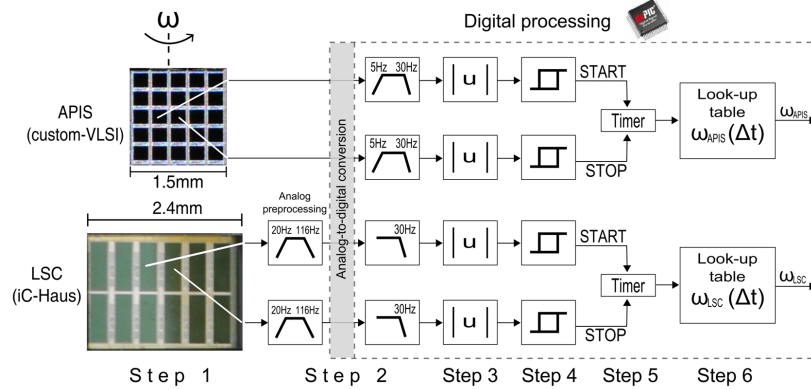


FIGURE B.1 – Traitement mis en œuvre afin de mesurer le flux optique à partir de deux pixels des rétines LSC et APIS. La vitesse angulaire est mesurée à partir des signaux de deux photodiodes adjacentes qui sont, dans un premier temps, filtrés spatialement en défocalisant la lentille placée face aux capteurs afin de leur offrir une sensibilité angulaire Gaussienne. Ces signaux sont ensuite filtrés temporellement pour éliminer le bruit et dériver le signal permettant de ne conserver que les fronts de contrastes. Le retard entre les deux signaux est mesuré après seuillage et permet de déduire visuellement la vitesse angulaire ω_{meas} qui est égale au ratio entre l’angle inter-récepteur $\Delta\varphi$ et le retard Δt . Ce traitement est mis en œuvre sur un microcontrôleur dsPIC33FJ128GP804 fonctionnant à 2kHz. D’après (Expert et al., 2011b).

deux capteurs de flux optique placés sur une carte électronique commune sont entraînés en rotation à l’aide d’un moteur à courant continu dont la vitesse est mesurée à l’aide d’un gyromètre. Cette vitesse est égale à la mesure théorique du flux optique en rotation dans un environnement stationnaire.

La Figure B.2 présente les résultats dynamiques des deux capteurs de flux optique pour 4 niveaux d’éclairement différents. On peut constater en particulier que, grâce à ses pixels adaptatifs, le rafraîchissement de la mesure du capteur APIS est le même quelque soit l’éclairement ambiant contrairement au capteur LSC dont le rafraîchissement augmente avec la luminance. Cependant, la dispersion sur la mesure provenant du capteur équipé de la rétine APIS est plus grande et augmente avec l’éclairement ambiant.

Les deux capteurs de flux optique ont donc prouvé qu’ils sont performants et peuvent être utilisés aussi bien en intérieur qu’en extérieur. En particulier, le capteur basé sur la rétine LSC est plus précis et a un rafraîchissement des mesures plus important dans sa gamme de fonctionnement qui s’étend sur 1,5 décades de luminance alors que le capteur basé sur la rétine APIS peut mesurer des vitesses angulaires sur 3 décades d’éclairement ambiant.

I.2 Comparaison avec un capteur de souris optique

Depuis quelques années, des équipes de recherche en robotique ont commencé à utiliser des capteurs de souris optique du commerce comme capteurs de flux optique à bord de micro aéronefs volants en extérieur. Ces capteurs sont en effet disponibles sur étagère, peu onéreux et à faible consommation étant donné qu’ils sont totalement passifs ce qui les rend parfaitement adaptés pour être embarqués sur des micro robots aériens où les contraintes de masse et de consommation sont très fortes. Cependant, jusqu’à maintenant, ces capteurs ont toujours été utilisés sur des robots volants seulement en extérieur : nous étions donc curieux de mesurer leurs performances sur une large gamme d’éclairement ambiant et en particulier en intérieur où la luminance est plus faible.

Nous avons donc choisi de comparer les performances de notre capteur basé sur une ré-

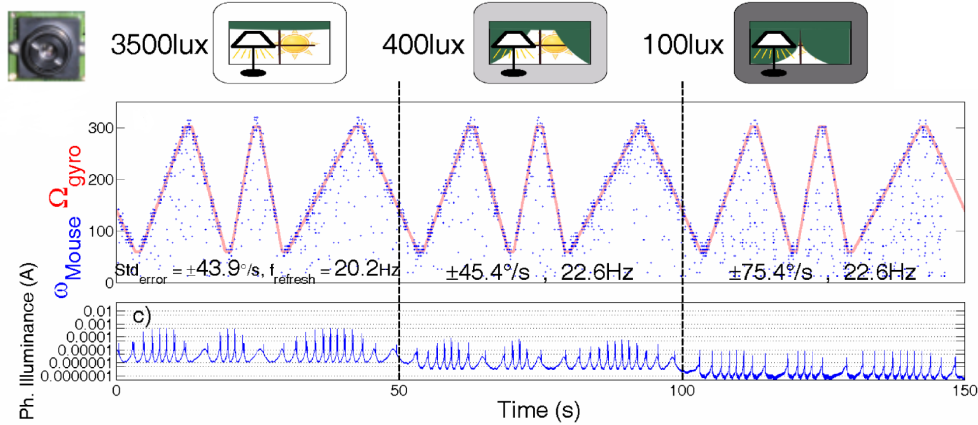


FIGURE B.4 – Réponse dynamique du capteur de souris ω_{Mouse} (points bleus) lorsque le capteur est en rotation dans un environnement stationnaire. La vitesse de rotation du capteur est contrôlée à l’aide d’un moteur à courant continu et varie entre $60^\circ/s$ et $300^\circ/s$. La vitesse de rotation imposée au capteur est représentée en rouge. On observe que la sortie du capteur est fortement bruitée et que la vitesse mesurée est très fréquemment sous-estimée. D’après (Expert et al., 2011a).

tine LSC et mesurant le flux optique à l’aide de seulement 2 pixels au capteur de souris ADNS-9500 fabriqué par Avago (Expert et al., 2011a). Nous avons utilisé le même banc de test que pour les expériences précédentes. Le capteur est placé en rotation dans un environnement stationnaire aussi bien en intérieur qu’en extérieur et la vitesse angulaire mesurée est comparée à la vitesse angulaire imposée au capteur mesurée à l’aide d’un gyromètre.

Comme on peut le constater sur la Figure B.3, la sortie du capteur de souris est très précise et fortement rafraîchie lorsque l’éclairage ambiant est important comme c’est le cas en extérieur. Ceci confirme que ce capteur est particulièrement adapté pour équiper des aéronefs volants en extérieur. Cependant, le capteur de souris a donné des résultats insuffisants en intérieur où la mesure de vitesse angulaire est très régulièrement sous-estimée (voir Figure B.4) car trop peu de contrastes sont détectés par le capteur visuel.

La conclusion de cette étude est que notre capteur basé sur seulement deux pixels est capable de concurrencer en terme de précision un capteur de souris composé de 900 pixels. Cependant, bien qu’ici une seule mesure de vitesse angulaire soit utilisée, l’avantage majeur des capteurs de souris optique est leur capacité à mesurer la vitesse angulaire selon les 2 directions orthogonales simultanément.

I.3 Réalisation d’un micro-capteur de flux optique d’un gramme

Dans les expériences précédentes, nous avons montré que nos capteurs bio-inspirés mesurant la vitesse angulaire à partir de seulement deux pixels sont précis, linéaires et robustes aux variations d’éclairage. Cependant, on peut deviner intuitivement que la mesure de tels capteurs peut être améliorée en fusionnant la sortie de plusieurs Capteurs Locaux de Mouvement (CLM) mesurant la vitesse angulaire dans une région d’intérêt.

C’est la raison pour laquelle nous avons développé un capteur de flux optique (voir Figure B.5) adapté aux contraintes importantes de masse et de consommation des micro-robots aériens (Roubieu et al., 2011, 2012). Les principales caractéristiques de ce capteur sont :

- une masse très faible inférieure à 1g (optique incluse),
- une taille réduite de $23.3 \times 12.3mm$,



FIGURE B.5 – Photo du capteur de flux optique pesant seulement 1g (taille : $23.3 \times 12.3 \text{ mm}$) composé d’une lentille (distance focale : 2 mm) placée au dessus d’une rétine LSC de 6 pixels (vue de dessus au centre) et d’un microcontrôleur 16 bit de Microchip (vue de dessous à droite). D’après (Roubieu et al., 2012).

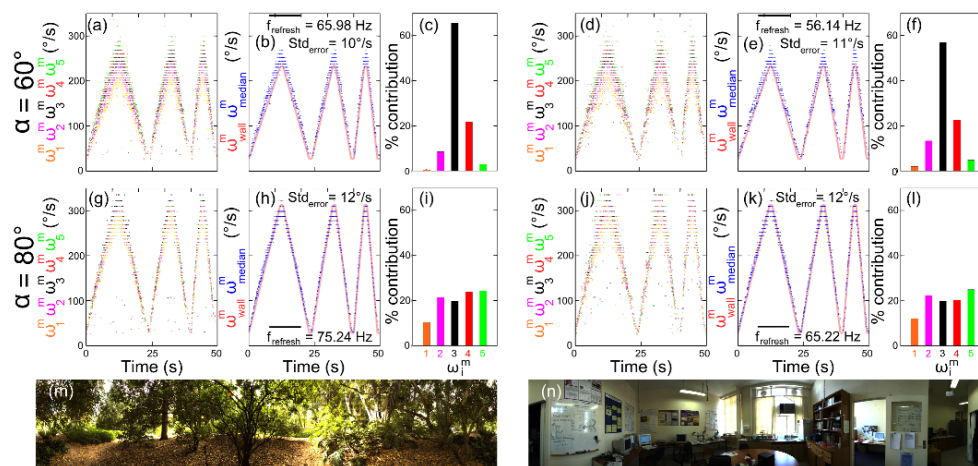


FIGURE B.6 – Réponse dynamique du capteur de flux optique composé de 5 Détecteurs Élémentaires de Mouvement mesurant le défilement angulaire d’un bandeau déroulant contrasté placé à une distance $D_h = 24 \text{ cm}$ du capteur. La réponse du capteur de flux optique est tracée pour deux angles d’orientation différents. Un moteur à courant continu est utilisé pour contrôler la vitesse de défilement du bandeau. (a), (d), (g) et (j) Réponse de chacun des 5 CLM. Etant donné l’orientation légèrement différente de chaque EMD, la vitesse angulaire mesurée diffère pour chaque capteur. (b), (e), (h), et (k) Réponse médiane du capteur avec sa dispersion (Std_{error}) et le rafraîchissement de la mesure ($f_{refresh}$). On constate qu’en prenant la médiane de la sortie de 5 CLM, on améliore fortement le rafraîchissement de la mesure tout en réduisant sa dispersion. (m) et (n) Panoramas naturels imprimés sur le bandeau déroulant utilisés pour caractériser les performances du capteur. D’après (Roubieu et al., 2012).

- une faible consommation électrique ($< 0.23W$).

Ce capteur de flux optique est basé sur une rétine LSC de 6 pixels équipée d'une lentille défocalisée lui conférant un champ de vision de 28.8° . La vitesse angulaire est mesurée à l'aide de l'algorithme du "temps de passage" calculant à 2kHz le temps de parcours d'un front de contraste défilant à la vitesse angulaire ω entre deux axes optiques formés par deux photodiodes adjacentes du capteur placées derrière une lentille.

Deux versions de l'algorithme ont été testées sur le microcontrôleur embarqué sur ce micro-capteur de flux optique.

La première version est basée sur l'opérateur médian qui fusionne 5 mesures élémentaires de mouvement pour mesurer le flux optique dans un sens préféré. Ainsi, la mesure fusionnée obtenue est plus précise et plus fréquemment rafraîchie grâce à cette médiane des 5 mesures locales. Les résultats de cette mise en œuvre sont présentés sur la Figure B.6. En comparant le résultat précédent obtenu à partir de seulement 2 pixels et la médiane des sorties de 5 mesures locales, nous montrons que la dispersion est divisée par au moins 1.7 passant de $17^\circ/s$ pour une seule paire de pixels à $11^\circ/s$ pour la médiane des 5 sorties. Dans le même temps, le rafraîchissement de la mesure est multiplié au moins par un facteur 4 passant de $15.7Hz$ à $67Hz$.

La seconde méthode de fusion permet aussi de mesurer le flux optique dans 5 directions différentes mais aussi d'en extraire le sens et la vitesse angulaire associée. Pour cela, 5 capteurs locaux de mouvement double sens sont calculés à partir des 6 pixels du capteur LSC (5 CLM estiment la vitesse angulaire dans une direction et les 5 autres l'estiment dans la direction opposée). En prenant le maximum des médians correspondant aux mesures de chaque direction, il est possible de discriminer le sens de défilement de la scène et ainsi d'estimer la direction et l'amplitude du flux optique sur la gamme $[-350^\circ/s; -80^\circ/s] \cup [80^\circ/s; 350^\circ/s]$. Les résultats de cette fusion sont illustrés sur la Figure B.7. Il apparaît que le capteur directionnel de flux optique mesure la vitesse angulaire avec une excellente précision (dispersion $< 10^\circ/s$) et linéarité (erreur de linéarité $< 1\%$) sous plusieurs luminances. De plus, aucune erreur n'est commise dans l'estimation du sens de défilement.

Ce capteur innovant de moins d'un gramme possède donc des caractéristiques idéales en termes de précision et de rafraîchissement couplées à une faible masse et une faible consommation pour être embarqués sur des micro-robots aériens.

I.4 Réduction des ressources calculatoires en interpolant linéairement les signaux visuels

Malgré les optimisations proposées au cours des précédentes études permettant de réduire le nombre d'opérations nécessaires pour calculer la vitesse angulaire à l'aide de l'algorithme du "temps de passage", la charge de calcul reste l'élément limitant empêchant d'implémenter au sein d'un même microcontrôleur un nombre plus important de CLM. En particulier, sur un robot volant, nous souhaitons mesurer le flux optique à partir de plusieurs directions et idéalement sur un large champ de vision.

Afin de réduire la charge de calcul du microcontrôleur, l'algorithme du "temps de passage" a été optimisé en interpolant linéairement les signaux visuels échantillonnés à une fréquence inférieure à la fréquence utilisée pour déterminer le retard (Expert et al., 2012). Pour cela, lors du dépassement du seuil choisi par un signal visuel, ce signal est interpolé linéairement à partir de la mesure précédente pour en déduire l'instant de dépassement du seuil avec une

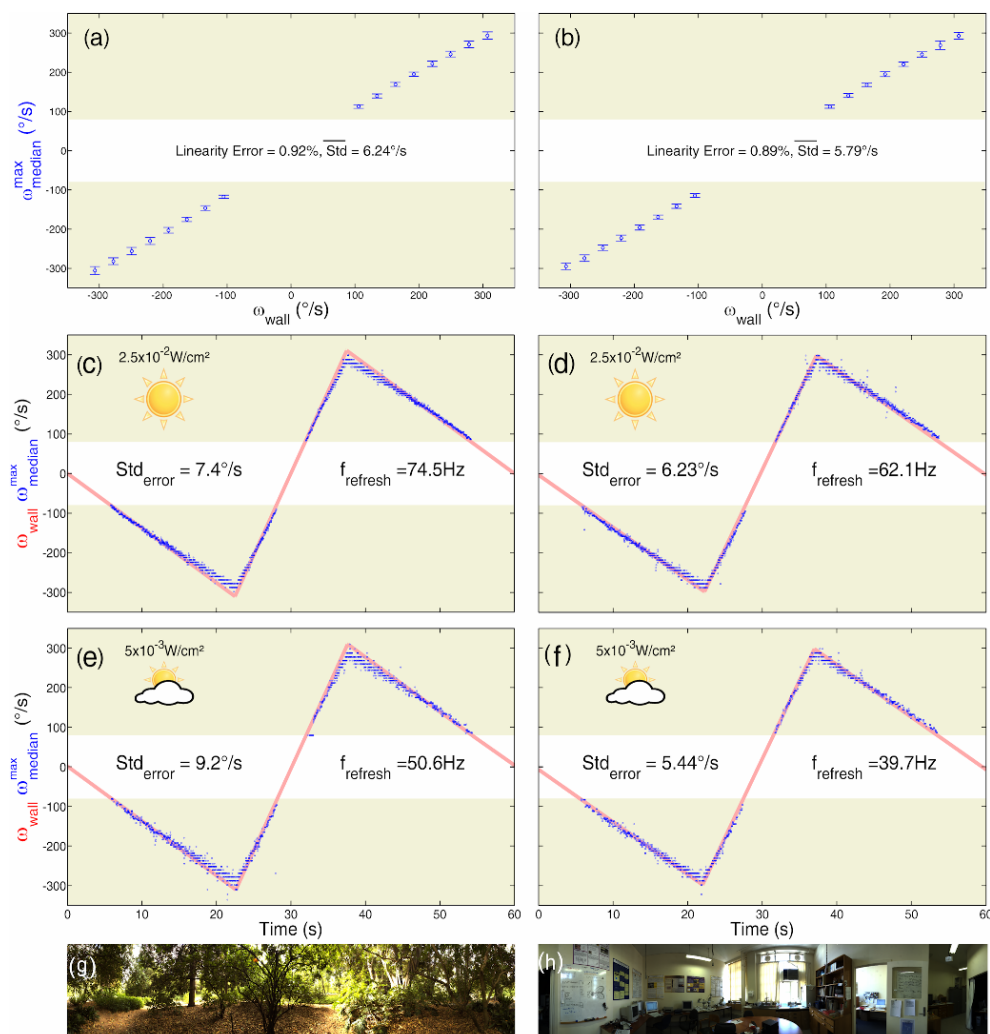


FIGURE B.7 – Réponses statique et dynamique du capteur de flux optique composé de 5 Capteurs Locaux de Mouvement double sens mesurant la vitesse et la direction de défilement angulaire d'un bandeau déroulant contrasté placé à une distance $D_h = 24 \text{ cm}$ du capteur. La réponse statique du capteur a été mesurée en calculant sur une durée de 15s et pour des pas de $30 \text{ }^\circ/\text{s}$ la vitesse de défilement du bandeau déroulant sur la gamme s'étendant de $[-315 \text{ }^\circ/\text{s}; -105 \text{ }^\circ/\text{s}] \cup [105 \text{ }^\circ/\text{s}; 315 \text{ }^\circ/\text{s}]$. A partir de la mesure moyenne pour chaque pas, l'écart à la linéarité a été mesuré démontrant la grande linéarité du capteur. On constate aussi que la dispersion des mesures est très faible grâce à l'opérateur médian. Les réponses dynamiques du capteur ont été tracées pour deux éclairagements ambiants et démontrent eux aussi une très bonne précision ainsi qu'un rafraîchissement très élevé des mesures. On constate aussi que le sens de défilement du contraste a été déterminé sans aucune erreur dans la gamme de fonctionnement du capteur. D'après (Roubieu et al., 2012).

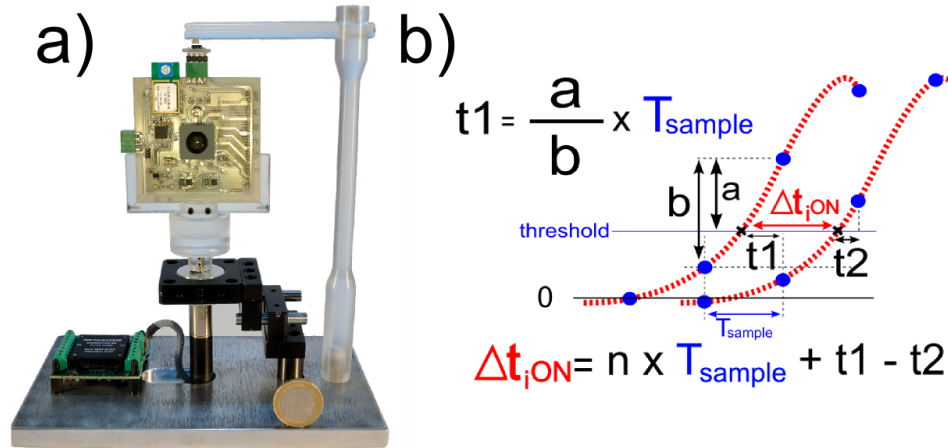


FIGURE B.8 – a) Photo de la carte électronique utilisée pour tester la nouvelle version de l’algorithme du “temps de passage interpolé”. Cette carte est équipée d’une rétine APIS composée de 25 pixels auto-adaptatifs. Chacun de ces pixels est composé d’une photodiode de $250 \times 250 \mu m$ connectée à un circuit logarithmique adaptatif ayant une dynamique de 100dB. b) Interpolation linéaire des signaux visuels permettant d’améliorer la résolution de la mesure du retard à partir de signaux échantillonnés à une fréquence T_{sample} plus faible. Dès qu’un signal dépasse le niveau de seuil, les durées $t1$ et $t2$ sont calculées pour en déduire le retard Δt_{iON} dans ce cas. D’après (Expert et al., 2012).

précision supérieure. Le retard entre les deux signaux visuels est ainsi estimé avec une haute résolution sans échantillonner à 2kHz (voir Figure B.8b).

Ce principe a été testé sur la rétine APIS composée de 25 pixels parmi lesquels une zone d’intérêt de 4×3 pixels a été sélectionnée. La mesure de vitesse angulaire a été d’abord simulée à partir de signaux acquis à plusieurs fréquences d’échantillonnage (100Hz, 200Hz et 500Hz) en plaçant le capteur de flux optique face à un bandeau contrasté défilant à vitesse variable (voir Figure B.8a).

Comme on peut le voir sur la Figure B.9 et comme on pouvait le supposer, la précision de la mesure obtenue augmente avec la fréquence d’échantillonnage mais nous avons obtenu des résultats très satisfaisants en terme de dispersion et de rafraîchissement pour une fréquence d’échantillonnage de 200Hz. C’est pourquoi cette valeur a été retenue et testée sur le microcontrôleur en comparaison avec des signaux échantillonnés à 1kHz sans interpolation (voir Figure B.10). Nous avons pu constater que la mesure interpolée est très précise et fortement rafraîchie tout en divisant la charge de calcul du microcontrôleur par un facteur supérieur à 4.

I.5 Conclusion

Toutes ces expériences ont permis de tester les performances de l’algorithme du “temps de passage” pour plusieurs rétines. Plusieurs optimisations ont été proposées permettant de réduire la charge de calcul notamment en interpolant linéairement les signaux visuels. Grâce à cela, davantage de capteurs élémentaires de mouvement peuvent être embarqués sur une même cible permettant, comme nous l’avons vu, d’obtenir une mesure plus précise, plus rafraîchie et aussi de déterminer le sens de défilement. Toutes ces caractéristiques rendent ces capteurs particulièrement adaptés pour être embarqués sur des micro-aéronefs et leur fournir des informations vitales pour contrôler de manière visuelle leur navigation.

L’ensemble de ces expériences ont été conduites pour utiliser les résultats sur le premier

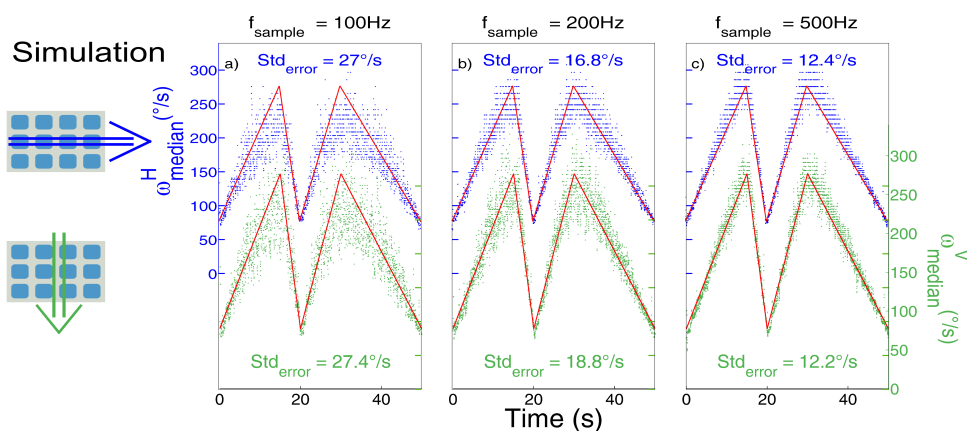


FIGURE B.9 – a-b-c) Réponses dynamiques simulées de la vitesse angulaire médiane mesurée pour trois fréquences d'échantillonnage pour un mouvement horizontal (points bleus) ou vertical (points verts). Les signaux ont été obtenus en plaçant le capteur face à un bandeau contrasté défilant à vitesse variable. Dans tous les cas, la mesure estimée en interpolant les signaux suit la valeur théorique (courbe rouge). On constate que la précision de la mesure augmente avec la fréquence d'échantillonnage et que la dispersion est faible à 200Hz. Cette valeur a été retenue car elle constitue un bon compromis entre précision de la mesure et charge de calcul. D'après (Expert et al., 2012).

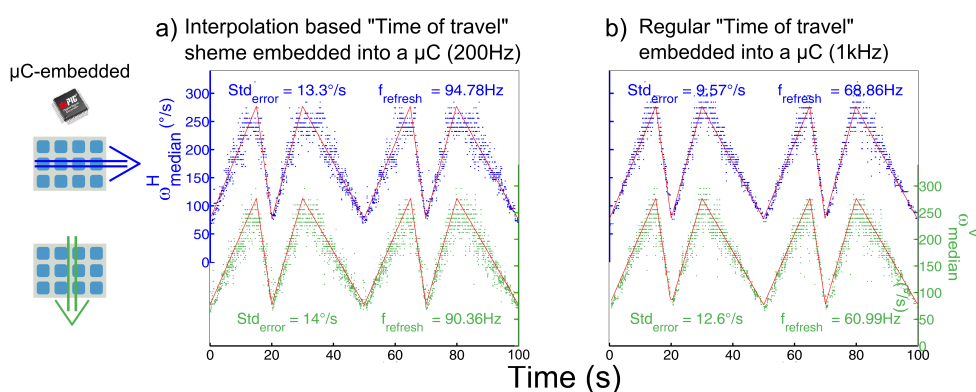


FIGURE B.10 – Comparaison entre les mesures de vitesse angulaire obtenues sur le microcontrôleur à 200Hz en interpolant les signaux visuels (a) et à 1kHz (b). Malgré une légère diminution de la précision de la mesure en interpolant les signaux visuels, la sortie du capteur à 200Hz est précise (*dispersion* < 15°/s) et fréquemment rafraîchie. D'après (Expert et al., 2012).

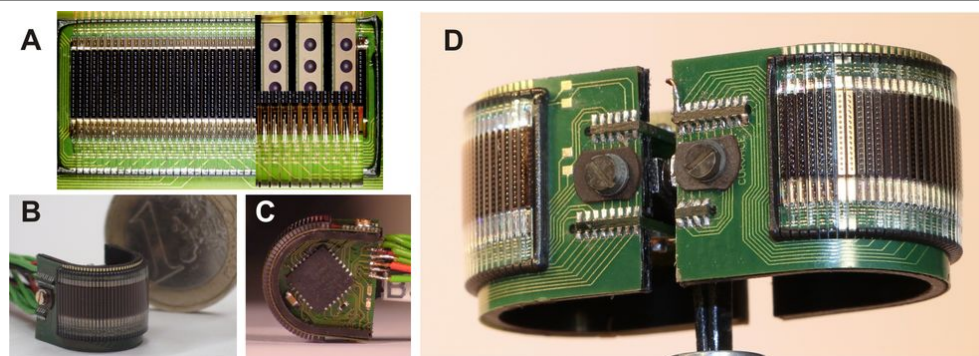


FIGURE B.11 – Photos du prototype CurvACE cylindrique. (A) Photo du capteur en version planaire après assemblage et sciage des colonnes. Sur le zoom à droite on peut observer le réseau de micro lentilles ainsi que le wire bonding connectant chaque colonne avec le PCB flexible. Le capteur peut être vu respectivement en perspective et de dessus en (B) et (C). Sur cette dernière photo, on peut voir un des deux microcontrôleurs placés sur les PCBs rigides à l'intérieur du capteur CurvACE. (D) Photo du capteur CurvACE offrant un champ de vision de 360° grâce à l'assemblage dos à dos de deux CurvACE semi-cylindriques. D'après (Floreano et al., 2013).

œil composé artificiel programmable dénommé CurvACE (Floreano et al., 2013) présentant un large champ de vision et composé de pixels s'adaptant automatiquement à l'éclairage ambiant.

II CurvACE : le premier œil composé courbe artificiel programmable

Jusqu'à maintenant, les capteurs que nous avons utilisés sont composés de quelques pixels et nous avons prouvé qu'ils permettent d'extraire avec robustesse le flux optique d'une région donnée de l'environnement. En regardant dans la nature, on peut constater que les animaux sont équipés de capteurs visuels à large champ afin de se déplacer dans leur environnement. En particulier, les insectes ailés, grâce à leurs yeux composés, peuvent détecter le mouvement dans pratiquement toutes les directions. Pour un robot volant, il apparaît évident qu'il est très utile d'être capable de regarder simultanément dans toutes les directions de l'espace en particulier pour éviter tous les obstacles. C'est la raison pour laquelle a été développé le premier œil composé artificiel programmable composé d'un réseau de micro-lentilles parfaitement aligné au dessus d'une rétine composée de pixels auto-adaptatifs développée en technologie VLSI elle-même placée sur un circuit électronique flexible. Ce capteur a été appelé CurvACE (Pericet-Camara et al., 2011).

Par comparaison avec les caméras traditionnelles, le capteur CurvACE présente un très large champ de vision de 180×60 degrés, une profondeur de champ quasi infinie, une meilleure sensibilité sans aucune aberration géométrique car la distance entre chaque pixel et sa lentille est constante. De plus, la forme du capteur permet l'intégration dans sa concavité d'unités de calcul et de capteurs comme des accéléromètres et des gyromètres qui sont utiles à la mesure du mouvement (voir Figure B.11).

Cet œil composé artificiel est composé de trois couches :

- un PCB flexible réalisant l'interconnexion entre chaque colonne du capteur CurvACE et les unités de traitement situées dans sa concavité,

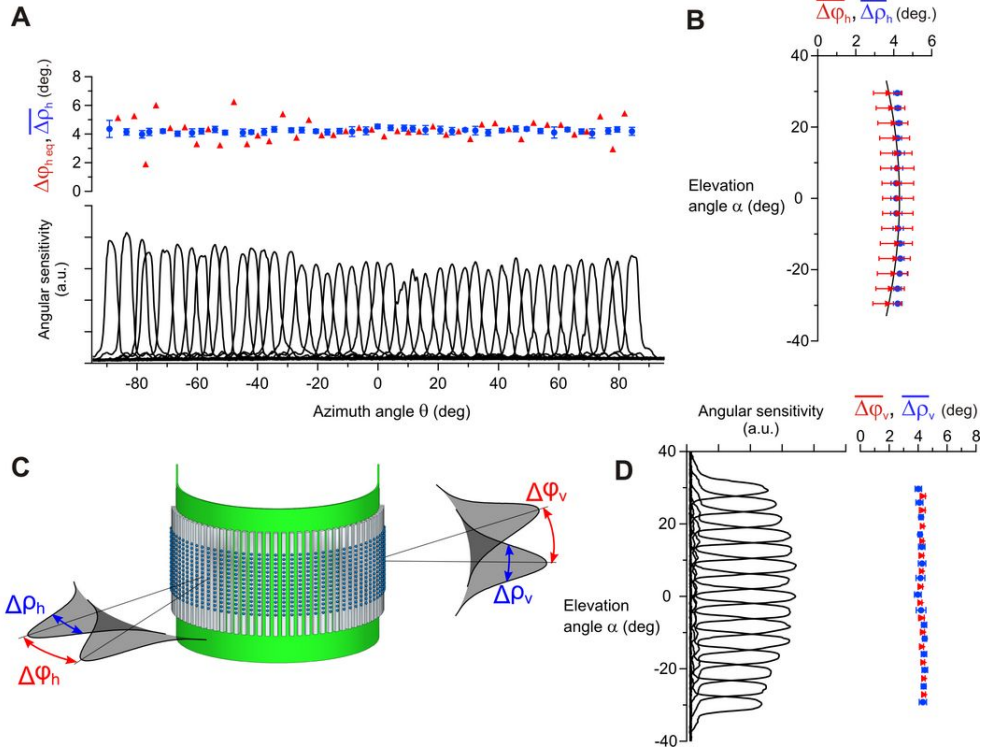


FIGURE B.12 – Caractérisation de la sensibilité angulaire du capteur CurvACE. (A-B-D) Fonctions de sensibilité angulaire mesurées selon la direction verticale et la direction horizontale. Comme représenté en (C), chaque pixel du capteur CurvACE présente une sensibilité angulaire Gaussienne due à la défocalisation de sa lentille caractérisée par ses angles d’acceptances horizontaux $\Delta\rho_h$ et verticaux $\Delta\rho_v$ et ses angles inter-ommatidiaux horizontaux $\Delta\varphi_h$ et verticaux $\Delta\varphi_v$. Conformément aux spécifications, chaque pixel présente des angles d’acceptances et inter-ommatidiaux égaux et proches de la valeur théorique de 4.2° . D’après (Floreano et al., 2013).

- une rétine composée de 42 colonnes de 15 ommatidies artificielles et où chaque colonne de 15 pixels possède son propre ADC et sa propre machine d’état,
- un réseau de micro-lentilles placé avec précision au dessus de la rétine plane.

Après superposition de ces trois couches, une technique complexe et brevetée de sciage permet de créer des colonnes de lentilles et de pixels et de courber le circuit imprimé flexible tout en conservant l’alignement des pixels avec les lentilles (Floreano et al., 2013). Ce processus présente l’avantage de pouvoir être décliné afin d’obtenir d’autres géométries de capteurs suivant les applications.

Contrairement à une caméra pour laquelle une seule lentille est placée face à la surface photosensible, chaque pixel du capteur CurvACE possède sa propre lentille qui a été volontairement défocalisée afin de lui offrir une sensibilité angulaire Gaussienne (voir Figure B.12) caractérisée par son angle d’acceptance $\Delta\rho$. La lentille va donc ainsi réaliser un filtrage spatial passe-bas facilitant l’extraction du flux optique. Les pixels sont séparés d’un angle inter-ommatidial $\Delta\varphi$ égal à 4.2° aussi bien dans la direction horizontale grâce à la courbure du capteur que dans la direction verticale grâce à un léger décalage de la distance des lentilles et du masque optique comparativement à la distance des pixels. La position des lentilles face à chaque pixel a été ajustée de manière à garantir $\Delta\varphi = \Delta\rho$.

Inspiré par le fonctionnement des rétines naturelles qui s’adaptent automatiquement à l’éclairage ambiant, les pixels du capteur CurvACE ont été réalisés en utilisant un cir-

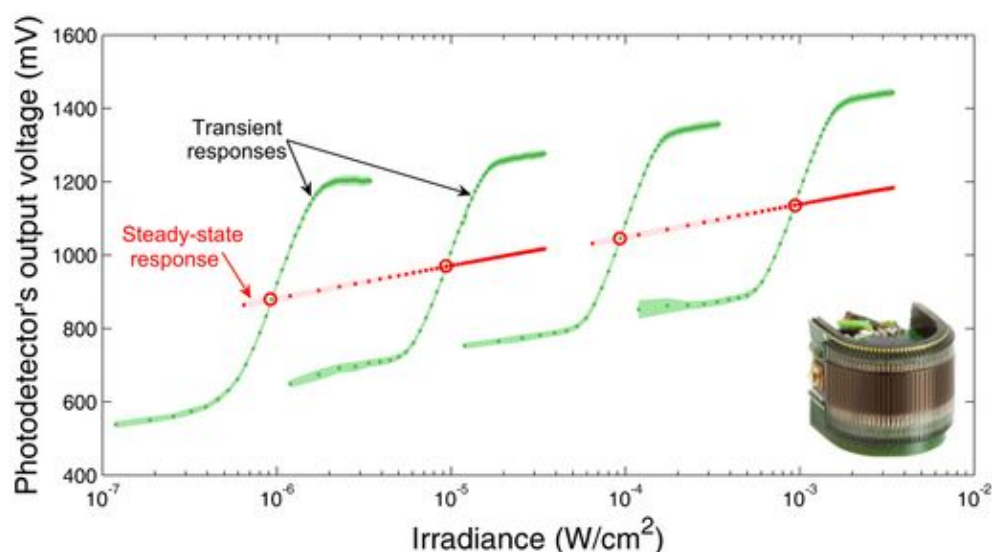


FIGURE B.13 – Capacité d’adaptation à l’éclairage ambiant du capteur CurvACE. La courbe en rouge représente la sortie des pixels en fonction de la luminance ambiante et les courbes vertes en forme de S représentent les réponses transitoires du capteur CurvACE à des incréments ou décréments de l’éclairage autour des positions représentées par les cercles rouges. Quelque soit le niveau d’éclairage ambiant, la sortie transitoire du capteur due à un contraste est similaire illustrant la capacité d’adaptation du capteur CurvACE aux variations des conditions lumineuses. D’après (Floreano et al., 2013).

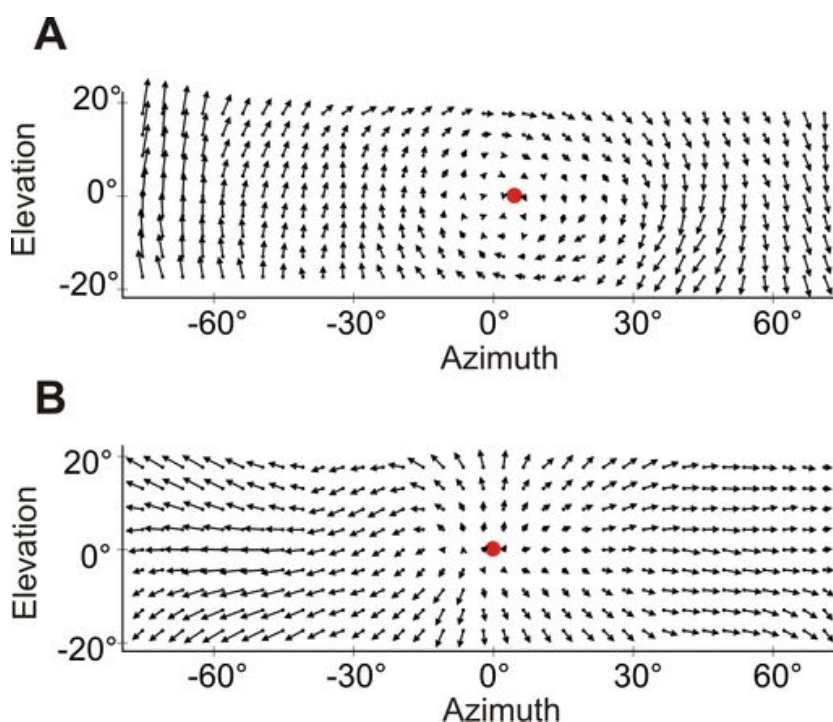


FIGURE B.14 – Champs de vecteurs de vitesses angulaires mesurés grâce aux signaux provenant du capteur CurvACE et à une version modifiée de l’algorithme de Lukas-Kanade lorsque le capteur est entraîné en rotation en roulis à $32^\circ/s$ face à un mur présentant des contrastes aléatoires blancs et noirs (A) ou bien lorsqu’il se dirige droit vers ce mur en translation à $3cm/s$ (B). Le point rouge représente respectivement le centre la rotation et le foyer d’expansion du flux optique. D’après (Floreano et al., 2013).

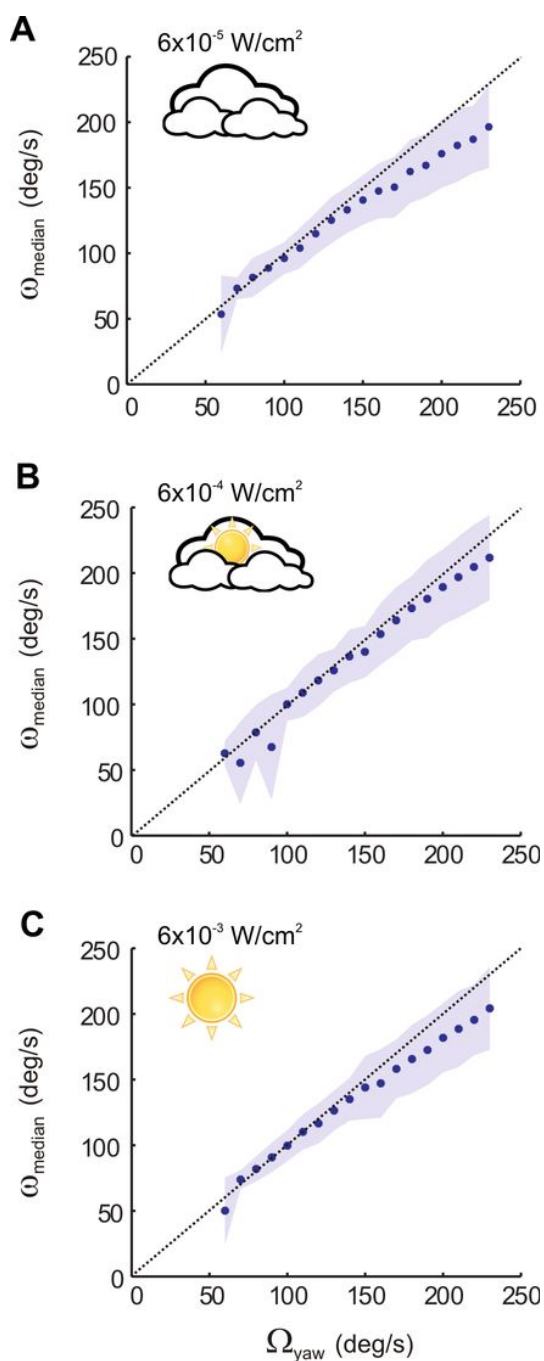


FIGURE B.15 – (A-C) Caractéristiques statiques du capteur cylindrique CurvACE mesurant le flux optique à l’aide de l’algorithme du “temps de passage” au sein d’une arène cylindrique de 105 cm de diamètre tapissée d’images naturelles. Pour trois niveaux d’éclairement, les performances du capteurs ont été mesurées à partir de la fusion des sorties provenant de 41 mesures locales de mouvement entre 2 pixels sur toute une ligne du capteur CurvACE lorsque le capteur est entraîné en rotation en lacet 10s à différents paliers séparés de $10^\circ/s$. La ligne en pointillés représente la courbe théorique. On constate que le capteur mesure la vitesse angulaire avec précision et les résultats sont inchangés suivant le niveau d’éclairement. D’après (Floreano et al., 2013).

cuit logarithmique s’adaptant automatiquement à l’éclairement ambiant sur plus de 100dB. La Figure B.13 illustre la capacité d’adaptation du prototype CurvACE car on constate que, quelque soit le niveau d’éclairement ambiant, la sortie du pixel sera similaire pour un contraste donné.

Afin de vérifier les performances du capteur CurvACE et sa capacité à mesurer le flux optique sur un large champ de vision, nous avons dans un premier temps utilisé une version modifiée de l’algorithme de Lukas-Kanade (Lucas & Kanade, 1981) pour mesurer le champ de vecteurs généré pour des mouvements spécifiques. La Figure B.14 présente le flux optique mesuré lors d’une rotation en roulis et lorsque le capteur se dirige en translation droit vers un mur contrasté. On constate que les champs de vecteurs mesurés reflètent clairement les mouvements subis par le capteur et on peut en particulier distinguer le centre de rotation et le foyer d’expansion. Dans un deuxième temps, nous avons mesuré quantitativement le flux optique mesuré à l’aide du capteur CurvACE lorsque celui-ci tourne autour de son axe de lacet dans une arène contrastée circulaire. La mesure obtenue à partir de l’algorithme du “temps de passage” peut ainsi être comparée directement avec celle d’un gyromètre. On constate sur la Figure B.15 que la vitesse angulaire mesurée suit précisément la vitesse de rotation imposée au capteur et ce quelque soit le niveau d’éclairement ambiant entre $6 \times 10^{-5} W/cm^2$ et $6 \times 10^{-3} W/cm^2$.

On a donc vu que nous avons développé dans le cadre du projet européen CurvACE le premier œil composé artificiel programmable. La version cylindrique de ce capteur a été testée et a démontré les performances du capteur pour mesurer le flux optique sur une large gamme d’éclairement ambiant sur un large champ de vision ($180^\circ \times 60^\circ$) tout en nécessitant peu de ressources calculatoires et en étant de taille et masse réduites.

Toutes ces caractéristiques font donc du capteur CurvACE le parfait candidat pour être embarqué sur des micro-robots aériens tels que le robot BeeRotor où la masse, l’énergie et les capacités de calcul sont fortement limitées.

III Le robot BeeRotor

III.1 Description du robot BeeRotor et de son environnement

Inspiré par de nombreuses expériences comportementales effectuées sur les insectes lors des dernières décennies, nous avons développé un robot aérien de 80 grammes seulement appelé BeeRotor permettant d’expliquer certaines prouesses réalisées par les insectes volants pour naviguer dans un environnement inconnu (Expert & Ruffier, 2012). En particulier, l’idée conductrice lors de la conception du robot était que les insectes se basent principalement sur leur vision et ne possèdent pas d’accéléromètre (Taylor & Krapp, 2007). De plus, pour se déplacer de manière autonome dans des environnements complexes et parfois non stationnaires, ces insectes ne semblent pas disposer d’informations sur leur altitude, leur attitude ou leur vitesse d’avance. De manière similaire, le robot BeeRotor a été équipé de capteurs sensoriels similaires à ceux existants chez les insectes ailés :

- un œil composé lui permettant de mesurer le flux optique sur un large champ de vision,
- un gyromètre qui permet, comme les balanciers chez les diptères, d’être sensible à la vitesse angulaire grâce à la force de Coriolis,
- un anémomètre sensible à la vitesse air comme les antennes et les poils des insectes.

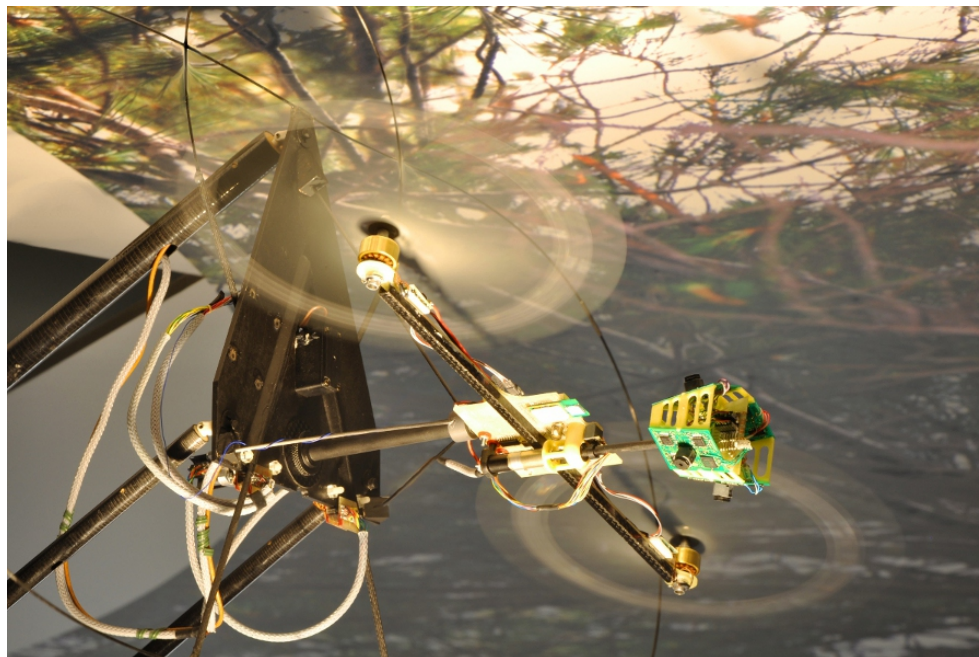


FIGURE B.16 – Photographie de l’hélicoptère captif BeeRotor dans son environnement expérimental. Ce robot de seulement 80 grammes est placé au bout d’un bras pantographique mais il contrôle de manière autonome son altitude et sa vitesse. Ce birotor est composé de deux rotors entraînés par deux moteurs Brushless contrôlant (i) l’élévation de l’hélicoptère qui dépend de la poussée moyenne imposée aux deux hélices et (ii) son angle de tangage et donc sa vitesse d’avance qui dépend du différentiel de poussée entre les deux hélices. Le robot possède aussi un moteur pas à pas pouvant orienter l’œil du robot. Ce dernier est composé de 4 capteurs visuel de mouvement mesurant le flux optique dans une région de l’espace. Le robot communique avec un PC à l’aide d’une liaison Bluetooth. D’après (Expert & Ruffier, 2012).

L’idée mise en œuvre sur le robot est de remplacer la référence par rapport au centre de la terre (repère inertiel) par une référence locale à savoir l’orientation du sol. L’ensemble des mesures utilisées par le pilote automatique est donc défini dans un seul repère associé à l’œil du robot.

La Figure B.16 est une photo du robot BeeRotor. Il est composé d’une carte électronique principale sur laquelle se trouve l’ensemble des capteurs et actionneurs du robot et sur laquelle s’effectue l’ensemble du contrôle du robot. Le robot se trouve au bout d’un bras pantographique fournissant seulement au robot son énergie et permettant de réaliser des expériences répétables. L’œil du robot (voir Figure B.17) est composé de 4 capteurs de flux optique mesurant le flux optique médian dans 4 régions d’intérêt à l’aide de l’algorithme du “temps de passage”.

L’œil du robot est découplé du corps du robot et ce degré de liberté est utilisé pour constamment réorienter l’œil du robot parallèlement à la surface la plus proche détectée par les capteurs de flux optique. Pour cela, l’ensemble des mesures de flux optique sont utilisées pour détecter, à partir de l’évolution du flux optique en fonction de la direction, l’orientation de l’œil relativement à la paroi. Cet angle est calculé à l’aide d’une approximation aux moindres carrés effectuée à l’intérieur du microcontrôleur principal sur les 10 mesures de flux optique générées par la surface la plus proche afin de déterminer l’orientation de la mesure maximale. Cette réorientation est essentielle pour naviguer de manière autonome sans connaissance de l’orientation du robot dans le repère inertiel.

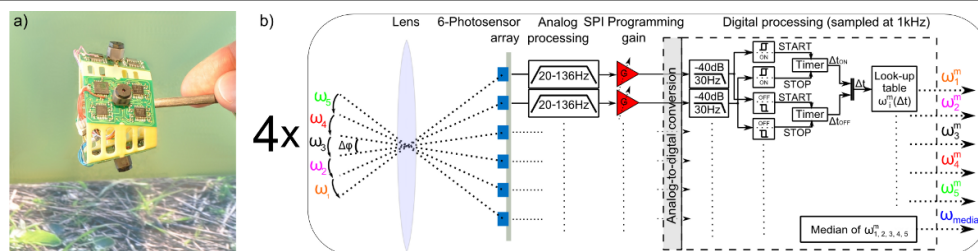


FIGURE B.17 – a) Photo de l’œil du robot BeeRotor composé de 4 capteurs de flux optique intégrant chacun une rétine LSC à partir de laquelle est mesurée la vitesse angulaire dans 5 directions grâce à l’algorithme du “temps de passage”. b) Traitement mis en œuvre sur chacun des 4 capteurs de flux optique. D’après (Expert & Ruffier, 2012).

En plus de la réorientation de l’œil, deux autres boucles de régulation sont utilisées pour contrôler l’altitude et la vitesse d’avance du robot à partir du flux optique (voir Figure B.18). A aucun moment, le robot n’a connaissance de ces grandeurs (altitude, vitesse) mais le robot est tout de même capable d’ajuster automatiquement sa distance avec les parois et sa vitesse d’avance de manière à naviguer tout en évitant les obstacles. L’altitude du robot est contrôlée grâce à un régulateur de flux optique (Ruffier & Franceschini, 2003, 2004, 2005) utilisant le flux optique maximal entre le flux optique ventral et le flux optique dorsal, celui-ci est maintenu à une valeur constante en agissant sur la vitesse de rotation des rotors. Ceci conduit à un comportement de suivi automatique de terrain. La deuxième boucle de régulation utilise la somme des flux optiques ventraux et dorsaux pour contrôler la vitesse de rotation en tangage et donc la vitesse d’avance du robot. Cette boucle repose sur deux boucles de régulation internes contrôlant respectivement la vitesse angulaire en tangage à partir de la mesure du gyromètre et la vitesse air du robot à partir de la mesure de l’anémomètre. Similairement au robot LORA dans le plan horizontal (Serres et al., 2008), l’utilisation simultanée d’une boucle régulant le flux optique maximal et la somme des flux optiques conduit le robot à automatiquement adapter sa vitesse d’avance à la taille du tunnel dans lequel il navigue. Le robot navigue dans un tunnel de 12 m de long (voir Figure B.19) dont le sol et le plafond sont tapissés d’images naturelles. Le flux optique perçu peut être fortement perturbé grâce aux reliefs placés sur le sol ainsi que les mouvements du sol aussi bien de haut en bas que d’avant en arrière.

III.2 Navigation autonome

La Figure B.20 illustre l'intérêt de la réorientation automatique de l'œil à l'aide du flux optique. En effet, en présence d'un obstacle, l'œil réorienté est capable de détecter l'augmentation de flux optique plus tôt et donc d'éviter la collision. De plus, cette réorientation permet de s'affranchir de la nécessité d'un capteur indiquant la verticale comme un accéléromètre.

Sur la Figure B.21 sont tracées les trajectoires du robot dans un environnement fortement non stationnaire. En effet, en plus des oscillations de bas en haut du sol, ce dernier tourne dans la même direction que le robot ou dans la direction opposée. Dans tous les cas, le robot a démontré sa capacité à automatiquement contrôler son altitude et sa vitesse tout en évitant les obstacles.

De plus, nous avons prouvé que le robot peut atterrir automatiquement aussi bien au sol qu'au plafond grâce à des stratégies simples utilisant le flux optique. Deux exemples ont été démontrés dans lesquels la vitesse d'avance du robot est progressivement réduite alors que le flux optique maximal généré par la surface la plus proche est maintenu constant. La Figure B.22 présente la trajectoire du robot lorsqu'on provoque un atterrissage automatique en diminuant progressivement la consigne de flux optique $\omega_{setSumOF}$ de la boucle de régulation contrôlant la vitesse d'avance du robot. On constate que cette stratégie permet d'atterrir en toute sécurité car la vitesse d'avance au moment du contact est proche de 0.

Nous avons aussi démontré sur le robot BeeRotor que ce dernier pouvait aussi voler de manière autonome sans la mesure de l'anémomètre et la boucle interne de régulation de la vitesse air. Cependant, à l'instar des insectes lorsqu'on les ampute de leurs antennes, les performances de l'hélicoptère s'en trouvent dégradées.

Enfin, nous avons démontré qu'il était aussi possible d'utiliser la mesure du flux optique vertical qui dépend du ratio entre la vitesse verticale et la distance aux parois. Cette grandeur varie fortement en présence d'une variation de relief (expansion) et peut donc être utilisée conjointement avec les autres boucles de régulation pour éviter des obstacles.

III.3 BeeRotor équipé de CurvACE

Bien que très performant, une des principales limites que rencontre le robot BeeRotor équipé de son œil composé comprenant 4 capteurs de flux optique est qu'il repose presque intégralement sur sa vision. En cas d'éclairage faible empêchant le capteur de détecter des contrastes ou au contraire trop important saturant les signaux, l'hélicoptère BeeRotor aveugle ou ébloui s'écrase après quelques secondes. C'est pour cette raison que nous avons équipé le robot de deux capteurs semi-cylindriques CurvACE montés dos à dos lui conférant un champ de vision de $360^\circ \times 60^\circ$ (voir Figure B.23).

Grâce à ses pixels adaptatifs et son très large champ de vision, il convient parfaitement aux besoins du robot. Parmi tous les pixels du capteur, 4 régions d'intérêt ont été choisies. Le robot contrôle son altitude et sa vitesse d'avance de manière similaire grâce à deux boucles de régulation maintenant une distance suffisante avec chaque paroi tout en ajustant la vitesse du robot selon la taille du tunnel à partir des mesures de flux optique données par le capteur CurvACE. Dans ces premières expériences, l'œil du robot est fixe.

Les résultats de l'hélicoptère équipé du capteur CurvACE sont présentés sur la Figure B.24. Le robot parvient à parfaitement éviter le relief au sol grâce au flux optique mesuré par le robot à partir des signaux provenant du capteur CurvACE. Nous avons montré que l'hélicoptère contrôle son altitude et sa vitesse d'avance à partir du flux optique tout en

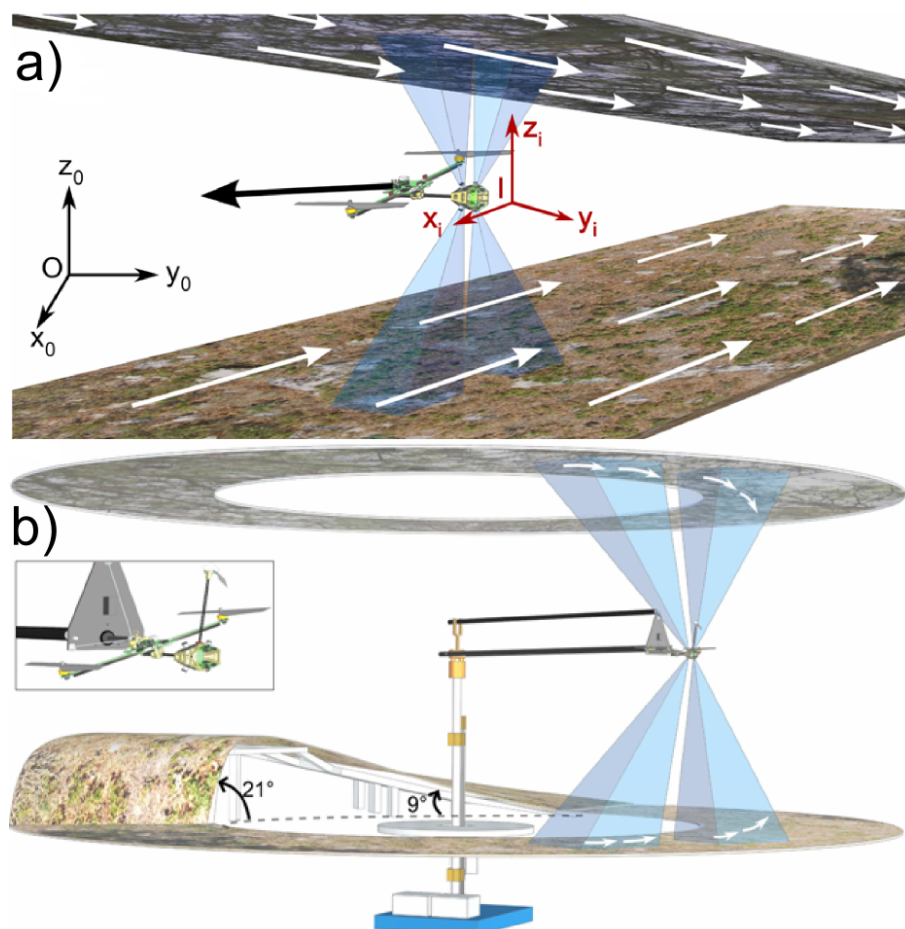


FIGURE B.19 – a) Dessin CAO du birotor et de son environnement. Ce robot navigue dans un tunnel de 12m de long dont le sol et le plafond sont tapissés d’images naturelles donnant naissance à un flux optique ventral et dorsal lors du déplacement du robot. Le robot ne possède aucune information de son altitude, son attitude ou sa vitesse dans le repère inertiel $(0, x_0, y_0, z_0)$. b) Différents reliefs ont été placés sur le sol pour tester les performances du robot lors de vol autonome en particulier sa capacité à éviter les obstacles. Le sol est contrôlé par deux moteurs permettant respectivement de le faire avancer ou reculer et de le faire monter ou descendre perturbant le flux optique ventral mesuré. L’œil du robot est composé de 4 capteurs de flux optique regardant respectivement devant au plafond, devant au sol, derrière au plafond et derrière au sol. Chacun de ces capteurs est incliné par rapport à la verticale d’un angle de 23° et possède un champ de vision de 24° .

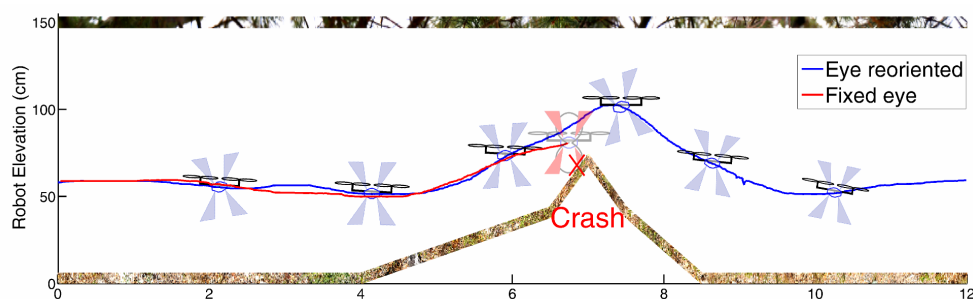


FIGURE B.20 – Trajectoires du robot BeeRotor lors d’un suivi automatique de terrain. La courbe rouge représente la trajectoire du robot équipé avec un œil fixe dans le repère du corps du robot. Comme on peut le constater, le robot ne détecte pas suffisamment tôt l’obstacle dans ce cas entraînant une collision. Au contraire, lorsque le robot possède un œil découplé se réorientant automatiquement parallèlement à la surface suivie à l’aide de sa vision, il parvient à éviter l’obstacle.

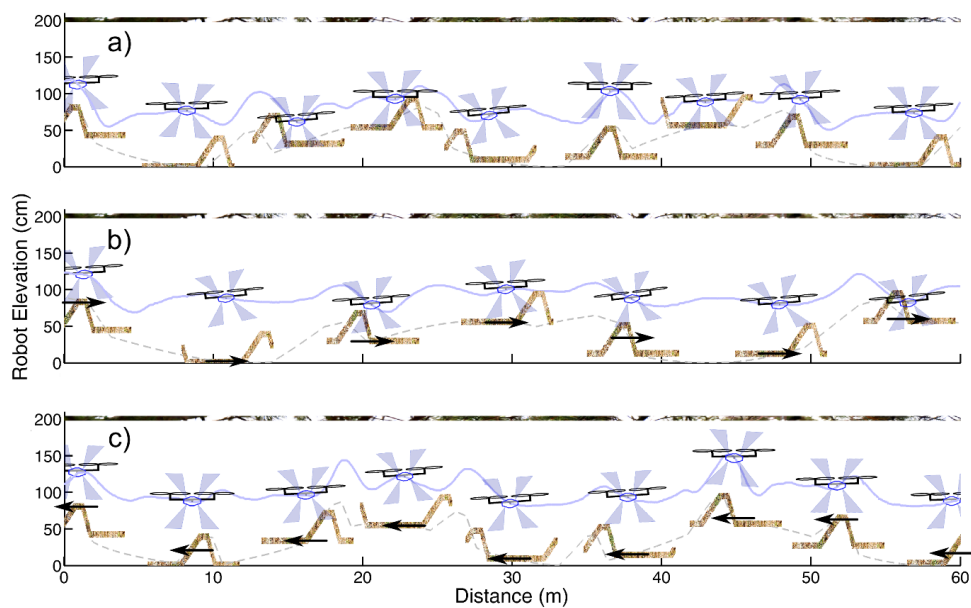


FIGURE B.21 – Trajectoires du robot BeeRotor sur 60m lors d'un suivi automatique de sol alors que ce dernier oscille de bas en haut et éventuellement avance ou recule par rapport au robot. Dans tous les cas, l'hélicoptère contrôle son altitude et sa vitesse d'avance à partir du flux optique lui assurant de garder une distance suffisante avec les parois et ainsi éviter les obstacles. **a)** Altitude du robot lorsque le sol oscille entre 0 et 64cm à une fréquence de 0.1Hz. Malgré les fortes variations du flux optique mesuré dues à l'obstacle et aux variations de la hauteur du tunnel, l'hélicoptère se déplace de manière autonome sans entrer en collision avec le sol ou le plafond tout en évitant les obstacles et en ajustant sa vitesse suivant la hauteur du tunnel dans lequel il navigue. **b-c)** Altitude du robot lorsqu'en plus d'osciller de bas en haut, le sol avance ou recule à une vitesse de 50cm/s. Lorsque le sol avance dans la même direction que le robot, ce dernier vole automatiquement à plus basse altitude et à une vitesse légèrement plus importante car le flux optique ventral perçu est plus faible est inversement lorsque le sol recule par rapport au robot.

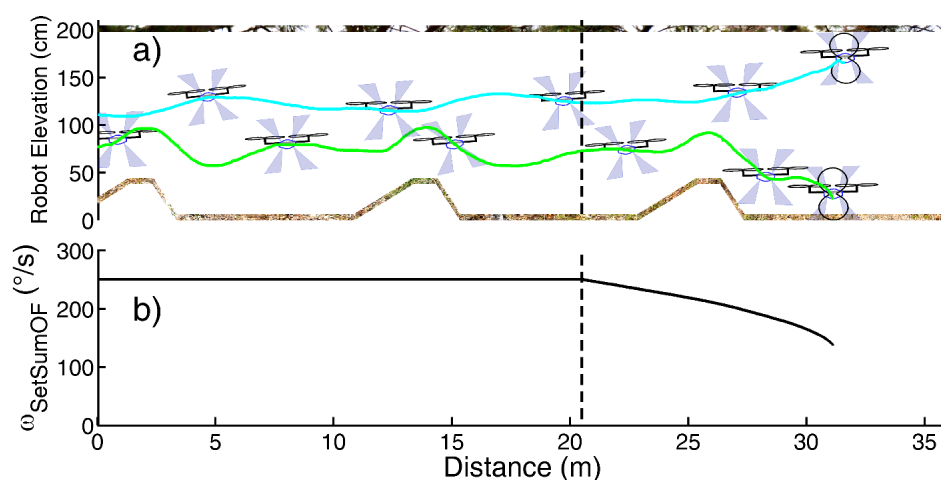


FIGURE B.22 – Atterrissage automatique au sol ou au plafond induit en réduisant progressivement la valeur de consigne $\omega_{setSumOF}$ de la boucle contrôlant la vitesse du robot. L'altitude comme la vitesse sont représentées en cyan quand le mur le plus proche détecté est le plafond et en vert dans le cas du sol. **a)** Au niveau de ligne en pointillés, l'atterrissage est provoqué en réduisant la consigne de la boucle de flux optique contrôlant la vitesse d'avance du robot. Automatiquement, cette dernière diminue alors que l'hélicoptère maintient son flux optique maximal constant en se rapprochant de la surface la plus proche. De cette manière, le robot atterrit automatiquement avec une vitesse quasi nulle au moment du contact avec le sol ou le plafond. **b)** Evolution de la consigne de la boucle régulant la somme des flux optique ventraux et dorsaux $\omega_{setSumOF}$ entraînant la réduction progressive de la vitesse d'avance de l'hélicoptère permettant un atterrissage en toute sécurité.

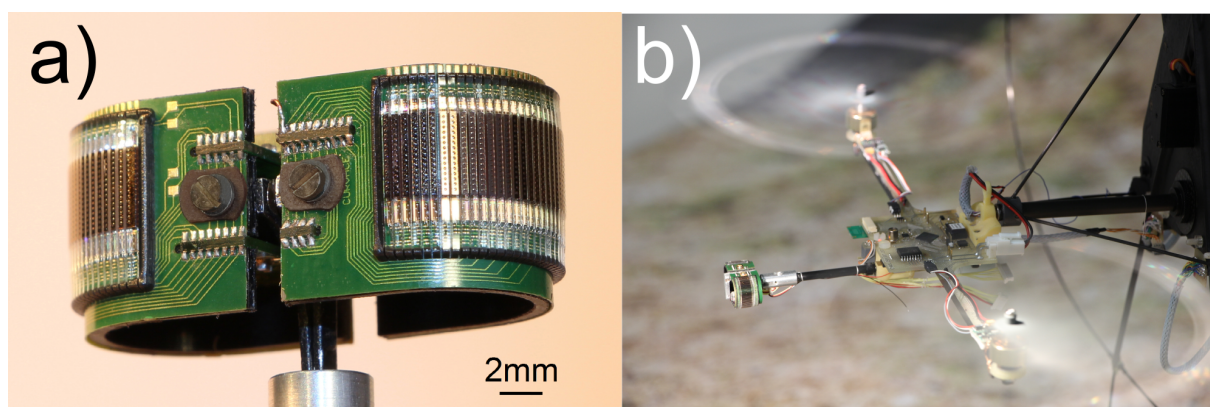


FIGURE B.23 – **a)** Photographie des deux capteurs semi-cylindriques CurvACE montés dos à dos. **b)** Photographie du robot volant BeeRotor équipé de deux capteurs semi-cylindriques CurvACE lui conférant un champ de vision de $360^\circ \times 60^\circ$.

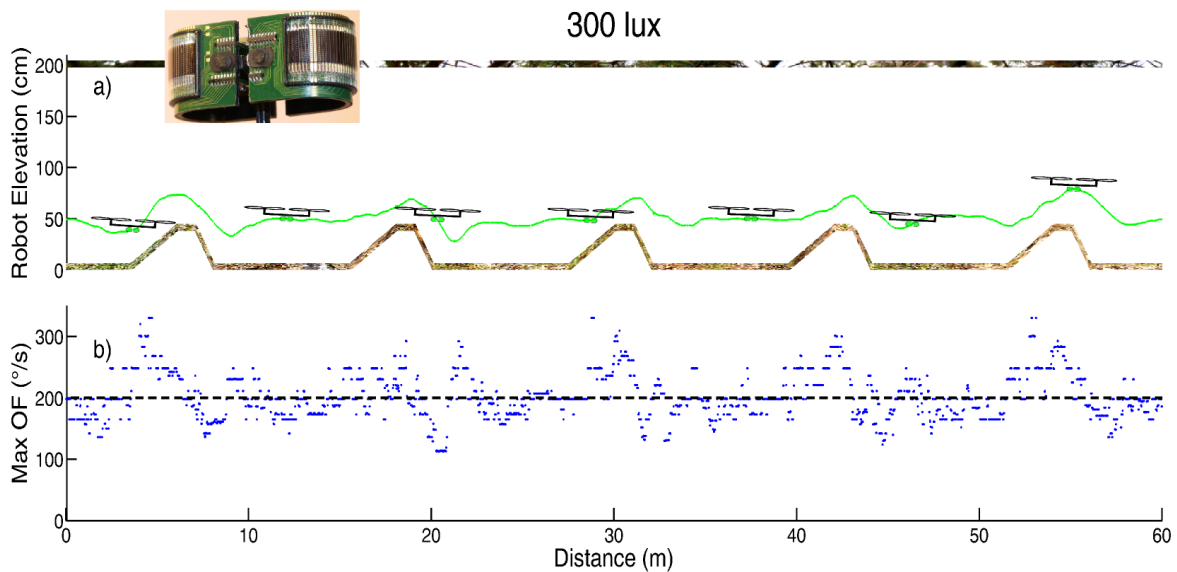


FIGURE B.24 – Trajectoires du robot BeeRotor équipé du capteur CurvACE lors d’un suivi automatique de sol à 300lux. **a)** Altitude du robot suivant le sol et évitant l’obstacle grâce aux deux boucles de régulation basées sur le flux optique mesuré à partir de CurvACE contrôlant l’altitude et la vitesse d’avance du robot. **b)** Flux optique maximal mesuré par le robot correspondant dans ce cas là au flux optique ventral. On constate que le robot maintient cette valeur autour de la valeur de consigne $\omega_{setMaxOF} = 200^\circ/s$ en agissant sur la poussée des rotors en particulier lors de l’augmentation du flux optique ventral due à l’obstacle.

évitant les obstacles pour une large gamme d’éclairement ambiant allant de 3 lux à 1000 lux même dans un environnement non stationnaire.

IV Conclusion

Dans ces travaux, trois principaux sujets ont été abordés dans lesquels la ligne conductrice était d’extraire dans les solutions existantes dans la Nature les idées permettant de développer des capteurs et des stratégies de contrôle simples pour un robot navigant de manière autonome dans un environnement complexe. Ceci nous a permis de développer et de perfectionner des capteurs de flux optique légers mesurant le flux optique à partir de diverses rétines à l’aide de l’algorithme du “temps de passage” aussi bien en intérieur qu’en extérieur. Ces expériences préliminaires ont contribué au développement du premier œil composé artificiel courbe CurvACE. Un premier prototype offrant un champ de vision $180^\circ \times 60^\circ$ a été caractérisé et sa capacité à mesurer le flux optique à partir de divers algorithmes a été démontrée. Le point d’orgue de ce travail a été le développement du robot bio-inspiré BeeRotor qui est équipé de capteurs et de stratégies de vol inspirés de ceux des insectes ailés. Se basant principalement sur le flux optique, ce robot est le premier hélicoptère à notre connaissance capable de naviguer de manière autonome dans un environnement non stationnaire tout en évitant les obstacles sans aucune connaissance de son altitude, sa vitesse d’avance ou son attitude dans le repère inertiel, c’est à dire sans accéléromètre.

Bibliographie

- Blanes, C. (1986). *Appareil visuel élémentaire pour la navigation à vue d'un robot mobile autonome*. Marseille : Master thesis in Neurosciences (DEA in French), Neurosciences, Univ. Aix-Marseille II.
- Delbrück, T. & Mead, C. A. (1994). Adaptive photoreceptor with wide dynamic range. In *IEEE International Symposium on Circuits and Systems (ISCAS)*, volume 4, (pp. 339–342)., London, UK.
- Expert, F., Roubieu, F., & Ruffier, F. (2012). Interpolation based "time of travel" scheme in a visual motion sensor using a small 2d retina. In *IEEE Sensors Conference*, (pp. 2231–2234)., Taipei, Taiwan.
- Expert, F. & Ruffier, F. (2012). Controlling docking, altitude and speed in a circular high-roofed tunnel thanks to the optic flow. In *IEEE International Conference on Robots and Systems (IROS)*, (pp. 1125–1132)., Vilamoura, Portugal.
- Expert, F., Viollet, S., & Ruffier, F. (2011a). A mouse sensor and a 2-pixel motion sensor exposed to continuous illuminance changes. In *IEEE Sensors 2011 conference*.
- Expert, F., Viollet, S., & Ruffier, F. (2011b). Outdoor field performances of insect-based visual motion sensors. *Journal of Field Robotics*, 28 (4), 529–541.
- Floreano, D., Pericet-Camara, R., Viollet, S., Ruffier, F., Brückner, A., Leitel, R., Buss, W., Menouni, M., Expert, F., Juston, R., Dobrzynski, M., L Eplattenier, G., Recktenwald, F., Mallot, H., & Franceschini, N. (2013). Miniature curved artificial compound eyes. *Proceedings of the National Academy of Sciences (PNAS)*, 110, 9267–9272.
- Franceschini, N., Riehle, A., & Nestour, A. L. (1989). *Facets of Vision*, chapter 17 : Directionally Selective Motion Detection by Insect Neurons, (pp. 360–390). Springer, Berlin, Eds : D.G. Stavenga, R.C. Hardie.
- Gibson, J. (1950). *The perception of the visual world*. New York : Boston.
- Koenderink, J. & van Doorn, A. (1987). Facts on optic flow. *Biological Cybernetics*, 56, 247–254.
- Lucas, B. & Kanade, T. (1981). An iterative image registration technique with an application to stereo vision. In *International Joint Conference on Artificial Intelligence (IJCAI)*, (pp. 674–679)., Vancouver, Canada.

- Pericet-Camara, R., Dobrzynski, M., L Eplattenier, G., Zufferey, J., Expert, F., Juston, R., Ruffier, F., Franceschini, N., Viollet, S., Menouni, M., Godiot, S., Brückner, A., Buss, W., Leitel, R. and Recktenwald, F., Yuan, C., Mallot, H., & Floreano, D. (2011). CURVACE - CURVed Artificial Compound Eyes. In *2nd European Future Technologies Conference and Exhibition (FET)*, Hamburg, Germany.
- Pichon, J., Blanes, C., & Franceschini, N. (1989). Visual guidance of a mobile robot equipped with a network of self-motion sensors. *Proceedings of SPIE, Mobile Robots IV, 1195*, 44–53.
- Riehle, A. & Franceschini, N. (1984). Motion detection in flies : parametric control over on-off pathways. *Experimental Brain Research, 54 (2)*, 390–394.
- Roubieu, F., Expert, F., Boyron, M., Fuschlock, B.-J., Viollet, S., & Ruffier, F. (2011). A novel 1-gram insect based device measuring visual motion along 5 optical directions. In *IEEE Sensors 2011 conference*, Limerick, Ireland.
- Roubieu, F. L., Expert, F., Sabiron, G., & Ruffier, F. (2012). Two-directional 1-g visual motion sensor inspired by the fly’s eye. *IEEE Sensors Journal, 13 (3)*, 1025–1035.
- Ruffier, F. & Franceschini, N. (2003). Octave, a bioinspired visuo-motor control system for the guidance of micro-air vehicles. In Rodriguez-Vazquez, A., Abbott, D., & Carmona, R. e. (Eds.), *SPIE Conference on Bioengineered and Bioinspired Systems*, volume 5119, (pp. 1–12), Maspalomas, Spain. Bellingham, USA.
- Ruffier, F. & Franceschini, N. (2004). Visually guided micro-aerial vehicle : automatic take off, terrain following, landing and wind reaction. In *Proceeding of IEEE International Conference on Robotics and Automation (ICRA)*, (pp. 2339–2346), New Orleans, USA.
- Ruffier, F. & Franceschini, N. (2005). Optic flow regulation : the key to aircraft automatic guidance. *Robotics and Autonomous Systems, 50(4)*, 177 – 194. Biomimetic Robotics.
- Ruffier, F., Viollet, S., Amic, S., & Franceschini, N. (2003). Bio-inspired optical flow circuits for the visual guidance of micro-air vehicles. *Proceeding of IEEE International Symposium on Circuits and Systems (ISCAS)*, 3, 846–849.
- Serres, J., Dray, D., Ruffier, F., & Franceschini, N. (2008). A vision-based autopilot for a miniature air vehicle : joint speed control and lateral obstacle avoidance. *Autonomous robot, 25*, 103–122.
- Taylor, G. & Krapp, H. (2007). Sensory systems and flight stability : what do insects measure and why? *Insect Mechanics and Control, 0*, 231–316.

FLYING ROBOT INSPIRED BY INSECTS: FROM OPTIC FLOW SENSING TO VISUALLY GUIDED STRATEGIES TO CONTROL A MICRO AERIAL VEHICLE

ABSTRACT: When flying in unknown environments, insects rely mostly on the angular movement of the surrounding objects of their environments on their retina called optic flow.

In this thesis, we first developed and characterized optic flow sensors robust to illuminance changes inspired by the visual system of the fly and computing the angular speed thanks to the "time of travel" scheme. In particular, we have compared the performances of sensors processing the visual angular speed based on a standard retina or an aVLSI retina composed of pixels automatically adapting to the background illuminance in indoor and outdoor environments. The results of such bio-inspired sensors have also been compared with optic mouse sensors which are used nowadays on Micro Aerial Vehicles to process the optic flow but only in outdoor environments. Finally, a new implementation of the "time of travel" scheme has been proposed reducing the computational load of the processing unit by decreasing the sampling rate thanks to a linear interpolation of the visual signals.

In the framework of the European project CurvACE, we also participated to the design and development of the first curved artificial compound eye including fast motion detection in a very large range of illuminations. In particular, we characterized such sensor showing its ability to extract optic flow using different algorithms. Finally, we also developed a tethered miniature aerial robot equipped with sensors and control strategies mimicking flying insects navigating in a high-roof tunnel. This robot may explain how honeybees control their speed and position thanks to optic flow, while demonstrating alternative solution to classical robotic approach relying on ground-truth and metric sensors. Based only on visuomotor control loops reacting suitably to the environment, this rotorcraft has shown its ability to fly autonomously in complex and unstationary tunnels.

KEYWORDS: Bio-inspired Robotics, Optic Flow, Micro Aerial Vehicle, Artificial Compound Eye, Autonomous Guidance, Collision-free Navigation

UN ROBOT VOLANT INSPIRÉ DES INSECTES : DE LA MESURE DU FLUX OPTIQUE AUX STRATÉGIES DE GUIDAGE VISUEL POUR UN MICRO HÉLICOPTÈRE

RÉSUMÉ : Lorsqu'ils volent dans un environnement inconnu, les insectes volants utilisent principalement le défilement angulaire des objets de l'environnement sur leurs rétines que l'on appelle flux optique. Dans ce travail, nous avons premièrement développé et caractérisé des capteurs de flux optique robustes aux changements de conditions lumineuses inspirés par le système visuel de la mouche et mesurant la vitesse angulaire à l'aide de l'algorithme appelé "time of travel". En particulier, nous avons comparé les performances de capteurs mesurant visuellement la vitesse angulaire à l'aide d'une rétine standard ou une rétine développée en technologie aVLSI (analog Very Large Scale Integration) composée de pixels s'adaptant automatiquement à la lumière ambiante aussi bien à l'intérieur qu'en extérieur. Les résultats de nos capteurs bio-inspirés ont aussi été comparés avec des capteurs de souris optique qui sont utilisés de nos jours sur les micro-robots aériens pour mesurer le flux optique mais seulement en environnement extérieur. Enfin, une nouvelle implémentation de l'algorithme "time of travel" a été proposée réduisant la charge de calcul de l'unité de traitement grâce à une diminution de la fréquence d'échantillonnage rendue possible en interpolant linéairement les signaux visuels.

Dans le cadre du projet européen CurvACE (Curved Artificial Compound Eye), nous avons aussi participé au développement du premier oeil composé courbé artificiel capable de mesurer le flux optique à haute vitesse sur une large gamme de lumière ambiante. En particulier, nous avons caractérisé ce capteur et montré sa capacité à mesurer le flux optique à l'aide de plusieurs algorithmes.

Finalement, nous avons aussi développé un robot aérien miniature attaché appelé BeeRotor équipé de capteurs et de stratégies de vol imitant les insectes volants et se déplaçant de manière autonome dans un tunnel contrasté. Ce robot peut expliquer comment les abeilles contrôlent leur vitesse et leur position à l'aide du flux optique, tout en démontrant que des solutions alternatives existent aux systèmes couramment utilisés en robotique et reposant sur des capteurs tels que le GPS, les capteurs de pression, les tubes Pitot.... Basé seulement sur des boucles de contrôle réagissant à l'environnement, cet hélicoptère a démontré sa capacité à voler de manière autonome dans un environnement complexe et mobile.

MOT-CLES : Robotique Bio-inspirée, Flux Optique, Micro Robot Aérien, Oeil Composé Artificiel, Navigation Autonome
